Advances in Portable TRASE MRI

by

Aaron R. Purchase

A thesis submitted in partial fulfillment of the requirements for the degree of

Doctor of Philosophy

in

MEDICAL PHYSICS

Department of Oncology
University of Alberta

Abstract

Magnetic resonance imaging (MRI) is a valuable medical diagnostic technique due to its exceptional soft tissue contrast. Unfortunately, standard clinical MRI systems have limited accessibility worldwide, especially in developing countries, due to high costs, high weight, large physical dimensions, and maintenance and operating complexity. Standard MRI systems are currently inaccessible to over half the world's population. In MRI accessible regions, they are the bottlenecks of the clinical workflow due to high patient volume and low scanner numbers. Portable, low-cost, and clinically relevant MRI systems have many applications worldwide, such as alleviating accessibility issues in developing countries, rural areas, emergency rooms and medical clinics for point-of-care diagnostic imaging. In addition, mobile MRI systems may find application in ground and air ambulance services, in the military, and even beyond Earth on long-duration spaceflight.

Standard MRI systems use gradients of the main magnetic field for spatial encoding, requiring expensive and bulky hardware. A novel MRI encoding method, called Transmit Array Spatial Encoding (TRASE), uses the phase of the radiofrequency (RF) field for spatial encoding signal rather than applying a switching B_0 gradient. TRASE removes the need for the entire standard B_0 gradient system and relaxes the main magnet's homogeneity requirement, leading to compact, lower cost, and portable MRI systems. However, the first in vivo TRASE MR wrist images, obtained in 2013, were acquired using an immobile 0.2 T magnet and with low spatial resolution due to RF hardware limitations. The objectives of this research were to (a) design and construct a new RF amplifier to improve TRASE spatial resolution; (b)

design and construct a new portable magnet for TRASE to reduce the overall weight, size and cost of the system; (c) investigate magnetic field modifications allowing in vivo TRASE imaging on the constructed portable magnet; and (d) design and construct an accurate magnet rotation system that would simplify the 2D TRASE MRI hardware and acquisition technique.

An RF power amplifier is an essential component in all MRI systems. Unfortunately, no commercial amplifier exists to fulfil the needs of the TRASE MRI technique, requiring a high duty cycle, high RF output power and independently controlled multi-channel capability. Therefore, we designed and constructed an RF power amplifier and tested it on the bench. In addition, the amplifier performance was tested using a 0.22 T MRI magnet with a twisted solenoid and saddle RF coil combination capable of single-axis TRASE. We showed that the amplifier is capable of sequential, dual-channel operation up to 50% duty cycle, 1 kW peak output per channel and highly stable 100 μs RF pulse trains. Furthermore, high spatial resolution one-dimensional TRASE was obtained with the power amplifier to demonstrate its capability.

Although TRASE resolution was improved with the new RF amplifier, the main magnet prevents portability and has high associated costs. Recently designed Halbach magnets, made of permanent magnet blocks distributed around a cylinder, used for portable MRI systems are much lighter and more compact than standard biplanar permanent or superconductive magnets. However, improved designs and manufacturing techniques aiming at a lower weight and smaller external size are of continuing interest, especially for space flight applications. In this work, we designed and constructed a 67 mT Halbach magnet with a very low aspect-ratio (length per inner diameter $\sim$ 1:1) that produces almost identical homogeneity (11,152 ppm) as simulations (11,451 ppm) within a 12.7 cm diameter, 1 cm long cylinder region of interest (ROI). The magnet support structure was 3D printed ring-by-ring and assembled coaxially. The final magnet weight is only 25 kilograms and may be disassembled for

transportation.

Although the constructed Halbach magnet is compact and portable, the remaining field inhomogeneity is not well suited to slice selection using the twisted-solenoid TRASE RF coils. Therefore, the bare Halbach magnet's field requires adjustments for in-vivo TRASE MRI. As a first approach to field adjustments, a simulation study was completed to determine the feasibility and performance of various permanent magnet block configurations used as a shim array to achieve a desired target field in the ROI. Although the presented shim arrays would be inexpensive and straightforward to manufacture, excitation volumes are always present outside the ROI, requiring further field optimization or development of a new receive system to allow in-vivo TRASE.

Despite the magnet's field inhomogeneity, magnet rotation allows a 2D TRASE image acquisition using two RF transmit coils rather than three, significantly reducing challenges with RF coil decoupling and reducing costs due to one less required RF amplifier channel. Accurate and high-resolution angular rotation of the Halbach magnet was achieved using an inexpensive stepper motor and driver. The proof-of-concept was verified by obtaining a set of 1D TRASE projections and using this data in a 2D TRASE reconstruction technique.

Preface

A section of Chapter 3 was published in the journal Magnetic Resonance Materials in Physics, Biology and Medicine (MAGMA):

Purchase AR, Palasz T, Sun H, Sharp JC, and Tomanek B. (2019). *A high duty-cycle, multi-channel, power amplifier for high resolution radiofrequency encoded magnetic resonance imaging.* Magn Reson Mater Phy. 32, 679-692.

I, Aaron R. Purchase, contributed to the design, construction and bench performance testing, MRI experiments and TRASE acquisition, manuscript drafting and critical revisions for the MAGMA publication. Dr. Boguslaw Tomanek, the principal investigator, significantly contributed to the writing and editing process and construction and performance testing. Dr. Tadeusz Palasz contributed to the initial design conception and provided technical support throughout the project. Dr. Hongwei Sun and Dr. Jonathan C. Sharp contributed significantly to the design dissemination for MRI experiments, TRASE experiments, and manuscript review.

A section of Chapter 4 was published in the journal of the Institute of Electrical and Electronics Engineers (IEEE) Access:

Purchase AR, Vidarrson L, Wachowicz K, Liszkowski P, Sun H, Sarty GE, Sharp JC, and Tomanek B. (2021). *A short and light, sparse dipolar Halbach magnet for MRI.* IEEE Access, Vol. 9, pp. 95294-95303.

For the IEEE publication, I, Aaron R. Purchase, contributed to most of the conception, design and construction of the magnet; B_0 mapping apparatus and 3D mapping of the magnets field; and manuscript drafting, revisions and critical revisions. Dr. Boguslaw Tomanek, the principal investigator, contributed significantly to manuscript editing and critical revisions. Dr. Logi Vidarsson contributed to the initial design approach and final manuscript editing. Dr. Keith Wachowicz contributed to the optimization technique and final manuscript editing. Dr. Piotr Liszkowski and Dr. Hongwei Sun contributed to the initial design approach and manuscript editing. Dr. Gordon E. Sarty contributed to the initial design approach considering the magnet's application to an MRI system on the International Space Station and final manuscript editing. Dr. Jonathan C. Sharp contributed to the initial design, application to TRASE MRI, and critical manuscript review.

Chapter 5 (magnet shimming) is a first-author manuscript. I, Aaron R. Purchase conducted the simulation study and field analysis of various permanent magnet arrays and their impact on the magnetic field produced by the constructed Halbach magnet. The purpose of the study was to search for best-performing designs that allow in-vivo TRASE MRI using the twisted-solenoid RF coils. Chapter 6 (magnet rotation) contributes to a larger ongoing portable TRASE project, and I will be a co-author of the manuscript. I, Aaron R. Purchase, designed and constructed an accurate rotation system for the constructed Halbach magnet and wrote the code for 2D TRASE reconstruction from the 1D TRASE radial data.

Acknowledgements

The research presented in this thesis was funded by the Natural Sciences and Engineering Research Council of Canada (NSERC), Grant numbers: RGPIN-03992 and RGPIN-2020-04414, and personally by the NSERC Postgraduate Scholarship-Doctoral Award.

This work could not have been completed without the support and guidance of many research colleagues, family members, and friends.

I would like to express my sincere gratitude to my supervisor Dr. Boguslaw Tomanek for the patience, motivation, and immense knowledge shared throughout my entire education at the University of Alberta (UofA). I am extremely grateful for his foresight and guidance, our inspiring discussions, and his trust in me to acquire knowledge and apply it safely in the laboratory, making the learning process much more meaningful.

I would also like to extend my appreciation to Dr. Jonathan Sharp for insightful discussions within and beyond research and for helping me to sharpen my ability to think critically and coherently. Special thanks to Dr. Gordon Sarty for many deep discussions that oriented my Ph.D. thesis toward portable MRI and MRI in space.

I am extremely grateful to committee members Dr. Keith Wachowicz, Dr. Nicola De Zanche, and Dr. B. Gino Fallone whom all provided valuable feedback and support throughout my graduate experience. Thank you Dr. Alan Wilman for taking part in my candidacy examination and defense, and Dr. Hans Jans for an active role during my candidacy examination. Thank you as well to Dr. J. Thomas Vaughan for serving as an external reviewer for my thesis and during my defense. All members and

examiners provided insightful questions and inspiring discussions during candidacy and defense, further strengthening the research presented in this thesis.

Many thanks to all the Medical Physics graduate students at the Cross Cancer Institute (CCI) for always being available and interested in taking discussions anywhere no matter how busy things were. A special thanks to fellow graduate student and collaborator Dr. Hongwei Sun for regular coffee breaks and food runs which ultimately led to discussions that rejuvenated curiosity and empowered design.

I thank Dr. Vyacheslav Volotovskyy (CCI), Dr. Tadeuz Palasz (Jagiellonian University), Dr. Piotr Liszkowski (AGH University of Science and Technology), Mr. Curtis Osinchuk (CCI), and Mr. Lance Spiridon (CCI) for technical support through my graduate journey, as well as the Medical Physics Division at the CCI for access to Opera3D magnetostatics simulation software and administrative support (Debbi Howorko, Brenda Sheen, Jocelyn Martin). I'd like to acknowledge Jen Freund in the Department of Oncology at the UofA for organizing the many parts associated with my Ph.D. journey, defense, and completion.

None of this research would have been possible without my family, especially my wife, Heather. She has been an incredible support for me from the very beginning: when I decided to quit teaching and do a second undergraduate degree, to when I chose to pursue a graduate program with a newborn at home, and now to the US as I embark on a journey into a post-doc position. Not once has she lost sight of my potential, even when quite often I did not have any faith in myself. I would also like to acknowledge that my daughter, Nina, has been a grounding figure for me as a graduate student. Her playful and goofy personality has consistently reminded me to stay focused and not lose sight of my goals.

Thank you to my mother, Brada, for her love, care, and wisdom such as "stop over-thinking everything" which became extremely valuable in research; it allowed me not to lose sight of the true objective. Joe, Paul, Deep, Danny, and Kim, thank you as well for your endless encouragement throughout this journey.

Finally, thank you to my late father, Derek, for embedding in me from a very young age the importance of a meaningful education, inspiring me to discuss and question everything. This whole endeavour started because of him.

Table of Contents

List of Tables

List of Figures

Chapter 1

Overview and Motivation

1.1 Background

Magnetic resonance imaging (MRI) provides high quality diagnostic images for an extensive range of diseases (in particular, cancer, neurological disorders or osteoporosis), among other imaging techniques, such as Computed Tomography (CT) and Ultrasound (US) [1, 2]. Nevertheless, CT scanners are still used today for diagnosis of many diseases such as stroke and US has greatly improved patient management such as maternal health. However, MRI provides important information, such as detailed quantitative and qualitative data regarding internal structures, physiological functions and molecular compositions of human tissues [3]. Figure 1.1 compares CT images of brain tumors to various MRI techniques [1]. Similarly, Figure 1.2 shows the advantages MRI offers compared to US in fetal and neonatal brain imaging [2].

MRI, a non-invasive and non-ionizing radiation imaging method, is possible due to the nuclear magnetic resonance (NMR) phenomenon. The NMR phenomenon is based on the interaction of atomic nuclei that possess intrinsic angular momentum (i.e., spin), such as protons, with static (B_0) and alternating (B_1) magnetic fields. Since human tissue contains water and fat, a source of many protons, the polarizing B_0 creates a net magnetization (M) from a collection of spins which is detectable when applying an alternating B_1 field. In addition to the B_1 field, magnetic field B_0 gradients are applied in three dimensions for spatial localization of the protons. The

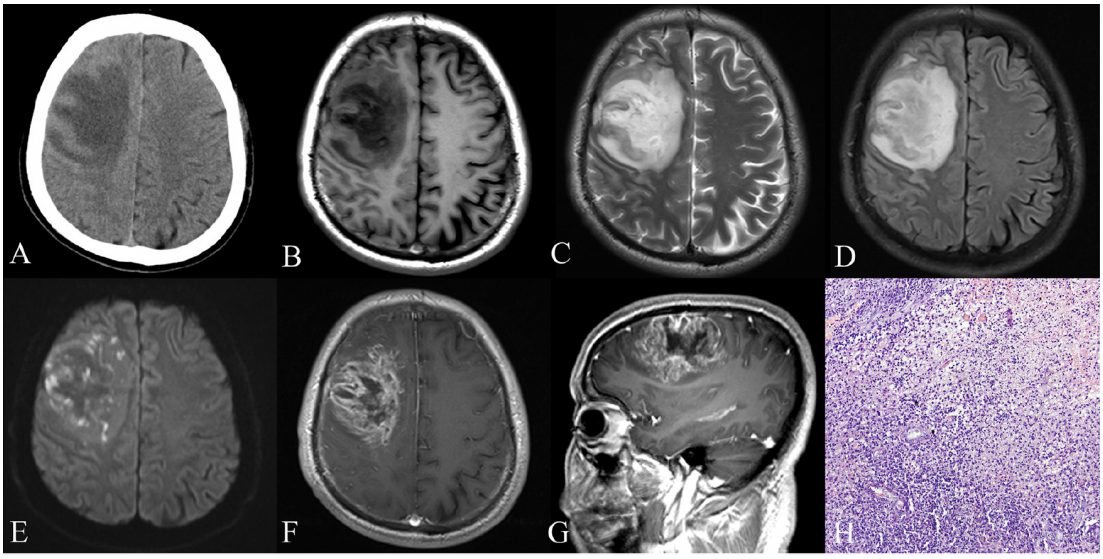

Figure 1.1: Images of the same brain using different diagnostic techniques [4]. A non-enhanced CT image of the brain compared to various MR imaging techniques. (A) CT, (B) T_1-weighted, (C) T_2-weighted, (D) FLAIR, (E) diffusion-weighted, and contrast-enhanced (F) transverse and (G) sagittal MRI images. (H) Histology confirmed a non-malignant brain lesion. Figures obtained from Huang et al. (2018) [4] with permission under the CC-BY-4.0 license.

subtle differences in proton density and/or relaxation times allows high-quality MRI of human anatomy. For this discovery, Peter Mansfield and Paul Lauterbur won the 2003 Nobel Prize in Physiology and Medicine [3]. Moreover, MRI is not limited to proton detection but can be applied to many other biologically relevant nuclei such as sodium-23 [5] or phosphorus-31 [6].

The first MRI systems were low-field (LF) systems (Figure 1.3); however, today, high field (HF) MRI systems represent about 85% of the market size in Europe and North America [7, 8]. Interestingly, in 1983, researchers proposed the application of a compact and easy to install very low-field (20 mT) MRI system for emergency use yet with moderate commercial and clinical success [9]. Nevertheless, faster MRI scanning studies more applicable to the clinic were enabled by higher field MRI systems, since stronger magnetic fields provide stronger MR signal per time (see Equation 2.8 and discussion of signal-to-noise in section 2.1.4) [8, 9]. Although HF MRI systems dominate, LF MRI systems are currently also used in the clinic due to novel hard-

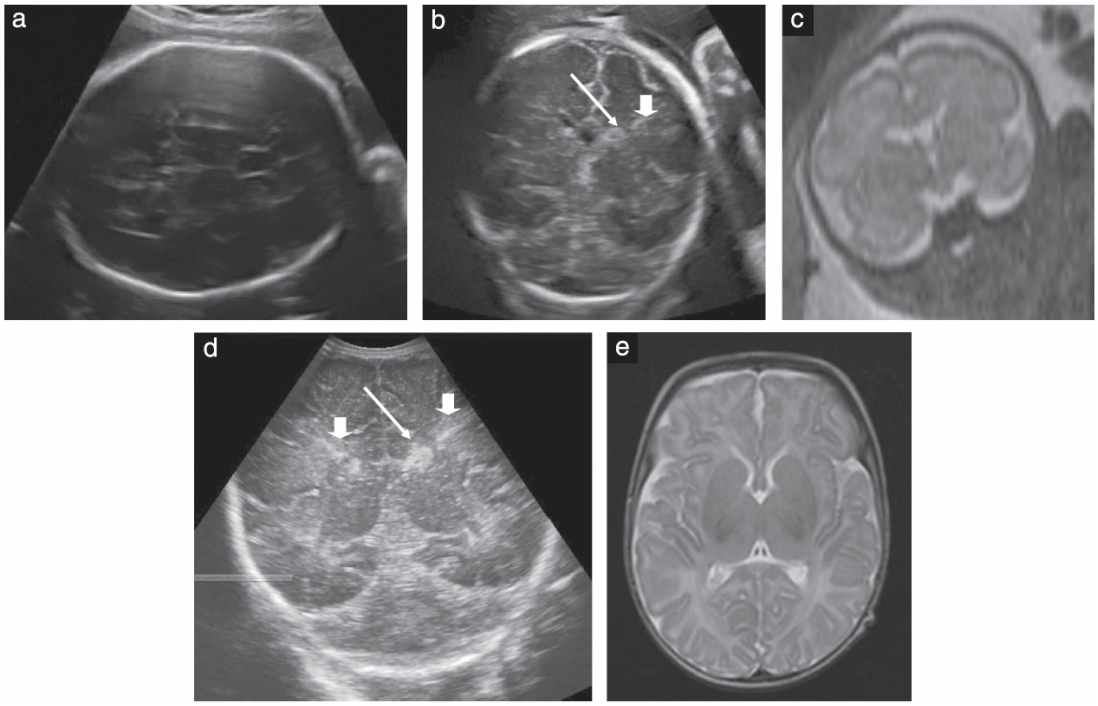

Figure 1.2: Images of the same brain using ultrasound and MRI scanners [2]. Fetal (a-b) ultrasound images and (c) T_2-weighted MRI scan. (d) Neonatal ultrasound compared to the (e) MRI scan. Figures obtained from Knoop et al. (2020) [2] with permission under the CC-BY-NC-ND license.

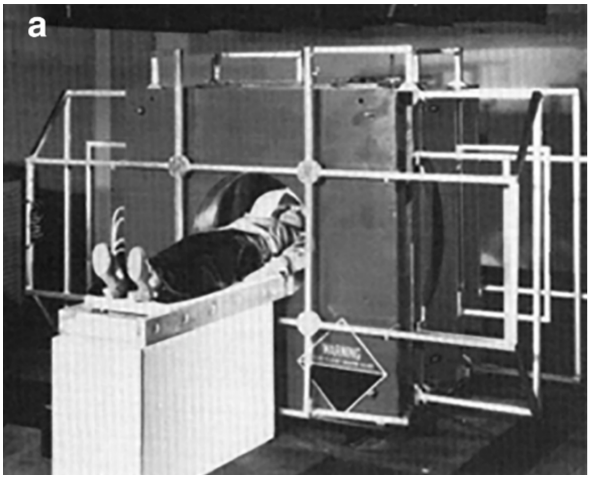

(b) Classification	MRI Field Strength
Ultra-high field (UHF)	> 7 T
Very-high field (VHF)	3 - 7 T
High field (HF)	1 - 2.99 T
Low field (LF)	1 mT - 0.99 T
Ultra low field (ULF)	< 1 mT

Figure 1.3: (a) One of the first MRI systems capable of producing human images was housed in Paul Lauterbur's laboratory [7]. It comprised an electromagnet generating a magnetic field strength of ∼93.9 mT (b) Classification of MRI systems by field strength [8]. Figure (a) obtained and modified from Marques et al. (2019) [7] with permission under the CC-BY-NC-ND license and table (b) was modified from Sarracanie et al. (2020) [8] with permission under the CC-BY license.

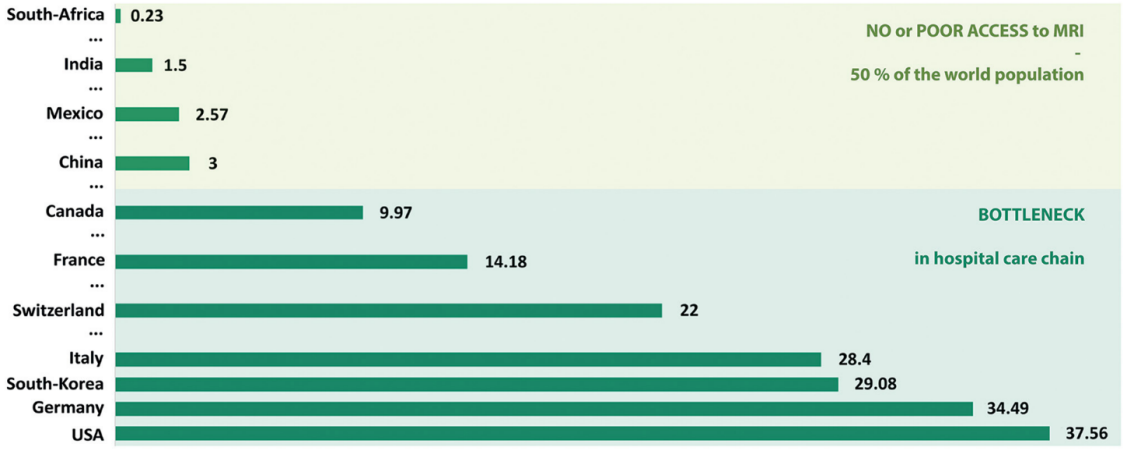

Figure 1.4: Global statistics regarding the number of MRI scanners per million people by country [8]. Figure obtained from Sarracanie et al. (2020) [8] with permission under the CC-BY license.

ware developments and techniques, such as parallel imaging or high quality gradients, enabling high resolution imaging within a reasonable scanning time [10]. These LF systems provide some advantages over high field systems, such as an open geometry allowing easier patient access, lower specific absorption rate (SAR) and easier integration with therapeutic equipment, such as the Linac-MR for adaptive radiation therapy [11]. Furthermore, LF systems may provide better contrast for certain tissues, for example, gray and white brain matter due to larger relaxation time differences at lower fields [12, 13].

Despite the importance for healthcare, MRI has limited accessibility worldwide. Currently, 54% of the world's population has only 1 MRI unit per 1 million people, and over 90% of developing countries has no access to MRI (Figure 1.4) [8, 14–16]. MRI systems are disproportionately available in high income regions; while in regions such as West-Africa only 85 MRI scanners serve a total population of 350 million, correlating with the countries low gross domestic product [16]. In addition, eleven countries in Africa with a population between 1 to 67 million have no MRI scanners [14]. While small amount of MRI scanners remain an issue in developing countries, MRI systems have become the bottlenecks of the clinical workflow contributing to

longer patient wait times in the developed countries (Figure 1.4) [8]. The current MRI research and clinical landscape focuses on improving sensitivity, spatiotemporal resolution and contrast agents, which promotes the model of "a general-purpose MRI scanner in a centralized healthcare location" to image all human body parts [17]. A recent survey reported that medical institutions in Canada had a median number of 1000 patients on a waitlist for an MRI exam; while some patients were waiting three years [18]. However, the survey noted that urgent cases for MRI exams are completed within 24 hours [18]. Strategies for dealing with long wait times put demands on facility personnel to increase MRI operation hours, purchase more scanners or upgrade current MRI systems to scan faster [18]. Although MRI is accessible in these locations, the immobility of MRI systems prevents access for certain patients such as newborns in the neonatal intensive care unit (NICU), since it is often life-threatening to move neonates to the MRI within a hospital [19]. Portable and low-cost MR systems could potentially alleviate many global healthcare pressures.

Although modern commercial MRI scanners can generate diagnostically useful images, they require ample dedicated physical space, have high purchasing costs (∼$1M CAD per 1T) and maintenance costs (∼$0.20M CAD per year). Standard MRI systems are also loud, immobile (although vehicle-mounted standard MRIs are feasible [20]), and require trained personnel to operate. These MRI disadvantages bring challenges to global healthcare systems [14–16]. Considering magnets used in standard clinical MRI systems, superconducting coils are used to produce a field strength of 1.5 T or 3 T. Superconducting magnets produce a homogeneous and strong magnetic field over a large imaging region (∼ 50 cm diameter sphere) [21]. Unfortunately, superconducting wire (kilometres of length is needed) is expensive and must be placed inside a large cryostat. The magnets are large (typically $>$ 2 m outer diameter and $>$ 2 m long) and heavy (3-6 tons) [21]. Considering a clinical 1.5T MRI scanner that costs a total of $800k USD (∼$200k USD for components assuming a 4× estimated markup), a recent paper identified that the magnet and cryostat hardware compo-

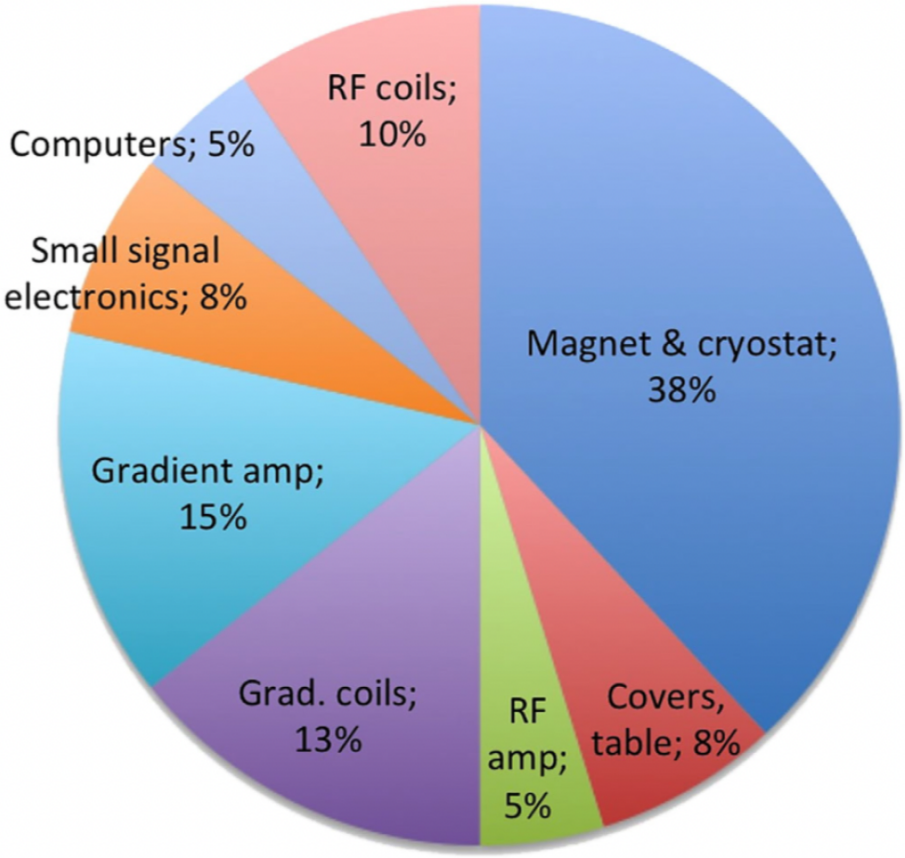

Figure 1.5: The estimated hardware "parts" costs for a new, low-end 1.5T MR scanner [17]. The authors note that these costs depend on the detailed specifications and are proprietary figures in the industry. Figure obtained from Wald et al. (2020) [17] with permission from John Wiley and Sons under license number 5324531161083.

nents alone contribute more than $76,000 USD of the total MRI system (Figure 1.5) [17]. Cryogen-free superconducting magnets are available but are similar in size and are as expensive as cryogenic versions [22], [23]. Permanent magnets producing a lower field (0.2 T or 0.5 T) are available, such as the 4-post or C-shape designs, but are even heavier than superconducting magnets due to the required magnetic pieces and steel yoke structure [21, 24].

In addition to sophisticated magnets, standard MRI systems contain complex and expensive switching gradients to generate the high-quality MR images, contributing to its limited accessibility. The MRI gradient amplifiers usually weigh over 200 kg and require a stable three-phase power supply and often water cooling [8, 17]. Stable

three-phase power is an issue for many developing countries due to frequent power outages and is not available for mobile MRI systems that are transportable on Earth or during space flight [14, 16]. In addition, the gradient coils reduce space available for the patient imposing an even larger size requirement for magnets. Wald et al. (2020) indicate that the hardware costs associated with the gradient coils and amplifiers needed for a clinical MRI system exceeds $56,000 USD (Figure 1.5) [17].

Considering progress in MRI technology, LF MRI hardware brings an opportunity for more portable MRI systems. An example is the first mobile MRI system that obtained FDA clearance, the "Swoop" MRI developed by Hyperfine Inc., Guilford, CT, USA (2020). The MRI system allows brain hemorrhage assessment in emergency departments and pediatric neurodevelopment studies [25]. The company recently announced global expansion starting in the United Kingdom and Pakistan, and one system is already used at a rural clinic in Canada [26]. The Swoop MRI system has many advantages, such as user-friendly operation with an Apple iPad and compact size (<140 cm tall; <86 cm width) that a technologist or nurse can move to the patient bedside with motorized wheels driven with a joystick [25]. The company claims a 35-fold reduction in power consumption (requires only a regular 110 V, 15 A power outlet), 20 times reduction in cost and a total weight of $\sim$ 650 kg ($\sim$ ten times lower weight compared to a standard 1.5 T MRI) [27]. The mobility of the "Swoop" MRI system is made possible using a new design of the biplanar permanent magnet array using laminate magnet formers to support magnetic blocks and a lightweight yoke, yet with a price of reduced field strength [28–30]. Promaxo Inc., Oakland, CA, USA, developed a portable MRI system for prostate imaging based on a mobile electromagnet design [31], [32]. Promaxo's prostate MRI allows imaging in the field external to the magnet based on new MRI acquisition methods [32]. It is specifically designed for use in the physician's office [31]. The MRI system intends to complement the doctor for quick in-office prostate screening and image-guided biopsies [31, 32].

1.2 Motivation

In addition to recent commercial developments in low field MRI mentioned above, several research groups have been redesigning the entire MRI system to remove the readout gradients by incorporating static B_0 gradients into inexpensive, lightweight, and compact Halbach magnets [33, 34]. Although the Halbach magnet is an appealing alternative for a mobile MRI, it has a very highly inhomogeneous bare magnetic field compared to standard biplanar or superconducting magnets. The high inhomogeneity of the Halbach magnet produces many challenges with field adjustments (shimming) to levels required by standard MRI acquisition techniques. To deal with this shortcoming, Stockmann et al. (2016) developed a new pulse sequence based on frequency sweeping, allowing high-quality MR imaging in the inhomogeneous field [35]. Cooley et al. (2020) reported high-resolution three-dimensional MRI scans of the brain using the Halbach magnet and the new pulse sequence [36]. Other research groups have designed and constructed sophisticated shimming arrays using various simulation methods to improve the homogeneity of Halbach magnets, making them applicable for high-quality MR imaging [37, 38]. O'Reilly et al. (2021) showed 3D MR images of the brain and knee using a 75 kg Halbach magnet by applying a new shimming technique [38]. Furthermore, new image reconstruction techniques such as a Model-based reconstruction rather than conventional Fourier-based methods allowed significant improvement of image quality in various mobile MRI systems [36, 39].

Several of the proposed LF imaging methods have removed the requirement of spatial spin encoding with the switching gradients (calling them "gradient-free" MRI techniques). An example is the Transmit Array Spatial Encoding (TRASE) method. The TRASE technique uses phase of the radiofrequency (RF) field rather than conventional B_0 gradients and has demonstrated spatial encoding ability as traditional MRI [40]. In addition to removing the B_0 gradient, TRASE also relaxes the magnet

homogeneity requirements, potentially further increasing the compact and portable nature of current low-cost LF MRI systems. However, this method shifts the requirements from the gradient chain to the RF chain as it requires multiple, high power and high duty cycle RF pulses to obtain high-resolution images.

As seen above, recent advances in LF MRI hardware and imaging techniques enabled reduction in cost, weight, complexity and size of an MRI system with acceptable image quality. Before this Ph.D. work, all TRASE experiments were performed using commercial RF power amplifiers (RFPAs) and immobile magnets, limiting portability and spatial resolution. Since TRASE resolution depends on the echo train length (see section 2.2.5), the low duty cycle provided by commercial RFPAs particularly limits the in-vivo image resolution due to the tissue's short T_2 relaxation [40]. The first project of this research was to design and construct an RFPA with multiple channels, maximum duty cycle and minimum delay times to improve in-vivo TRASE spatial resolution capability [41]. As the outcome of this work, a first-author paper was published [41]. Furthermore, this research was used in an additional publication that demonstrated sub-millimeter TRASE utilizing the constructed amplifier and a pair of highly efficient twisted-solenoid RF coils [42]. In addition, the development of new contrast agents for clinical MRI was taken as a side project during the PhD program which led to another publication [43].

So far, TRASE MRI experiments have primarily been carried out on a 0.2 T standard 4-post permanent magnet which is large and immobile [40, 42, 44]. While TRASE MRI can be performed with any standard MRI magnet, its costs, size, immobility, and high specific absorption rate (SAR) prevent the widespread use of TRASE MRI. Therefore, we designed and constructed a short and light Halbach magnet, significantly improving the portability and reducing costs of a TRASE MRI system. The LF provided by the Halbach magnet reduces the TRASE limitations due to SAR which are prevalent at HF (since SAR $\propto B_0^2$). Yet, in-vivo TRASE remained challenging with the constructed Halbach magnet due to the remaining field inhomo-

geneity. Therefore, we performed a simulation study of various shimming methods of the Halbach magnet to improve its field to enable in-vivo TRASE imaging. Furthermore, considering the complexity of 2D TRASE imaging, we designed and constructed an accurate magnet rotation system custom to the Halbach magnet to simplify 2D TRASE MRI hardware and image acquisition.

I believe that with my contributions and further advances in MRI hardware and techniques, some MRI options will be cheaper, easier to operate, more portable and able to produce clinically relevant images in acceptable time. Furthermore, it may reach populations with no current access to MRI systems, such as developing countries and the remote Canadian north. Portable MRI systems may even be installed on the International Space Station (ISS) or available during long space flights to the Moon and other planets for monitoring the detrimental effects of bone and muscle deterioration in astronauts as well as the typical applications of disease diagnosis that may happen over months and years of life away from healthcare available on Earth.

1.3 Overview

1.3.1 Thesis objectives and aims

As shown above, MRI based on the TRASE technique is a promising technique, if proper hardware is developed. Therefore, the objectives of the thesis were associated with contribution to this development:

1. A novel RF amplifier can be developed for high-resolution TRASE MRI, meeting the requirements of a multi-channel, high duty cycle and high power capability.

2. The entire TRASE MRI system can be compact, portable and low-cost using a non-standard, yokeless, permanent Halbach magnet. The dipolar Halbach magnet is suitable for TRASE with twisted-solenoid RF coils and a dedicated RF amplifier. A novel technique of 3D printing of magnet formers and high-quality magnetic pieces can be used in the magnet construction to manufacture

the magnet with the field distribution corresponding closely to simulation.

3. An array of small permanent magnet blocks can be added to the simulated bare Halbach magnet to improve the homogeneity of the B_0 field required by TRASE MRI. This approach is investigated as a simple and low-cost shimming method rather than the more complex and higher cost shim gradient coils or modified RF coils methods.

4. A low-cost and compact magnet rotation system can be constructed and demonstrated for a simplified 2D TRASE MRI system, using the lightweight magnet, RF amplifier, and simple acquisition of a series of radial 1D TRASE lines used to reconstruct an image over a 2D slice.

1.3.2 Thesis outline

The thesis is arranged in seven chapters. The first chapter (this chapter) provides an overview and motivation for pursuing low-field MRI, and in particular, a new encoding method (TRASE) to increase the portability and lower the cost of MRI systems. The following five chapters (2 - 6) cover, respectively, the theory of NMR, MRI, and TRASE; construction and application of a high duty cycle RF amplifier and novel Halbach magnet; magnet shimming approaches; and a low-cost magnet rotation system to allow simple 2D TRASE MRI. The thesis concludes (Chapter 7) with further possible advances in the developed hardware as well as future directions to improve the TRASE technology.

Chapter 2

Chapter 2 introduces the principles of conventional MRI, focusing on hardware needed for high-resolution imaging. Then, the basics of the TRASE method as a novel approach to one- and two-dimensional MR encoding is presented, and the hardware requirements for a TRASE MRI system are considered. The first TRASE RF hardware that allowed wrist images using a standard low-field MRI system is presented.

The relationships between the RF coil geometry and the TRASE k-space trajectory is also explored and compared to the standard MRI encoding technique. Finally, the relationship between the MRI hardware and TRASE image resolution is described.

Chapter 3

Chapter 3 expands on the published article in Magn Reson Mater Phy, 32: 679-692 entitled "A high duty-cycle, multi-channel, power amplifier for high-resolution radiofrequency encoding magnetic resonance imaging" [41]. This chapter begins with a basic introduction to transistors function and operation of amplifier electronics. It is followed by analysis of an ideal TRASE amplifier. Then, the method of adapting commercially available electronic components to the design and construction of an RF amplifier for TRASE is presented. The performance testing and results obtained with the RF amplifier are also shown. The chapter is concluded with the results showing the application of the RF amplifier to TRASE MRI at 0.2 T.

Chapter 4

Chapter 4 expands on the published article in the journal IEEE Access and is entitled "A Short and Light, Sparse Dipolar Halbach Magnet for MRI" [45]. This chapter begins with a basic explanation of the magnetic dipole concept and the classification of magnetic materials. Special attention is made to ferromagnetic materials and their behaviour in a magnetic field. Furthermore, the field produced by the dipolar Halbach magnet is introduced and the pitfalls related to fast analytical solutions of the magnetic field are discussed. The conclusions are then applied to the practical design, optimization, and construction of a compact and lightweight Halbach magnet aiming specifically toward a mobile TRASE MRI system. Details of the construction of a home-made 3D magnetic field mapping tool used for the Halbach magnet are also discussed.

Chapter 5

Chapter 5 addresses the field inhomogeneities of the constructed Halbach magnet. Since standard shimming methods have limitations, this chapter proposes new solutions suitable for shimming the constructed Halbach magnet using an array of small permanent magnet pieces, considering the three-dimensional magnetic field. A shim simulation study based on the target field method is presented, considering the size and orientation of each block in a cylindrical array and their impact on the field homogeneity. An introduction of an axial gradient to the Halbach magnet is also considered and analyzed for slice-selective in-vivo TRASE.

Chapter 6

Chapter 6 presents the theory and application of the potentially simpler and less expensive TRASE MRI system using magnet rotation. Analysis of the rotating B_0 and B_1 fields and its application to simplified TRASE is provided. The magnet rotation system was used to test and verify the 2D TRASE MR reconstruction from a series of 1D TRASE profiles.

Chapter 2

Basics of MRI and TRASE

2.1 Basics of an MRI technique

2.1.1 Hardware in a standard MRI system

A standard MRI scanner and associated hardware are illustrated in Figure 2.1. It consist of four main sub-systems:

1. The primary function of the **magnet** is to generate a strong, static magnetic field (B_0) that polarizes the spins in an imaged object [47]. Standard clinical MRI systems typically use large, heavy and expensive superconducting (1.5 T or 3 T) or permanent magnets (0.2 T or 0.5 T).

2. The **radiofrequency (RF) sub-system** is needed to transmit RF power to the spins and receive the NMR signal. The transmit RF coil and the RF amplifier are used to apply an alternating magnetic field (B_1) to excite the spins. After the RF pulse is turned off, the variable magnetic field produced by the precessing spins induces an electromotive force in a receive RF coil.

3. The **gradient sub-system** produces a perturbation of the B_0 field (typically linear) [48]. The 3D field perturbation results in spatial distribution of spins' Larmor frequencies which is exploited for imaging using the Fourier Transform [49].

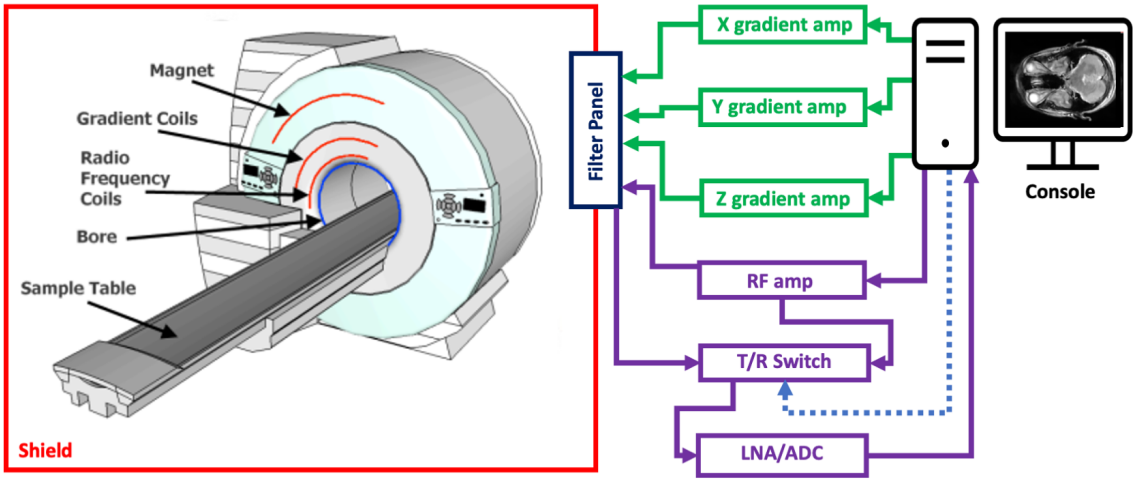

Figure 2.1: A standard MRI system comprising of four main hardware sub-systems. The gradients (green) and RF (purple) subsystems are shown. The high amplitude gradient waveforms and RF pulses are transmitted into an RF shielded room (red) by the filter panel (dark blue). The patient lies on the table in the MRI system surrounded by the RF coil, gradient coils and the main magnet. Connections from the filter panel to the corresponding coils inside the room are not shown. A transmit-receive (T/R) switch allows the same RF coil to be used for RF transmission and receiving of the NMR signal. During receive of the signal, a low noise amplifier (LNA) is used to increase the signal strength and the analog-to-digital converter (ADC) digitizes the signal for use by the console. Figure was modified from Haynes and Holmes (2013) [46] permissions granted.

4. The MRI **console** consists of one or more computers and digital systems that control the timing and generation of RF pulses and gradient waveforms as well as data acquisition, processing and image display.

2.1.2 The B_0 field

Nuclear spins in a magnetic field

Quantum mechanics states that the proton obeys Fermi statistics with spin one-half (I = 1/2) [50]. The magnetic moment ($\vec{\mu}$) is related to the spin by:

$$\vec{\mu} = \gamma \hbar \vec{\mathrm{I}} \tag{2.1}$$

where γ is the gyromagnetic ratio of the nuclei (for the proton, $\gamma = 2.67506 \times 10^8$ rad s^{-1} T^{-1}) and $\hbar$ is the reduced Planck's constant ($\approx 1.05 \times 10^{-34}$ J·s), denoting

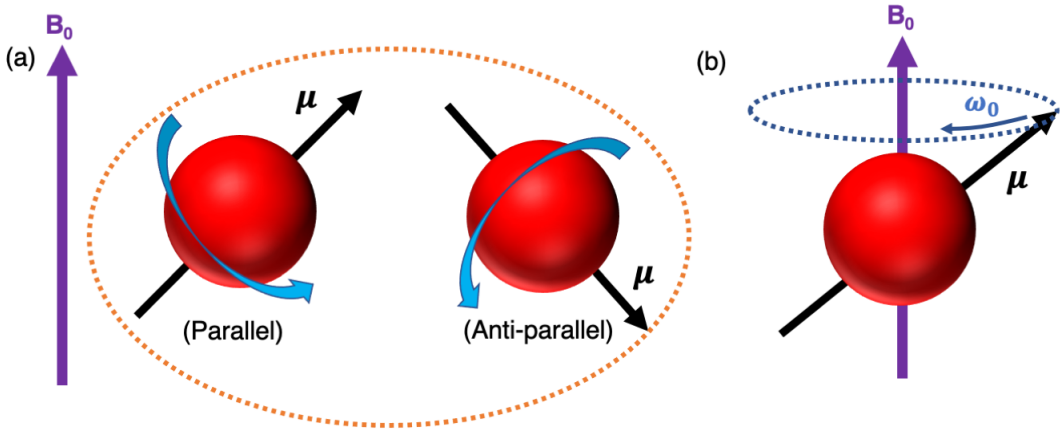

Figure 2.2: (a) A particle with spin-$\frac{1}{2}$ in an external magnetic field has two eigenstates, parallel (low-energy) and anti-parallel (high-energy). (b) The particle precesses about the external magnetic field at the Larmor frequency.

a quantized unit of angular momentum. A particle with a magnetic moment in an external magnetic field has the energy, E (in Joules):

$$E = \vec{\mu} \cdot \vec{B} \tag{2.2}$$

There are two eigenstates for half-spin particles resulting in an energy difference, ΔE (Figure 2.2a):

$$\mathrm{E}_{\uparrow} = -\frac{1}{2}\gamma\hbar B \tag{2.3}$$

$$\mathrm{E}_{\downarrow} = +\frac{1}{2}\gamma\hbar B \tag{2.4}$$

$$\Delta E = \mathrm{E}_{\downarrow} - \mathrm{E}_{\uparrow} = \gamma\hbar B \tag{2.5}$$

Using Planck's energy-frequency relation ($\mathrm{E} = \hbar\omega_0$), protons precess about an external magnetic field (B_0) at the Larmor frequency (ω_0):

$$\vec{\omega}_0 = -\gamma\vec{\mathrm{B}}_0 \tag{2.6}$$

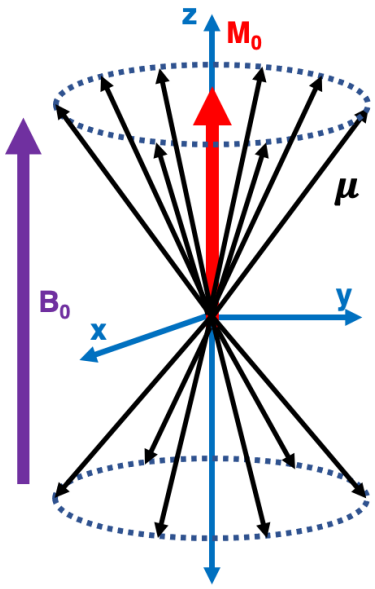

Figure 2.3: A net magnetization is created by a large population of protons (spin-1/2) in the external B_0 field (along the z-axis). In this system, the low-energy state ($E_\uparrow$) is slightly favoured, producing a net magnetization (M_0) along the static magnetic field (B_0).

Net magnetization

Considering an ensemble of protons, the fractional number of parallel spins to anti-parallel spins is given by the Boltzmann factor [50]:

$$\frac{N_\uparrow}{N_\downarrow} = e^{\frac{\Delta E}{k_B T}} \tag{2.7}$$

where k_B ($\approx 1.38\times10^{-23}$ J·K^{-1}) is the Boltzmann's constant and T is the temperature (K). Assuming that thermal energy is much higher than the energy difference of proton states ($\gamma\hbar B_0 << k_B T$), one can find by a Taylor series approximation the net proton magnetization per unit volume (M_0):

$$M_0 = \frac{\rho\gamma^2\hbar^2 B_0}{4k_B T} \tag{2.8}$$

where ρ is the spin density (i.e., the number of protons per unit volume).

Spin alignment along B_0, namely the net magnetization (M_0), contributes to the NMR signal (Figure 2.3). For example, at B_0 = 1T, only 3 protons in 1 million will contribute to the NMR signal (assuming standard room temperature, T = 293 K).

Table 2.1: Properties of selected NMR sensitive nuclei [51]. †The gyromagnetic ratio of the nucleus is obtained by multiplying the quantity by $2\pi\times10^6$. ‡Calculated at the same field strength, temperature and equal number of nuclei. Table was obtained from Tomanek and Sharp (2012) with permission from John Wiley and Sons under license number 5324540169446.

Nucleus	Natural Abundance [%]	Spin I	Frequency† [MHz/T]	Relative NMR sensitivity‡
^{1}H	99.89	1/2	42.5749	1.00000
^{2}H	1.5×10^{-2}	1	6.5357	0.06284
^{13}C	1.108	1/2	10.7050	0.06322
^{14}N	99.63	1	3.0756	0.01392
^{15}N	0.37	1/2	4.3141	0.01026
^{17}O	3.7×10^{-2}	5/2	5.7719	0.21443
^{19}F	100	1/2	40.0535	0.88506
^{23}Na	100	3/2	11.2615	0.34983
^{31}P	100	1/2	17.2348	0.03949
^{35}Cl	75.53	3/2	4.1715	0.16387
^{37}Cl	24.47	3/2	3.4724	0.04800
^{39}K	93.10	3/2	1.9870	0.03326
^{41}K	6.88	3/2	1.0903	0.01089
^{43}Ca	0.145	7/2	2.8644	0.09506
^{57}Fe	2.19	1/2	1.3756	0.00100

At B_0 = 20 mT, only 6 protons in 100 million contributes to the signal. The relative NMR sensitivity, defined as the ratio of the net magnetization relative to hydrogen, for a various nuclei is calculated and listed in Table 2.1. The natural abundance for

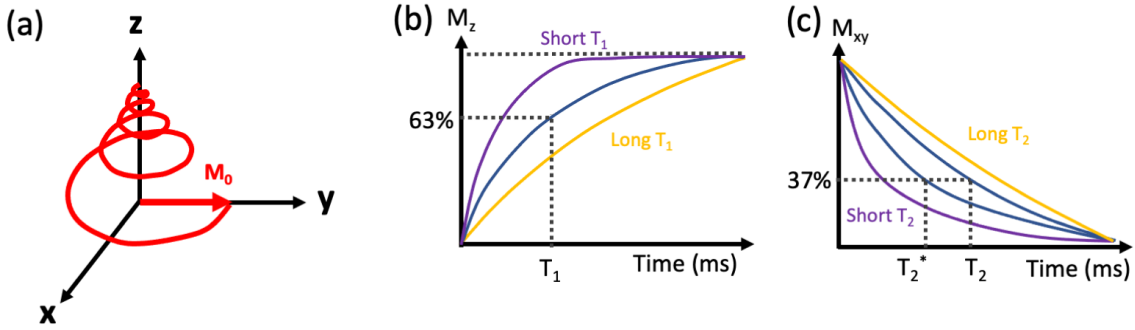

Figure 2.4: The time evolution of the net magnetization after application of a time varying magnetic field, B_1. (a) The net magnetization (M_0) returns to equilibrium along the z-axis (i.e. the direction of B_0). (b) The longitudinal recovery and (c) transverse decay of the net magnetization, according to Equation 2.11. Samples with different relaxation times are shown.

each selected nucleus is also listed in Table 2.1. Select atomic species such as ^{1}H, ^{31}P or ^{19}F can be detected by NMR due to an unpaired nucleon (protons or neutrons), contributing to a net nonzero spin [51, 52]. Other biologically relevant nuclear species, such as ^{12}C, have paired protons and neutrons, contributing to a zero net magnetic moment, making them invisible in NMR. The hydrogen nucleus (i.e. the proton) is more prevalent in the human body (i.e., from water) than other nuclei and is often the subject of human NMR and MRI studies. Since sodium-23 and phosphorus-31 are a thousand times less abundant in the human body, NMR and MRI applied to these nuclei becomes challenging because of the very low signal [47].

2.1.3 Bloch equations

In 1946, Felix Bloch described the NMR phenomenon with the following equation [53]:

$$\frac{d\vec{M}}{dt} = \gamma \vec{M} \times \vec{B}_{ext} + \frac{1}{T_1}(M_0 - M_z)\hat{z} - \frac{1}{T_2}\vec{M_{xy}} \tag{2.9}$$

where $\vec{M}$ is the net magnetization produced by an ensemble of spins, $\vec{B}_{ext}$ is the total magnetic field applied to the spins, and T_1 and T_2 are the relaxation times.

Equation 2.9 can be expanded into a set of differential equations [53]:

$$\begin{aligned}
\frac{\mathrm{dM_x}}{\mathrm{dt}} &= \gamma\Big(\mathrm{M_y B_0} + \mathrm{M_z B_1}\sin(\omega t)\Big) - \frac{\mathrm{M_x}}{\mathrm{T_2}} \\
\frac{\mathrm{dM_y}}{\mathrm{dt}} &= \gamma\Big(\mathrm{M_x B_1}\cos(\omega t) - \mathrm{M_x B_0}\Big) - \frac{\mathrm{M_y}}{\mathrm{T_2}} \\
\frac{\mathrm{dM_z}}{\mathrm{dt}} &= -\gamma\Big(\mathrm{M_x B_1}\sin(\omega t) - \mathrm{M_y B_1}\cos(\omega t)\Big) - \frac{\mathrm{M_z - M_0}}{\mathrm{T_1}}
\end{aligned} \tag{2.10}$$

where ω is the frequency of the $\mathrm{B_1}$ field. Following a 90° pulse at time, t = 0, the solutions to the Bloch equations for the simplest case (i.e. $\vec{\mathrm{B}}_{\mathrm{ext}} = \mathrm{B_0}\hat{z}$) is [53]:

$$\begin{aligned}
\mathrm{M}_{xy}(t) &= \mathrm{M_0}\exp(i\omega_0 t)\exp\left(\frac{-t}{\mathrm{T_2}}\right) \\
\mathrm{M}_z(t) &= \mathrm{M_0}\Big[1 - \exp\left(\frac{-t}{\mathrm{T_1}}\right)\Big]
\end{aligned} \tag{2.11}$$

The total magnetic field, $\vec{\mathrm{B}}_{\mathrm{ext}}$, consists of the static polarizing magnetic field ($\mathrm{B_0}$) and an applied magnetic field ($\mathrm{B_1}$). Following the applied $\mathrm{B_1}$ field, the spins lose energy to their surroundings with the spin-lattice relaxation time ($\mathrm{T_1}$). The spins also exchange energy by interacting with each other, causing coherence loss in the net magnetization. This is termed the spin-spin relaxation time ($\mathrm{T_2}$). $\mathrm{T_1}$ and $\mathrm{T_2}$ describe the time behaviour of the net magnetization in the longitudinal and transverse planes, respectively (Figure 2.4b,c).

$\mathbf{T_2^*}$ decay

The effective field seen by the spins can vary in time (irreversible) and be subject to static $\mathrm{B_0}$ inhomogeneities (reversible) [47]. Therefore, the measured transverse relaxation time (defined as $\mathrm{T_2^*}$) is shorter than $\mathrm{T_2}$ due to the combination of reversible and irreversible pathways of the signal decay. The transverse relaxation time, $\mathrm{T_2^*}$, is calculated according to:

$$\frac{1}{T_2^*} = \frac{1}{T_2} + \frac{1}{T_2'} \tag{2.12}$$

where $\mathrm{T_2'}$ is the relaxation contribution due to time-independent static $\mathrm{B_0}$ field inhomogeneities. The spin-echo pulse sequence uses two or more pulses to remove the impact of static $\mathrm{B_0}$ inhomogeneities on transverse NMR signal [54]. The example

in Figure 2.5 shows a 90° pulse (flipping the net magnetization to the xy plane as described in the details below) followed by a series of ('refocusing') 180 degree RF pulses, each reversing the dephasing caused by the static inhomogeneities.

2.1.4 The B_1 field

The perpendicular (to B_0) and time-varying magnetic field (B_1) perturbs the net magnetization such that it can be detected (i.e. the NMR signal). The B_1 frequency has to be equal or near the Larmor frequency.

Radio-frequency (RF) transmission

The external field applied to the spins can be expressed as $\vec{B}_{ext} = B_0\,\hat{z} + B_1\,x'$ where the B_1 (the RF field) is at rest in the reference frame that rotates in the same sense as the spins (Figure 2.6a) and assumed to be pointing along the x'-axis, perpendicular

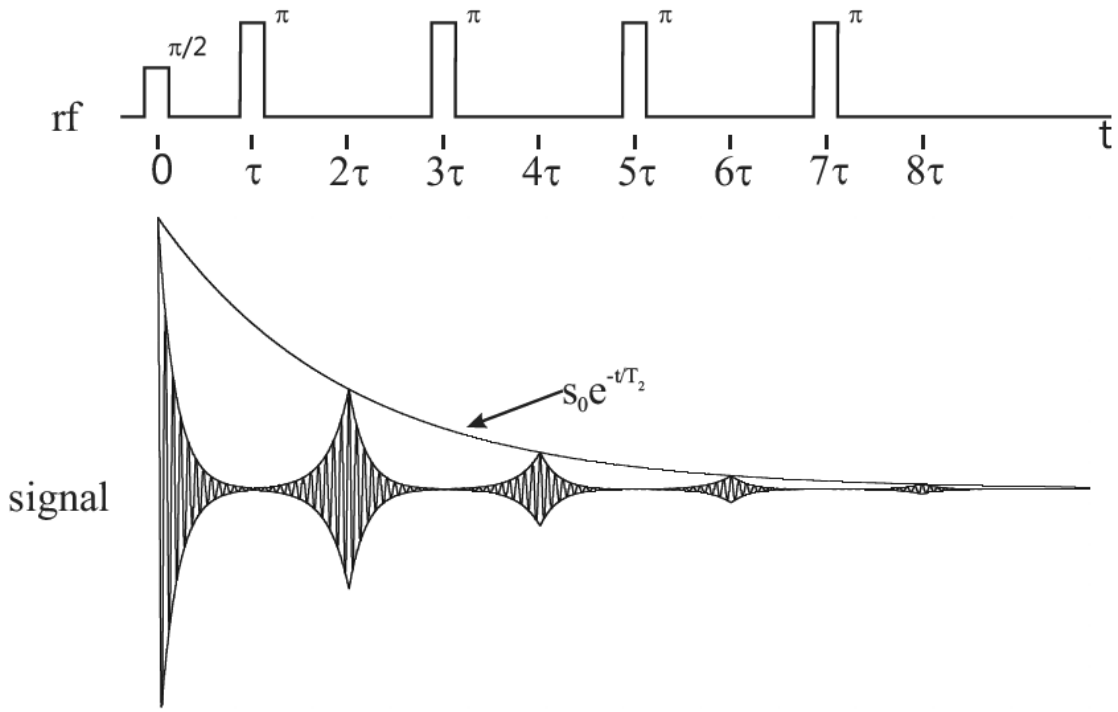

Figure 2.5: The multi-echo spin-echo pulse sequence is applied to refocus NMR signal loss due to static field inhomogeneities [54], [47]. Figure was obtained from Brown et al. (2014) [47] with permissions from John Wiley and Sons under license number 5324841201883.

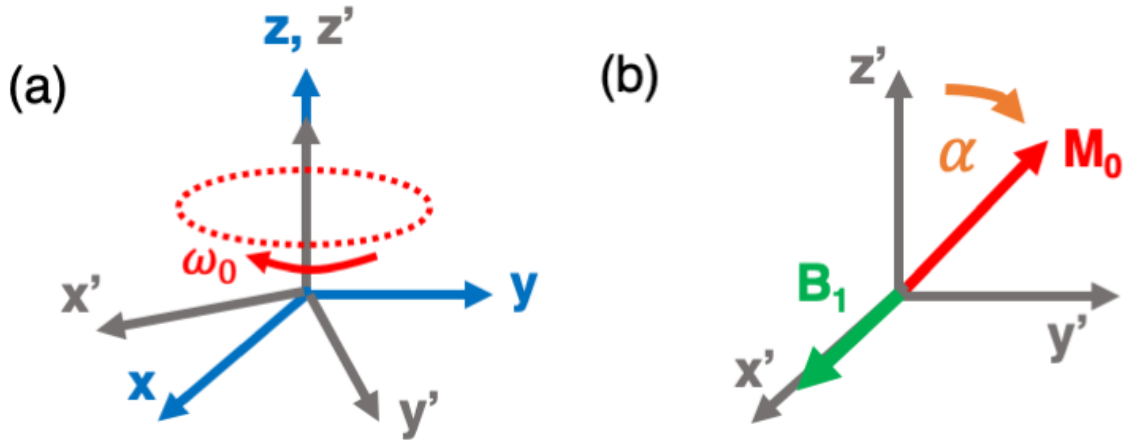

Figure 2.6: The action of the RF pulse in the rotating reference frame. (a) The rotating reference frame (x',y',z') circulates at the Larmor frequency (ω_0) around the z-axis (direction of the static B_0) of the laboratory frame (x,y,z). (b) An RF field, perpendicular to the static B_0 field, applied to the spins at the frequency ω_0 is static in the rotating frame. As a result, spins only experience the B_1 field and the net magnetization flips into the transverse plane (x',y').

to B_0 (Figure 2.6b) [50]. Neglecting the relaxation, the Bloch equation (Equation 2.9) in the rotating frame is simplified [50, 53]:

$$\left(\frac{d\vec{M}}{dt}\right)_{rot} = \left(\frac{d\vec{M}}{dt}\right)_{lab} - \vec{\omega} \times \vec{M} \tag{2.13}$$

$$= \gamma \vec{M} \times \vec{B_{eff}} \tag{2.14}$$

Therefore, the effective field experienced by the spins in the rotating frame is [50]:

$$\vec{B}_{eff} = \left(\vec{B}_0 - \frac{\vec{\omega}}{\gamma}\right)\hat{z} + B_1\hat{x}' \tag{2.15}$$

The Bloch equation shows that the magnetization experiences only the B_1 field ($\vec{B}_{eff} = B_1\ \hat{x}'$), hence it rotates around B_1 and tilts from the z-direction into the transverse (x',y') plane. The angle by which the net magnetization is tilted is proportional to the amplitude (B_1) and duration (τ) of the RF pulse, known as the flip angle (α):

$$\alpha = \gamma \int_0^{\tau} \vec{B_1} dt \tag{2.16}$$

Signal reception

As a result of M_0 tilting, the transverse component of M_0 (i.e. M_{xy}) can be detected by a receive RF coil. The component of the net magnetization, precessing in the transverse plane, induces an electromotive force (ϵ) across the RF coil(s) terminals according to Faraday's law of induction [55], [56]:

$$\epsilon = -\frac{d\Phi_B}{dt} \tag{2.17}$$

where Φ_B is the magnetic flux (in Wb) through the coil loop (Figure 2.7). The receive coil (e.g. solenoid) must produce (or receive) the B_1 field in the plane perpendicular to B_0 [55], [56]. Since the NMR signal is very weak ($\sim \mu$V), a low-noise pre-amplifier is required during reception to enhance the signal for digitization and further processing by the console [56], [55].

Signal-to-noise (SNR) and B_0 field strength

Signal-to-noise ratio (SNR) in an MRI experiment depends on the external magnetic field strength as well as many other factors, such as RF coil quality factor, its geometry, electronic noise, etc. [56, 57]. Nevertheless, as seen from Equation 2.8, the net magnetization is proportional to the external field strength ($M_0 \propto B_0$). Since $\Phi \propto M_0 e^{-i\omega_0 t}$ and $d\Phi / dt \propto M_0 \cdot \omega_0$, the signal voltage ($V_s$) induced in the coil is:

$$V_s \propto B_0^2 \tag{2.18}$$

In addition, the thermal noise voltage (V_n) (i.e. Johnson-Nyquist Noise [58, 59]) is:

$$V_n = \sqrt{4k_B T R \Delta f} \tag{2.19}$$

where R is the resistance (Ω) across the terminals of the receiver coil and Δf is the receiver bandwidth. When coil losses dominate ($R \propto \sqrt{\omega_0}$) or sample losses dominate ($R \propto \omega_0^2$), the signal-to-noise (SNR) ratio (V_s / V_n) is [60, 61]:

$$\text{SNR} \propto \begin{cases} B_0^{7/4}, & \text{if coil losses dominate} \\ B_0, & \text{if sample losses dominate} \end{cases} \tag{2.20}$$

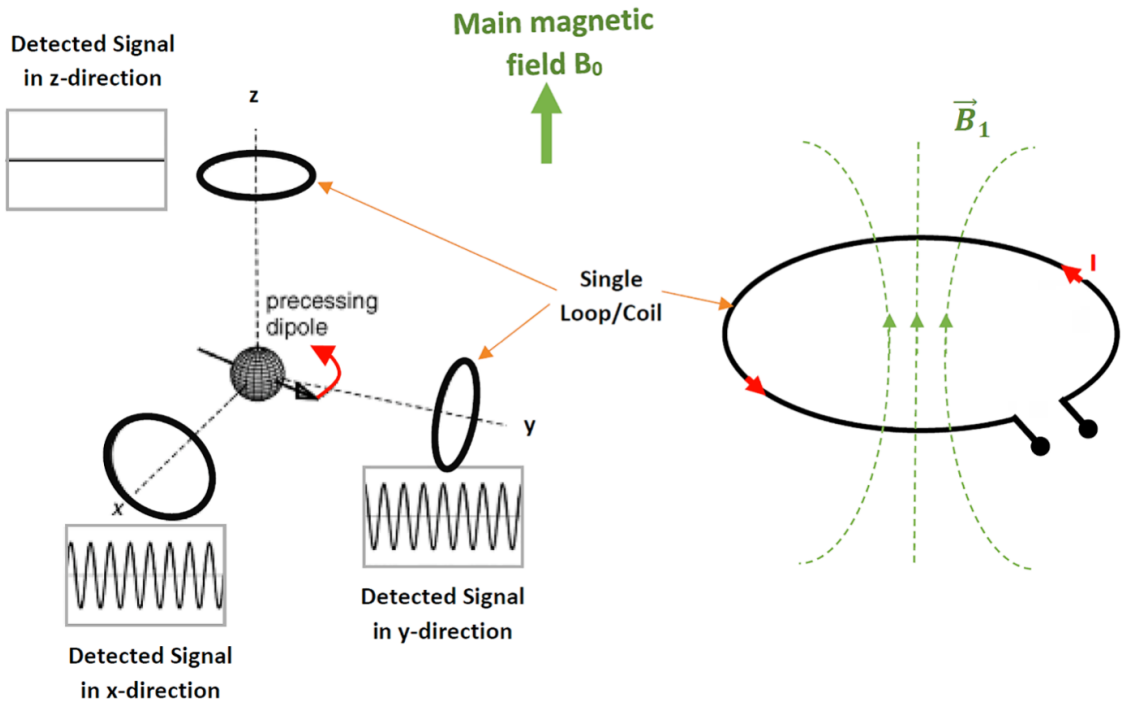

Figure 2.7: Following the tipping of the M_0 into the transverse plane, the RF coils are then used to receive the NMR signal [55]. A precessing net magnetization in a transverse plane (x,y) induces a voltage across terminals of the coils oriented in different orthogonal positions. No signal is detected for a receive coil oriented along the precession axis (i.e. the z-axis). Figure obtained from Gruber et al. (2018) [55] with permission under the CC-BY-NC 4.0 license.

Because the coil losses typically dominate at low field ($<$ 5 MHz), it introduces additional signal reduction to the already low signal due to the low field strength. Litz wire (stranded and twisted) has been used in coil construction to reduce noise, improving the SNR at low fields [62]. SNR is also improved by increasing the number of averages (i.e., SNR $\propto \sqrt{N_{acq}}$ where N_{acq} is the number of acquisitions). Therefore, increasing the number of acquisitions (i.e., increasing the scan time) in a low-field system may produce sufficient SNR for MRI.

2.1.5 MR imaging

While NMR signal has been observed since Rabi et al. (1938), the first MR images were collected by Lautebur et al. (1973) by spatially encoding spins using B_0 field gradients [49, 63].

The NMR signal received by an RF coil from a volume V is given by [47, 64]:

$$S(t) = \int dV \vec{B}_1^{-}(\vec{r}) \cdot \vec{m}(\vec{r}, t) \cdot e^{-i(\vec{k}(t)\cdot\vec{r}+\omega_0 t)} \tag{2.21}$$

where $\vec{B}_1^{-}$ is the receive coil field distribution; $\vec{m}$ is the precessing magnetization at the position, $\vec{r}$; $\vec{k}(t)$ is the phase accumulation due to the applied gradients:

$$\vec{k}(t) = \frac{\gamma}{2\pi} \int_0^{\tau} \vec{G}(t)dt \tag{2.22}$$

where $\vec{G}(t)$ is the gradient over the volume (V) and τ is the duration of the gradient pulse. It is evident, from Equation 2.21, that the measured signal S(t) is the Fourier Transform (FT) of $\vec{B}_1^{-} \cdot \vec{m}$ [47, 64]. Therefore, by application of the magnetic field gradients ($\vec{G}$), the inverse FT of the signal, S(t), can be used to produce an image of the spatial distribution of spins, $\vec{m}(\vec{r},t)$. The relationship between k-space ($\vec{k}$) and the real image ($\vec{m}$) is shown in Figure 2.8 [65]. The low spatial frequencies are located centrally in the k-space and contribute to image contrast. The high spatial frequencies, located at the k-space periphery, contribute to the edges and details in the reconstructed MR image [65, 66]. The finite extent to which all k-space data is acquired in MRI always leads to some blurring in the images. Higher resolution requires going further out in k-space.

An example of k-space acquisition

The echo-planar imaging (EPI) technique, as shown in Figure 2.9, is an example of a fast MR imaging technique [67]. EPI can acquire the full k-space following a single RF excitation pulse (single-shot EPI) due to application of the gradients of the magnetic field to create so called gradient echoes. As shown in Figure 2.9, negative gradients ($-G_y$ and $-G_x$) are applied in two orthogonal directions to set the first point in k-space. The $+G_x$ (readout) gradient applied during the acquisition of the NMR signal creates the first line in k-space (frequency encoding). During NMR acquisition, the NMR signal is digitally sampled producing a series of points along the k-space line. At the end of the first k_y line, the $+G_y$ (phase encode) gradient is applied ($+\Delta k_y$), and the

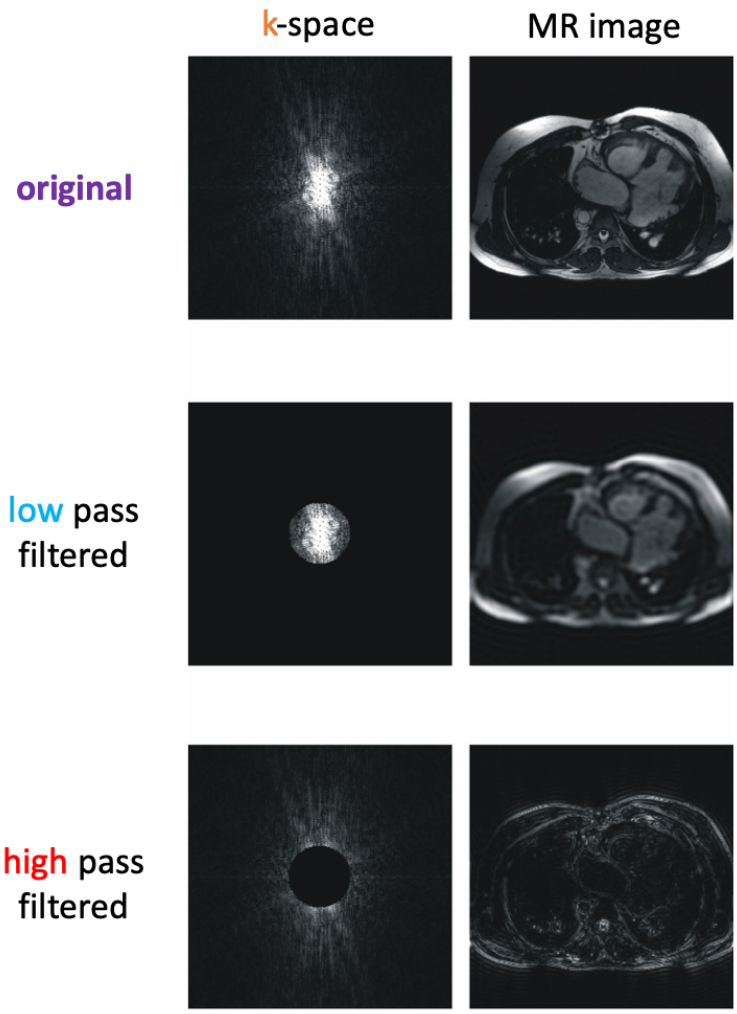

Figure 2.8: The raw data (k-space) and the corresponding image produced by 2D Fourier transformation of the k-space data [65]. (top) The desired MR image produced by the inverse Fourier Transform of the k-space data. (middle) The k-space data filtered to contain only the centrally-located low frequency data providing only image contrast; hence, the image blurring. (bottom) The k-space data filtered to contain only the peripheral high frequency data corresponding to the reconstructed image edges and details. Figures obtained and modified from Moratal et al. (2008) [65] with permission under the CC-BY-SA license.

NMR data is sampled again with a -G_x gradient, along the k_x axis. The frequency and phase encoding are repeated until all k-space points are filled. In addition to the EPI technique, hundreds of pulse sequences have been designed with various k-space trajectories, such as spiral MRI [68].

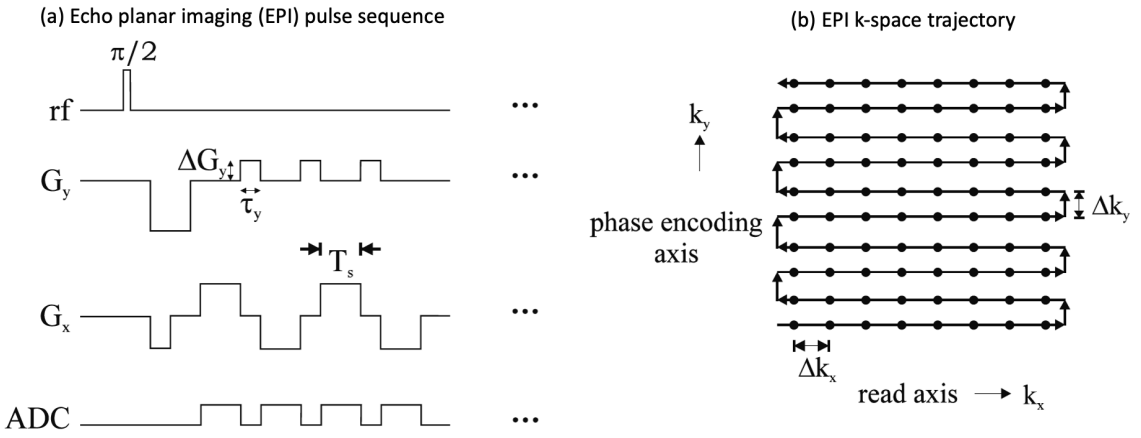

Figure 2.9: The Echo Planar Imaging (EPI) pulse sequence and k-space trajectory. (a) The EPI sequence consists of an RF pulse, two orthogonal gradients, and the NMR acquisition of the signal (ADC). (b) The k-space trajectory. Points in k-space are obtained by digital sampling of the NMR signal during the ADC window. Both figures were modified from Brown et al. (2014) [47] with permissions from John Wiley and Sons under license number 5324841201883.

Spatial resolution and k-space

Since the MR image is related to k-space through FT (assuming a uniform Cartesian sampling), the field-of-view (FOV) is associated with the k-space step (Δk) [47, 65, 69]:

$$\Delta \mathrm{k} = \frac{1}{\mathrm{FOV}} \tag{2.23}$$

Therefore, the extent of the acquired k-space ($\mathrm{k_{max}}$) is related to the image pixel separation (Δx):

$$\mathrm{k_{max}} = \frac{1}{2\Delta \mathrm{x}} \tag{2.24}$$

By obtaining more k-space data that is further from the k-space center, higher image spatial resolution can be achieved.

Image contrast and $\mathbf{B_0}$ field strength

Since the 1960s, researchers have been measuring $\mathrm{T_1}$ and $\mathrm{T_2}$ relaxation times in human tissue at a wide range of field strengths. They found that the relaxation times ($\mathrm{T_1}$ and $\mathrm{T_2}$) vary among tissue at the same field strength, but they also depend on

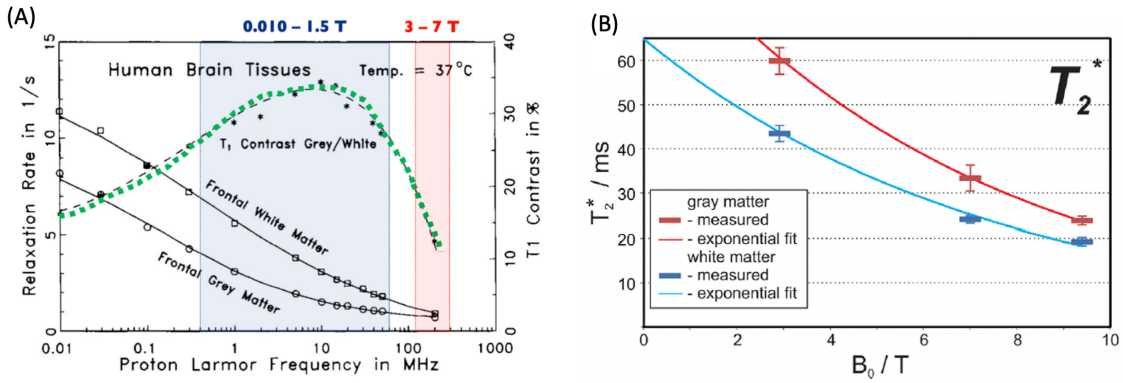

Figure 2.10: The T_1 and T_2 relaxation times of brain matter at different field strengths. (A) T_1 of white and grey matter and T_1 contrast between the white and grey matter of the human brain at different field strengths (green dotted line). (B) T_2^* of grey and white brain tissue (longer at lower field strengths) [8, 12, 70]. Figure (A) was obtained from Sarracanie et al. (2020) with permission under the CC-BY license and Figure (B) was obtained from Pohmann et al. (2016) [70] with permission from Johns and Sons Inc under license number 5324541307150.

the external magnetic field strength (B_0). For example, T_1 contrast between grey and white brain matter tissue is relatively constant from 10 mT to 1.5 T ($\sim$ 10% deviation) and reaches a maximum at B_0 of 0.5 T (Figure 2.10A) [12], [8, 13]. For B_0 = 3 to 7 T, the T_1 contrast is gradually decreasing because the difference in T_1 are getting smaller; hence, a reduction in contrast between grey and white matter. Washburn-Campbell et al. (2021) noted higher T_1 contrast at 0.55 T than at 1.5 T between air and tissue interfaces in the lungs as well as the gray and white brain matter [71]. In addition, although lower magnetic fields produce lower SNR, the T_2^* relaxation is longer at lower fields (Figure 2.10B) [8]. Therefore, more k-space points could be collected following one excitation pulse [7, 70, 71], allowing techniques such as 2D EPI diffusion weighted imaging at ultra low fields (50 mT) [72].

2.2 TRASE MRI

To obtain an MR image, an excitation pulse that tips the net magnetization (M_0) into the transverse plane (M_{xy}) is required (see section 2.1.4). It is followed by various

spatial encoding methods utilizing the phase (ϕ) of the spins:

$$\mathrm{M_{xy}} = \mathrm{M_0} e^{i\phi(\vec{r})} \tag{2.25}$$

Conventional MRI encoding is based on a $\mathrm{B_0}$ gradients that varying linearly in space ($\vec{\mathrm{B}} = \vec{B}_0 + \vec{\mathrm{G}}_0 \cdot \vec{\mathrm{r}}$). In conventional MRI encoding methods (see Equation 2.22), spins experience a phase accumulation ($\Delta\phi$) in the presence of a linear $\mathrm{B_0}$ gradient ($\vec{\mathrm{G}}_0$) [40]:

$$\Delta\phi = \gamma \vec{\mathrm{G}}_0 \cdot \vec{\mathrm{r}} \tau \tag{2.26}$$

where $\vec{\mathrm{r}}$ is the position of the net magnetization and τ is the duration of the gradient pulse. Unlike standard encoding methods, the recently introduced encoding method called TRASE uses the phase gradients of the RF field to spatial encode signal rather than applying a switched $\mathrm{B_0}$ gradient [40, 73].

2.2.1 $\mathrm{B_1}$ phase gradient and k-space

In the TRASE method, a unique RF coil geometry produces a linear phase gradient of the $\mathrm{B_1}$ field [40, 73]:

$$\vec{\mathrm{B}}_1 = |\vec{\mathrm{B}}_1| e^{i\phi_1(\vec{r})} \tag{2.27}$$

The phase (ϕ_1) is defined in terms of the RF phase gradient ($\vec{\mathrm{G}}_1$) produced by the coil:

$$\phi_1(\vec{r}) = \vec{\mathrm{G}}_1 \cdot \vec{r} = 2\pi \vec{k_1} \cdot \vec{r} \tag{2.28}$$

where $\vec{k_1}$ in the inherent phase variation of the RF field and is represented by an offset point in k-space (see the 'coil k-space origin' in Figure 2.11a).

Excitation pulse

An excitation pulse (i.e. $\alpha = 90°$ in Equation 2.16) applied to a uniform $\mathrm{B_1}$ phase coil (e.g. saddle), imparts zero phase dispersion to the spins; therefore, $\mathrm{k_1} = 0$ in Equation 2.28. However, using an RF coil with a $\mathrm{B_1}$ phase gradient ($\vec{\mathrm{G}}_1 = 2\pi\vec{\mathrm{k}}_1$) immediately imparts phase accumulation to the spins following an excitation pulse,

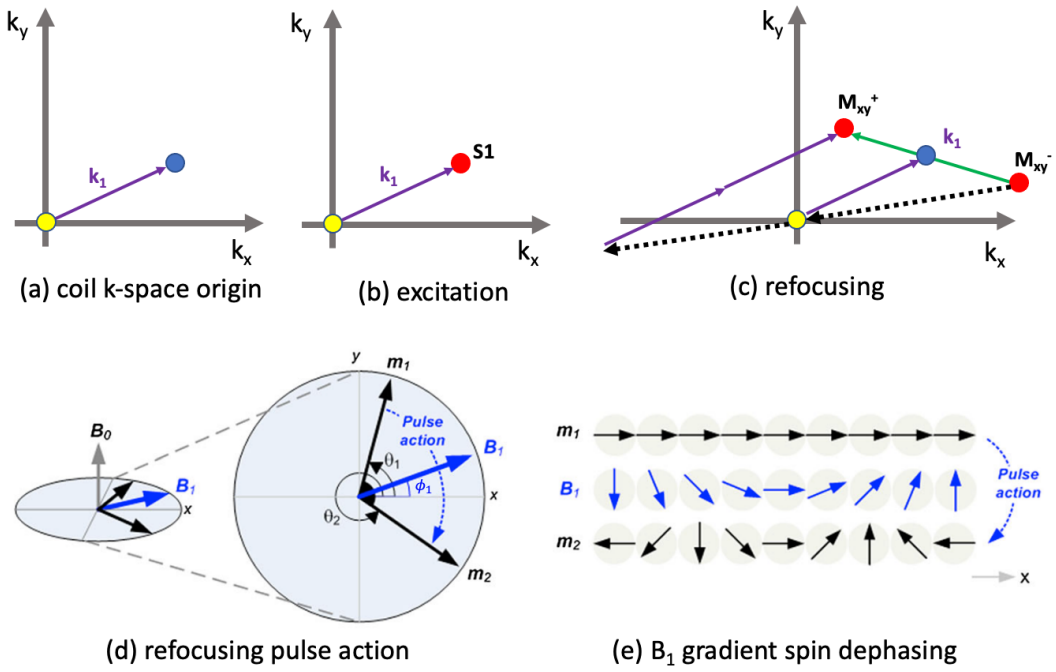

Figure 2.11: k-space representation in RF phase gradient fields [73]. (a) The RF phase gradient is represented by a single point in k-space, defined by k_1, the "coil k-space origin". (b) An excitation pulse (90°) with a B_1 phase gradient brings the spins directly to the state S1 in k-space. (c) An arbitrary spin state (M_{xy}^{-}) reflects symmetrically about the RF coil's k-space origin when applying a refocusing pulse (180°) bringing the spin state to (M_{xy}^{+}). (d) The transverse spins are reflected about the local B_1 field using a refocusing pulse. (e) Spin dephasing along the x-axis produced by the RF pulse with the phase gradient. Figures a-c were obtained and modified from Sharp et al. (2010) [73] with permission from John Wiley and Sons under license number 5324550271241 and Figures d,e were obtained from Sharp et al. (2013) [40] with permission from John Wiley and Sons under license number 5324550497045.

defined by the inherent phase of the RF coil, $k_1 \neq 0$ (see S1 in Figure 2.11b). The phase accumulation due to the RF gradient excitation is equivalent to phase imparted by a conventional B_0 gradient in a finite time (see Equation 2.25).

Refocusing pulse

Following the excitation pulse, RF phase gradients impart spin phase accumulation and then the raw k-space data is acquired (see Section 2.1.5). Assuming the excitation pulse was already applied to the spins, let's consider first the action of a refocusing pulse (i.e. $\alpha = 180°$ in Equation 2.16) on the spins using a B_1 phase gradient coil

($\vec{G}_1^{A} = 2\pi\vec{k}_1^{A}$; where A is the coil label in a set of transmit coils). The phase change of the spins at position, $\vec{r}$, due to the applied refocusing pulse is (Figure 2.11d):

$$\theta_2 - \theta_1 = 4\pi\vec{k}_1^{A} \cdot \vec{r} - 2\theta_1 \tag{2.29}$$

Under the action of a single 180° pulse, the net magnetization state experiences a dephasing according to:

$$M_{xy}^{+} = M_{xy}^{-} e^{i(4\pi\vec{k}_1^{A}\cdot\vec{r} - 2\theta_1)} = M_{xy}^{-} \underbrace{e^{i2\cdot 2\pi\vec{k}_1^{A}\cdot\vec{r}}}_{*} \underbrace{e^{-i2\theta_1}}_{**} \tag{2.30}$$

where M_{xy}^{-} is the transverse magnetization before the pulse; M_{xy}^{+} is the transverse magnetization after the pulse; ** is the phase factor contributing to the reflection about the origin; * is the phase factor contributing to the additional k-space phase shift due to the B_1 phase gradient. The reflection about the local B_1 field is equivalent to a refocusing pulse in standard MRI techniques using uniform RF coils (see dotted black arrow in Figure 2.11c). However, using a B_1 phase gradient coil, the refocusing pulse produces an additional k-space shift of $2\vec{k}_1^{A}$. Nevertheless, the total 180° pulse action using a phase gradient coil is equivalent to a point reflection about the RF coil's k-space center (see green arrow in Figure 2.11c).

k-space traversal

A single RF phase gradient coil does not allow k-space traversal since the spin state will only move from m_1 to m_2 or vice versa (Figure 2.11d,e). However, by applying an additional refocusing pulse using a second RF coil with a different phase gradient, say $\vec{G}_1^{B} = 2\pi\vec{k}_1^{B}$, the cumulative phase change becomes:

$$\Delta\phi = \theta_3 - (\theta_2 - \theta_1) = 2 \cdot 2\pi(\vec{k}_1^{A} - \vec{k}_1^{B}) \cdot \vec{r} \tag{2.31}$$

due to two reflection points about each coil k-space origin (Figure 2.12a). Therefore, a translation in k-space (Δk_{BA}) is achieved using multiple RF coils with different B_1 phase gradients and refocusing pulses (Figure 2.12a):

$$\Delta k_{BA} = 2(k_1^{B} - k_1^{A}) \tag{2.32}$$

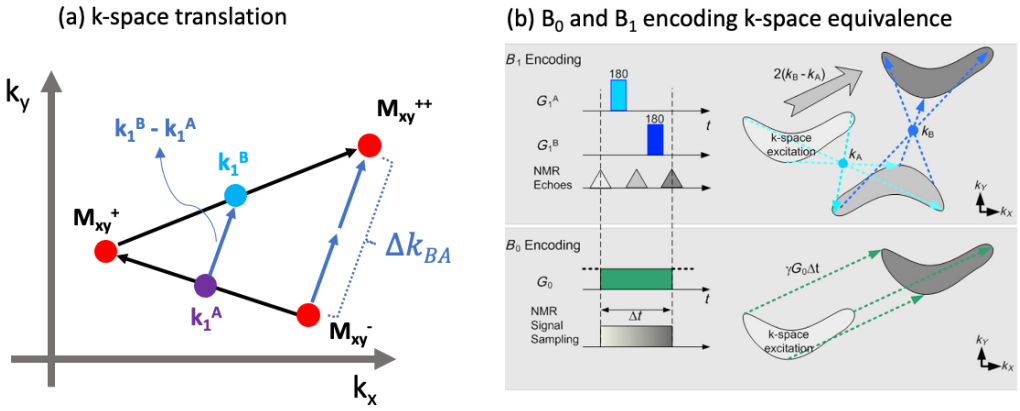

Figure 2.12: RF encoding using refocusing pulses and two B_1 phase gradient coils [40]. (a) A translation in k-space (Δk_{BA}) is achieved using two B_1 phase gradients ($\vec{k_1}^A$, $\vec{k_1}^B$) and refocusing pulses. (b) B_1 encoding is equivalent to applying a B_0 gradient (G_0). Figure (a) was modified from Sharp et al. (2010) [73] with permission from John Wiley and Sons under license number 5324550271241 and Figure (b) was modified from Sharp et al. (2013) [40] with permission from John Wiley and Sons under license number 5324550497045.

The B_1 encoding method applies two reflection points ($\vec{k_1}^A$,$\vec{k_1}^B$) in k-space using refocusing pulses and is equivalent to applying a linear B_0 gradient for a finite length of time (see Figure 2.12b) [40].

2.2.2 The twisted-solenoid RF coil

Several RF coils sets were developed since the conception of TRASE, such as the dual Maxwell-Helmholtz [40, 44], dual twisted-birdcage [73] and two twisted-solenoid RF coils [42, 74]. The twisted-solenoid RF coil (Figure 2.13A) provides a relatively linear transverse RF phase gradient (Figure 2.13C) with low B_1 inhomogeneity over 65-75% of the coil diameter [42, 74]. In this RF coil design, the phase gradient is achieved by a single current path rather than larger Dual Maxwell-Helmholtz RF coils that require high power phase shifters and fast switching circuits [40, 42, 44].

Sun et al. (2019) optimized the twisted solenoid to produce a phase gradient in the same plane as the B_0 field, for use in biplanar or Halbach permanent magnets [74]. The authors showed that the cartesian B_1 field components produced by the

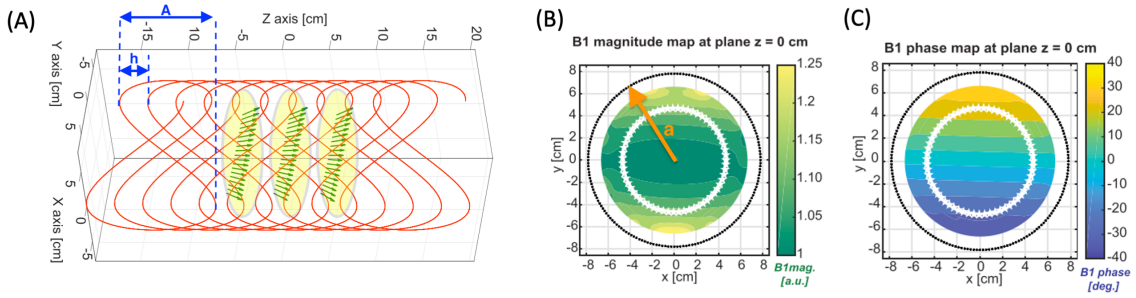

Figure 2.13: The twisted-solenoid RF coil and select B_1 amplitude and phase plots determined from the Biot-Savart Law calculations [42]. (A) The twisted-solenoid coil geometry. (B) A B_1 magnitude plot in a transverse plane (z = 0 cm). (C) A B_1 phase plot at z = 0 cm. Figures A-C were modified from Sun et al. (2020) [42] with permission.

twisted-solenoid RF coil are (in cylindrical coordinates (ρ,θ,z)) [74]:

$$B_x = -\mu_0 \frac{I}{h} \frac{A\rho}{a^2} \sin(\theta + \psi) \tag{2.33}$$

$$B_y = -\mu_0 \frac{I}{h} \frac{A\rho}{a^2} \cos(\theta + \psi) \tag{2.34}$$

$$B_z = \mu_0 \frac{I}{h} \tag{2.35}$$

where μ_0 is the permeability of free space, I is the current, A is the twist which controls the phase gradient strength, a is the radius of the coil and h is the pitch (turns per meter) (Figure 2.13A,B). The winding shift (ψ) is the initial angular position of the coil winding which is related to twice the coil former rotation [74]. Assuming a B_0 direction along the x-axis, the B_x component becomes a concomitant RF field and does not contribute to B_1. Therefore, the magnitude and phase of the B_1 field is [74]:

$$|B_1| = \sqrt{B_y^2 + B_z^2} \tag{2.36}$$

$$\phi_B = \tan^{-1}\left(\frac{-B_y}{B_z}\right) \tag{2.37}$$

Since the RF phase gradient is $\vec{G_1} = (\frac{\partial \phi_B}{\partial x}, \frac{\partial \phi_B}{\partial y})$, and for simplicity, assume that $\psi = 0$, the RF phase gradient (G_x) is [74]:

$$G_x = \frac{1}{a^2} \frac{A}{1 + \left(\frac{A}{a}\right)^2 \left(\frac{x}{A}\right)^2} \tag{2.38}$$

and $G_y = 0$. Similarly to Sun et. al (2019), if $\psi = \pi$ (i.e. a coil former rotation of $\pi/2$), then the RF phase gradient direction is reversed (i.e. -G_x). Figure 2.13B,C shows the B_1 amplitude and phase distribution for a single twisted-solenoid RF coil producing a phase gradient along the y-axis (i.e. $\psi = \pi/2$). Sun et al. (2020) used two twisted solenoid coils rotated by 90° producing *opposite* phase gradients allowing sub-millimeter resolution 1D TRASE since the k-space point separation was doubled [42]. As one can conclude from the above, an advantage of a twisted solenoid coil (or magnet) rotation produces a change of the RF phase gradient direction through an object, which potentially allows 2D reconstruction from a set of 1D acquisitions (see more details in Chapter 6). In addition, since high speed switching and high decoupling between RF coils are requirements for TRASE, PIN diode switches and geometric decoupling techniques are often used. Some additional advantages of using two twisted-solenoid RF coils and geometric decoupling techniques are complete removal of the PIN diode switches, less complex hardware, faster switching, scalability, large usable imaging region, and overall compact cylindrical design [42, 74].

2.2.3 1D TRASE acquisition

Figure 2.14 shows the acquisition of a one-dimensional (1D) TRASE k-space trajectory. As shown in Section 2.2.1, TRASE requires multiple RF transmit coils (Figure 2.15), each with different phase gradients that move the received signal further out in k-space using refocusing pulses. The two-coil configuration allows 1D TRASE consisting of a single 90° excitation RF pulse followed by sequential high-power 180° RF refocusing pulses applied to two B_1 phase gradient coils [40, 44, 73]. The NMR signal is acquired between each refocusing pulse producing points on a single line in k-space. Figure 2.15 shows two possible RF coil configurations enabling 1D TRASE: a twisted-solenoid/saddle coil set and two twisted solenoid RF coils [42]. The large k-space step provided by two twisted solenoids producing opposite phase gradients allows higher 1D TRASE spatial resolution compared to the solenoid and saddle

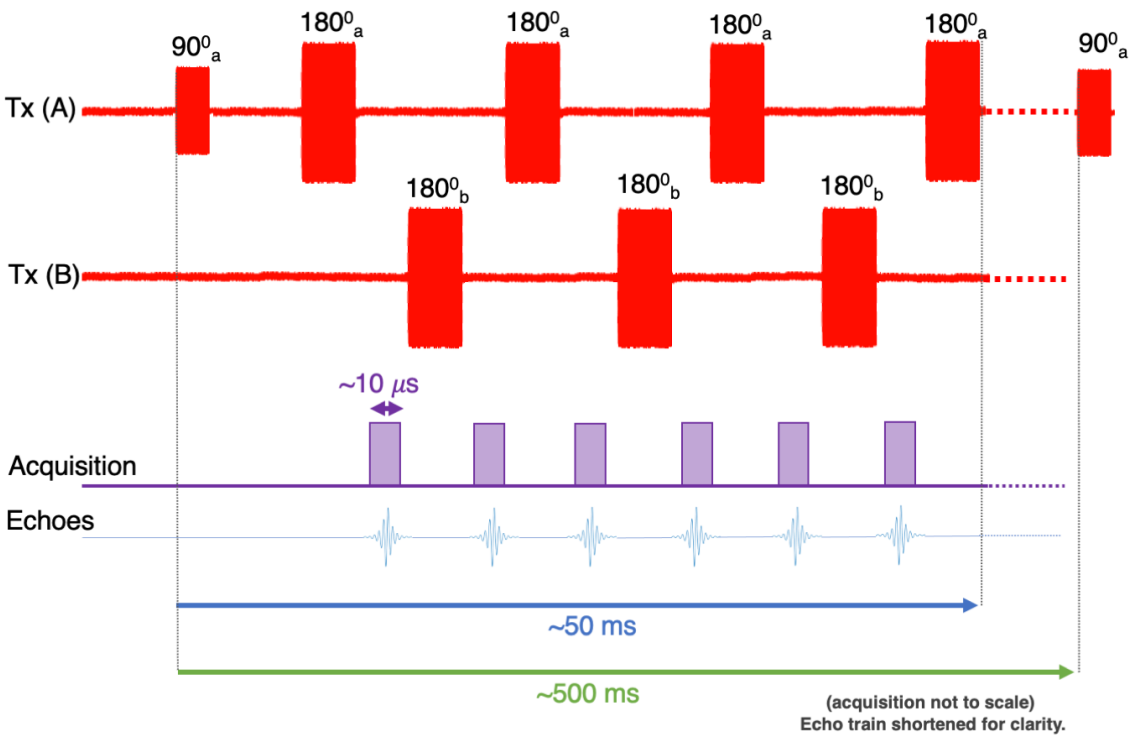

Figure 2.14: Two-coil TRASE pulse sequence and the acquired NMR signal (echoes). The RF excitation pulses are applied sequentially by two phase gradients coils (Tx(A), Tx(B)). The NMR signal is acquired between the refocusing pulses.

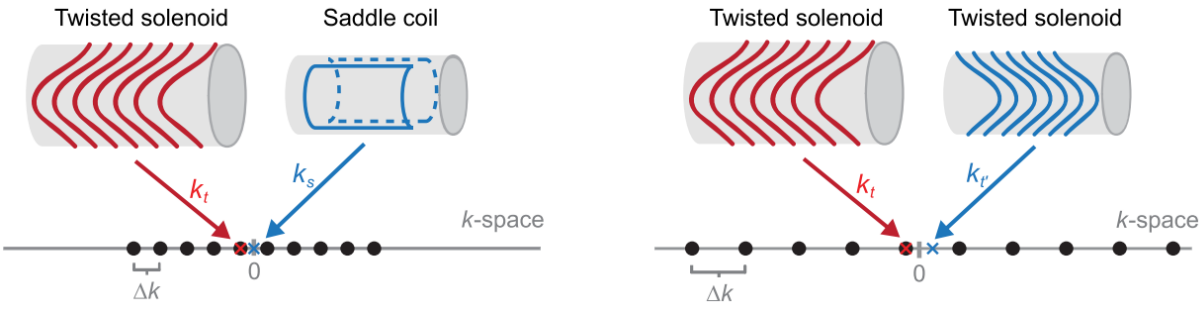

Figure 2.15: Two different RF coil sets that allow 1D TRASE. (a) The twisted-solenoid provides an RF phase-gradient (k_t) and a uniform field is produced by the saddle coil ($k_s = 0$). (b) Two twisted-solenoid RF coils with opposite phase gradients double the k-space jump producing high spatial resolution. Figures were obtained from Sun et al. (2020) [42] with permission.

pair [42]. Both configurations require a single amplifier with switches, two separate amplifiers, or a two-channel RF amplifier as discussed in Chapter 3.

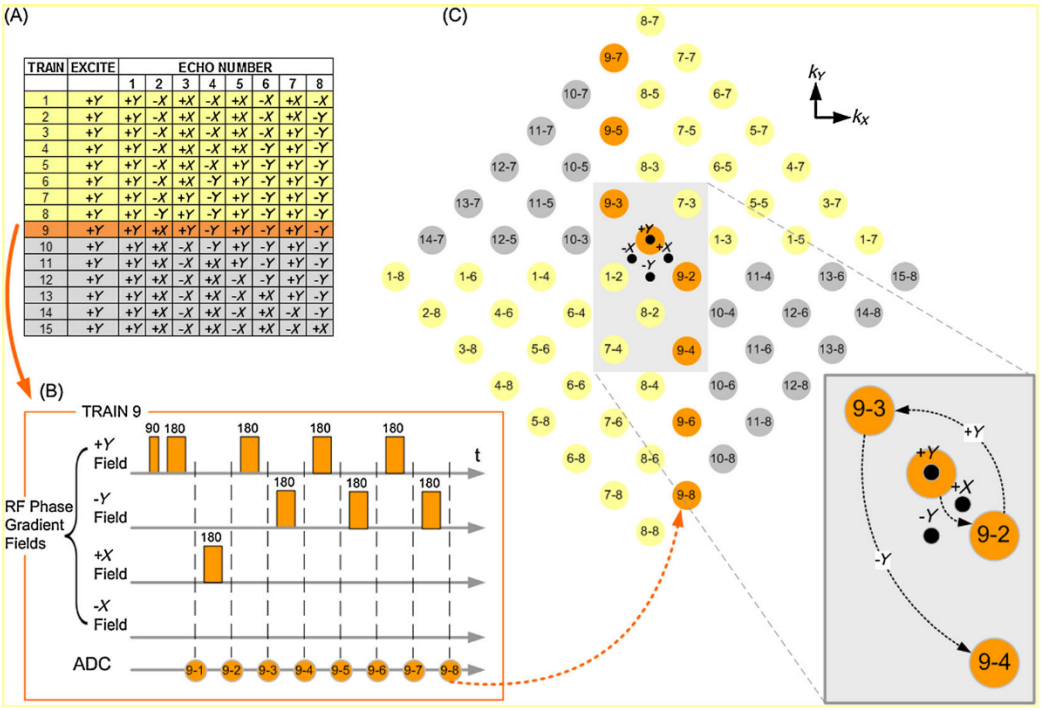

Figure 2.16: Acquisition of a two-dimensional TRASE MR image. (A) A table of 15 possible RF pulse trains to traverse 2D k-space. (B) The B_1 pulses and acquisition windows for the specific train # 9. (C) The k-space trajectory and the four B_1 phase gradient coil origins (+Y, -Y, +X, -X) are shown. The RF pulse trains in (A) allows an 8 × 8 2D k-space coverage. Figures were obtained from Sharp et al. (2013) [40] with permission from John Wiley and Sons under license number 5324550497045.

2.2.4 2D TRASE acquisition

Two-dimensional (2D) TRASE acquisition is more complex than 1D since three or more B_1 phase gradients are required; hence more RF coils [40]. The multiple RF coils must be sufficiently decoupled to avoid image distortions [42, 75, 76]. An example of 2D cartesian k-space TRASE acquisition is shown in Figure 2.16 [40]. In this example, four RF coils each with different B_1 phase gradients are represented by offset points in k-space (+X, -X, +Y, -Y in Figure 2.16). An example of the TRASE pulse sequence and RF phase gradients is demonstrated for train # 9 (orange label, Figure 2.16B). Similar to 1D TRASE, the RF refocusing pulses are switched sequentially between each RF coil. After each refocusing pulse, the NMR signal is collected by sampling the echo, filling a single k-space point in the 2D plane. The corresponding sampled

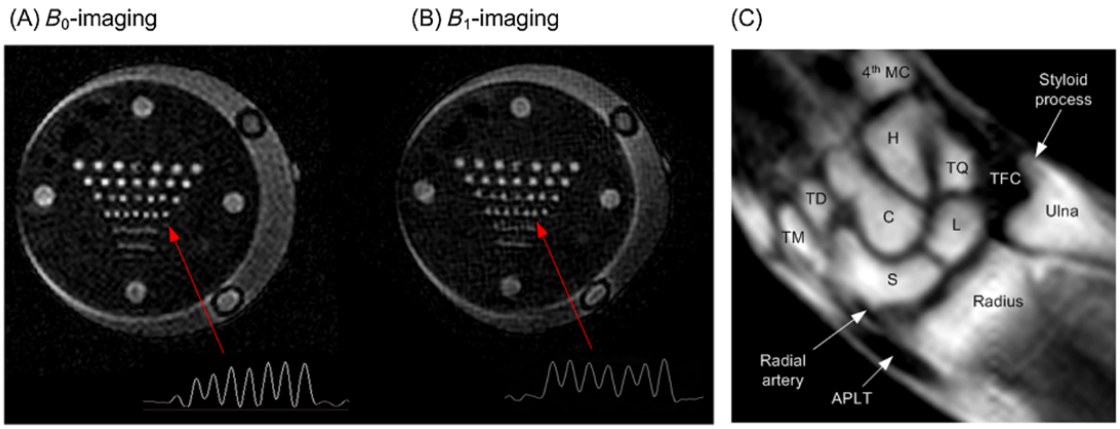

Figure 2.17: First high-resolution in-vivo TRASE images of the human wrist. Thin-phantom MR images using (A) conventional B_0 encoding (spin echo, TE = 14 ms, TR = 1 s) and (B) TRASE B_1 encoding (echo spacing = 700 mus, TR = 500 ms, pulse duration = 500 μs). (C) A 2D TRASE image of the human wrist (pixel size = 1.1 mm, number of echoes = 200, pulse spacing = 1.1 ms, pulse duration = 500 μs). Figures were obtained from [40].

k-space points for train # 9 are shown in Figure 2.16C on the 8 × 8 k-space grid. A zoomed picture of the coil k-space origins and the acquired k-space points after a select number of refocusing pulses are shown for clarity. Once all the echo trains are completed (Figure 2.16A), the 2D image is reconstructed using the inverse FT applied to the 2D k-space data [40]. Sharp et al. (2013) obtained phantom images and high-resolution 2D TRASE MR images of the wrist using a dual Maxwell-Helmholtz RF coil set and a 0.2 T bi-planar permanent magnet MR system with a standard slice selection method using a B_0 gradient (Figure 2.17) [40].

2.2.5 TRASE spatial resolution

Since k-space data is equivalent for both TRASE and standard Fourier MR imaging, the TRASE pixel size can be calculated as per Equations 2.23 - 2.24: $\Delta x = 1 / FOV = 1 / (N \Delta k)$ where N is the number of pixels along 1D of k-space. In TRASE, the echo train length (ETL) equals the number of k-space reflections of size $\Delta k = \Delta k_{BA}$

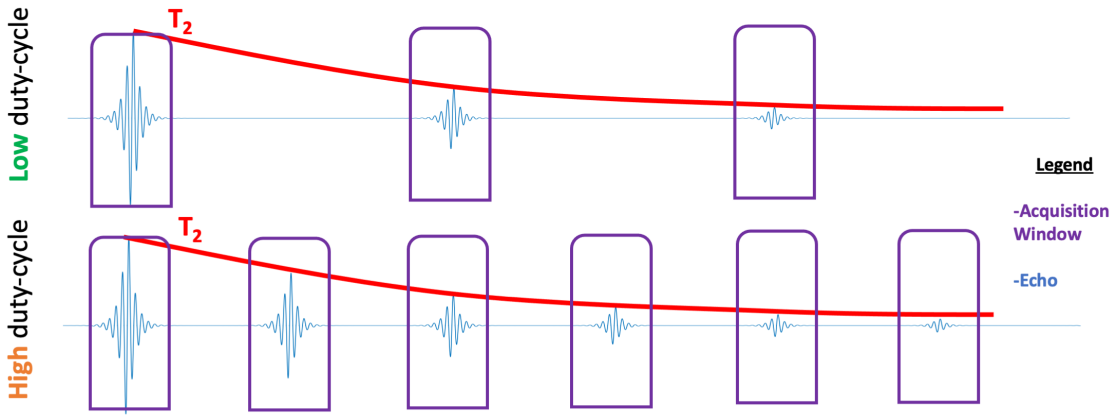

Figure 2.18: The effect of T_2 signal decay in long RF pulse trains using low or high duty cycle RF pulses. A high pulse rate increases the number of achievable k-space points (echos) before the NMR signal reaches the noise level, providing higher TRASE spatial resolution than low duty cycle.

(see Figure 2.12); therefore, the TRASE pixel size is:

$$\Delta x = \frac{1}{\Delta k_{BA} \cdot ETL} \tag{2.39}$$

However, T_2 signal decay limits the ETL, reducing the number of collected k-space points (hence, spatial resolution) before the NMR signal reaches the noise level. Qin (2012) showed that the point spread function broadens due to T_2 relaxation in long echo trains, such as TRASE, causing image blurring [66]. Qin (2012) also determined that the total echo train time (T_{ET}) should be shorter than $1.2 \times T_2$ [66]:

$$T_{ET} = ETL \cdot (T_p + T_{acq}) \leq 1.2T_2 \tag{2.40}$$

where T_p is the RF pulse duration and T_{acq} is the duration of the NMR acquisition window. Sharp et. al. (2013) noted that in-vivo resolution (wrist images in Figure 2.17) was hindered by the low duty cycle of the commercial RF amplifier ($\sim$10%). For the highest possible TRASE resolution, very short and very frequent RF pulses are required (see Figure 2.18) to collect as many k-space data points during the signal decay. This is particularly important for in-vivo tissues that exhibit short $T_2 \sim 50$ ms.

Chapter 3

A High Duty Cycle RF Amplifier for TRASE MRI[1]

3.1 Basics of RF amplifier operation

The major component of RF amplifiers is the transistor. In addition, an RF amplifier also usually comprises of a pre-amplifier, power supplies, filters and matching circuits.

3.1.1 Basics of the transistor

The basic principle of a transistor is to amplify or switch electrical signals. There are many types of transistors for various applications such as broadcasting, cellphones and mobile networks, computers, switches, audio and RF amplifiers for many industrial, scientific and medical applications. Despite the wide range of transistors, there are two prominent families of transistors used for these applications: (a) Bipolar junction transistors (BJTs) and (b) field-effect transistors (FETs) [77]. There are three leads of the BJT: collector, base and emitter (Figure 3.1A,B,D). BJTs commonly require input current at the base to allow a large current to flow from the emitter to the collector [77]. Similarly, the three major leads of the FET are the source, gate and drain (Figure 3.1C,E). FETs require only a small voltage at the gate with little or no gate current affecting the dynamics of the transistor (Figure 3.1C,E) [77]. FETs, in general, are cheaper to manufacture and extremely small [77].

[1] A section of this chapter was published in A.R. Purchase et al. Magn Reson Mater Phy: 32, 679–692.

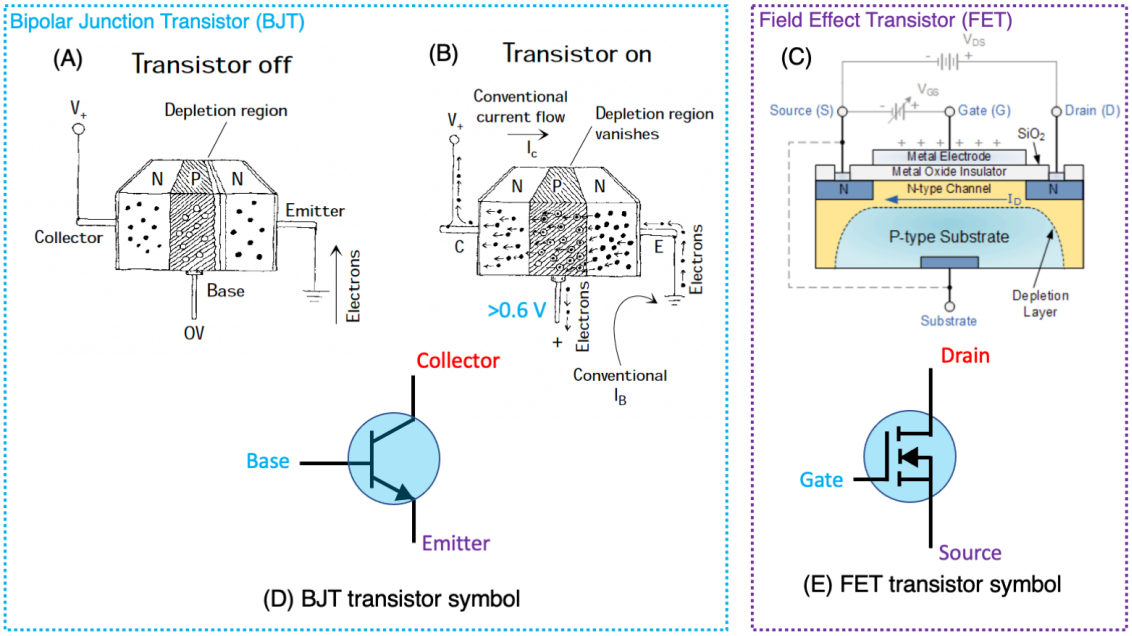

Figure 3.1: An illustration of the BJT and FET. (A) The OFF state of the BJT. With no voltage at the base, a depletion region prevents current flow. (B) The ON state of the BJT. With a positive voltage (> 0.6 V) at the base, the depletion region is eliminated allowing a current to flow through the transistor (emitter-to-collector). (C) The ON state of the FET. V_{DS} and V_{GS} is the drain-to-source voltage and the gate-to-source voltage, respectively. A positive voltage on the gate terminal controls the current between the source and drain. The (D) BJT and (E) FET symbols. Figures A,B were modified from Scherz (2000) [77] with permission from McGraw-Hill under license number 1230468-1 and Figure C were modified from Electronics-Tutorials with permission (https://www.electronics-tutorials.ws/transistor/tran_6.html).

Following the introduction of FETs and BJTs, a robust transistor, the laterally-diffused metal-oxide-semiconductor (LDMOS), was developed in the 1970s [78–80]. It showed superiority in performance compared to other transistors. The LDMOS transistors remain the dominant component of RF amplifiers operating at a frequency between 1 MHz and 3.5 GHz, due to their high linearity, high efficiency, high gain, and relatively lower costs than other transistors [78, 79].

The operation of transistors can be explained using the BJT theory as its principles can be generalized to all transistors. Figure 3.1A shows the OFF state (no current flow between collector and emitter) and Figure 3.1B shows the ON state of a BJT [77]. The BJT consists of three adjacent layers of n-doped and p-doped layers. The doped

layers intentionally have impurities, such as phosphorus or boron, to modulate their electrical properties. The n-type layer contains free electrons that move in the crystal; p-doped layers readily accept electrons due to electrically conductive "holes". In BJTs, the n- and p-doped layers alternate (NPN or PNP), allowing control of current flow through the transistor. For example, in the OFF state (0 V at the base) for an NPN transistor, a depletion region forms between an n- and p-doped layer due to free electrons in the n-type layer filling the holes in the adjacent p-type layer because there is no potential difference between these layers. The depletion region prevents the flow of electrons from the emitter to the collector (Figure 3.1A) [77]. However, when a small bias voltage (> 0.6 V) is applied at the base, the depletion region vanishes, allowing electrons to move through the transistor since the p-type layer is thin. Furthermore, increasing the bias voltage increases the emitter-to-collector current in proportion to the current gain (β) specific to the transistor ($I_C = \beta I_B$) [77]. The large current is provided by the DC power supply unit (V_+ in Figure 3.1) [77]. In addition, if the NPN transistor is reverse biased (i.e. a negative voltage at the base), the depletion region size increases, further preventing current flow. Since the NPN base acts as a current "source" (assuming a conventional current), the voltage and currents in PNP transistors are reversed, and the base serves as a current "sink." For the FET, the gate terminal is electrically isolated from a P-type substrate by a metal oxide layer, preventing current flow in the gate (Figure 3.1C,E). However, when a voltage is applied to the gate terminal, attracting the electrons in the substrate, an N-type channel is formed allowing current between the source and drain. The gate voltage determines the thickness of the channel, which in effect, controls the current dynamics in the transistor. Furthermore, LDMOS transistors operate similarly to standard FETs and with high output power capability; therefore, I used the LDMOS as a basis for the TRASE RF amplifier design. The details, including materials and engineering, of BJTs, FETs and LDMOS transistors are out of the scope of this thesis and could be found in other publications, for example [78–81].

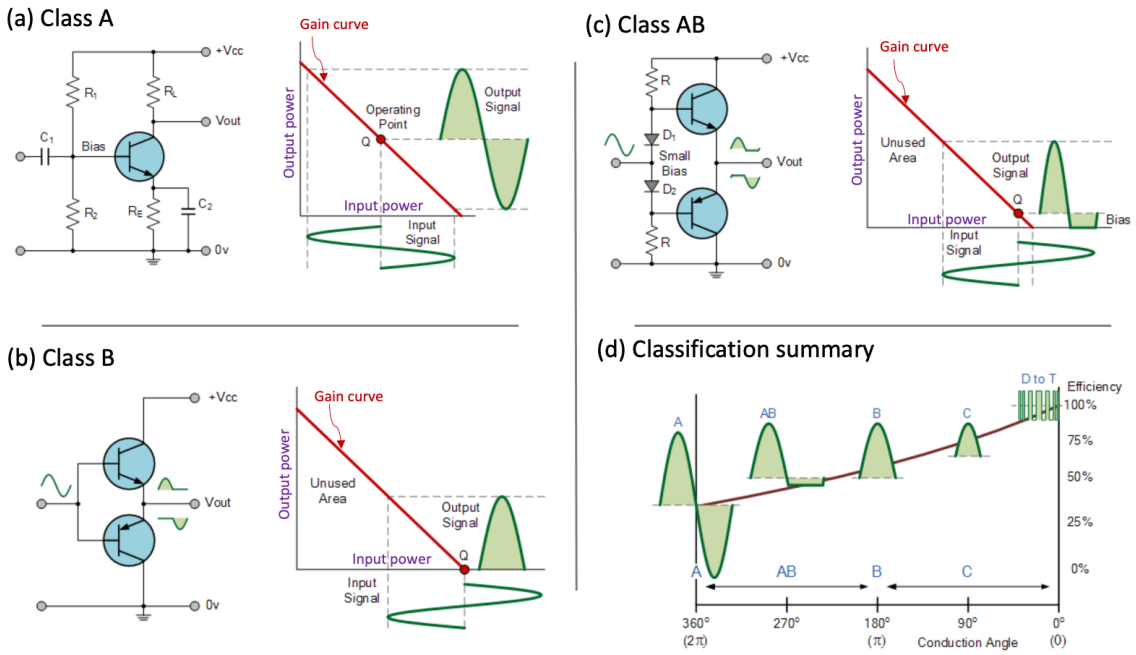

Figure 3.2: Classification of RF amplifier operation. An example electronic schematics and RF output response for (a) Class A, (b) Class B, and (c) Class AB amplifier operation. (d) A classification summary comparing the conduction angle (determined by the bias point Q) and the power efficiency of an amplifier. All figures modified from Electronics-Tutorials [82] with permission.

3.1.2 Classification of RF amplifiers

Regardless of the transistor technology used in amplifiers, the operating performance depends on the voltage provided at the base or gate (i.e. bias). Therefore, the amplifiers are divided into classes (A, B, AB, C, D, etc) depending on the bias voltage point (Q in Figure 3.2).

Class A

The bias of the class A amplifier is set at the voltage enabling best RF output linearity, compared to all other classes (see Figure 3.2a) [77, 81]. Unfortunately, this operation suffers power inefficiency (i.e. high heat generation) since the transistor conducts the during entire RF input cycle [77], [81]. The conduction angle is a measure of the portion the RF input cycle which the transistor generates RF output. For class A operation, the conduction angle is 360°.

Class B

To improve power efficiency of the class A RF amplifiers, class B uses two back-to-back transistors in the push-pull configuration (see Figure 3.2b). The back-to-back transistors typically consists of a NPN and a PNP where NPN is on for a positive gate voltage and PNP is on for a negative gate voltage. Class B improves the power efficiency since each transistor conducts for only one-half of the RF input cycle; a conduction angle $\sim$180° [77, 81]. Although class B improves power efficiency, the design suffers distortion of the RF output waveform due to the "dead-band" of the transistors. The dead band arises since both transistors are not conducting when the RF input voltage is low (-0.6 $< V_{in} <$ 0.6 V); therefore, the RF output voltage immediately falls to zero [77, 81].

Class AB

The class AB operation is a trade-off between the RF output linearity produced by class A and the power efficiency produced by class B. By application of a small DC bias voltage, both the NPN and PNP bias voltages avoid the dead-band (Figure 3.2c) [77, 81]. More specifically, the NPN and PNP bias stays above +0.6 V and below −0.6 V, respectively, for the Class AB amplifier in Figure 3.2c [77, 81]. In effect, the class AB RF amplifier maximizes both power efficiency and RF output linearity. Since high RF power and pulse shape fidelity are required in NMR and MRI, class AB is the most common type of RF amplifier used in these applications.

Class C and others

Since classes A, B, and AB amplifiers produce heat during operation, large heat sinks and fans are required leading to bulky designs. Class C, D, and others operate with a very short conduction angle (below 90°). For class C or D, the goal is highest possible power efficiency since it allows more compact and cheaper amplifiers. RF output nonlinearities and distortions are inevitable but may be reduced or mitigated

using other components such as filters [77, 81]. Although beyond the scope of this thesis, class D amplifiers have been designed and used successfully as inexpensive, compact and efficient devices for some portable NMR and MRI systems but often with limited peak RF output power (< 150 W) [83].

3.2 RF pulses in TRASE

Although TRASE removes the costly B_0 gradient system, it introduces new requirements for RF power amplifiers. TRASE requires the generation of multiple, short, high-power RF pulses to collect as many k-space data points as possible within the T_2 decay window. Since commercial RF power amplifiers do not meet these requirements, TRASE spatial resolution is limited [40, 44].

Figure 3.3 shows a one-dimensional (1D) TRASE pulse sequence. Figure 3.4 shows the corresponding 1D k-space trajectory. 1D TRASE consists of a single 90° excitation RF pulse followed by two-channel (A and B) transmission of short, high-power 180° RF refocusing pulses applied to two independently driven RF coils. The signal is acquired between each refocusing pulse to fill a single line of k-space. The total echo train length is limited by T_2 decay, restricting the spatial resolution, particularly in-vivo due to short T_2 relaxation times of tissues [40]. 2D or 3D TRASE requires more RF pulses, hence more RF coils and more RF amplifiers (see Chapter 2) [35, 40, 44, 73].

3.3 RF amplifier requirements for TRASE

Since commercial amplifiers do not meet the requirements for TRASE, a new RF amplifier design was needed. For maximal TRASE MR image resolution, high-power RF output, high duty cycle, fast switching times and minimal blanking RF output noise are essential (Table 3.1).

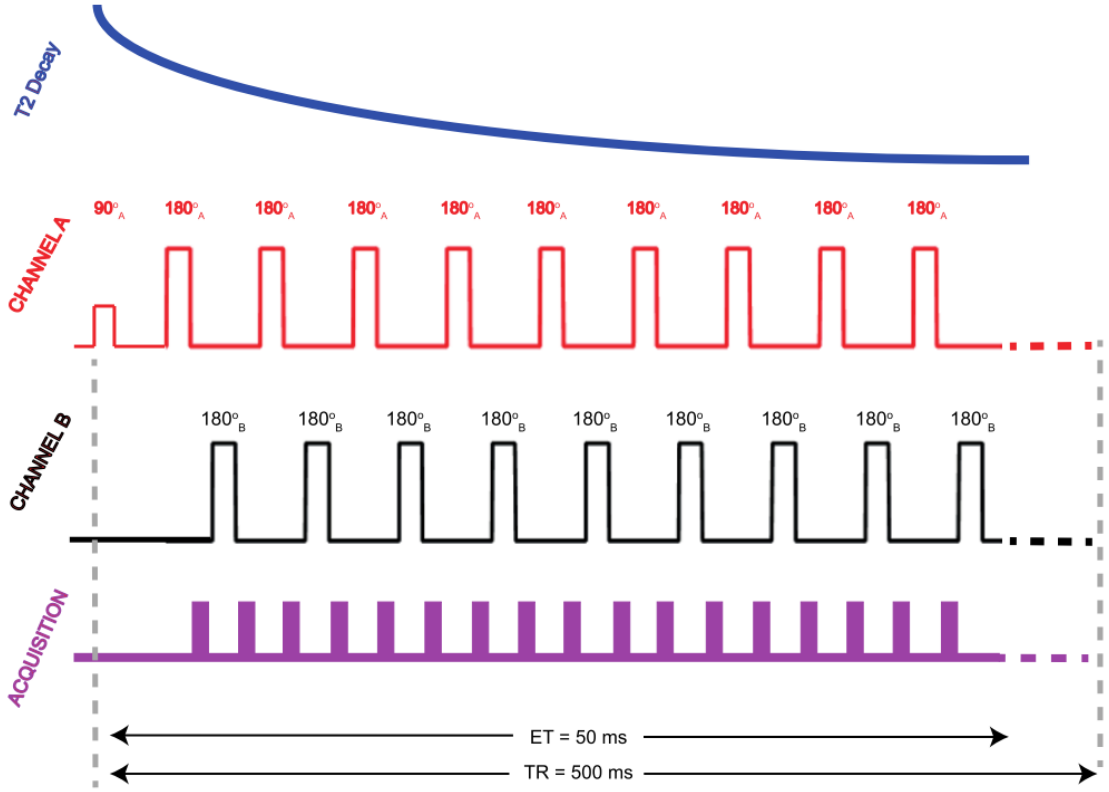

Figure 3.3: Two-channel 1D TRASE pulse sequence. Echo data acquisition (purple) occurs between the 180° RF pulses. The total acquisition time (train length) is limited by the T_2 decay (top blue line). Typical parameters of TRASE: echo train time (ET) is 50 ms, 128 data points, and repetition time (TR) is 500 ms.

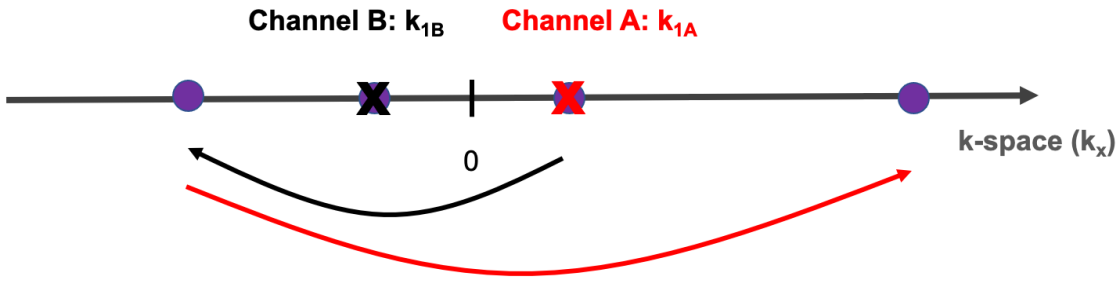

Figure 3.4: The 1D TRASE k-space trajectory.

Table 3.1: Requirements for the RF power amplifier used in TRASE MRI

Specification	1D TRASE requirement
Peak RF power output	$\geq$ 1 kW
Number of channels	$\geq$ 2
RF duty cycle	$\geq$ 50%
Blanked noise level (BNL)	$\leq$ -171 dBm/Hz
Pulse-to-rising/falling edge (PRE, PFE)	$\leq$ 10 μs
RF rise/fall transition time (RRT, RFT)	$\leq$ 5 μs
Pulse duration	$\leq$ 100 μs
Harmonics strength at 1 kW	$<$ - 12 dBc
Class	AB
Total gain	+60 dB

3.3.1 Duty cycle

The use of low field ($<$ 1 T $\sim$ 42 MHz) commercial MRI RF amplifiers (Table 3.2) for TRASE is limited for several reasons. They are placed in "fault mode" by a protection circuit that prevents higher than $\sim$20% duty cycle, a certain pulse width or over peak RF output power [91]. The reason for this protection is to reduce possible damage to the RF amplifier due to overheating [91] and to limit potential overheating of the patient (i.e. limit the specific absorption rate (SAR)) [92]. It should be however noted, that because SAR increases proportionally to B_0^2, higher duty cycle RF trains can be applied at lower fields ($<$ 0.5 T). Still, commercial RF amplifiers for low field limit the duty cycle $<$ 20% [92]. Although high duty cycle RF amplifiers do exist, for example, for hydrogen decoupling [93], they operate at low RF output power ($<$ 100 W) and high frequency ($>$ 65 MHz); hence, they cannot be used for TRASE at low fields. The Tomco BT01000-Delta is an example of such an amplifier (see Table 3.2).

Only a few commercial MRI amplifiers are manufactured to operate at low frequency (e.g., Analogic, Tomco, CPC) but with low duty cycle (Table 3.2). Holland

Table 3.2: Specification of selected commercial amplifiers used in MRI. [a]Specifications taken from commercial data sheets. [b]Measured blanking noise level for center frequency of 9.27 MHz and bandwidth of 100 kHz. [c] Defined as 0 to 90% amplitude (or vice versa). [d]Specification sheet does not state how the measurement was made. [e]Measured using pre-gated RF input.

RF amplifier	Peak power (kW)	Number of channels	Operating freq. (MHz)	Maximum duty cycle (%)	Blanking noise level (dBm/Hz)	Pulse-to-rising/ falling edge (μs)	RF rise/fall transition time (μs)	Minimum pulse length (μs)	Harmonic strength (dBc)
Analogic AN8100[84]	3	1	5-30	10	<-160[a] / -171.1[b] (meas.)	20[c]	N/A	100	<-25
Tomco BT00500[85]	0.5	1	0.1-30	20	N/A / -171.9[b] (meas.)	1[d]	0.2[d]	<10	$\leq$ -25
CPC 0.2 T 500 M[86]	0.5	1	0.1-10	10	20 dB[a] (over therm.)	1[d]	1[d]	N/A	< - 12
MKS Instruments S35[87]	18	1	63.87	50	<-150[a]	50[d]	N/A	100	< - 40
Tomco BT01000-Delta[88]	0.1	1	100-600	100	¡ 10 dB (over therm.)	0.3/0.15[d]	0.2/0.1[e]	N/A	< - 10
Ultra Electronics 3900-1[89]	0.3	1	6-220	10	25[a] dB (over therm.)	2[d]	0.5[d]	N/A	N/A
Analogic AN8111[90]	6	1	5-30	10	< -160[a]	20[c]	N/A	N/A	< - 25

and Heysmond produced an RF amplifier for pulsed low field NMR capable of delivering 300 W continuous-wave (CW) or up to 800 W pulsed RF with a duty cycle below 5% [94]. To my knowledge, currently, no commercial RF amplifier exists that satisfies all the requirements for high-resolution TRASE MRI.

3.3.2 Noise blanking and timing

Disabling the RF power amplifier output stage ('gating') during signal acquisition reduces electronic noise which is crucial in MRI to maximize SNR [91]. Long delays between gating and the RF output pulse are an undesired consequence of the RF amplifier switching especially at high duty cycle ($\geq 50\%$) with short RF pulses ($\sim$100 μs), leading to reduced RF output pulse fidelity for CW RF input.

The timing parameters pertinent to any RF amplifier performance are as follows (Figure 3.5):

- Pulse-to-rising edge (PRE) time - the interval from the gate pulse "on" to the beginning of the RF output pulse.
- RF rise transition (RRT) time - the delay from the beginning of the RF output pulse to the 100% RF output amplitude.
- Pulse-to-falling edge (PFE) time - the delay from the gate pulse off to the beginning of the RF output amplitude decay.
- RF fall transition (RFT) time - the delay from the beginning of the RF output amplitude decay until the RF output reaches noise level.

For example, a rectangular gate input to the transistor bias control circuit may become non-rectangular (due to RC integration) and shape the envelope of the RF output [95]. A high duty cycle and short rectangular RF pulse train output is a requirement of the RF amplifier to obtain high-resolution TRASE; therefore, minimizing these delays is essential to maximize the total echo train length, hence the

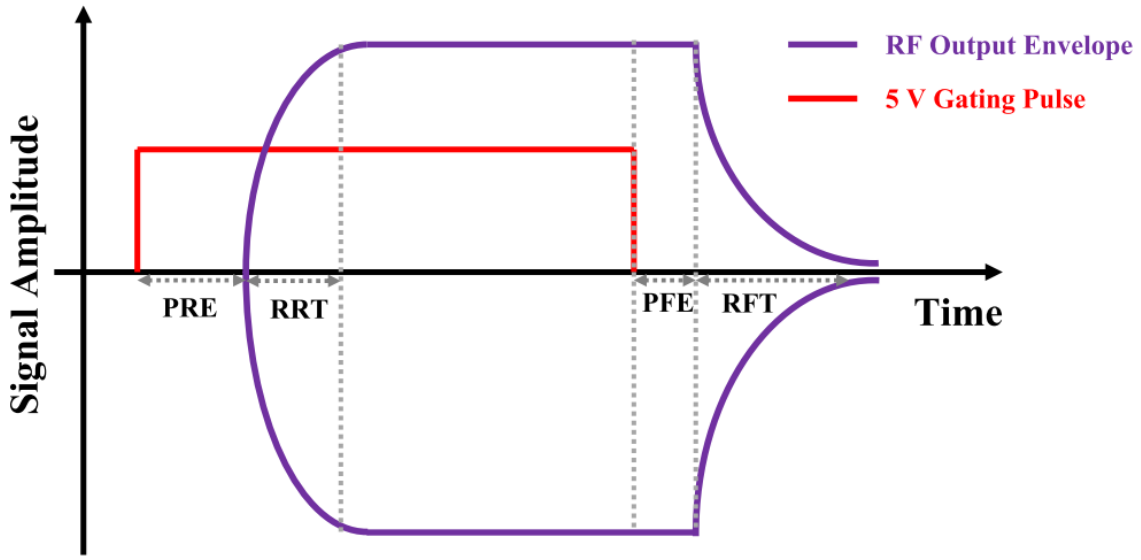

Figure 3.5: An illustration of the relationships of timing parameters between the gate pulse (red) and RF output (purple) for a single pulse during RF amplifier operation: pulse-to-rising edge (PRE) time, RF rise transition (RRT) time, pulse-to-falling edge (PFE) time and RF fall transition (RFT) time.

spatial resolution. Any additional timing delay reduces pulse fidelity and total echo train length. An increase of RRT or RFT leads to longer pulses necessary for RF 180° refocusing pulses, effectively reducing spatial resolution of TRASE. It should be noted that long PRE and PFE times present in commercial MRI RF amplifiers (e.g., Analogic or MKS S35) reduce the time available for data acquisition. This is yet another drawback of the available commercial RF amplifiers.

3.3.3 Size and weight

Most commercial amplifiers are single channel, large and heavy. To meet the TRASE requirement for a multi-channel amplifier, many single channel commercial amplifiers could be combined, but it would lead to extremely expensive and bulky systems which is definitely not suitable for a portable MRI. A significant reduction in total amplifier size could be made using a common power supply unit for multiple pulsed RF channels.

3.4 Methods

3.4.1 Design aims

MRI RF power amplifiers amplify low power RF pulses (0–1 mW) generated by an MR console to high power (order of kW). The console also provides gating pulses ('blanking') to switch the amplifier on during RF transmission and off during data acquisition to reduce amplifier noise. A transmission line feeds the RF output to an RF coil matched to 50 Ω and tuned to the Larmor frequency.

Considering the TRASE applications of the amplifier, the aims of the design were (Table 3.1):

- Design and construct a dual-channel RF amplifier system, achieving 1 kW peak pulsed output per channel.
- Achieve a minimum total gain of + 60 dB per channel.
- Minimize blanking noise to a level comparable to commercial RF amplifiers.
- Minimize all timing delays (RRT, RFT, PRE and PFE).
- Use a common main power supply unit for both RF outputs (channels).
- Implement an efficient air-cooling system for heat dissipation for both channels.

3.4.2 Detailed design

To clarify the discussion on the RF amplifier design for TRASE, I define the following parameters:

- Bias voltage refers to 2 V applied directly at the transistor gate.
- Blanking refers to a 0 V bias (i.e., switching a 5 V gating input to 0 V switches the transistors off).
- Gating pulse means the 5 V pulse provided to switch the amplifier on.

- Blanking noise power (BNP) is the average noise power (dBm) within 100 kHz bandwidth centered at the operating (Larmor) frequency with no applied gating signal and 50 Ω termination at RF input of the RF amplifier. A ∼0.22 T permanent magnet was used in this work; therefore, the operating frequency of the amplifier was 9.27 MHz.

- Blanking noise level (BNL) was introduced to remove the dependence of the spectrum analyzer resolution bandwidth (RBW) noise and the window bandwidth (BW) noise on the BNP measurement to estimate the noise level in a 1 Hz window. Therefore, BNL(dBm/Hz) = BNP(dBm) - 10log(RBW) - 10log(BW).

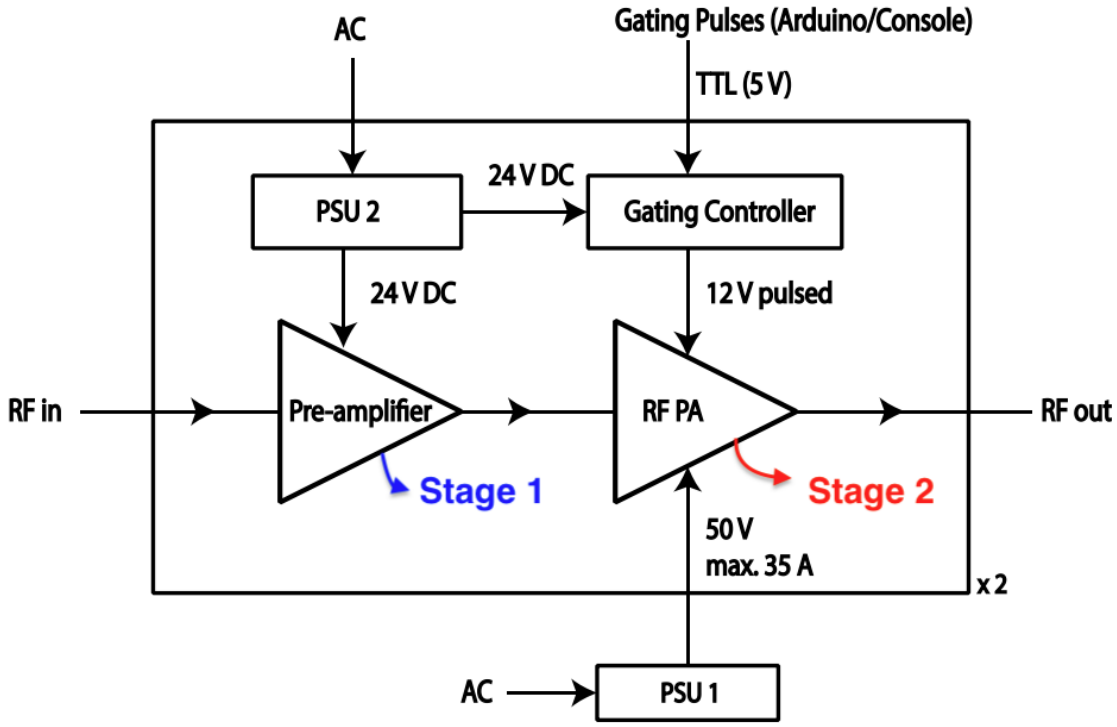

Figure 3.6: A block diagram of the RF power amplifier. An RF input is amplified by a pre-amplifier which provides input (0–1.5 W) to the main power amplifier deck (RF PA). The 24 V power supply (PSU 2) provides power to both the gating controller and the pre-amplifier. The power supply (PSU 1) provides a high DC power source to multiple, main RF amplifier (RF PA) units. For dual-channel operation the design is duplicated ('× 2'). AC is a standard alternating current power source (120 VAC, 60 Hz)

Several modules using commercially available components were selected to satisfy

the design aims. Figure 3.6 shows a block diagram of the two-stage RF amplifier with a 5 V gating pulse, RF input, RF output and two 120 V AC power connections.

A two-stage amplifier design was selected to achieve a + 60 dB gain (Figure 3.6). In the first stage, a pre-amplifier (ZHL 1–2 W + by Mini-Circuits, USA) was used to amplify a 9.27 MHz RF input (0–1 mW) by + 33 dB. This particular pre-amplifier was used for its reliability, small dimensions and consistent gain over a wideband of operating frequencies [96]. This pre-amplifier operates in class-A mode with high RF output linearity minimizing potential signal distortions [96]. A 2.1 A, 24 V power supply (PWR-242-AE, Advantech Co. Ltd., Taiwan) was used for the pre-amplifier. In the second amplification stage, an amplifier based on the BLF 188xr transistor (NXP Semiconductors, The Netherlands) was selected for its high efficiency, excellent thermal stability, + 25 dB gain, 1 kW RF output, broadband frequency of operation (1.8–54 MHz) and excellent continuous wave (CW) performance [97, 98].

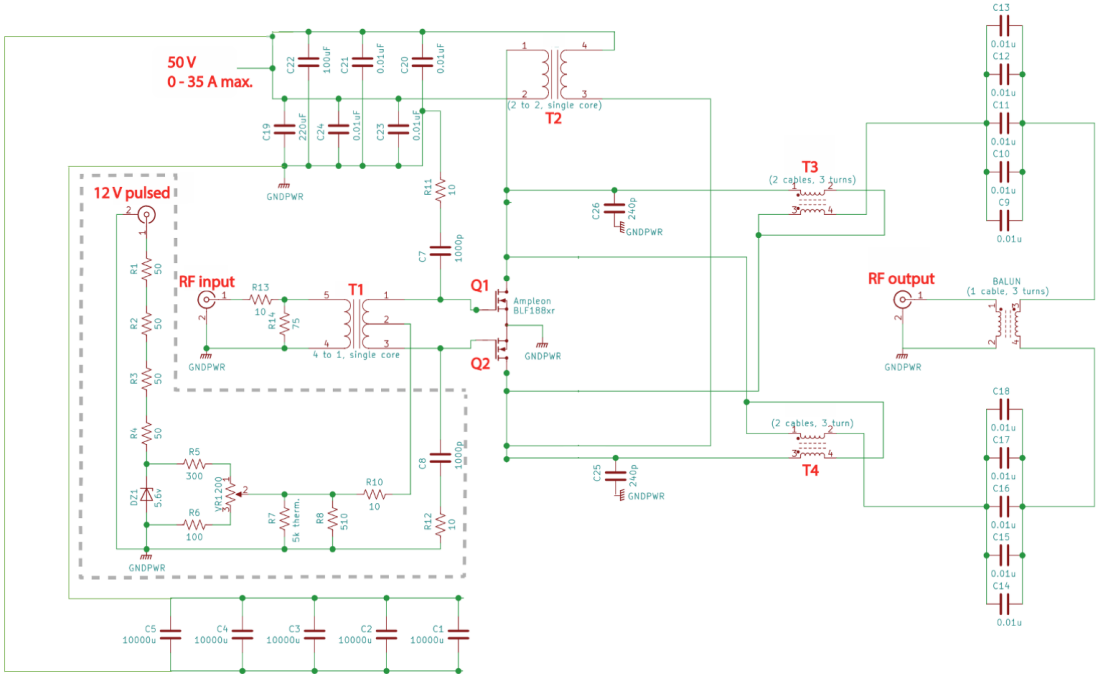

Figure 3.7: The main RF amplifier (second stage) circuit was modified from W6PQL Amateur Radio Station [97]. The main RF amplifier consists of five circuits: RF input (from pre-amplifier), bias network (dashed gray box), main power (50 V from TDK-Lambda GEN50-30 for transistors), transistors (Q1, Q2) and RF output circuit (all components are shown to the right of Q1 and Q2 transistors).

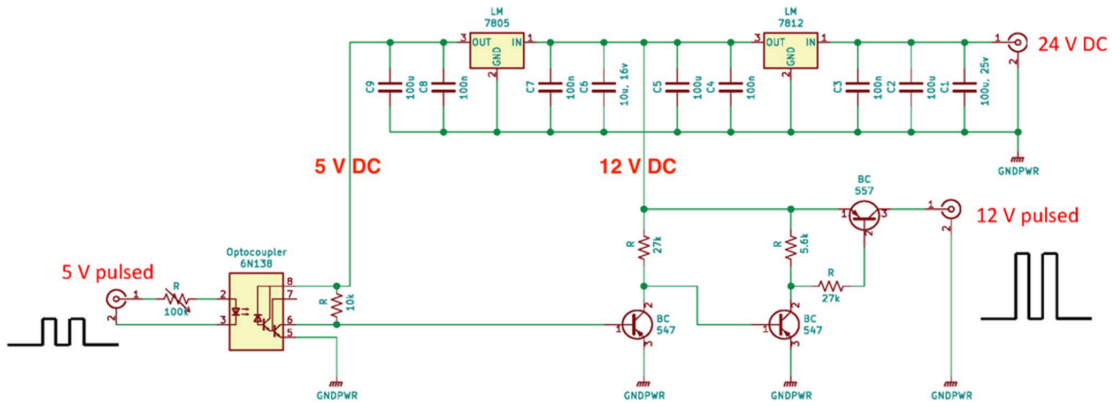

Figure 3.8: An optically isolated gating controller circuit. A 5 V gating TTL input signal from the console or Arduino controls 12 V, 30 mA DC output connected to the 12 V biasing network of the main amplifier (Figure 3.4). The 24 V input is connected, along with the pre-amplifier, to the PWR-242-AE power supply (Advantech Co. Ltd., Taiwan)

As the basis for the circuit, a 1 kW RF amplifier commonly applied in amateur radio broadcasting was used [97]. The circuit diagram for the second amplification stage is shown in Figure 3.7. However, in radio communication, BLF188xr transistors are commonly used in a continuous wave (CW) mode rather than the pulsed mode required for MRI. Therefore, a gating controller (Figure 3.8) was constructed to generate 12 V gating pulses to drive the second amplification stage (Figure 3.7) from a pulsed 5 V gating source. Fast switching of the bias (see dashed line Figure 3.7) was accomplished through a simple circuit comprising resistors (R1–R8, R10, R12), a Zener diode (DZ1), a potentiometer (VR1 200), and a capacitor (C8). Capacitors that were parallel to the resistors (R7, R8) in the original W6PQL version [97] were removed to reduce delays (PRE and PFE) caused by the RC integrating effect. However, although they slightly increased RF noise level (∼5%) during RF transmission, there was a negligible change in the blanking noise level. The 24 V power supply (PWR-242-AE, Advantech Co. Ltd., Taiwan) used for the pre-amplifier was also used to power the gating controller. The optocoupler eliminated potential ground noise originating from a 5 V TTL signal generated by the console.

Gating operation

The gating controller (Figure 3.8) operates as follows. A 5 V gating pulse input activates the optocoupler (6N138) and bias of bipolar junction transistors (BC 547) such that the transistor (BC 557) applies 12 V to the BLF188xr power transistor bias network (dashed line in Figure 3.7). The voltage regulators (LM 7805, LM 7812) reduce 24 V DC to stable 5 V and 12 V DC levels for the gating controller circuit (Figure 3.8). The variable resistor (R 100 k) provides fine adjustments around 1 V across the light-emitting diode (LED) to match its sensitivity to the phototransistor. These adjustments minimize delays (PRE, PFE) introduced by the gating controller. The 12 V pulsed gating output (Figure 3.8) was connected to the 12 V input of the main amplifying deck (Figure 3.7).

Power supply unit

The power supply (TDK Lambda GEN50-30, TDK-Lambda Americas Inc., USA) was selected for the second amplifying stage due to its small vertical dimension occupying minimal space in a rack as well as its low noise and low ripple (due to AC to DC conversion) specifications [99]. The power supply unit maintains constant 50 V at the RF transformer input (T2 in Figure 3.7) and delivers the required current (0–30 A). This power supply unit, in our design, is used for two RF output channels but could be used for more RF output channels (i.e., to maintain 50 V and up to 30 A total current for multiple BLF188xr units). Five 10 mF capacitors (C1–C5) per main amplifying deck were added in parallel to the 50 V main power supply for pulsed operation [100]. The capacitors are charged during the blanking period and discharge fast during transmission ensuring continuous and stable power delivery in pulsed RF conditions.

3.4.3 Theory of operation

The designed and constructed TRASE amplifier operates in class-AB as a push–pull design. Both Q1 and Q2 transistors (Figure 3.7) operate at different times depending on the phase of the RF input at the transformer (T1). An unbalanced RF input is applied at the T1 input. The T1 transformer splits the RF input and shifts the relative phase of the RF inputs by 180° which are subsequently applied at the gates of Q1 and Q2, producing the required on-off cycle for push-pull operation. In addition, the required gate DC voltage is applied to the output of T1 to balance the RF applied to both gates. The small DC voltage is applied through a bias network which is regulated and impermeable to RF interference due to the Zener diode and a series of resistors. In addition, a thermistor is used to regulate the bias voltage due to temperature fluctuations and the 510 Ω resistor prevents over correction.

The optimal operating conditions for the BLF188xr transistors provided by the main power supply is a drain voltage of 50 V, which corresponds to a minimal power dissipation when blanked (i.e. a minimal drain leakage current of 2.8 μA [98]). The drain leakage current is the current flowing through the transistor even when switched off. The gating controller (Figure 3.8) allows the RF output of the transistors to switch off to the level of the drain leakage current; therefore, minimizing the blanking noise level for MRI operation. The voltage directly applied by the bias network (dashed gray line, Figure 3.7) is matched to the gate-source threshold voltage of approximately 1.9 V [98]. The additional capacitors (C1–C5, Figure 3.7) on the main power supply circuit decrease the transient response time of the power supply during pulsed operation. The transient response time describes how quickly the power supply can recover from a change in the load condition. The main power supply used here has a transient response time of 20 ms [99], insufficient for high-power (1 kW) and short (100 μs) RF pulses; therefore, capacitors were added to rectify this issue. The capacitors act as a power source which may be charged during blanking and

discharged at a faster rate than the main power supply during gating.

Furthermore, the RF output matching circuit (T3, T4, and balun) used here is common for many push-pull LDMOS transistors devices, including those based on the BLF188xr units, since 2013 (see CD-101-13, NXP Semiconductors, Netherlands) [101]. More specifically, T3 and T4 are used to match the 12.5 Ω gate-to-drain impedance of the transistors to the 50 Ω RF coaxial transmission line. Both output transmission lines are highly balanced by this transformer configuration minimizing the even harmonics in the amplified RF output waveform. In addition, the balun allows a connection between the balanced transistor outputs to the unbalanced RF coil, providing equal and opposite voltage on the output relative to ground. Therefore, a maximum amount of power is transferred to the RF coils by using the matching circuit.

3.4.4 Enclosure of the two-channel RF amplifier

The assembled two-channel amplifier is shown in Figure 3.9. Except for the main power supply, all components were installed in an aluminum enclosure mounted in a standard 19" rack. Internal components were secured to three aluminum heat sinks and an aluminum base plate.

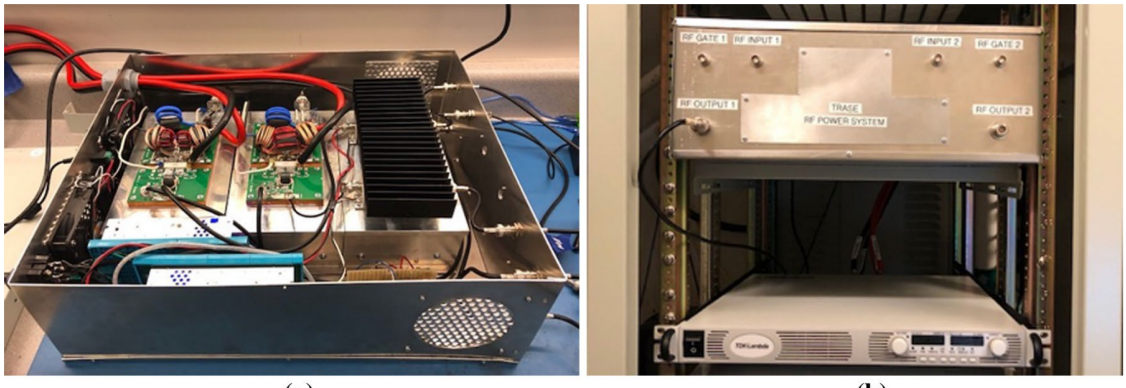

(a) (b)

Figure 3.9: (a) Modules of the TRASE 2-channel RF power amplifier mounted inside the aluminium enclosure and (b) placed in a rack for MRI operation with the power supply visible at the bottom.

3.4.5 Experimental setup

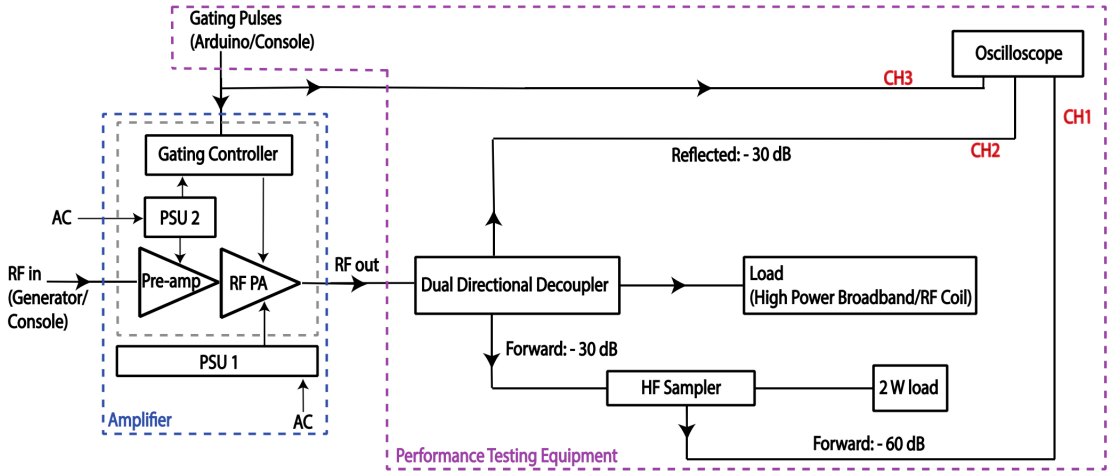

Figure 3.10: Testing setup for a single transmit channel of the RF amplifier on the bench and with an MRI console. The RF output was measured at - 60 dB, 50 Ω (CH1), reflected RF output at - 30 dB, 50 Ω (CH2) and the 5 V gating pulses (CH3) at high impedance. Forward and reflected power was monitored on the oscilloscope after attenuation.

Figure 3.10 shows the general setup for on-the-bench and with the MR console testing. The following parameters of the amplifier were measured: forward and reflected RF power, timing relationships, harmonics and blanking noise level. Three different setups were used for the performance testing:

- For on-the-bench testing, RF generation from a waveform generator (AFG 3022, Tektronix, USA), gating pulses generated by a microcontroller (Arduino MEGA 2560, Ivrea, Italy), and a high-power broadband load (50 Ω, 200 W, Wenteq Microwave Corporation, USA) were used. Continuous-wave (CW) RF input was provided by the waveform generator and the RF output was switched using the gating pulses alone. The broadband load minimized reflected power. The RF input, gating pulses and RF output were monitored for a range of RF pulse lengths (100-500 μs), duty cycles (10-50%) and RF output power levels (0-400 W; 400 W-1 kW using a maximum 20% duty cycle).

- For testing with the MR electronics, we used an MR console (TMX, MRI-Tech, Calgary, Canada) [102] to generate both pulsed RF and gating pulses, with RF output driving the high-power broadband load.

- For TRASE testing, the same MR console was used and the RF coils (saddle and twisted RF coils [74]) were used instead of the broadband load. Performance was tested by acquiring a 1D TRASE projection of a two-bottle phantom with $CuSO_4$ + NaCl-doped water.

An operating frequency of 9.27 MHz RF input and 5 V gating pulses were used in each setup. The forward RF power was monitored on an oscilloscope (MDO4054B-3, Tektronix, USA) with 60 dB attenuation using a dual directional coupler (DDS-1, PreciseRF, USA) and high-frequency sampler (HFS, PreciseRF, USA). The reflected RF power was monitored with 30 dB attenuation using the dual directional coupler.

3.4.6 Performance testing

The amplifier performance was assessed, on-the-bench and with an MRI console, for the RF output power, timing and delays, pulse stability and fidelity, blanking noise level, RF waveform linearity and 1D TRASE capability.

RF output power

On-the-bench, the RF input voltage was varied using the waveform generator and monitored using the setup shown in Figure 3.10. Direct peak-to-peak voltage measurement from the oscilloscope was converted to RMS power assuming 50 Ω according to:

$$P_m = \frac{V_{rms}^2}{50} = \frac{\left(\frac{V_{pp}}{2\sqrt{2}}\right)^2}{50} = V^2/(4 \times 10^8) \tag{3.1}$$

where P_m is RMS power (W) and V is measured peak-to-peak voltage (mV_{pp}).

The RF output power P_T (W) is given by $P_T = P_m \times 10^{0.1|dB|}$, where P_m is the measured RF power (W) at the scope and dB is the added attenuation. The RF

power response curve for each channel was obtained.

Timing parameters

The main push-pull RF broadcasting amplifier was initially designed for CW, not for pulsed operation. Therefore, investigations of delays between the gating circuit and RF output were carried out on the bench. The RF output was switched using 5 V gating pulses while holding a CW RF input. With the console testing, switching times were measured using a pulsed RF input, 5 V gating pulses and high-power broadband termination as a load. Additionally, the 12 V output of the gating controller circuit was monitored. Timing parameters shown in Figure 3.5 were measured using the setup shown in Figure 3.10.

Pulse stability and fidelity in long RF pulse trains

The purpose of this performance test was to monitor stability of the peak RF output voltage and possible variations in timing parameters over long pulse trains. A CW 9.27 MHz RF input was used, with 5 V gating pulses generated by a pre-programmed microprocessor (Arduino MEGA 2650, Ivrea, Italy). Duty cycle from 10 to 50%, 100 μs pulse length and a broadband load was used. The peak output voltage and timing parameters (RRT, RFT, PRE and PFE) were measured for the first and the last pulse in a 256 RF pulse train length (ETL) as needed for TRASE.

Blanking noise level

As mentioned, the RF noise output between RF pulses is critical for data acquisition since maximizing SNR for TRASE MRI, and any MRI technique, is required. Unfortunately, most commercial RF amplifier specifications do not describe how blanking noise was measured. To compare the blanking noise of the TRASE RF amplifier to commercial designs (Analogic AN8110 and Tomco BT00500), we performed noise power measurements at a center frequency of 9.27 MHz, bandwidth (BW) of 100 kHz and resolution bandwidth (RBW) of 83.0 Hz. First, the baseline noise introduced

by the oscilloscope was measured by terminating the RF port with 50 Ω. The noise power (dBm) was measured in a 100 kHz bandwidth centered at 9.27 MHz. Next, the amplifier RF output was connected directly to the RF port and the noise level of the blanked RF amplifier output was measured. The blanking noise level (BNL) was calculated as: dBm/ Hz (scope) = dBm - 10log10(RBW) - 10log10(BW) = dBm - 69.19 [103]. The noise output of the amplifiers was measured with each RF amplifier input terminated to 50 Ω and no applied gating signal.

Power linearity and harmonics strength

To measure amplifier linearity, output harmonics using the fast Fourier transform (FFT) mathematical function of the oscilloscope was used. As per Bowick [104], harmonic distortion can be expressed as:

$$V_{out} = \alpha V_{in} + \beta V_{in}^2 + ... \tag{3.2}$$

where α and β are coefficients [104]. To obtain the impact of each harmonic on the RF output, voltages of each harmonic from the FFT of the RF output were used. Each harmonic was recorded from the FFT of the RF output. The harmonic strength (dBc) is defined as dBc = 20 log(Vh/Vc), where Vh is the peak voltage of the harmonic (mV) and Vc is the peak voltage (mV) of the RF amplifier operating frequency. The strength of the first six harmonics was monitored for RF output power from 0 to 1 kW.

One-dimensional (1D) TRASE

For 1D TRASE, a TMX MR console [102], 0.22 T permanent magnet (MRI-Tech, Canada), TRASE RF amplifier, saddle and twisted solenoid RF coils were used [74]. The RF amplifier channel 1 was connected to the saddle coil via a transmit/receive switch. The twisted solenoid coil was connected directly to the amplifier channel 2. Two cylindrical phantoms (diameter × height = 3.4 cm × 5 cm and 3.8 cm × 7 cm) filled with 61.6 mM NaCl + 7.8 mM $CuSO_4$ were aligned with their long axis

along the phase gradient produced by the twisted solenoid RF coil. The RF input to each amplifier channel was adjusted for maximum spin-echo amplitude. The pulse sequence parameters used for TRASE acquisition were: 200 μs pulse length, 900 μs pulse separation, 11% duty cycle and 128 echo train length. Unfortunately, the console limited the achievable duty cycle to 11% RF pulse trains; however, higher duty cycle was achieved on-the-bench.

3.5 Results of performance testing

3.5.1 RF output power

Output linearity was measured according to the procedure described in Section 3.4.6. The results of the power response are shown in Figure 3.11. The first six pulses of a pulse train length of 128 operating at peak power (1 kW), 50% duty cycle and 100 μs pulse length are shown in Figure 3.12. The RF power response was stable for all duty cycles.

3.5.2 Timing parameters

The delay between the 5 V input (100 μs) pulses and 12 V output (Figure 3.8) during bench testing is shown in Fig. 3.13. A delay of 2.5 μs and 25 μs is visible between the 5 V and 12 V rising and falling edges, respectively. The gating controller's (Figure 3.7) turn-off time changes, depending on the 5 V pulse length but does not change when varying RF input power because it is an isolated drive for the 12 V bias network. The delay is sensitive to the 5 V pulsed input signal amplitude and may be minimized, to the above levels, by adjusting the variable resistor (R 100 k, Figure 3.8). The results of timing performance tests with the console, as per Section 3.4.6, are shown in Figure 3.14. The PRE and PFE between the 12 V pulsed and RF output was measured to be 2 μs and 1 μs, respectively. The console was programmed to introduce a 10 μs delay between the 5 V gating pulse and the RF input to minimize pulse overshoot and RRT of the RF output (Figure 3.15). The PFE (15 μs) between

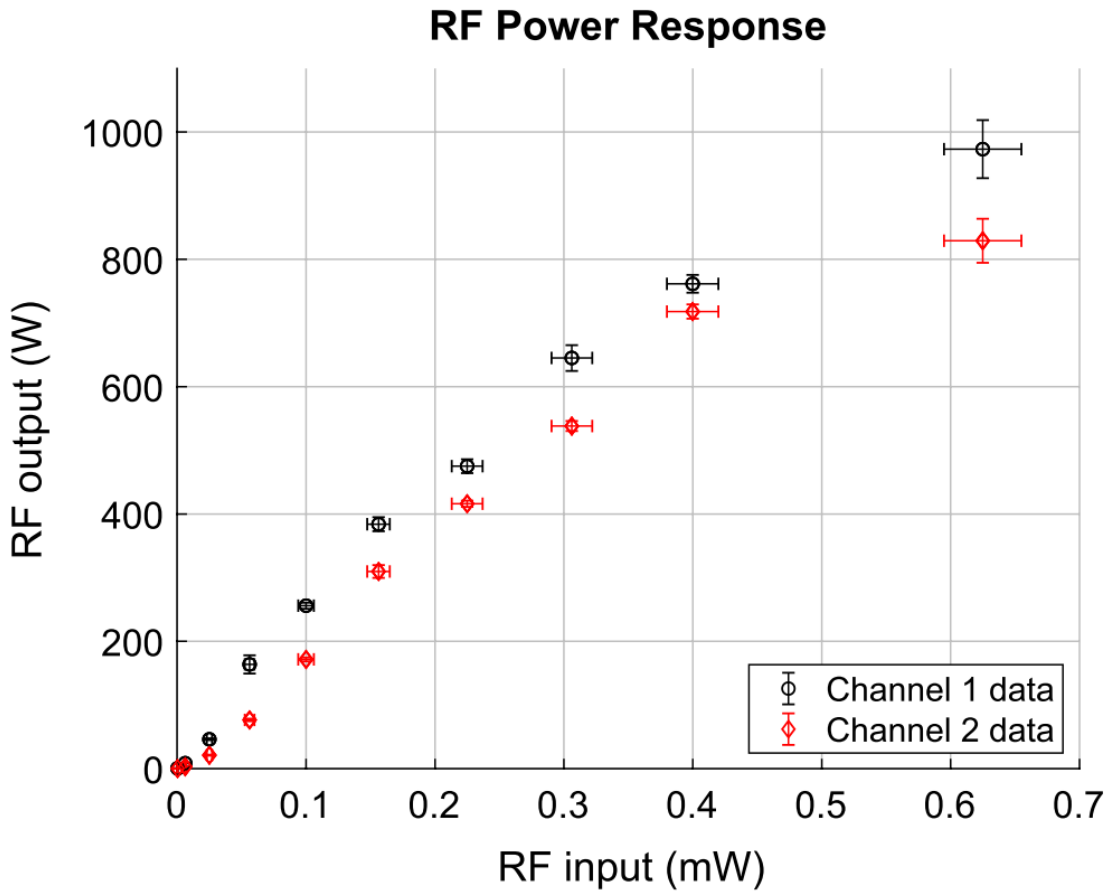

Figure 3.11: Performance testing of the TRASE RF power amplifier output. The total RF power output for channel one (black) and channel two (red) as a function of RF input power. Deviations up to 2 dB between each channel are due to minor differences in the construction of the transformer (T2, Figure 3.7).

the 12 V falling edge and the RF output can be minimized to 2 μs by switching off the 5 V gating pulse at an earlier time.

3.5.3 Pulse stability and fidelity in long RF pulse trains

Measurements of RF output power and timing parameters were made as per Section 3.4.6. Negligible differences ($< 1\%$) were measured in pulse timing parameters, pulse length and peak RF output voltage between the first and last pulse of the train.

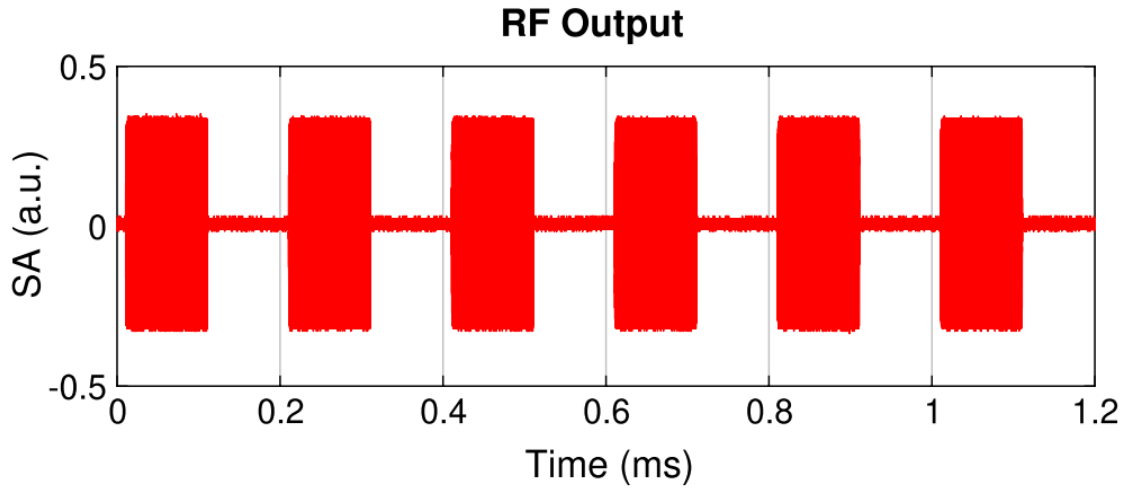

Figure 3.12: First 6 pulses in an RF pulse train of 128 with 50% duty cycle, 100 μs pulse length and 1 kW peak RF output (60 dBm) in channel one of the TRASE amplifier. Channel 2 behaves identically (not shown). Signal amplitude (SA) is in arbitrary units.

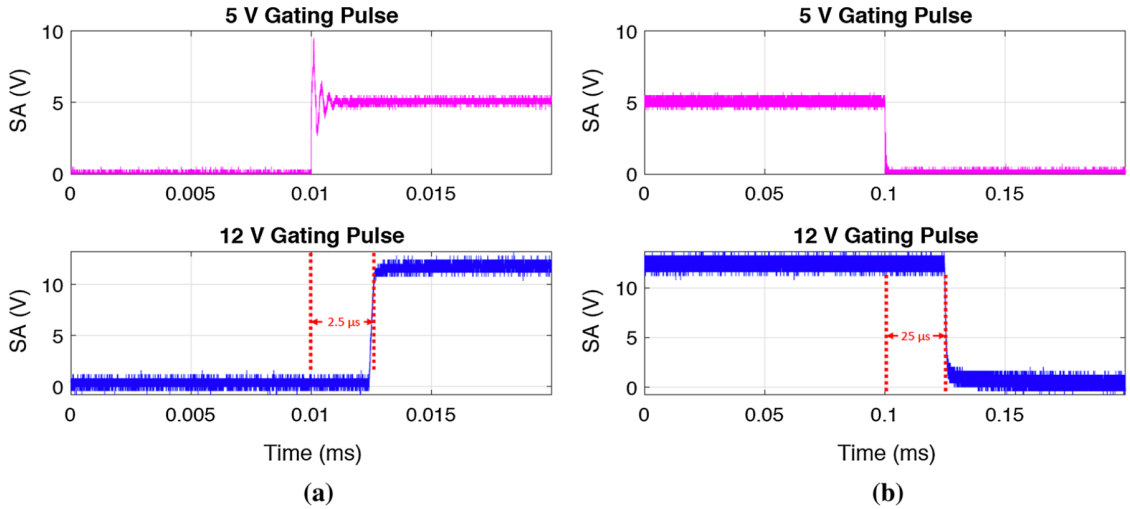

Figure 3.13: Simultaneous monitoring of the 5 V input gating pulses (from console) and the 12 V output of the bias controller circuit (Figure 3.8). A 5 V input pulse (pink) is shown. (a) A delay of 2.5 μs was measured between 50% signal amplitude of the 5 V pulse rising edge and 50% signal amplitude of the 12 V pulse rising edge. The rising edge delay did not change when the pulse length, RF input or duty cycle was varied. (b) A delay of 25 μs was measured between 50% signal amplitude of the 5 V pulse falling edge and 50% signal amplitude of the 12 V pulse falling edge. The falling edge changes depending on the 5 V pulse length. These delays are an effect of the optocoupler sensitivity and may be compensated for during pulsed operation. Signal amplitude (SA) is expressed in absolute voltage values.

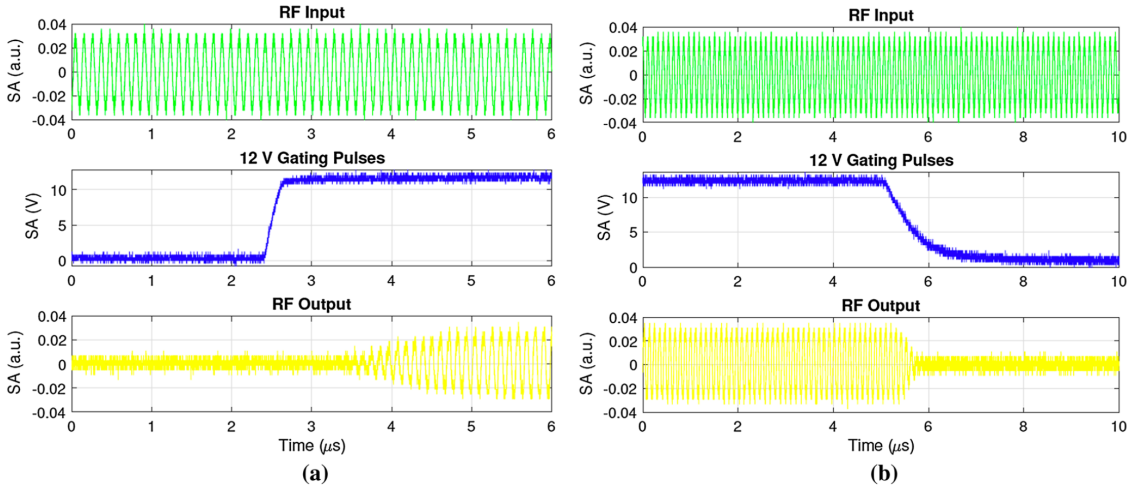

Figure 3.14: The operation of the TRASE amplifier with CW RF input (green) is shown. (a) RF input and RF output at the pulse rising edge. (b) RF input and RF output at the pulse falling edge. The PRE (12 V) is 2 μs, PFE (12 V) is 1 μs, RRT is 2 μs and RFT is 1 μs. Signal amplitude (SA) is absolute voltage values for gating pulses and arbitrary units for RF pulses

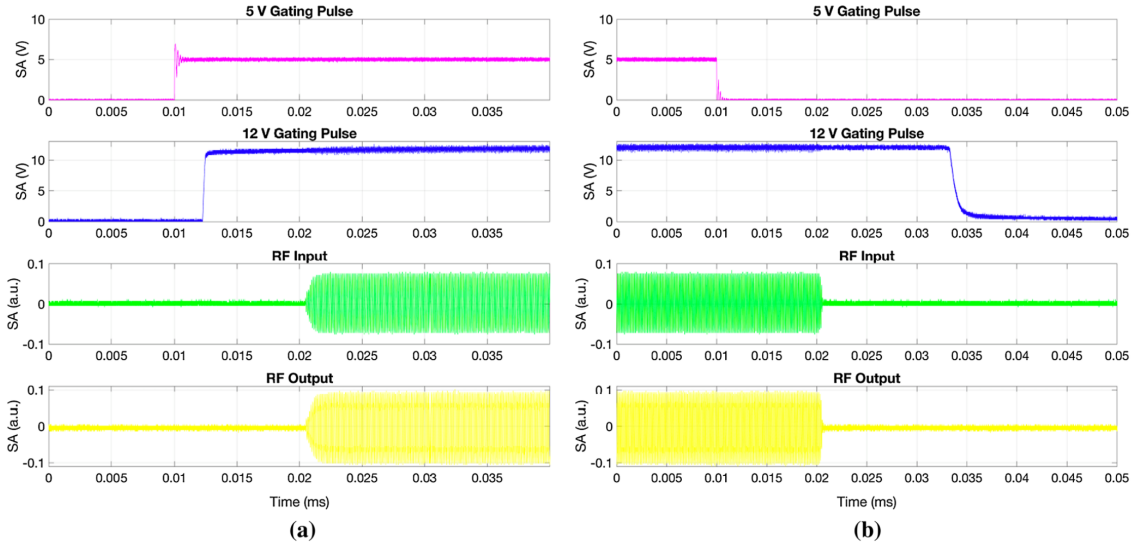

Figure 3.15: The operation of the TRASE amplifier is shown with pulsed RF input (green), 5 V gating pulse (pink), 12 V pulses (blue), and RF output (yellow) to observe the effect of the gating circuit delay during pulsed operation. The pulse rising edge (a) and falling edge (b) of a single pulse is presented.

3.5.4 Blanking noise level

The blanking noise level (BNL) of the TRASE RF amplifier was similar to the commercial RF amplifiers (AN8110 and Tomco BT00500). The BNL for all amplifiers

was measured at - 172.2 ± 1.1 dBm/Hz.

3.5.5 Power linearity and harmonics strength

The third harmonic was the largest one but remained less than or equal to -10 dBc for a range of RF output power (0-1 kW). The other harmonics consistently remained negligible (less than - 30 dBc).

3.5.6 One-dimensional (1D) TRASE

The results of the 1D TRASE experiment with the constructed RF amplifier are shown in Figure 3.16. Figure 3.16b shows the profile through a phantom obtained by the Fourier Transform of the acquired echoes shown in Figure 3.16a. The phantoms used are shown in Figure 3.16c.

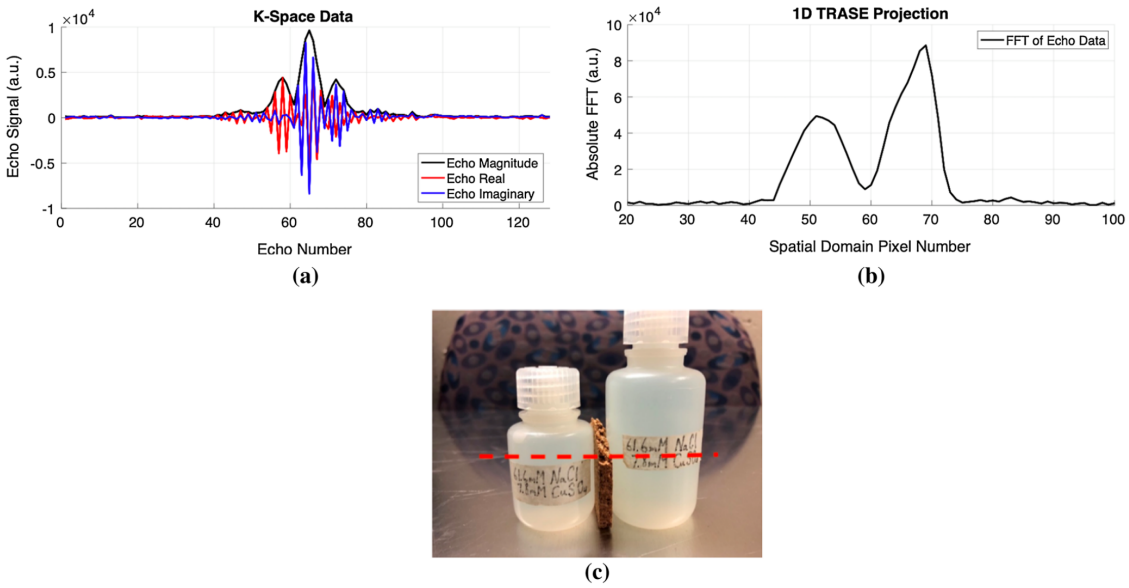

Figure 3.16: One-dimensional (1D) TRASE using the TRASE RF amplifier. A Fourier transform of the acquired k-space data (a) is shown in (b). The phantoms (diameter × height = 3.4 cm × 5 cm and 3.8 cm × 7 cm) filled with 61.6 mM NaCl + 7.8 mM CuSO4 and separated by a 5 mm cork spacer were used. The parameters used for TRASE are no slice selection, echo spacing = 900 μs, pulse length = 200 μs and 11% duty cycle per channel. The duty cycle was limited by the MRI console during TRASE acquisition.

3.6 Discussion

The designed TRASE RF power amplifier, adapted from amateur radio, for pulsed RF output at high duty cycle (minimum of 50%) and 1 kW RF power output dedicated for TRASE MRI was successfully constructed and tested. Blanking noise levels of the amplifier were compared with commercial MRI RF amplifiers, showing results close to 50 Ω thermal noise for all amplifiers.

Minor differences in RF power output between the channels of the TRASE RF amplifier (approximately + 2 dB in channel 1 compared to channel 2) are due to minor differences in construction. For example, wire-to-wire proximity may introduce capacitance in the transformer (T2 in Figure 3.7), shifting the cutoff and attenuating the operating frequency and harmonics of the RF output. Future designs will comprise identical RF choke components. However, slight differences in gain for each channel can be compensated when used for TRASE MRI as the amplitudes are independently controlled because power demand is not equal for each channel (RF coils require different power levels due to different quality factors and loading) [74].

The large third harmonic (− 10 dBc) remains a limitation of the current RF amplifier at 9.28 MHz and should be addressed in future designs. As per the measurements, up to 100 W at 27.81 MHz (third harmonic) may be reflected back to the amplifier when operating at 1 kW with a narrowband tuned load. However, no damage is expected to the LDMOS transistors, since they are extremely rugged (can withstand mismatch of VSWR $>$ 65) [98]. Reflected RF power may cause damage to output circuitry. The transformer (T2 in Figure 3.7) also acts as passive power protection to the high frequency-reflected power. Nevertheless, the significant third harmonic has to be considered, particularly in clinical applications to meet the International Electrotechnical Commission (IEC) regulations [105]. Harmonics strength were not directly measured at an operating frequency of 2.8 MHz; however, the RF output waveform showed negligible distortion compared to 9 MHz up to 800 W per channel.

Performance tests verified pulse stability and fidelity under various conditions. At both 3 MHz and 9.28 MHz operating frequency, no measurable differences were noticed in timing performance when varying the duty cycle (between 10 and 50%), RF output power (between 0 and 1 kW), pulse lengths (between 100 and 500 μs) and pulse train lengths up to 256. The bias controller circuit (Figure 3.8) introduces a delay between 5 V pulsed DC input and 12 V pulsed output. The 5 to 12 V switching off delay (PFE) remains a concern of the TRASE amplifier but is compensated by decreasing the 5 V gating pulse length that a console can easily accommodate. Although a 50% duty cycle is desirable for TRASE, the constructed amplifier can operate at CW (100%) duty cycle per channel. However, the remaining timing delays limit the duty cycle to about 90%.

One-dimensional TRASE was obtained to show that the amplifier is suitable for TRASE MRI. A twisted solenoid and saddle RF coil array were used, with an expected pixel separation of 2.50 mm [74]. In our experiment, we evaluated the distance between the middle of the two phantoms L = (34 mm + 38 mm)/2 + 5 mm = 41 mm, which in theory corresponds to N = 41/25 = 16.4 pixels. The number of pixels agrees with our measured 1D profile (see Figure 3.16b), where the middle of two cylindrical phantoms appeared at pixel # 52 and # 68, respectively, hence N' = 68 - 52 = 16. Therefore, the measured profile verifies the expected k-space trajectory, indicating the correct operation of the proposed RF amplifier. However, the profile shape is impacted by the various magnetic field and phantom factors, such as nonlinear phase gradient along the encoding direction, B_1 inhomogeneities along the length of the phantom and additional signal originating from the necks of the bottles.

3.7 Conclusions

In this work, a two-stage, class-AB, push-pull RF amplifier dedicated for TRASE MRI was proposed. The RF amplifier, adapted from amateur radio communication, was constructed and tested on the bench and with a 0.22 T MRI system. Such

a design satisfied all requirements of TRASE (Table 3.1) except for the prominent third harmonic strength. A specification summary for the TRASE amplifier based on measurements with the MRI console is provided in Table 3.3. Improvements to the RF coils and the TRASE technique are currently in progress to fully integrate the RF amplifier with the MR system.

The TRASE RF power amplifier proved to be superior to commercial RF power amplifiers needed for the TRASE technique. The amplifier is capable of up to 1 kW RF output, 100 μs RF pulses, 50% RF duty cycle pulse trains with high pulse stability and fidelity, required by TRASE. The amplifier rectifies major limitations of duty cycle and timing present in commercial RF power amplifiers making possible future sub-millimeter in vivo spatial resolution TRASE MRI. Future two-dimensional, high-resolution TRASE MRI systems are envisioned to provide a four channel operation and a single power supply unit.

The TRASE RF amplifier is also versatile. Although the amplifier was tested with a single frequency (9.27 MHz), the main amplification stage was initially constructed for wideband radio operation between 1.4 and 54 MHz [97]. Therefore, the amplifier can be adapted for TRASE in MR fields between 33 mT and 1.27 T. The constructed amplifier is now being used for TRASE on a 67 mT Halbach magnet (see Chapter 4).

If future designs of the amplifier should require a higher RF output power ($>$ 1 kW), a reduction of harmonics ($<$ 10 dBc) or a reduction in dimensions and weight, some solutions already exist or need further development. For TRASE MRI requiring power greater than 1 kW, high-power combiner circuits are currently available for the W6PQL amplifier deck and may be integrated into the TRASE amplifier [97]. In addition, the future RF amplifier could contain a dedicated diplexer, a device that splits incoming signals depending on frequency, that would filter the RF output and dump harmonic energy to a built-in load. Additionally, the size and weight may be reduced by removing or reducing the size of the large heat sinks, allowing space MRI systems that limit the peak RF power and duty cycle [106–108].

Table 3.3: Tested parameters of the constructed TRASE RF power amplifier obtained with the MRI console. [a]Capable of 100% duty cycle operation at 500 W per channel using the specified 1500 W power supply unit. [b]PRE and PFE can be reduced to 2 μs by reducing 5 V gating pulse length. [c]Parameter limited by console minimum RF pulse length.

Parameter	TRASE amplifier specification
Peak RF power output	1 kW
Number of channels	2
RF duty cycle	0-50%[a]
Blanked noise level (BNL)	-171 $\pm$ 1.1 dBm/Hz
RF rise transition time (RRT)	$\leq$ 2 μs
RF fall transition time (RFT)	$\leq$ 1 μs
Pulse-to-rising edge (PRE)	7.5[b] μs
Pulse-to-falling edge (PFE)	15[b] μs
Pulse duration	>60[c] μs
Third harmonic strength at 1 kW	- 10 dBc
1,2,4-6 harmonic strength at 1 kW	< - 30 dBc
Class	AB
Total gain	$\sim$ +60 dB

Chapter 4

A Portable Halbach Magnet for TRASE MRI[1]

4.1 Introduction

Costs, weight and size of standard clinical MRI systems are primarily associated with the magnet (see Chapter 1) [17, 109]. Therefore, there is a trend to reduce the costs and improve the portability of an MRI system by producing permanent MRI magnets generating low fields (10 – 100 mT). While standard permanent MRI magnets produce ∼200 mT, lower field permanent magnets often do not require a large and heavy steel yoke due to weaker forces and reduced extent of the stray field (e.g. biplanar C-shaped magnet (∼68 mT) by Hyperfine Inc., USA [27]). Another type of permanent magnet (the Halbach magnet) was invented by Klaus Halbach, in 1980, as an inexpensive magnet alternative for particle accelerators [110]. The Halbach magnet consists of ferromagnetic blocks oriented around a cylinder to produce a vertical magnetic field (Figure 4.1). The geometry enables an efficient use of the permanent magnets, since the magnetic field from each block is directed inward to a hollow cylinder and angled correctly to superimpose, maximizing the inner field strength. In addition, Halbach magnets produce a near zero-field outside the magnet, except at the open ends, usually not requiring a yoke. The Halbach design is a lighter and cheaper low field MRI

[1] A section of this chapter was published in A. R. Purchase et. al. IEEE Access, vol. 9, pp. 95294-95303.

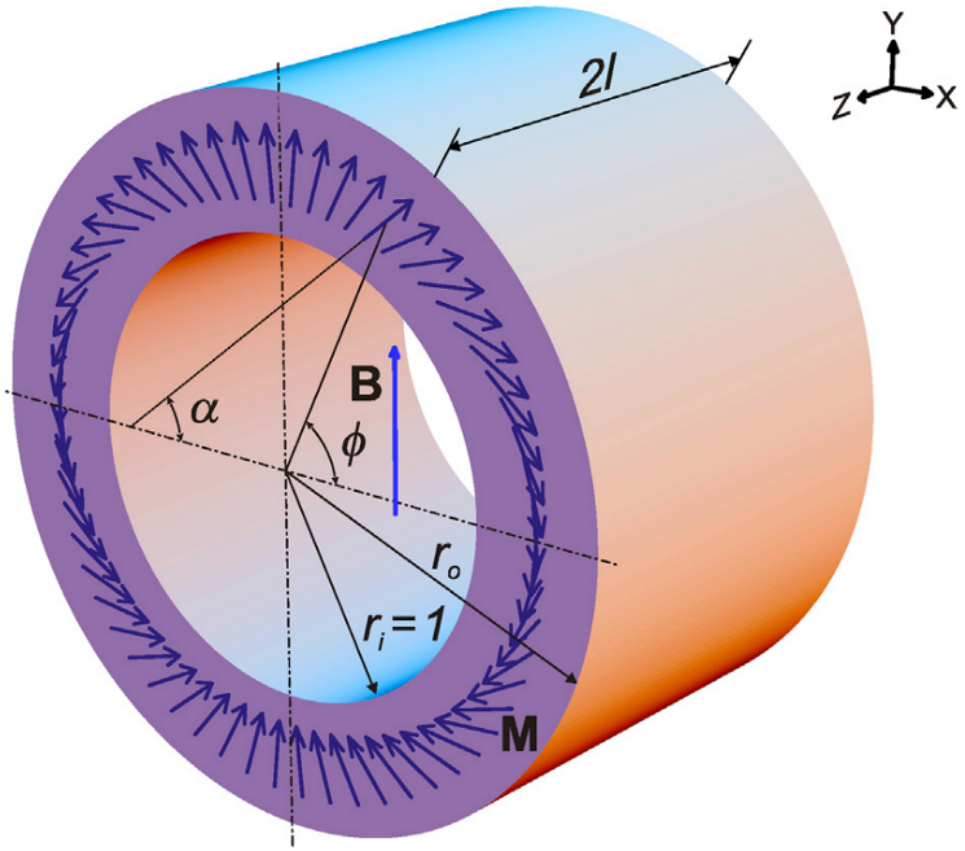

Figure 4.1: The Halbach magnet. The Halbach geometry produces a vertical internal field by rotating the magnetized blocks twice around the circumference. Figure was obtained from Turek and Liszkowski (2014) [111] with permission from Elsevier under license number 5324560502784.

magnet alternative (< 0.1 T) compared to other permanent magnet designs [36, 38].

Halbach magnets were not used in MRI for many years because they produce highly inhomogeneous magnetic fields, which is unsuitable for standard MRI techniques. However, recent advancements in MRI hardware and imaging techniques enabling MRI in a less homogeneous field than standard MRI, showed that further reduction of associated costs, weight, size and complexity of the MRI system is indeed possible using a Halbach magnet [36–38, 112, 113]. For example, O'Reilly et al. (2021) constructed a portable (∼105 kg), low-field (∼50 mT) MRI system, with a material price below $20k, based on a new Halbach magnet optimization technique as well

as hardware and software improvements intended for imaging of hydrocephalus in children [37, 38]. 3D MR images of the knee and brain were obtained at 2 mm isotropic resolution in less than 12 minutes using this system [38]. Cooley et al. (2015) constructed a portable (∼122 kg), low-field (∼80 mT) adult brain MRI scanner based on the novel rotational spatial encoding method (rSEM) [112, 113]. The group used the frequency swept 3D rapid acquisition and relaxation enhancement (RARE) pulse sequence in the inhomogeneous B_0 field to avoid a conventional MRI readout gradient and associated hardware [112]. Regardless of non-linearity present in the Halbach magnet's field, 3D MR in-vivo images of an adult brain were obtained in 16 minutes [36].

As seen above, the development of MRI technology have enabled new magnet designs. The Halbach magnet is also suitable for TRASE using the twisted-solenoid RF coils, since the magnet's homogeneity requirement is relaxed (∼1000 ppm) [41, 42, 74, 114]. Yet, further reduction in size and weight of the magnet is desired to address existing issues and to push the technology forward, allowing such applications as MRI in remote areas and on the battlefield, in air and ground ambulances, in emergency and operating rooms, and, possibly, on a space station. Therefore, we proposed a new Halbach magnet and construction method that minimizes large inhomogeneities produced by short lengths and imperfect material.

4.2 Basics of magnetism and permanent magnets

Magnetic fields are created by electric charges that are in motion. In a magnetic material, the electron orbits the nucleus (orbital angular momentum) and spins about its axis (spin angular momentum), producing a magnetic dipole moment (as seen similarly in the nucleus in Chapter 2). However, when an external magnetic field is applied to a material, there is a net alignment of magnetic dipole moments and the media becomes polarized (i.e. magnetized).

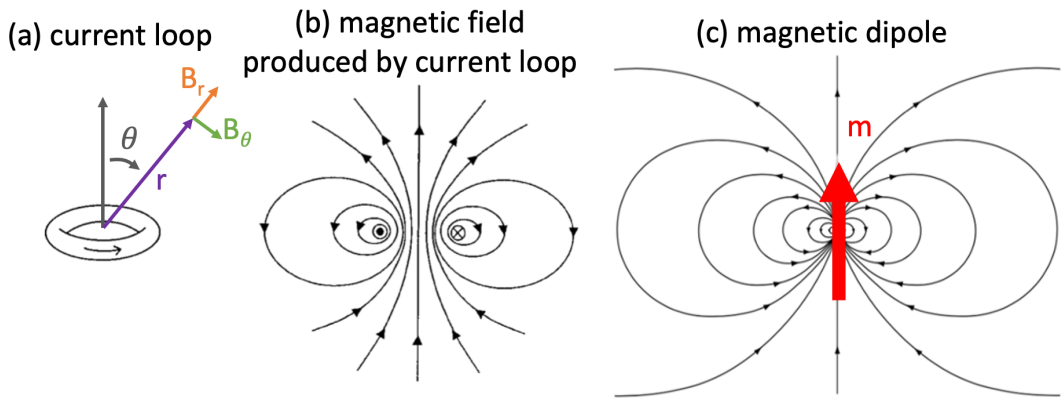

Figure 4.2: The magnetic field produced by a current loop (a) in the plane perpendicular to the plane of the current loop (b). (c) The magnetic dipole produces a field corresponding to an infinitesimally small current loop. All figures were modified from J.M.D. Coey (2010) [115] with permission.

4.2.1 Magnetic dipole moment

The magnetic field produced by a dipole is calculated by assuming a small loop of current (Figure 4.2a,b) (in spherical coordinates):

$$\mathrm{B_r} = 2\left(\frac{\mu_0 \mathrm{m}}{4\pi r^3}\right)\cos\theta; \quad \mathrm{B}_\theta = \left(\frac{\mu_0 \mathrm{m}}{4\pi r^3}\right)\sin\theta; \quad \mathrm{B}_\phi = 0 \tag{4.1}$$

where m is the magnetic dipole moment (m = I A, where A is the area enclosed by the current, I, in the loop) and $\mu_0 = 4\pi\times10^{-7}$ [H/m] is the permeability of free space. The resulting magnetic field of the magnetic dipole is shown in Figure 4.2c in a plane. Generally, most materials are not magnetized because the magnetic dipole moments are randomly oriented and cancel each other at room temperature, leading to a zero net magnetization.

4.2.2 Classification of materials

Many materials produce a magnetic field at room temperature when placed in an external magnetic field. Depending on their behaviour in the external field, they can be divided into diamagnetic, paramagnetic and ferromagnetic materials (Figure 4.3). Other classifications exist but are outside the scope of this thesis (see [115]).

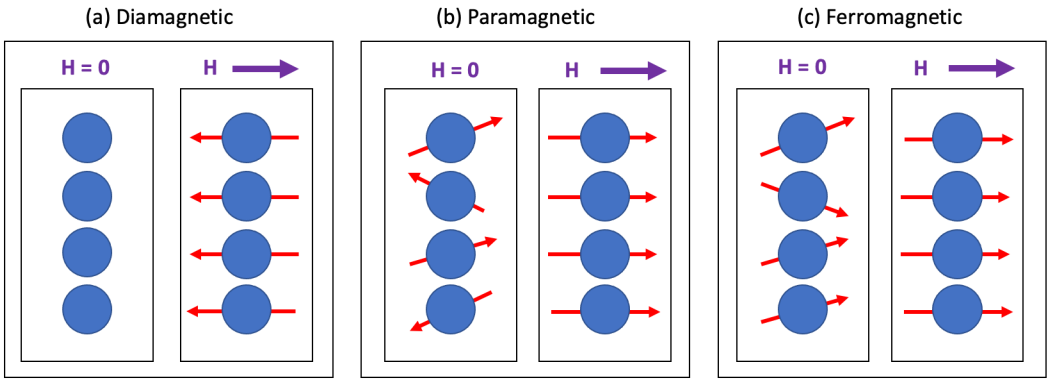

Figure 4.3: Classification of magnetic materials based on their magnetization in an external magnetic field (H) [116]: (a) diamagnetism, (b) paramagnetism, and (c) ferromagnetism.

Magnetic susceptibility

Magnetic susceptibility (χ_m) quantifies the strength of the internal field ($\vec{M}$) produced within a material when placed in an external magnetic field ($\vec{H}$):

$$\vec{M} = \chi_m \vec{H} \tag{4.2}$$

Table 4.1 shows select materials and their magnetic susceptibilities. For diamagnetic materials, $\chi_m < 0$ and $|\chi_m| << 1$; bismuth is one of the strongest diamagnetic materials. For paramagnetic materials, $\chi_m > 0$ and $|\chi_m| << 1$; gadolinium is one of the strongest paramagnetic materials, commonly used as contrast agents in MRI. For ferromagnetic materials, $\chi_m >> 1$.

Diamagnetism

Diamagnetic materials do not have a net magnetic moment at the atomic level because all electrons are paired (Figure 4.3a). However, when a diamagnetic material is placed in an external magnetic field, the electron orbital angular momentum changes to *oppose* the direction of the external field. The change in the orbital angular momentum is weak for diamagnetic materials, as shown by the very low (and negative) magnetic susceptibilities (Table 4.1).

Table 4.1: Magnetic susceptibilities of select magnetic materials [117].

Material	**Classification**	**Magnetic Susceptibility (χ_m)**
Bismuth	Diamagnetic	-1.7×10^{-4}
Copper	Diamagnetic	-9.7×10^{-6}
Water	Diamagnetic	-9.0×10^{-6}
Oxygen	Paramagnetic	$+1.7\times10^{-6}$
Aluminium	Paramagnetic	$+2.2\times10^{-5}$
Gadolinium	Paramagnetic	$+4.8\times10^{-1}$
Cobalt	Ferromagnetic	+250
Carbon steel	Ferromagnetic	+100
Permalloy	Ferromagnetic	+8000

Paramagnetism

Paramagnetic materials have a net magnetic moment at the atomic level due to unpaired electrons but are randomly oriented when not in an external magnetic field; therefore, producing a zero magnetization (Figure 4.3b). Because the coupling between the magnetic dipole moments is weak, when placed in an external magnetic field, the magnetic dipole moments experience a torque that aligns them to the direction of the external magnetic field. Magnetic susceptibilities of paramagnetic materials are low but are positive since they magnetize with the external magnetic field (Table 4.1). Paramagnetic materials lose their net magnetization when the external magnetic field is removed due to thermal agitation dominating the spin coupling, randomly orienting the magnetic moments. One application of paramagnetic materials is their use as contrast agents in MRI (see Appendix A).

Ferromagnetism

Ferromagnetic materials have a strong net magnetic moment due to strong coupling between magnetic dipoles (Figure 4.3c). Hence, spontaneous alignment of the dipoles occurs over macroscopic regions (domains). Therefore, the magnetization ($\vec{\mathrm{M}}$) of the ferromagnetic material can be viewed as a collection of individual domains:

$$\vec{\mathrm{M}} = \frac{\sum_i \vec{\mathrm{M}}_\mathrm{i} \mathrm{V}_\mathrm{i}}{\sum_i \mathrm{V}_\mathrm{i}} \tag{4.3}$$

where $\vec{\mathrm{M}}_\mathrm{i}$ is the magnetization of the "i-th" domain, V_i is the volume of the "i-th" domain, and $\sum_\mathrm{i} \mathrm{V}_\mathrm{i}$ is the total material volume. Ferromagnetic materials have exceptionally high magnetic susceptibilities compared to diamagnetic and paramagnetic materials; for example, the magnetic susceptibility of permalloy is more than five orders of magnitude stronger than gadolinium (see Table 4.1).

An important quantity in magnetism is also the magnetic flux density or magnetic field strength ($\vec{\mathrm{B}}$), that is a measure of the total magnetic field:

$$\vec{\mathrm{B}} = \mu_0 \vec{\mathrm{H}} + \mu_0 \vec{\mathrm{M}} \tag{4.4}$$

where $\vec{\mathrm{H}}$ is the external magnetic field [A/m], $\vec{\mathrm{M}}$ is the magnetization [A/m] defined by Equations 4.2 and 4.3 and μ_0 is the magnetic permeability of free space. Figure 4.4 illustrates the $\vec{\mathrm{B}}$, $\vec{\mathrm{H}}$ and $\vec{\mathrm{M}}$ fields present inside and outside a magnetized block. In Figure 4.4d, the magnetic flux density is calculated at an arbitrary point, P, inside the block using Equation 4.4. However, in the space outside the block, the magnetization is zero; therefore, $\vec{\mathrm{B}} = \mu_0 \vec{\mathrm{H}}$. Furthermore, all magnetized materials also exhibits an internal magnetic field that *opposes* the magnetization, called the "self-demagnetization" field ($\mathrm{H_d}$ in Figure 4.4a).

To analyze the behaviour of a ferromagnetic material, such as neodymium-iron-boron (NdFeB), let's consider an unmagnetized ferromagnetic block placed in an external auxiliary magnetic field, $\vec{\mathrm{H}}$ (that could be produced, for example, by a solenoid). Initially, the magnetization is zero ($\mathrm{M} = 0$) at the starting point on the blue curve

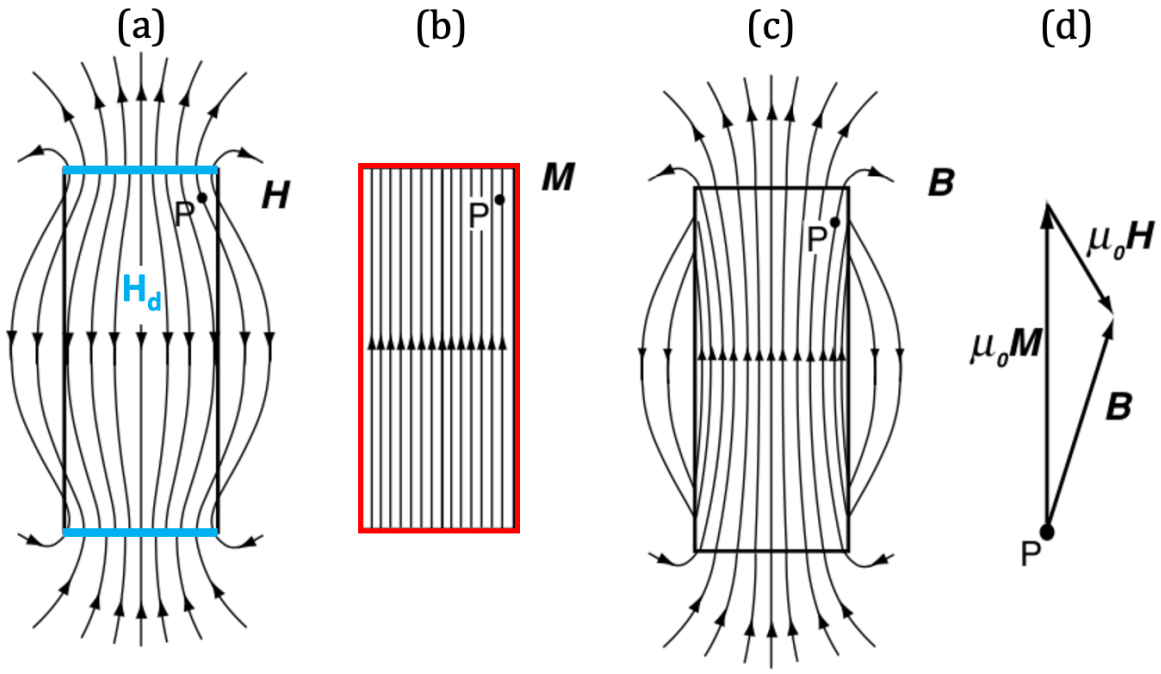

Figure 4.4: Visualization of the relationship between the auxiliary field ($\vec{H}$), magnetization ($\vec{M}$) and magnetic flux density ($\vec{B}$). The distribution of the (a) auxiliary field and (c) magnetic flux density produced by the magnetized block (b) where $\vec{B} = \mu_0\vec{H} + \mu_0\vec{M}$ (d). The auxiliary field originates from the north and south surfaces (blue) of the magnetized block (red). The magnetized block produces its own internal field (H_d) which opposes the magnetization ('self-demagnetization'). All figures were modified from J.M.D. Coey (2009) [115] with permission.

in Figure 4.5. As the external field increases, the domains in the material start to align with the external field, producing a magnetic field that is superimposed with the external field. The material's magnetization and magnetic flux density curves are shown as the red and purple curves in Figure 4.5, respectively. Eventually, all the domains align with the external magnetic field reaching the magnetization saturation and any further increase in the magnetic flux density ($\vec{B}$) is solely provided by the external magnetic field, as seen by a linear increase when $\vec{M}$ is saturated. Then, as the external magnetic field decreases, the magnetic flux density decreases but does not return to the same starting point when the external magnetic field is reduced to zero. At this point, the ferromagnetic block maintains its own magnetic flux density, namely the magnetic remenance that is proportional to the material's magnetization

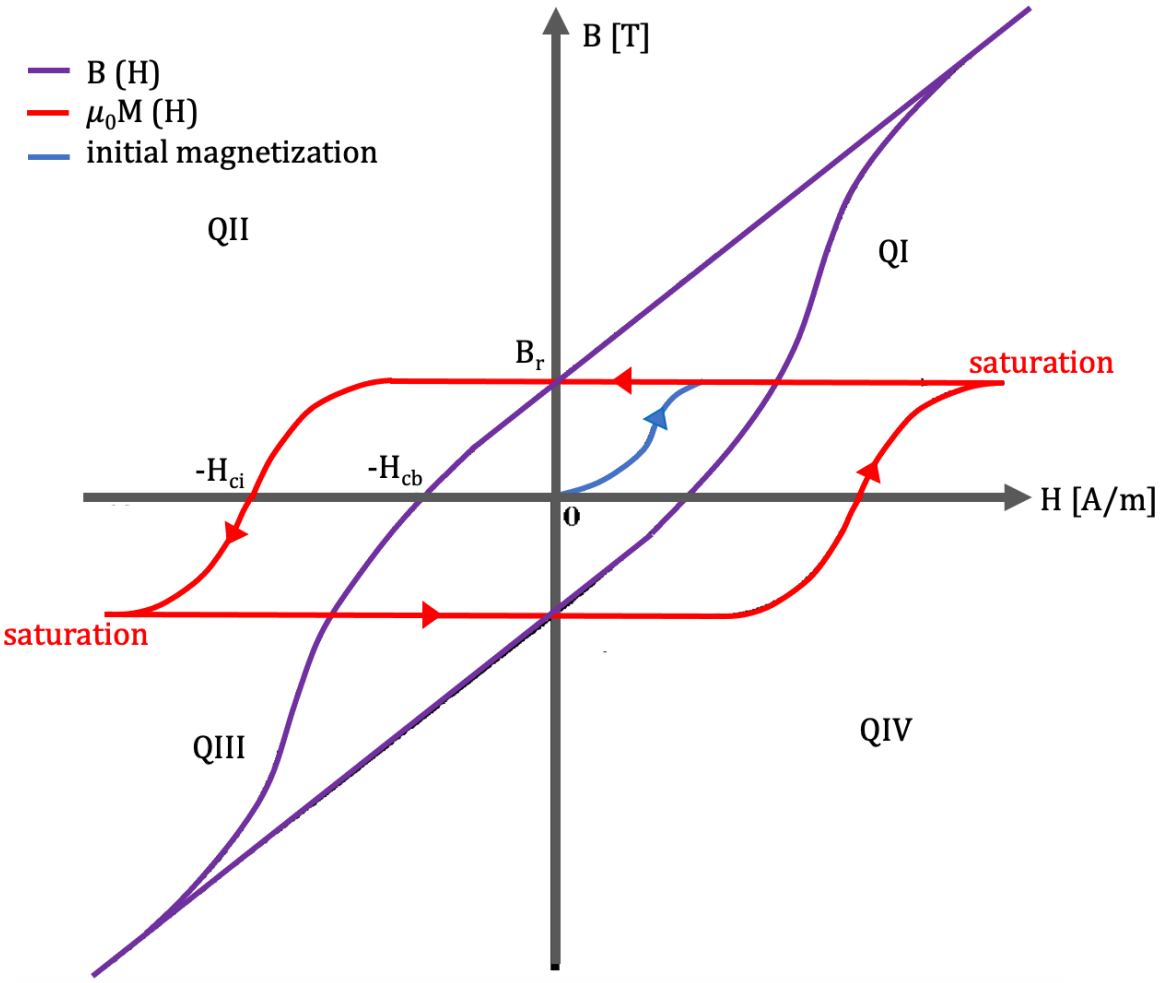

Figure 4.5: A ferromagnetic hysteresis loop. The blue curve shows the initial magnetization of the material. The magnetization (red) and magnetic flux density (purple) of a ferromagnetic material is shown as a function of the auxiliary field ($\vec{H}$). The magnetic flux density ($\vec{B}$) is a measure of the auxiliary field ($\vec{H}$) and the materials magnetization ($\vec{M}$). The hysteresis loop is sectioned into four quadrants (QI, QII, QIII, QIV). Figure was modified from Sung et al. (2003) [118] with permission from Elsevier under license number 5324570465338.

($B_r = \mu_0 M_r$).

Suppose the external field now increases in the opposite direction until the point where the magnetic flux density ($\vec{B}$) is reduced to zero (i.e. the coercive field H_{cb}). The point at which the magnetic flux density is zero (H_{cb} on Figure 4.5) does not always mean that $M = 0$. The intrinsic coercivity (H_{ci}) is defined at the point when the external field strength that deteriorates the magnetization which is different than

H_{cb} where the external auxiliary magnet field cancels the magnetic flux density. Only when $\vec{H} << \vec{M}$ (i.e. soft magnets) that the magnetic flux density (Equation 4.4) can be approximated as $\vec{B} \approx \mu_0 \vec{M}$ and therefore $H_{ci} \approx H_{cb}$ [118]. For most ferromagnets, the intrinsic magnetization is still maintained even though the external magnetic flux density is zero (B = 0 when H = -H_{cb}) and a much larger external magnetic field must be applied to remove the magnetization (i.e. hard magnets); therefore, $H_{ci} > H_{cb}$. In ferromagnetic materials, the lag between the magnetic flux density and the externally applied field is known as magnetic hysteresis (Figure 4.5).

4.3 Types of Halbach magnets

In this research, we focused on the design, construction and application of a Halbach magnet for TRASE MRI. The Halbach magnet design is fundamentally a distribution of magnetic dipoles around the circumference of a hollow cylinder (see blue regions in Figure 4.6). Halbach's original paper (1979) shows different possible configurations of magnetic pieces comprising the magnets such as radial, dipole and quadrupole geometries (see Figure 4.6). The number of magnetization rotations around the circumference, known as space cycles, defines the magnetization distribution and the magnetic field strength produced inside the Halbach magnet. For example, the radial Halbach magnet (Figure 4.6a) generates an axial magnetic field strength when the magnetization rotates by one space cycle, which has been used to produce a longitudinal B_0 field for portable NMR and MRI (i.e. the "Inward-Outward Auger pair") [119, 120]. A vertical uniform internal field (i.e. dipole in Figure 4.6b) is generated with two space cycles which was applied in portable MRI with efficient solenoid RF coils [37]. A vertical internal field gradient (i.e. quadrupole in Figure 4.6c) is generated with three space cycles and was used as a rotational spatial encoding field (rSEM) for mobile and low-cost MRI [112]. Since this Ph.D. work focused on application of the efficient twisted-solenoid TRASE RF coils (see Chapter 2), the aim was to produce the uniform and vertical field as generated by a dipole Halbach magnet (Figure 4.6b).

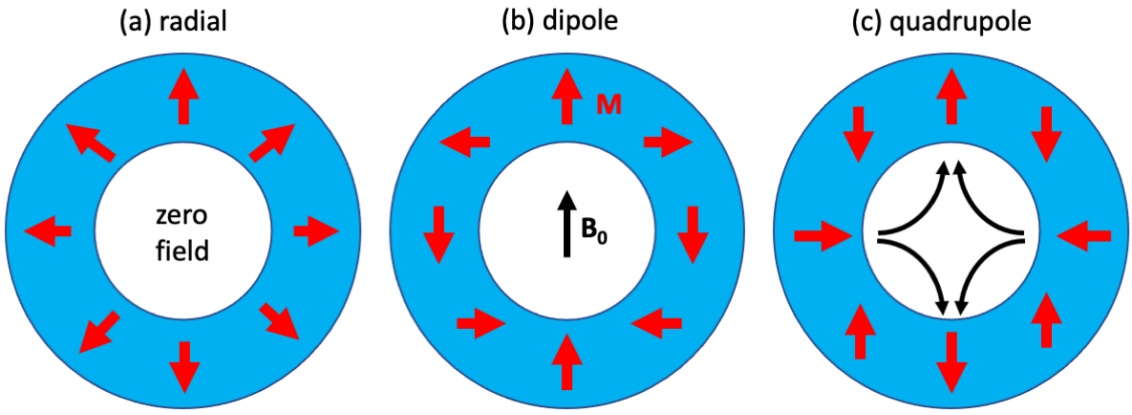

Figure 4.6: Multipolar Halbach magnet designs and their internal fields: (a) radial, (b) dipole, and (c) quadrupole. The magnetic fields are produced by rotating the magnetization around the circumference of a cylinder by (a) one, (b) two, and (c) three space cycles.

4.3.1 Magnetic field produced by an ideal dipole Halbach magnet

The ideal Halbach magnet is infinitely long and has a continuous distribution of magnetization (Figure 4.1). In the case of the ideal dipole Halbach magnet, the magnetic dipole formula (Equation 4.1) is integrated to generate the magnetic field strength ($\vec{\mathrm{B}}$) produced by an infinitely long rod with transverse magnetization (see Figure 4.7a). The magnetic field produced at any radial point from the rod is (in cylindrical coordinates):

$$B_\rho = \left(\frac{\mu_0 \lambda}{2\pi\rho^2}\right)\cos\phi; \quad B_\phi = \left(\frac{\mu_0 \lambda}{2\pi\rho^2}\right)\sin\phi; \quad B_z = 0 \tag{4.5}$$

where m = λdz and λ is the number of magnetic dipoles per unit length. Therefore, at any given radius (ρ) from the infinite rod's axis, the magnitude of the magnetic field is:

$$|\vec{\mathrm{B}}| = \frac{\mu_0 \lambda}{2\pi\rho^2} \tag{4.6}$$

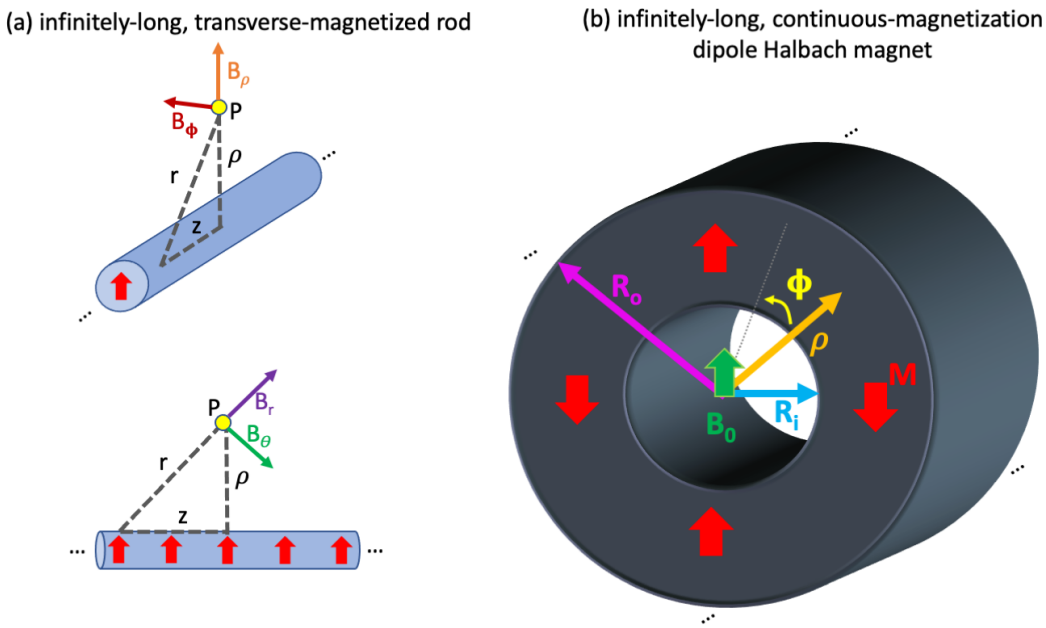

Figure 4.7: Parameters used to calculate the magnetic field strength at the point P produced by the ideal dipole Halbach magnet. (a) Magnetic field strength at a point, P, produced by an infinitely-long rod [121]. The magnetized rod can be viewed as an infinitely long line of magnetic dipoles. The spherical coordinates system is (r,θ, ϕ), cylindrical coordinates is (ρ,θ,z) and the dipole orientations are red arrows. (b) Integration of the field produced by the transverse-magnetized rod is used to calculate the magnetic flux density inside the dipole Halbach magnet. General Halbach magnet parameters are the inner radius (R_i), outer radius (R_o), the magnetized volumes (black) and orientations (red), and the magnetic field (B_0) is perpendicular to the longitudinal axis.

Since the magnetization of the material is defined as the number of magnetic dipoles per unit volume (as seen in Equation 4.3); m = M dV; λ = M da, where da = ρ dρ dϕ is the infinitesimal cross-sectional area of magnetization (see black region in Figure 4.7b). After integration over the magnetization volume ($\phi : 0 \rightarrow 2\pi$; ρ: $R_i \rightarrow R_o$), the magnetic field strength anywhere inside the bore of a dipole Halbach magnet is:

$$\boxed{B = \mu_0 M \ln\left(\frac{R_o}{R_i}\right)} \tag{4.7}$$

where R_i and R_o in the inner and outer radii, respectively (see Figure 4.7b) [115, 122].

Equation 4.7 is plotted in Figure 4.8 for different ferromagnetic materials (i.e.

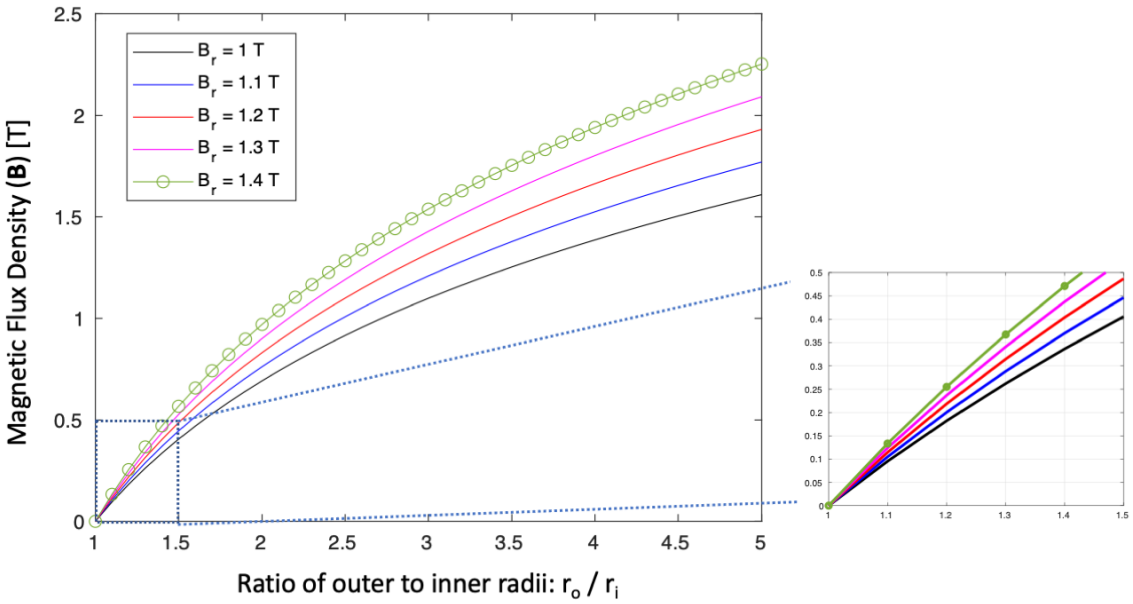

Figure 4.8: The magnetic field strength ($\vec{B}$) produced inside a dipole Halbach magnet with different sizes (ratio of outer to inner magnet radii) and material remanence (B_r). The field strength calculations used Equation 4.7 and B_r of 1T, 1.1T, 1.2T, 1.3T and 1.4T which are comparable to measured values of ferromagnets. The calculation assumed the magnet is infinitely long and has a continuous distribution of magnetization.

different B_r), indicating potential issues in producing a Halbach magnet with higher field strengths (B > 0.5 T) for portable and low-cost MRI systems. The strongest remanent field produced by a ferromagnetic material to date is $B_r \sim 1.4$ T, which limits the maximum field strength (B < 0.5 T) achieved by a reasonably sized Halbach magnet for MR imaging (inner bore diameter < 50 cm). For example, assuming a magnetic remanence (B_r) of 1.4 T, an inner bore diameter of 40 cm (for head MRI ~ 20 cm imaging region) and a magnet length that is twice the diameter (maximizing homogeneity and patient accessibility), a magnetic flux of 60 mT in a Halbach magnet requires an outer diameter (OD) of ~42 cm; a 0.2 T requires an OD of 46.2 cm; a 0.5 T requires an OD of 57.2 cm; and 1.5 T requires an OD of ~116.8 cm. The magnet pieces alone weighs and costs greater than 1000 kg and $100k USD, respectively, for a field strength above 0.5 T for a Halbach magnet based head MRI system. For some MRI applications, such as the neonatal MRI, the smaller required imaging region

allows higher field Halbach magnet's with reasonable size and costs. Furthermore, considering a whole-body adult-sized Halbach magnet (ID $\sim$ 100 cm) for MRI, a magnetic flux of 60 mT requires an OD of 104 cm; a 0.2 T requires an OD of 120 cm; a 0.5 T requires an OD of 148 cm; and a 1.5 T requires an OD of 280 cm. In the whole-body case, the 60 mT whole-body Halbach magnet would weigh and cost similar to the head-sized Halbach magnet at 0.5 T. Field strength and magnet compactness must be considered in the MRI system design, otherwise the Halbach magnet is not viable for whole-body imaging.

As seen by this simple calculation, any further increase in the inner bore size or magnetic field strength (above 0.5 T) would lead to a Halbach magnet (for head imaging) with costs and size similar to standard MRI magnets due to the exponential relationship between outer radius and magnetic field strength (Equation 4.7). The only reasonable cost-effective approach is to reduce the inner bore radius to maintain a high magnetic flux density. Unfortunately, this would limit clinical MRI applications since a small sized bore can only accommodate smaller anatomy, in addition, to the RF coils and gradient coils. A Halbach magnet with a reduced magnetic field strength allows construction with no heavy and large steel yoke, a low total volume of permanent magnets (low cost) and a compact size (large imaging region per small outer diameter) [36–38, 112].

4.3.2 Magnetic field produced by a truncated and segmented Halbach magnet

Since any constructed Halbach magnet must have a finite length and segmented magnetization, its MRI applications are limited due to large magnetic field inhomogeneities. Ni Mhiochain et al. (1999) showed the magnetic flux density at the geometric isocenter of a Halbach magnet due to truncation and segmentation is [123]:

$$B_c = \frac{\sin(\frac{2\pi}{k})}{\frac{2\pi}{k}} B_r \Big[\ln R_0 - \ln \Big(\frac{l + \sqrt{l^2 + R_0^2}}{l + \sqrt{l^2 + 1}} \Big) - \frac{l}{\sqrt{l^2 + R_0^2}} + \frac{1}{\sqrt{l^2 + 1}} \Big] \tag{4.8}$$

where k is the number of segments (i.e. magnetic blocks), l is the aspect ratio (length of the Halbach magnet to the inner diameter), and the outer magnet radius (R_o) is normalized to the inner magnet radius (R_i). Note that as $l \to \infty$ and $k \to \infty$, Equation 4.8 simplifies to Equation 4.7 (i.e. the ideal Halbach magnet). Expanding on Ni Mhiochain et al.'s work, Turek and Liszkowski (2014) provided equations that allow calculations of the magnetic flux density at any point within the entire Halbach magnet's bore [111]. An example is shown in Figure 4.9. Note that the field non-uniformity shown in Figure 4.9c is caused by the magnet's length truncation (Figure 4.9a) and segmented magnetization (Figure 4.9b). The magnetic field homogeneity η [ppm] is:

$$\eta = \frac{\Delta B}{B_c} \times 10^6 \tag{4.9}$$

where ΔB is the difference between maximum and minimum magnetic field strength in the diameter spherical volume (DSV), which should be equal to or larger than the region of interest (ROI) for MR imaging. B_c is the magnetic flux density at the geometric isocenter of the Halbach magnet. The homogeneity within the central plane shown in Figure 4.9c is greater than 200,000 ppm due to strong perturbations at the edges of the ROI [111].

For a standard dipolar Halbach magnet, analytical solutions to the magnetic field equations provide some design insights. Analytical solutions showed that a 4:1 aspect ratio provides a reasonable homogeneity over half the inner diameter (∼1000 ppm before shimming). Yet, such a long magnet is heavy and claustrophobic, hence its limited clinical applications [111]. A shorter magnet (aspect ratio ∼2:1) generates an inhomogeneity of ∼10,000 ppm over half the inner diameter, requiring complex design approaches and sophisticated shimming techniques allowing MRI [37, 38, 111, 124]. In Halbach magnets with aspect ratio <1.5:1, the produced inhomogeneity is too large (>100,000 ppm) for standard MR imaging techniques [111, 123]. For these reasons, the Halbach magnet has not been fully adapted for MRI using traditional imaging techniques. However, several research groups have proposed new approaches

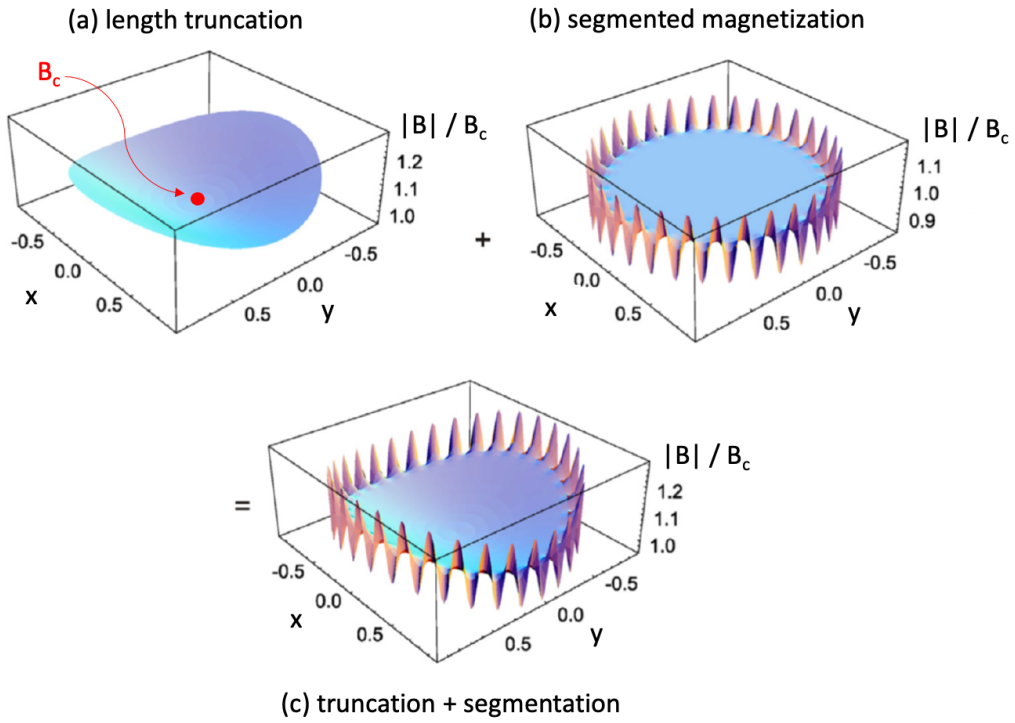

Figure 4.9: Visualization of the analytical solution of the magnetic field equations for the dipolar Halbach magnet with the length truncation and segmentation [111]. (a) The field perturbation due to length truncation. B_c is the magnetic flux density at the geometric isocenter of the Halbach magnet for k = 32, $R_o = 1.1$, and $l = 1$. (b) The field perturbation due to segmentation of the magnetization only. (c) The total field perturbation (truncation + segmentation) within the plane is the superposition of (a) and (b). Vertical axes on each plot show the magnitude of the magnetic flux density |B| on the plane, normalized to the field at the geometric isocenter (B_c). Figure was obtained from Turek and Liszkowski (2014) [111] with permission from Elsevier under license number 5324560502784.

to improve the homogeneity of a short and segmented Halbach magnet, by optimizing blocks size and shape [120, 125, 126], diameters of rings [37, 38], elliptical arrangement of blocks [127], spacing between rings [128], magnetization directions of blocks [127, 129], or material remanence and coercivity [36, 112, 113, 130].

4.3.3 Numerical field solution of the Halbach magnet

Analytical solutions would be suitable for fast calculation of the magnetic field to design and optimize a Halbach magnet for MRI. While analytical solutions do exist (shown above) they are prone to errors because they assume incorrectly that

neighbouring ferromagnetic blocks of the magnet do not interact. Furthermore, they also neglect essential material characteristics such as demagnetization/magnetization effects (e.g. H_{cb} and H_{ci}), leading to the constructed magnet's homogeneity that significantly deviate from the calculations. Since the numerical solutions using the finite element method (FEM) have shown significantly higher accuracy (∼1 ppm) in simulations than analytical methods, FEM was used in this work to design and optimize the Halbach magnet. The main advantage of FEM over analytical methods of simulating the magnetic flux density of Halbach magnets is that B(H) curves (see purple curve in Figure 4.5) can be included in the magnetic field simulations. Magnetostatics simulations of magnetic fields using FEM software, such as Opera3D (Dassault Systeme, France), accept the accurate B(H) curve (Figure 4.11) for a specific material and solves the Gauss' magnetostatics law ($\vec{\nabla} \cdot \vec{B} = 0$) directly. Since $\vec{B} = \mu\vec{H}$ and the divergence of a gradient is always zero, the auxiliary field strength can be expanded in terms of a magnetic scalar potential ($\vec{H} = -\nabla\phi$), hence FEM can solve directly:

$$\vec{\nabla} \cdot \mu\vec{\nabla}\phi = 0 \tag{4.10}$$

for any given geometry of magnetic blocks.

For the FEM calculations, the B(H) curves for the blocks, N52 and N40UH, were measured by the manufacturer (Courtesy of Binic Magnet Co. Ltd., China). Figure 4.10 shows the B(H) curves for these two types of ferromagnetic material: (a) N52 (N = NdFeB; maximum energy product (maximum energy stored in the magnet) = 52 MGOe; coercivity ≥ 796 kA/m; remanence = 1.4 T) or (b) N40UH (N = NdFeB; maximum energy product = 40 MGOe; coercivity ≥ 899 kA/m; remanence = 1.2 T).

A comparison of magnetostatic field solutions

Analytical and numerical methods may show significant differences in the results of calculations of the magnetic field strength produced by Halbach magnets [36, 38, 112, 113, 119, 131]. Taking this into account, we used both methods to calculate the

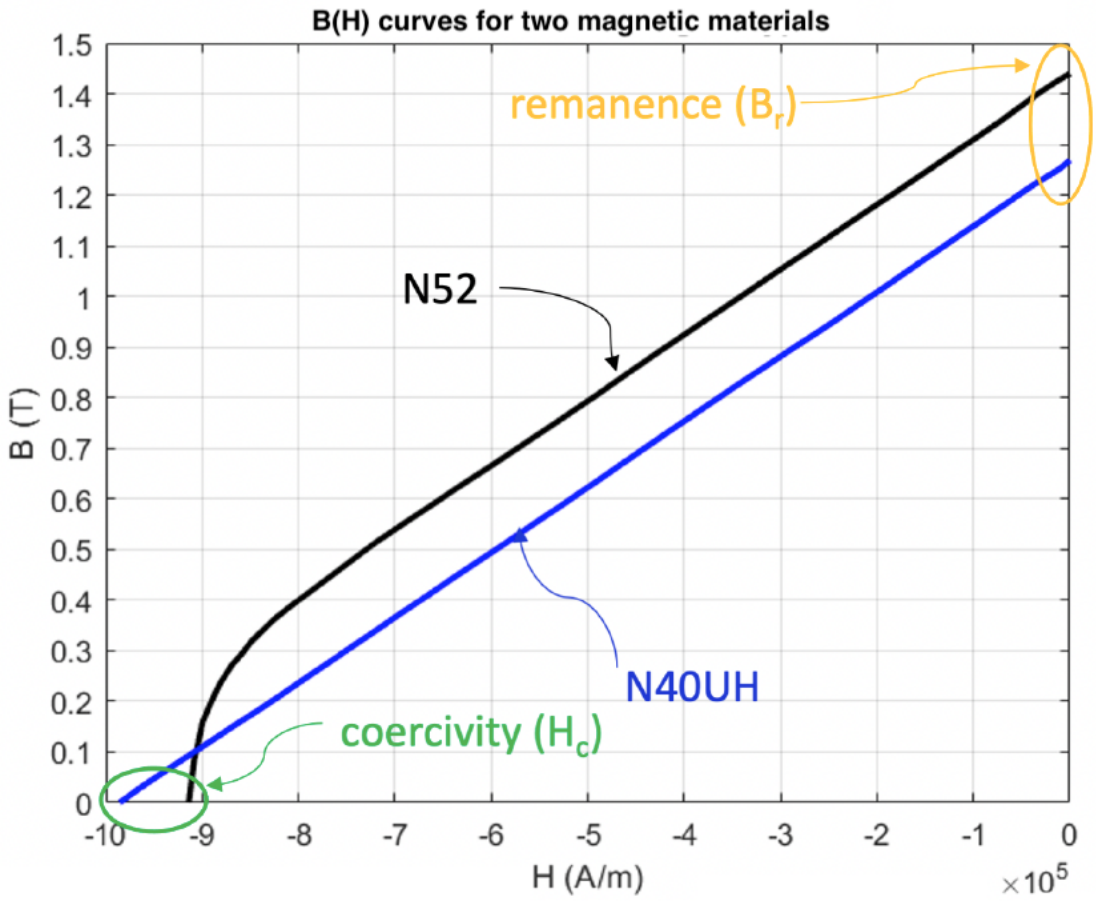

Figure 4.10: Accurate B(H) curves for two magnetic materials N52 and N40UH used in finite element simulations. B(H) curves are measured specifically in QII (see QII in Figure 4.5 for comparison) since the block is in its own magnetic field. Permission granted by Binic Magnet Co. Ltd., China.

magnetic flux inside a fixed-size Halbach magnet for comparison (Figure 4.11a,b). Using a remanent field (B_r) of 1.4 T, which is a common value for N52, the analytical method predicted a field strength at the geometric isocenter (B_c) of 0.30435 T and a peak-to-peak homogeneity in a 9 cm diameter spherical volume (DSV) of 150 ppm (Figure 4.11c).

The magnetic field strength of the same Halbach magnet was simulated using FEM and the B(H) curves presented in Figure 4.10. The model of the Halbach magnet is shown in Figure 4.11a. For blocks made of N52 material, the FEM predicts a magnetic field strength at the geometric isocenter (B_c) of 0.29657 T and a peak-to-peak

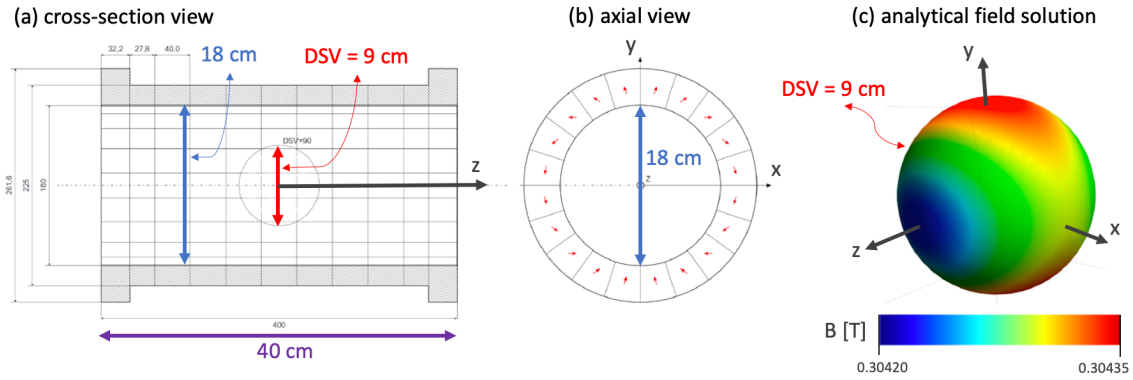

Figure 4.11: A Halbach magnet geometry and the predicted field distribution obtained using the analytical method. (a) The cross-sectional view of the Halbach magnet. (b) An axial view of the Halbach magnet showing the segmented magnetization (red arrows). (c) The plot of the magnitude of the magnetic flux density over a 9 cm diameter spherical volume (DSV).

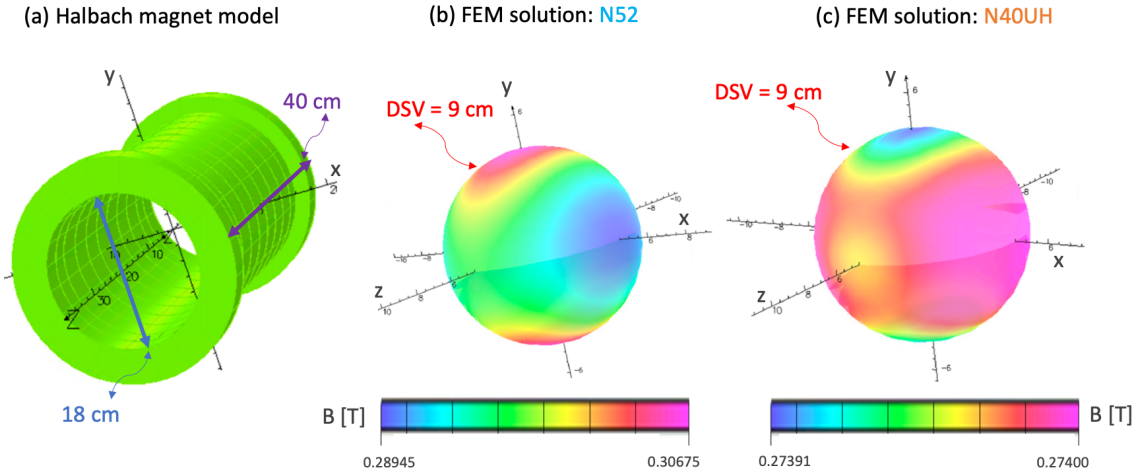

Figure 4.12: The same Halbach magnet as in Figure 4.12 and the predicted field distribution using the finite element method (FEM) for two types of magnetic material. (a) The three-dimensional model used for field calculation by Opera3D magnetostatics FEM simulation software. (b) The magnetic field distribution using the N52 B(H) curve (black line Figure 4.11) in FEM simulation. (c) The magnetic field distribution using the N40UH B(H) curve (blue line Figure 4.11) in FEM simulation.

homogeneity in a 9 cm DSV of 58,350 ppm (Figure 4.12b). For N40UH blocks, the FEM predicts a field strength at the geometric isocenter (B_c) of 0.27400 T and a peak-to-peak homogeneity in a 9 cm diameter spherical volume of 479 ppm (Figure 4.12c). A comparison of the Halbach magnet parameters acquired by analytical and finite element solutions is shown in Table 4.2.

Table 4.2: A summary of the Halbach magnet parameters using analytical and finite element solutions.

Field Analysis	Ferromagnet Properties	B_c [T]	B_{max} (DSV) [T]	B_{min} (DSV) [T]	η [ppm]
Analytical	B_r = 1.4 T	0.3060	0.30435	0.30420	150
FEM	N52 (BINIC) B_r = 1.4 T H_{cb} = 796 kA/m H_{ci} = 876 kA/m	0.29657	0.306753	0.289448	58,350
FEM	N40UH (BINIC) B_r = 1.2 T H_{cb} = 899 kA/m H_{ci} = 1990 kA/m	0.27400	0.274037	0.273906	479

Although analytical solutions can accurately predict the magnetic flux density at the geometric isocenter of a Halbach magnet, they fail to approximate the magnet field homogeneity [120, 131]. It is likely because analytical solutions assume the magnetic material has an infinite coercivity and constant remanence (i.e. the ferromagnetic pieces do not interact). An infinite coercivity means that no matter how strong the external magnetic field is, the blocks maintain a magnetic flux density near B_r. As seen from FEM simulations (Figure 4.12), the field homogeneity can vary drastically depending on the magnetic material used in the construction since coercivity is finite and the B(H) curves are non-linear. For example, N52 type ferromagnets are among the strongest permanent magnets due to their high remanent field (B_r). For this reason, N52 material is commonly used for MRI permanent magnets since the highest magnetic flux density can be achieved. Unfortunately, N52 has a lower coercive field than other types of materials such as N40UH (see Figure 4.10). Therefore, preliminary simulations suggest that magnetization/demagnetization effects impact the homogeneity in the final design. Using the accurate B-H curve for N40UH material

in calculations predicts a 150× improvement in the magnetic field homogeneity compared to the accurate N52 due to its higher coercivity. Furthermore, since N40UH has a lower remanent field, the Halbach magnet has a slightly lower magnetic field strength (∼0.27 T) than using N52 (∼0.30 T). As seen from the above discussion, selection of a suitable ferromagnetic material is critical for MRI magnet design.

4.4 Design and construction of a Halbach magnet for TRASE

4.4.1 Introduction

So far, the homogeneity of superconducting and bi-planar permanent MRI magnets has been optimized within a diameter spherical volume (DSV) [21]. This allows MRI over a large region of interest (ROI) using gradients of the magnetic field with selective RF pulses. Unfortunately, optimization of homogeneity over the spherical volume when used in the design of portable Halbach magnets prevents the construction of magnets with low aspect ratio (<1.5:1) suitable for standard MRI techniques. To deal with the inhomogeneities, RF pulses with a specific bandwidth (BW) can be applied allowing excitation of the region with inhomogeneities corresponding to the BW. For example, Perlo et al. (2004) achieved a set of 1 mm thick 2D MR images using a highly-inhomogeneous single-sided permanent magnet by exploiting the magnet's sensitive volumes [132]. Therefore, we proposed that a cylindrical ROI may be considered for imaging rather than the entire DSV. The thin cylindrical region would define a single selected "natural" slice for a two-dimensional Transmit Array Spatial Encoding (TRASE) imaging scheme [40, 73, 108].

4.4.2 Methods

As a construction of a Halbach magnet for whole body MRI with a large spherical ROI is not feasible at this point, we proposed to design a sparse Halbach magnet with a low aspect ratio and a cylindrical ROI for TRASE MRI of human extremities. The

sparse design uses cubical blocks of the same size and magnetization. Sparse Halbach magnets are also less expensive due to a simple block manufacturing process and construction compared to the segmented Halbach magnet (shown in Figure 4.11b). For the first Halbach magnet design, a minimum imaging cross-section of 12.7 cm diameter was set to accommodate 84% of human ankles [133]. Since the primary application was ankle MRI on the International Space Station (ISS), its maximum dimensions were specified by the Canadian Space Agency [134]. The target magnetic flux density and homogeneity were selected based on other research that achieved high quality MR images within a Halbach magnet [36, 135]. The weight and cost of the magnet were arbitrarily set for this work.

Aims of the magnet design

1. Magnetic flux density between 50 and 70 mT.
2. ROI no smaller than 12.7 cm diameter and 1 cm long cylinder.
3. Homogeneity over ROI better than 12,000 ppm peak-to-peak. Based on preliminary tests, the sparse Halbach magnet with 8 rings would have a high inhomogeneity ($>$ 150,000 ppm) which could be improved by 10 $\times$ after optimization. This homogeneity is also reasonably achievable considering Halbach magnet designs presented in the literature [37, 113].
4. Magnet inner bore diameter no less than 20 cm.
5. A total magnet weight less than 30 kg.
6. An overall magnet size less than 45 cm $\times$ 45 cm $\times$ 45 cm.
7. Less than $3000 material costs.

Detailed magnet design

For the simulations, we used 320 permanent magnet blocks of size 2.54 cm × 2.54 cm × 1.27 cm magnetized along their short axis. The blocks were arranged in pairs with a 3 mm spacing, with the blocks magnetization in the same direction, allowing secure mounting (due to their self-attraction) to 3D printed formers [108], [136]. The initial geometry, before optimization, comprised of 16 block pairs per ring with centers distributed on eight 32 cm diameter rings (Figure 4.13). Two of the eight rings were nested, consisting of 32 block pairs each, to minimize the impact of field perturbation produced by the finite length of the magnet (see Figure 4.9a) [111, 123, 137]. The block pairs were evenly spaced by $\Delta\theta = 22.5^0$ ($\Delta\theta = \theta_{i+1} - \theta_i$ where i = 1..16 is the block number; θ is the angle of deviation from the x-axis) to allow enough space for the block pairs radial movement throughout the optimization process (Figure 4.13). The magnetization of each block pair was rotated by $\phi_i = 270^0 + 2\theta_i$ to generate a dipolar internal magnetic flux density (black arrow in Figure 4.13A). Although non-negligible fabrication inconsistency in the size, shape and magnetization of the blocks have been noted by other researchers [33, 36, 37, 119], magnetic pieces with minimal fabrication variability are commercially available. There are manufacturers that provide high quality magnetic blocks with very low variances in magnetization strength and direction ($< 1\%$ and $< 3°$, respectively) as well as very small size variation ($<$ 0.1 mm) [138]. For the magnet construction, we used sintered neodymium magnetic pieces type N40UH (as seen in Figure 4.10) with high coercivity (>1000 kA/m), high remanent fields ($<$ 1.2 T) and low costs ($4 USD/block) [138].

Optimization procedure

Achieving high homogeneity ($<$ 1000 ppm) in a low aspect ratio (less than 1.5:1) Halbach magnet is difficult. The magnet length truncation affects the field homogeneity in an axial plane (see simulated B_0 in Figure 4.13A). Since the finite length of the magnet is the primary cause of inhomogeneities, we optimized the radial positions

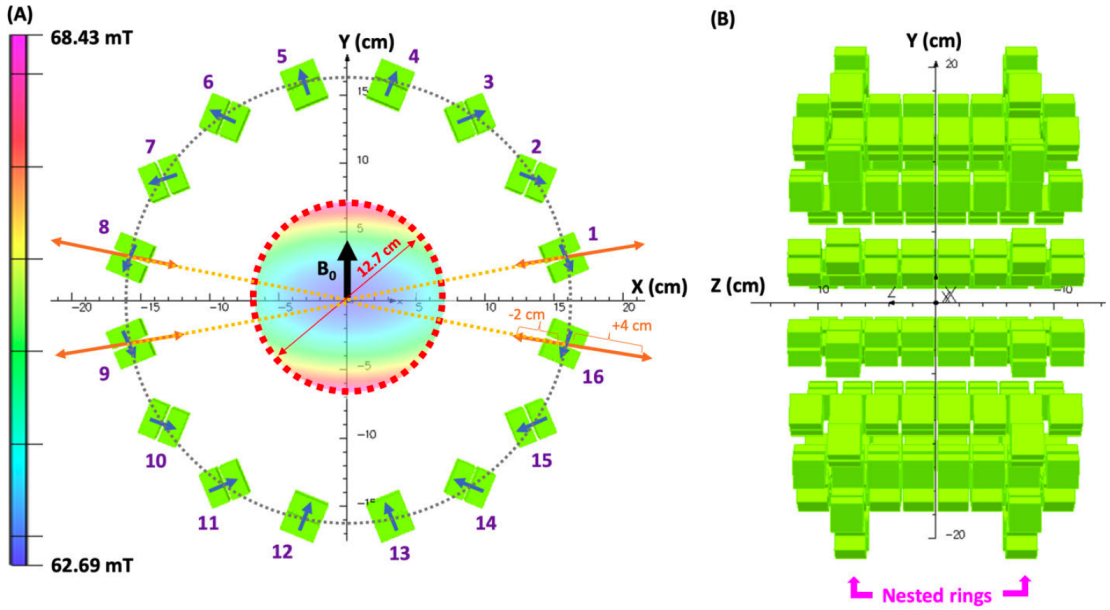

Figure 4.13: The initial geometry of the sparse Halbach magnet. (A) An axial view of one ring showing sixteen block pairs (green) centered on a 32 cm diameter circle (dashed grey). The blue arrows represent the block pair magnetization direction that generates a vertical magnetic field (black arrow). A genetic algorithm was used to find the optimal radial positions of the block pairs (orange arrows). A simulated B_0 map in a central plane shows the low-order field variation in a 12.7 cm diameter area (red dashed circle). (B) A sagittal view of the magnet showing eight coaxial rings 3 mm apart.

of the block pairs in the entire magnet (Figure 4.13A) because of a stronger effect on the magnetic field variation compared to the remanence and magnetization directions (see Equations 4.5 and 4.6) [139]. As the initial configuration for optimization, we used eight symmetrical rings placed along the z-axis (Figure 4.13B). Simulations included the B(H) curve provided by a manufacturer for N40UH (blue curve in Figure 4.10). Calculations of the homogeneity based on the predicted field distribution produced by magnetostatics FEM simulation (Opera3D, Cobham, UK) were used for the optimization of the block pair positions.

Since the genetic algorithm (GA) was proven successful in Halbach magnet design [113, 131], we chose to employ the GA optimization process in this work. C.Z. Cooley et al. (2017) was first to use the genetic algorithm to optimized the ferromagnetic

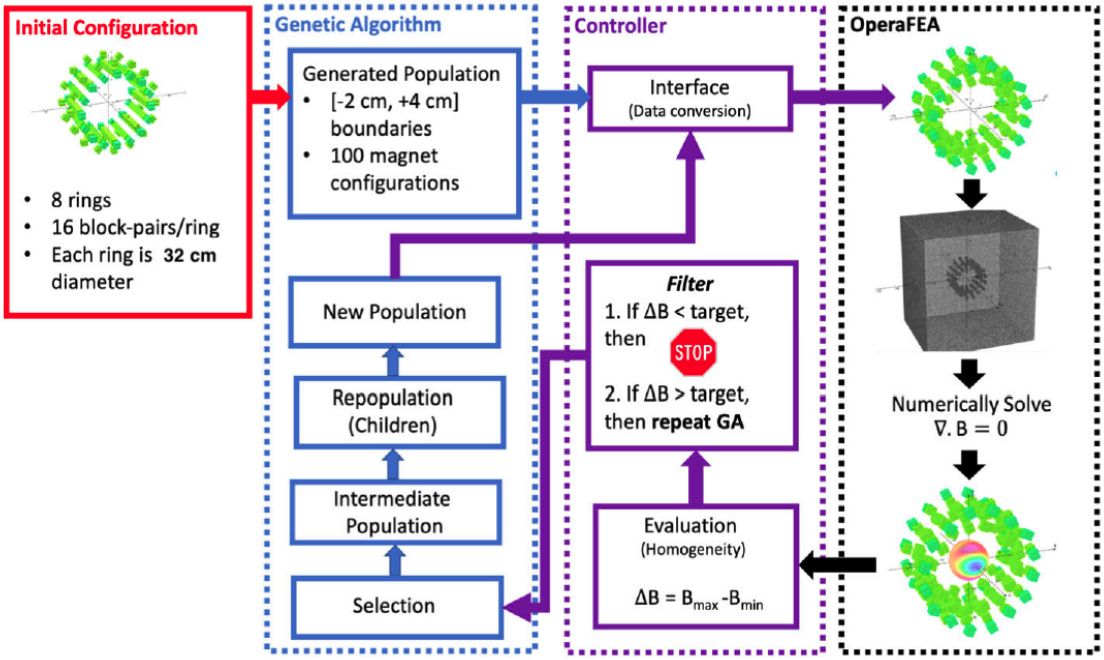

Figure 4.14: The data flow of the field simulation and optimization. The initial geometry (red) is input into a genetic algorithm that generates 100 random magnet configurations based on the user constraints. A controller of the data flow between the genetic algorithm and finite element magnetostatics (FEM) simulation software was written in Matlab. After a single geometry is simulated, the controller also computes the B_0 homogeneity based directly on the simulated field data and selects configurations based on the most homogeneous fields.

material at fixed positions in Halbach magnet design, achieving impressive results. As a result of their optimization approach, they achieved an average field strength of 127.5 mT and improved the simulated magnetic field homogeneity from 137,870 ppm to 13,669 ppm over a 20 cm DSV (magnet length $\sim$ 46 cm; inner diameter $\sim$ 27 cm) [113]. Unfortunately, the magnet based on this design was not constructed. However, O'Reilly et al. (2019) used the GA to optimize diameters of the rings of a sparse Halbach magnet achieving a simulated peak-to-peak homogeneity of 400 ppm over the 20 cm DSV (magnet length $\sim$ 51 cm; inner diameter $\sim$ 27 cm) [37]. In this case, the Halbach magnet was constructed and the measured homogeneity was $\sim$13,000 ppm, and the GA was used again to optimize an array of small ferromagnets to add the the Halbach magnet, improving the homogeneity to $\sim$2,500 ppm. In our work, we used

a GA optimization process in MATLAB (Global Optimization Toolbox, MATLAB, MathWorks, USA) which mimics evolution by natural selection [113, 140]. The GA uses genetic operators, such as mutation and crossover, on the magnet models and selects designs with the best homogeneity and field strength [113]. Therefore, over time, the GA selects the most homogeneous design. In our work, the GA was applied to the sixteen variables of the magnet (positions of 4 block pairs per ring $\times$ 4 rings) to minimize the difference between the maximum and minimum field (Equation 4.9) within a 12.7 cm diameter and 1 cm thick ROI (Figure 4.14). The remaining block pairs were symmetrically distributed and optimized; hence no need for simulations. The radial position of each block pair was varied within -2 cm to +4 cm of a 32 cm diameter circle for each ring independently (orange arrows in Figure 4.13A). In the nested rings, comprising an inner ring distributed at 23.8 cm and outer ring at 40.2 cm, the block pairs sharing a common radial axis were moved simultaneously (Figure 4.13B). The GA was programmed to generate 100 magnet configurations per generation and 350 generations in total. Regardless of the blocks optimal positions, the magnet geometry maintains an internal diameter of 20 cm, providing sufficient space for RF coils and the imaged object yet constraining the external size to less than 45 cm $\times$ 45 cm $\times$ 45 cm.

Construction of the magnet

Once the optimal positions of the block pairs were determined, the models of each ring were exported directly from Opera3D Modeler (Opera3D, Cobham, UK) to a computer aided design (CAD) software (Autodesk Fusion 360, California, USA). CAD software was used to generate eight ring formers with specific pockets for the block pairs (Figure 4.15A). The block sizes were enlarged in the models by 0.18 mm in all directions to compensate for the manufacturing errors of formers and to allow tight fitting of the magnetic blocks. The block models were then subtracted from the ring models to produce cavities for the block pairs. Finally, the former models

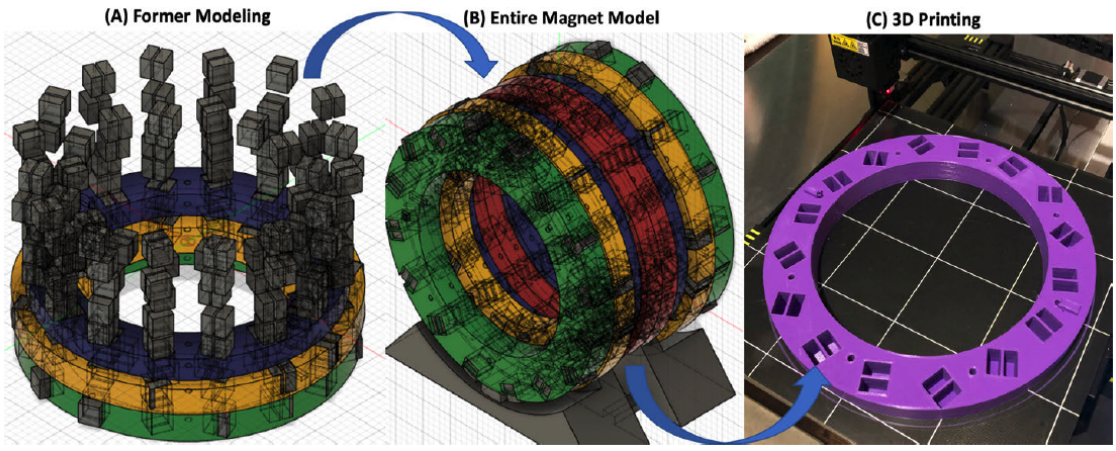

Figure 4.15: Workflow of the design and construction for ring formers. (A) The computer-aided design modelling of formers for the magnetic blocks. The optimized magnet geometry is cut from the model formers creating pockets in the rings. (B) The entire geometry consists of eight coaxial rings separated by 3 mm in a custom stand. (C) Each ring is 3D printed.

were converted to a geometry code (i.e. the .gcode file) using slicer software (Cura, Ultimaker, Netherlands) to prepare for 3D printing.

For 3D printing of the ring formers, polylactic acid (PLA) was used (Figure 4.15C and Figure 4.15e-h) [108, 141]. Using the slicer software, we adjusted the settings for the most robust yet lightweight ring formers (octet infill pattern, infill = 20%, wall thickness = 2 mm) [142]. The block formers were then printed, one at a time, using a 3D printer (Anycubic Chiron, Shenzhen, China) and eight spools of PLA (1.75±0.05 mm, 1 kg spool, Overture3D, USA) in various colors (Figure 4.16e-h). The total 3D printing time for all the formers was ∼652 hours. Using these settings, the weight of each 3D printed ring was ∼0.4 kg and each nested ring ∼0.8 kg. After each print, the ring thickness, block pair pocket spacing, and size were measured with a caliper (Digital Caliper, Tacklife, USA) to ensure less than 0.2 mm deviations from the original CAD models. Any remaining imperfections in the formers were sanded using a multi-function rotary tool (Tacklife Rotary Toolkit, Tacklife, USA).

Before fitting blocks into formers, the magnetization direction of each block was measured using a 3-axis Hall probe (THM1176, MetroLab, Switzerland) and marked

Figure 4.16: Construction and assembly of the Halbach magnet. Photos of the four (out of 8 total) designed (a-d) and manufactured (e-h) formers. The other four rings (not shown) are identical. The 3D printed formers with N40UH magnetic blocks fitted into pockets are shown. Eight cylindrical (6.35 mm diameter) cuts in the CAD models allow throughput for brass rods, and the pegs/holes in formers minimize ring shifting when compressed. (i-j) Flange brass nuts are tightened, compressing the rings (blue arrows) into their optimized geometry.

before fitting blocks into the formers (Figure 4.16e-h). In addition, 3D printed plugs, using PLA, were fitted into the remaining space of the former pockets to minimize shifts during assembly and transportation. Beginning with the back-end ring (Fig-

ure 4.16a,e), eight 6.35 mm diameter threaded brass rods were fed through each ring, one at a time, allowing vertical suspension of the rings due to magnetic repulsion. The rings were then compressed (blue arrows in Figure 4.16j) and tightened with brass nuts in a symmetric fashion analogous to tuning a drum. Compression was considered sufficient when a piece of paper did not slide through the ring gaps. The weakly diamagnetic brass rods and nuts had a negligible impact on the field and withstands the repulsive forces between rings [36, 112]. The magnet construction allows disassembling the structure for transportation and shipping.

Three-dimensional (3D) magnetic field mapping

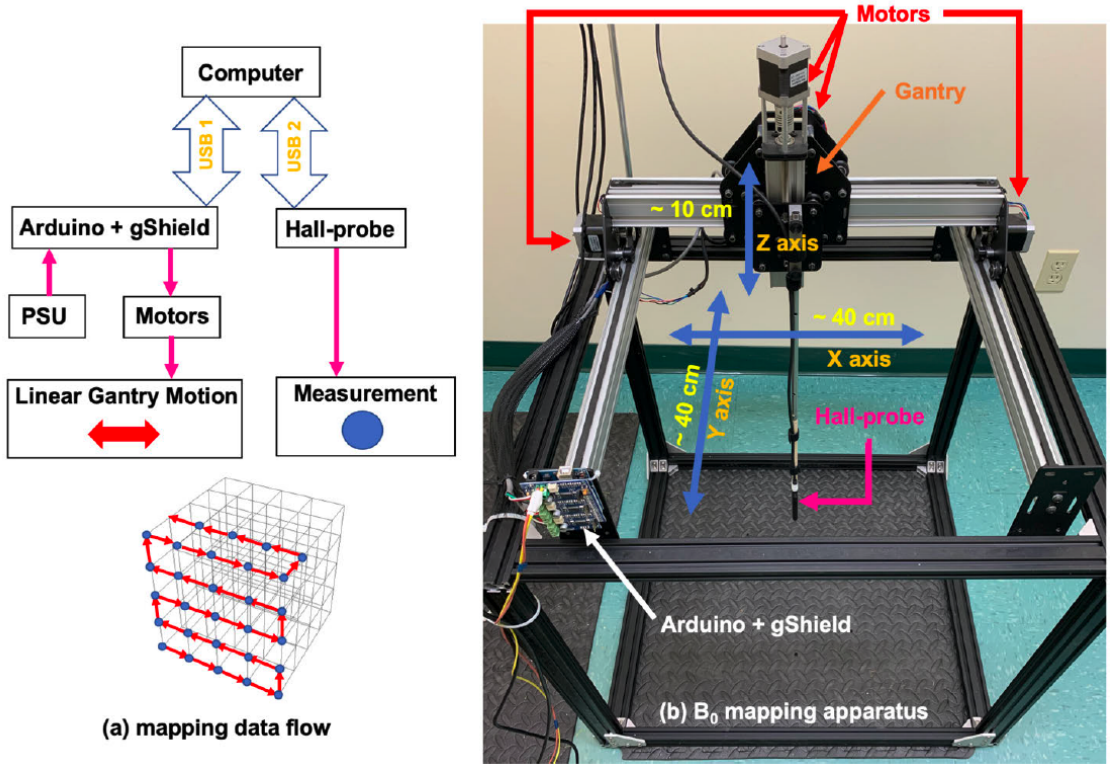

Figure 4.17: The 3D magnetic field mapping data flow and apparatus. (a) An in-house Python code was used to stream positional coordinates (g-code) to an Arduino-gShield microcontroller by universal serial bus (USB 1). The g-code is interpreted by the microcontroller and translated into linear motion of the Hall probe in all three dimensions. (b) After a discrete movement, the Hall-probe is triggered to obtain 30,000 magnetic field measurements (B_0). The average magnetic field value is sent back to a computer by a second universal serial bus (USB-2).

The magnetic field strength produced by the assembled magnet was measured using a 3-axis Hall probe and computer numerical control (CNC) (Figure 4.17) [143, 144]. A holder with 3D positioning of the probe was made using commercially available 3D printer hardware railing and a modified 3-axis CNC gantry (Shapeoko 2, Carbide 3D, USA). The CNC gantry (Figure 4.17b) was precisely positioned by a programmable Arduino-gShield (Synthetos, Adafruit, USA). The motors were supplied by a 24 VDC power supply (LS150-24, TDK-Lambda Americas Inc., Japan). Although the stepper motor accuracy was considered sufficient ($\sim$1 mm), improved calibrations such as micro-stepping could further increase positioning accuracy in future application [144]. The Hall probe was attached to the gantry head through a 9.5 mm aluminum tube. The automation was achieved by combining and modifying open-source Application Program Interfaces (APIs) that were built specifically for the THM1176 Hall probe [145] and GRBL-based CNC controllers [146]. The cardinal axis of the Hall probe was aligned with the field direction to maximize measurement accuracy (0.3 G). Additionally, the Hall probe was triggered to obtain 30,000 averages per measured point (6800 samples per second), increasing measurement precision to 0.02 G. The field measurements and positioning of the probe were automated using an in-house Python code (available at [147]) to map $|B_0|$ at 3 mm $\times$ 3 mm $\times$ 1 mm steps over a 13.5 cm $\times$ 13.5 cm $\times$ 1 cm region centered at the magnet geometric isocenter. A total of 22,275 points were collected to create the 3D map requiring about 30 hours. Other research groups have demonstrated more efficient and very accurate (sub-millimeter) mapping systems with higher current external drivers [144]. Peak-to-peak homogeneity was then calculated using Equation 4.9 based on the simulated and measured B_0 maps.

4.4.3 Results

Final simulated magnetic field

The initial Halbach magnet simulation provided 93474 ppm homogeneity within the ROI. The optimization of the positions of the block pairs using GA provided a significant improvement in the simulated homogeneity (11451 ppm). The simulated field strength varies from 66.73 mT to 67.49 mT over the ROI in the optimized design (Figure 4.18i, ii). The optimized positions of the block pairs in each ring relative to the initial 32 cm diameter circle are listed in Figure 4.18iii and illustrated in Figures 4.18iv-vii. A positive value means that the block pair center is shifted outward from the circle; a negative value means inward shift (i.e. closer to the magnets center axis). The magnet is symmetric about the z-axis; therefore, blocks in -z mirror those in the +z. In addition, the block pair positions are shown for quadrant I (QI) only since movements in QII, QIII and QIV are symmetric.

Three-dimensional (3D) magnetic flux mapping

The longitudinal axis (z) of the constructed magnet was oriented vertically for B_0 measurements (Figure 4.19a-c). To show minute differences between simulated and measured fields, the simulated (Figure 4.20d) and measured (Figure 4.19e) B_0 maps were subtracted for eleven planes (z = -0.5, -0.4, -0.3, -0.2, -0.1, 0, +0.1, +0.2, +0.3, +0.4, +0.5 cm). Error maps for the three axial planes (out of eleven total) over the ROI are shown in Figure 4.19f. The error maps reveal that the measured field is lower by 0.21 mT than the simulated field strength at the periphery of the cylindrical ROI. This deviation is more apparent by comparing projections of the simulated and measured fields along the cardinal axes of the Halbach magnet (Figure 4.20). The measured field drops 0.21 mT at x = 6 cm (Figure 4.20a) and 0.17 mT at y = 4.5 cm (Figure 4.20b).

The simulated and measured field was then compared to find the maximum peak-to-peak field variation ($\Delta B_0 = B_{max} - B_{min}$) within the cylindrical ROI. As seen from

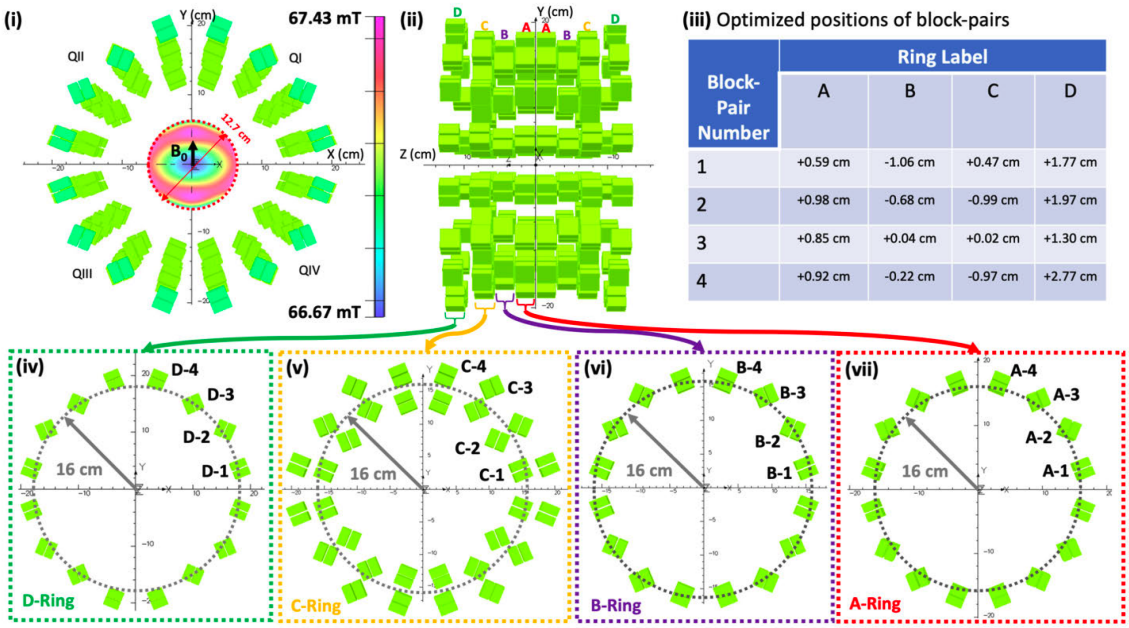

Block-Pair Number	Ring Label A	B	C	D
1	+0.59 cm	-1.06 cm	+0.47 cm	+1.77 cm
2	+0.98 cm	-0.68 cm	-0.99 cm	+1.97 cm
3	+0.85 cm	+0.04 cm	+0.02 cm	+1.30 cm
4	+0.92 cm	-0.22 cm	-0.97 cm	+2.77 cm

Figure 4.18: The final geometry of the sparse Halbach magnet. The block pairs positions were varied in each ring separately to achieve maximum homogeneity in a 12.7 cm diameter, 1 cm long inner cylindrical ROI using the genetic algorithm optimization. (i) An axial view of the optimized magnet showing block pair positions in all eight rings. (ii) A sagittal view of the optimized magnet. (iii) The optimum positions of each block-pair from the initial 32 cm diameter circle. Shifts of the block pair positions are shown only for blocks in the first quadrant (QI). (iv-vii) A visualization of the final block pairs positions for each ring leading to the optimized homogeneity (11451 ppm) within the cylindrical ROI.

Table 4.2, the measured B_0 homogeneity corresponds to the simulated homogeneity (11451 ppm) within the limited accuracy and precision of the 3D field mapping apparatus.

A summary of magnet specifications and costs

The simulated and constructed magnet specifications are summarized in Table 4.3. The final constructed Halbach magnet has a field strength ~66.7 mT and a measured peak-to-peak homogeneity of 11152 ppm, while simulated homogeneity is 11451 ppm. The constructed magnet has an aspect ratio ~1:1, overall outer dimensions ~43 cm × 43 cm × 25 cm, and weight 25 kg (total blocks weight ~19 kg, formers ~4 kg, brass rods + nuts ~2 kg). The material cost is ~$2,000 (320 magnets = $1,550, 8

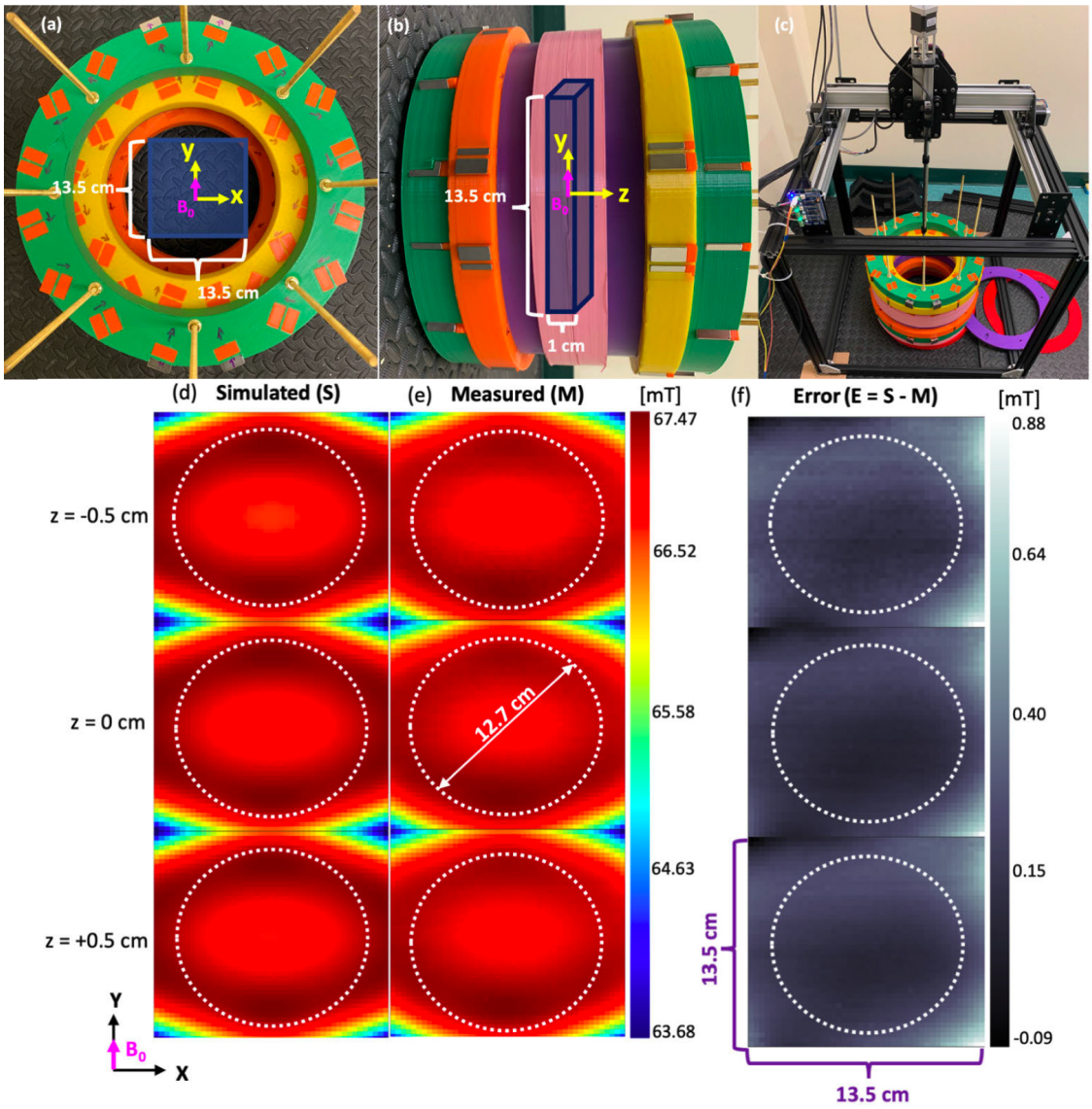

Figure 4.19: The apparatus and setup used for field mapping and the measurement results within the ROI. (a) An axial view of the constructed optimized magnet showing cross-section of the measured region. (b) A sagittal view of the assembled magnet and the measurement volume. (c) The automatic system of B_0 mapping. (d) Simulated (e) measured and (f) error maps in the three axial planes over the measured region.

spools of PLA = \$240, eight 6.35 mm diameter threaded brass rods = \$112, sixteen flange brass nuts = \$16).

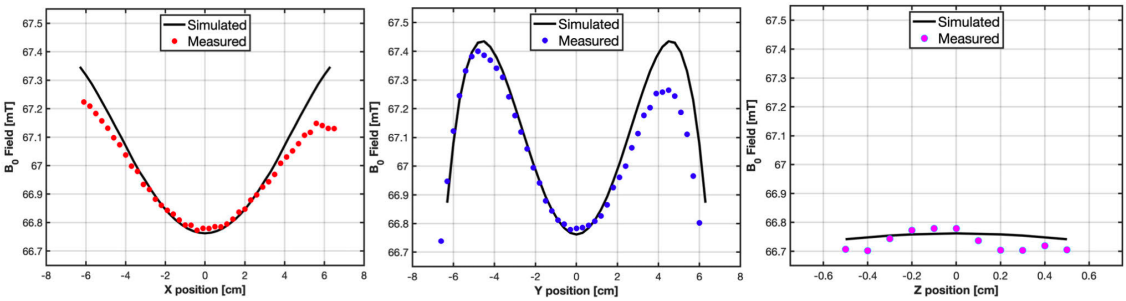

Figure 4.20: The measured (dotted lines) and simulated (solid lines) field deviations along the (a) x-axis, (b) y-axis, and (c) z-axis of the Halbach magnet. The measured field deviations from the simulated fields are visible at x = 6 cm and y = 4.5 cm.

Table 4.3: Comparison of the simulated and measured field strength and homogeneity in the cylindrical region of interest (ROI).

Parameter	Simulated	Measured
B_{max} = Maximum field in ROI [mT]	67.4948	67.4335
B_{min} = Minimum field in ROI [mT]	66.7303	66.6888
$\Delta B = B_{max}$ - B_{min} [mT]	0.7645	0.7447
B_c = Magnetic field at isocenter [mT]	66.7621	66.7768
η = Homogeneity [ppm]	11451	11152

Magnet testing with the wrist

The Carr-Purcell-Meiboom-Gill (CPMG) [150] pulse sequence was used to detect T_2 signal decay from the wrist using the constructed Halbach magnet. The custom-built TRASE MRI hardware comprised: (1) the described above Halbach magnet [114], (2) the TRASE amplifier system [41], (3) a 10 cm diameter solenoid RF coil, and (4) a custom console [149]. The magnet, RF coil, and subject were housed inside a custom-built Faraday cage. The preliminary data in Figure 4.21 shows that the magnet can be used to provide sufficient signal for NMR and a possible 2D MRI experiment.

1D TRASE using a phantom

The next step was to test the magnet for use with TRASE. For this experiment, the two twisted solenoid RF coils were oriented at 90° to each other to produce opposing

RF phase gradients [148]. The 1D TRASE profile result is shown in Figure 4.22. The shape of the projection is not exactly as expected due to the remaining field inhomogeneities of the Halbach magnet.

4.4.4 Discussion of magnet results

The constructed Halbach magnet with an aspect ratio of ∼1:1 produces a 66.7 mT magnetic field strength. This new design significantly reduces the weight and size of the sparse Halbach magnets constructed so far [36, 38, 112, 131] by truncating the magnet length and limiting the imaging volume. The magnet design and its accurate realization removes the technology risk identified by the Canadian Space Agency for magnet designs suitable for MRI on the ISS [106, 134, 151]. We envisioned the 12.7 cm diameter 1 cm thick ROI disk would allow 2D TRASE imaging of a single slice through an astronaut's leg. Although reducing the sensitive volume is not desired, a multi slice technique could be applied by moving the object or the magnet. The magnet

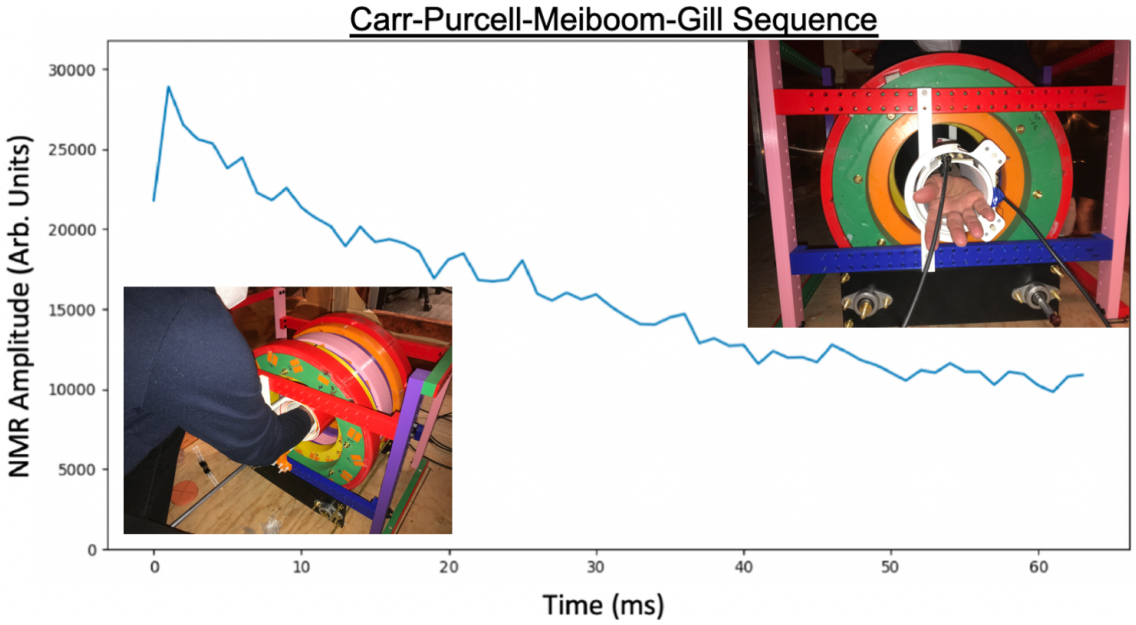

Figure 4.21: The signal decay (T_2) from the wrist using custom-built TRASE hardware [41, 114, 148, 149]. The CPMG pulse sequence with the following parameters was used [150]: number of averages = 1, echo spacing = 1 ms, operating frequency = 2.84 MHz, pulse duration = 90 us (both excitation and refocusing pulses), and number of echoes = 64.

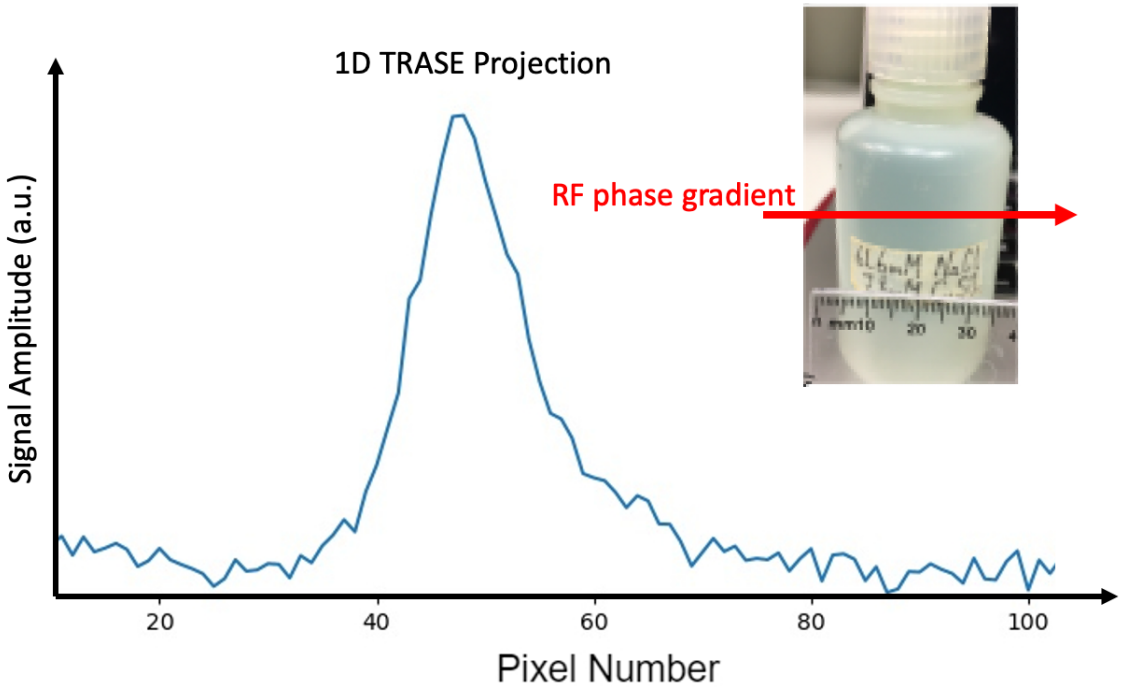

Figure 4.22: A 1D TRASE projection using custom-built hardware [41, 114, 148, 149]. Number of averages = 16, echo spacing = 1 ms, operating frequency = 2.836 MHz, pulse duration = 200 μs (both excitation and refocusing pulses), and number of echoes = 128.

parameters were achieved using permanent magnet blocks type N40UH, with small size variability, and minimal differences in the magnetization direction and strength. The small (de)magnetization of the N40UH material ensures minimal variations of the magnetization within the magnetic blocks, and ultimately, decreases the discrepancy between the simulated and measured homogeneity. Additionally, an accurate B(H) curve of the N40UH material was used in simulations. The GA optimization method of the block pairs positions to achieve maximum field homogeneity was used.

To ensure magnet durability, lightweight and mechanical strength, the block formers were 3D printed. As visible in Figure 4.20, there is a small discrepancy (up to 0.21 mT) between the simulated and measured values of the magnetic field. We speculate that these field deviations are mostly due to the variations in block size, magnetization strength and direction, and the rounded edges of magnets which are not modelled in simulations. Asymmetries in x and y directions, visible in Figure 4.20,

are likely caused by the differences of the magnetic fields (strength and direction) in the proximity of the blocks due to imperfections in their production. In addition, inaccuracy ($\sim$0.3 mT) may further influence the field measurements when the magnetic field direction deviates from a cardinal axis of the probe occurring close to the inner bore surface. Further increase in the measurement accuracy near the inner bore could be achieved by automating rotation of the Hall probe to align with the magnetic field. Other factors, such as minute differences in tensions between the brass rods and nuts around the circumference of the magnet, temperature instability of ferromagnets and imperfections of the ring formers can also contribute to magnetic field inhomogeneity. Furthermore, the alignment of the B_0 mapping apparatus to the magnet and residual stepper motor imperfections also contribute to systematic errors. Fortunately, the minute decrease of the measured field in these regions has a negligible impact on the actual magnetic field homogeneity despite the typical challenges such as block fabrication errors and magnet former imperfections that disturb field homogeneity in constructed permanent magnet arrays. The presented design could be modified to meet the requirements of specific imaging techniques, such as rotational spatial encoding method (rSEM) or MRI with linear field gradients.

Some MRI applications require higher homogeneity than the constructed Halbach magnet. Fortunately, a five-fold improvement in homogeneity was achieved in other sparse Halbach designs by using an array of small-sized permanent magnets for shimming [37, 135]. These techniques may be adapted further to improve the field homogeneity of the constructed magnet without reducing bore space (see 5). In addition, small deviations in the compression provided by each rod may impact the homogeneity. Although rings should be tight, adjustment of rod tensions may also provide limited control of the magnetic field homogeneity ($\sim \Delta$300 ppm based on preliminary work using this method).

4.4.5 Conclusions

In this work, we simulated the field of a sparse Halbach magnet and optimized the positions of the blocks in the entire design to reduce dominant magnetic field inhomogeneities caused by the short length of the magnet. The low magnetic variability between the ferromagnets (N40UH) and the high precision 3D printing of formers allowed construction of a Halbach magnet with parameters matching simulated values. By limiting the imaging volume to a cylindrical region, the length and weight of the magnet was reduced, relative to other approaches. The magnet meets Canadian Space Agency specifications for an ankle MRI for the ISS and the design is suitable for many other low-field portable MRI applications.

Chapter 5

Shimming of the Halbach Magnet for Slice-selective 2D TRASE

5.1 Introduction

The constructed high-duty cycle RF amplifier (Chapter 3) allowed high-resolution 1D TRASE when used with the twisted-solenoid RF coils [41, 42, 74]. As seen in Figure 5.1, the RF phase gradients (G_1 and G_2) produced by the twisted solenoid coils are in the same plane as the B_0 field [42, 74]. Unfortunately, with this type of RF coil, there is no available method to encode spins along the magnet's longitudinal axis, other than the axial distribution of the B_0 field. Although the magnetic field in the constructed magnet was optimized for maximum B_0 homogeneity in a cylindrical region of interest (ROI), the remaining B_0 inhomogeneity and axial B_0 field distribution prevent the use of the Halbach magnet for high-quality in-vivo 2D TRASE MR imaging. The B_0 distribution causes complicated aliasing of NMR signal along the longitudinal axis of the magnet, deteriorating the MR image. Therefore, the appropriate field adjustments in the constructed magnet are required.

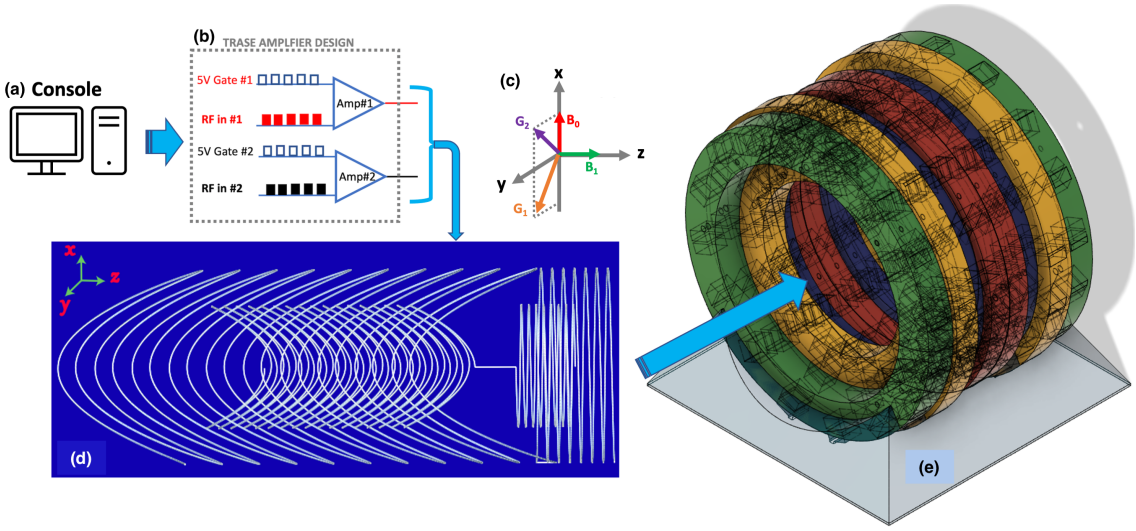

Figure 5.1: Hardware used for 1D TRASE MRI: (a) console, (b) RF amplifiers, (c) coordinate system, (d) twisted-solenoid coils and (e) a Halbach magnet. The vertical B_0 field in the dipolar Halbach magnet allows the application of the efficient twisted-solenoid RF coil(s) that can generate a longitudinal B_1 field with perpendicular phase gradients (G_1, G_2) [41, 42, 74]. For 2D TRASE MRI, a third RF coil (uniform or phase gradient) or magnet/RF coil rotation is required (not shown) and both phase gradients need to be oriented at 90° to each other. Figure (d) was obtained from Sun et al. (2020) [42] with permission from John Wiley and Sons under license number 5324570909616.

5.1.1 Conventional MRI slice selection

In conventional MRI, an object is placed in a uniform B_0 magnetic field (Figure 5.2). The specific slice (Δz) is selected using simultaneously a linear magnetic field gradient gradient (G_z) and a selective radiofrequency (RF) B_1 field ($B_1 \propto |\vec{B_1}|\text{sinc}(\omega_0 t)$), with center frequency (f_c) and bandwidth (Δf), corresponding to the Larmor frequency of the selected spins (light gray in Figure 5.2) [47]. Following the slice selection, the frequency and phase encoding gradients are applied and 2D k-space is acquired (Chapter 2). Furthermore, a different volume of spins may be selected by changing the center of the RF frequency to match the spin frequencies in the desired volume, for example, within the brain rather than the leg. In a standard MRI exam, however, the imaged body part is usually moved to the geometric isocenter of the main magnet before imaging to maximize B_0 homogeneity and gradient linearity over the object.

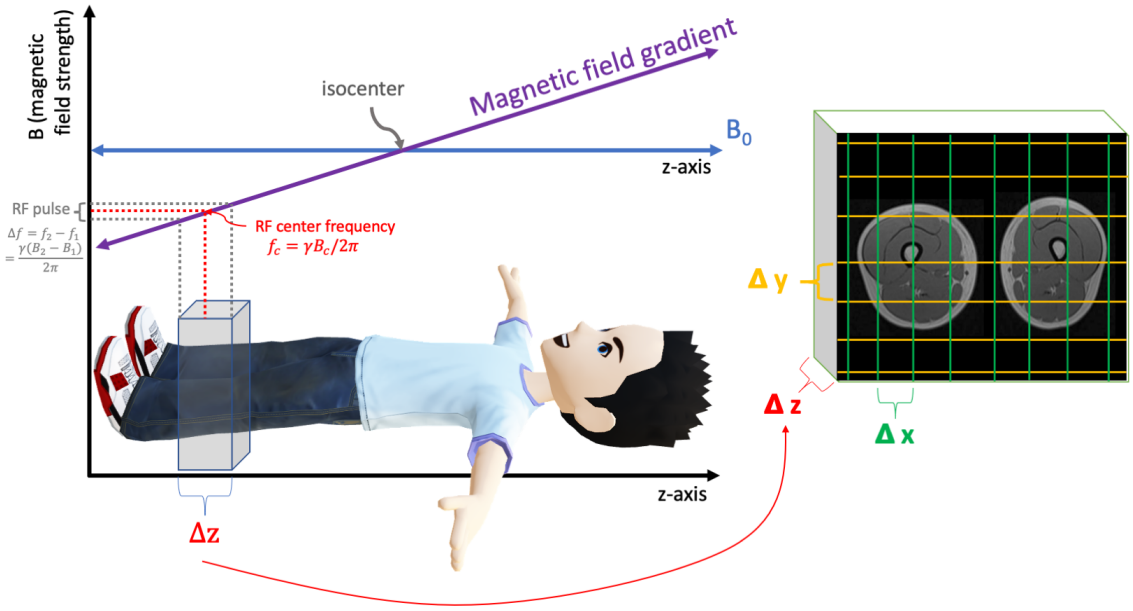

Figure 5.2: A basic illustration of a conventional MRI slice selection method. In standard MRI encoding, a linear gradient of the magnetic field (G_z) is switched on and the slice-selective RF pulse, with specified center frequency and bandwidth, is applied to excite spins in a selected region (Δz). Frequency and phase encoding is carried out within the slice following an excitation pulse. The leg MR image was modified from Zhou et al. (2019) [152] with permission granted under CC-BY 4.0 license.

The applied gradient(s) creates an intentional B_0 inhomogeneity required for slice selection followed by standard MR frequency and phase encoding (Figure 5.2) [47].

5.1.2 B_0 field adjustments (shimming)

Although the constructed Halbach magnet was optimized to produce the most homogeneous B_0 field, it was still not sufficient for 2D TRASE imaging. In theory, since a traditional gradient and selective RF pulse excites a distribution of frequencies, the non-selective (hard) RF pulses used in TRASE with an inhomogeneous B_0 field selects a specific volume of spin frequencies corresponding to the BW of the RF pulses. Since the TRASE uses ~100 μs RF pulses, an approximate range of spin frequencies of ~3 kHz is selected, corresponding to approximately 0.07 mT range in the Halbach magnet's field. The applied single 100 μs hard pulses (20 kHz BW) refocus spins within 3 kHz in a long RF pulse train, corresponding to flip angles between 160° to

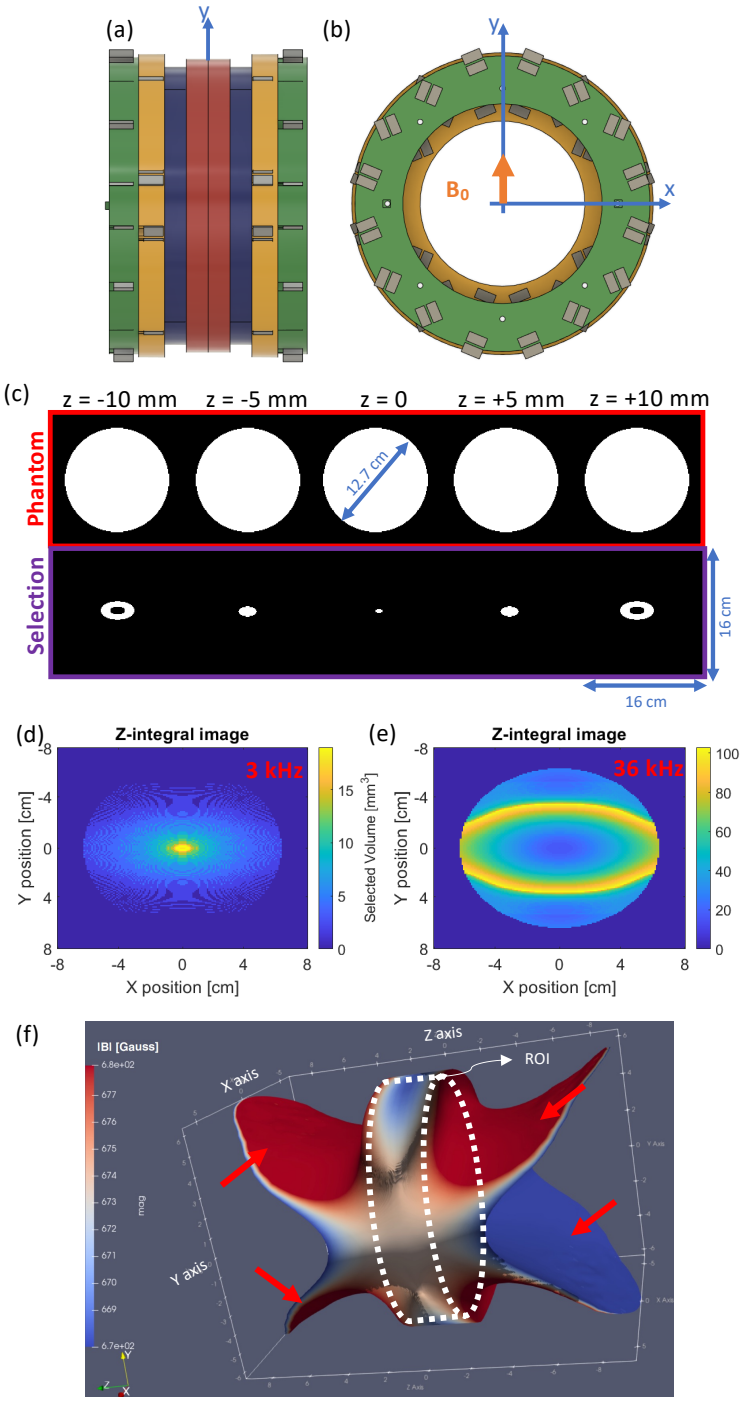

Figure 5.3: The magnetic field produced by the bare Halbach magnet and the volume selection using field inhomogeneities. (a,b) The CAD model of the bare Halbach magnet. (c) The selected sub-volume of a cylindrical phantom (12.7 cm diameter and 18 cm long) assuming a perfect rectangular RF frequency (f = 2.838 ± 0.0015 MHz). (d) A 2D image based on the B_0 inhomogeneity assuming perfect xy-plane encoding (3 kHz BW). (e) A larger RF transmit bandwidth (36 kHz) excites the entire inhomogeneous ROI ($\Delta B_0 = 0.74$ mT). (f) The 3D view of the selected volume for various transmitting frequencies. Volumes outside the ROI (red arrows) are also excited.

200° [74]. Therefore, the 3 kHz RF BW is used to illustrate the volumes selected in the inhomogeneous bare Halbach magnet (Figure 5.3) contributing to the image. Assuming a uniform phantom (12.7 cm diameter and 18 cm long) placed in the bare (unshimmed) Halbach magnet, the volume selected with a 3 kHz BW is shown in Figure 5.3. In these conditions, the simulated 2D MR images ('z-integral image') have artifacts caused by the axial B_0 distribution of the Halbach magnet, shown for two RF bandwidths of 3 kHz (Figure 5.3d) and 36 kHz (Figure 5.3e). The simulated images clearly contain signals from volume selection outside the ROI (red arrows in Figure 5.3f) which alias back into the ROI creating the artifacts (yellow rings in Figure 5.3e). A standard method to overcome B_0 inhomogeneity is to apply active shimming (a wire carrying current distributed on a cylindrical former) that generates a B_0 distribution *opposite* to the B_0 inhomogeneity [153]. With an active shimming approach, the Larmor frequency would be outside of the BW on both sides (along the z-axis) of the ROI removing signal aliasing. Although this method could also provide flexibility with adjusting the field due to drifting caused by the temperature instability of the NdFeB magnets, it requires an additional coil and power supply, reducing bore space, increasing hardware costs, and possibly increasing electromagnetic interference (EMI).

Several groups have improved the field homogeneity or the built-in gradient linearity in a constructed Halbach magnet by adding an array of small-sized ferromagnets (i.e. a shim array) [36, 37, 112, 135]. O'Reilly et al. (2019-2020) used a genetic algorithm to optimize the size and magnetization orientations of each block in the shim array to improve B_0 homogeneity of a constructed Halbach magnet [37, 135]. The homogeneity was improved from ∼13,000 ppm to ∼2,500 ppm, which was sufficient to obtain high-resolution knee and brain MR images [37, 135]. McDaniel et al. (2019) used an interior-point optimization strategy for the shim array to reduce the root mean square residual error of the built-in B_0 gradient linearity (from 0.27 mT to 0.13 mT) in the Halbach magnet [36, 112, 154]. Cooley et al. (2020) obtained

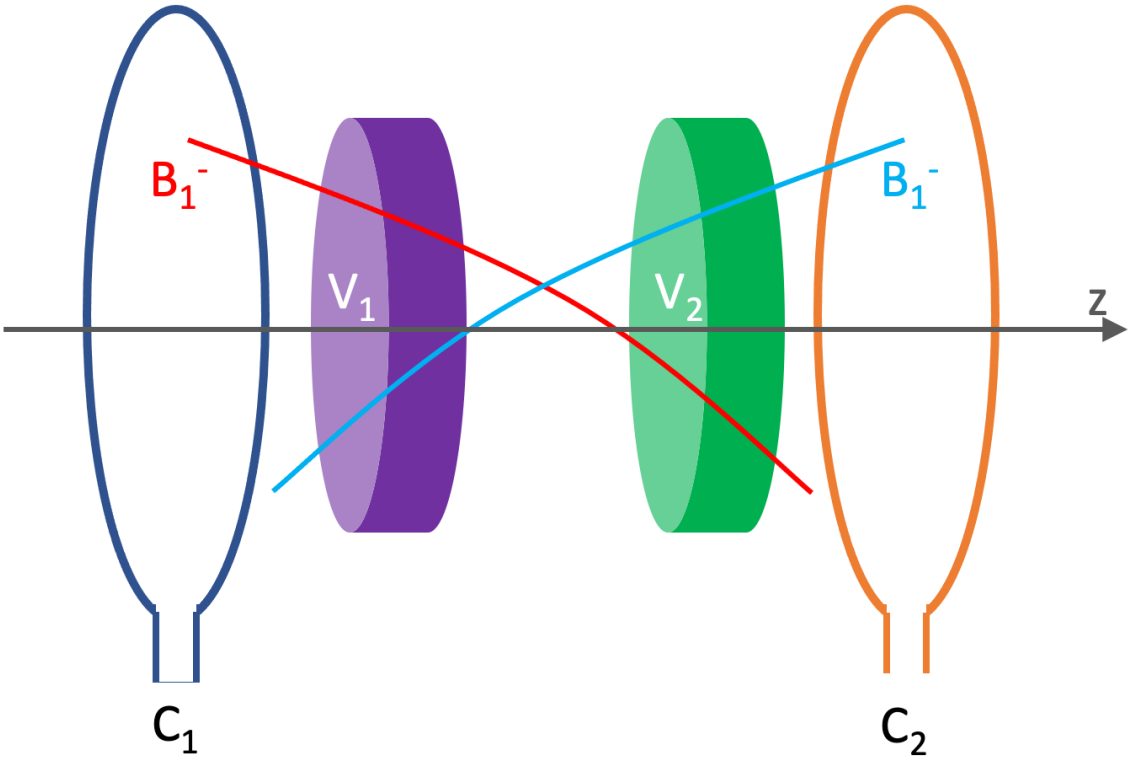

Figure 5.4: An illustration of a two-loop receive coil set to disentangle two axial excited volumes [155]. Each receive coil (C_1, C_2) collects signal from both excited volumes (V_1 and V_2). The sensitivity (B_1^-) of the coils is different for each coil for the corresponding volumes. The receive coils could unwrap V_1 from V_2 volumes into viable 2D TRASE images.

high-resolution 3D adult brain images on the portable MR scanner by adding the shim array to the Halbach magnet [36].

In our work, we aimed to shape the B_0 field in the existing Halbach magnet to create a linear, built-in axial B_0 gradient using an array of small permanent magnets to enable slice-selection (single or multi-slice) 2D TRASE. However, any built-in B_0 gradient always contains some non-linearity, producing unwanted excited volumes outside the cylindrical ROI. One method to address this problem is to develop a multi-channel receive chain to exploit parallel imaging techniques such as sensitivity encoding (SENSE) [10]. For example, Figure 5.4 shows two excited volumes (V_1 and V_2) with two nearby receive loop coils (C_1 and C_2). Each receive coil contains signal from both excited volumes (V_1 and V_2), causing aliasing in 2D TRASE images. Since

the receive coils fields drop off along the z-axis (i.e. $B_1^- \propto \frac{1}{z^3}$), each coil's sensitivity for a specific slice is different. Therefore, a sensitivity encoding matrix could be used to disentangle both axial slices, V_1 and V_2 [155]. Any further discussion of the mathematical proofs and resulting simulations of disentanglement of axial slices applicable to TRASE MRI can be found in the work by Dr. Gordon Sarty (2022) [155].

5.2 Methods of shimming the Halbach magnet

5.2.1 Design of an axial B_0 gradient

A method commonly used to adjust the field of a Halbach magnet is an additional shim array consisting of ferromagnets fixed in place within the bore or external to the magnet. Therefore, to maintain the small external size of the Halbach magnet, we optimized blocks inside the bore. For example, two asymmetric dipole rings (two rings oriented at 180° to each other) may be added to a Halbach magnet to produce an axial B_0 gradient. In Equation 4.1, we assume that each block in the rings is a dipole which is a good first order approximation but neglects effects such as the block shape and demagnetization and their impact on the total magnetic field. The total magnetic field is a superposition of field produced by all the dipoles. By the dipole approximation (ring radius = 16 cm and B_r = 1.2 T for N40UH), the magnetic field strength at the geometric isocenter (B_{center}) was determined as 9.43 mT (Figure 5.5a) by superposition. This was confirmed to be B_{center} = 9.63 mT by finite element simulation using the N40UH B-H curve in Chapter 4. The differences between the field calculations using the dipole approximation and finite element methods are that the analytical approach neglects important ferromagnetic properties such as the shape of the block or demagnetization effects (see Chapter 4). Furthermore, the magnetic field strength reduces by $\sim B_{center} / d^3$ along the central axis (Figure 5.5b) and may be oriented with a second ring to produce an axial gradient (Figure 5.5c). For

both rings separated by 22 cm, the axial gradient strength is estimated at 62 mT/m (dipole approximation) and 70 mT/m (finite element method) over a 1 cm thick region between them. As can be seen from this approach the gradient strength may be adjusted in accordance with changes in the block sizes, locations (ring spacing and diameters) and magnetization orientations. The dipole approximation can be extended to large arrays of small-sized ferromagnets used in the shim array to also improve the homogeneity or axial gradient linearity in a Halbach magnet [37, 113].

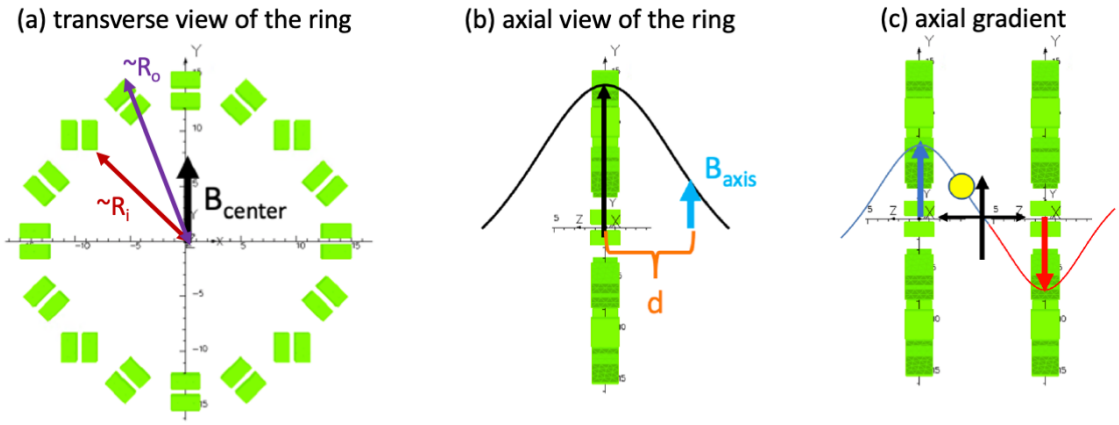

Figure 5.5: An axial gradient is induced in the magnetic field of a Halbach magnet using two asymmetric rings. (a) The transverse view of a dipole Halbach ring consisting of 16 block-pairs with an inner radius of $\sim R_i$ and outer radius of $\sim R_o$. (b) The magnetic field at the center of the ring reduces by $\sim 1/d^3$ (B_{axis}) where d is the distance from the center of the ring. (c) Two dipole rings oriented at 180° to each other induces an axial B_0 gradient (blue and red curves).

5.2.2 Shimming proposal

To make the constructed magnet suitable for 2D TRASE, simulations and optimizations of a shim array should:

1. Maximize the B_0 homogeneity (< 1000 ppm; this number is based on preliminary simulations involving the twisted-solenoid RF coil [74]) in the ROI of 12.7 cm diameter and 1 cm long cylinder and removing volume selection outside the ROI, or

2. Introduce a linear axial B_0 gradient, enabling single (or multi) slice 2D TRASE imaging.

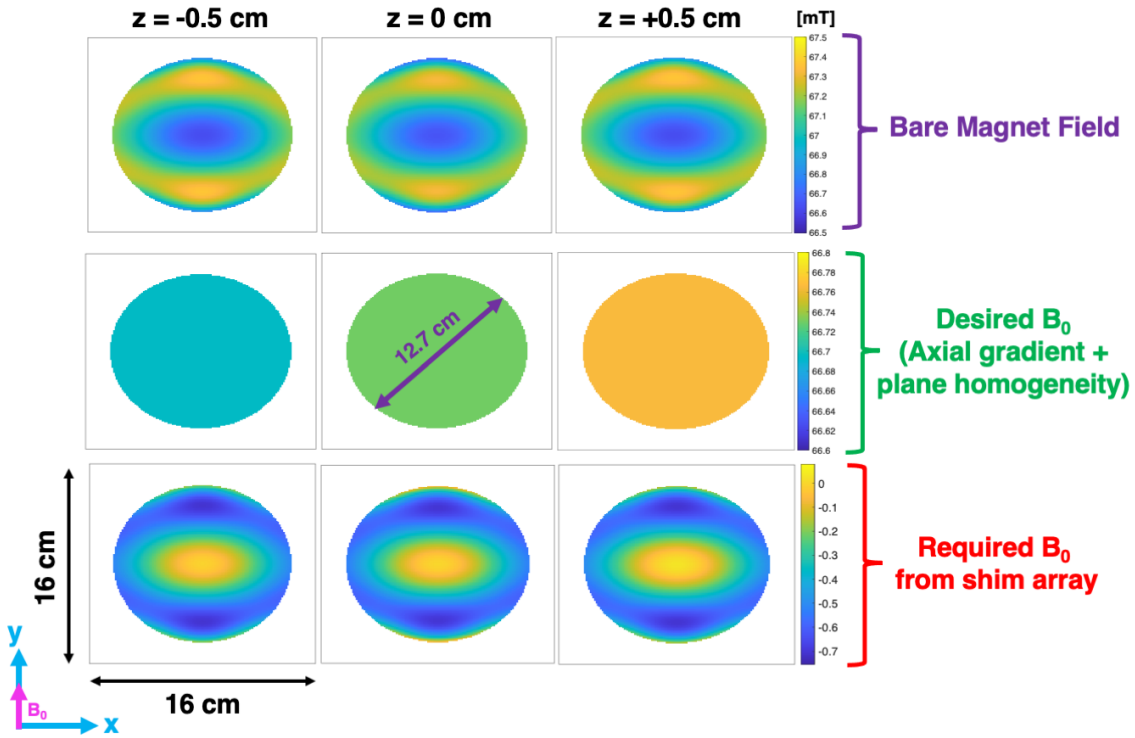

Figure 5.6: The top row shows the simulated magnetic field for the bare Halbach magnet at select xy-planes along the z-axis (z = -5, 0, +5 mm). The center row shows the desired B_0 field at each axial position to generate a perfectly linear axial gradient of 7 mT/m (i.e. a slice thickness of 10 mm for a 3 kHz BW). A homogeneous ROI target aim is also used in some simulations that follow. The target field produced by the shim array (bottom row) is the desired B_0 minus the bare Halbach magnet's field. It shows the field required from a shim array to produce a perfectly linear B_0 gradient over the cylindrical ROI in the bare Halbach magnet.

Reduction of the B_0 inhomogeneity (of the bare magnet) can be accomplished by increasing the length of the magnet array, and in addition, introduction of the axial B_0 gradient is necessary to enable slice-selection for 2D TRASE. We chose to place blocks inside the Halbach magnet's bore since constraints on external size are currently required for the ISS application. Figure 5.5 (top row) shows the bare Halbach magnet's field in select xy-planes over the entire ROI along the z-axis (z = -5 mm, 0 mm, +5 mm). Initially, we aimed at a perfect axial gradient of 7 mT/m

(middle row in Figure 5.5) as this would provide a single ∼10 mm thick axial slice, assuming sufficient signal for 2D TRASE imaging and 3 kHz BW pulse. However, the choice of axial gradient strength should be part of the optimization process to provide flexibility at targeting out-of-ROI excitation issues and allowing multi-slice imaging over the ROI. A summary is shown below (Table 5.1) of six methods that may improve B_0 homogeneity (two methods) or the axial gradient strength and linearity (four methods).

5.2.3 Initial shim geometry

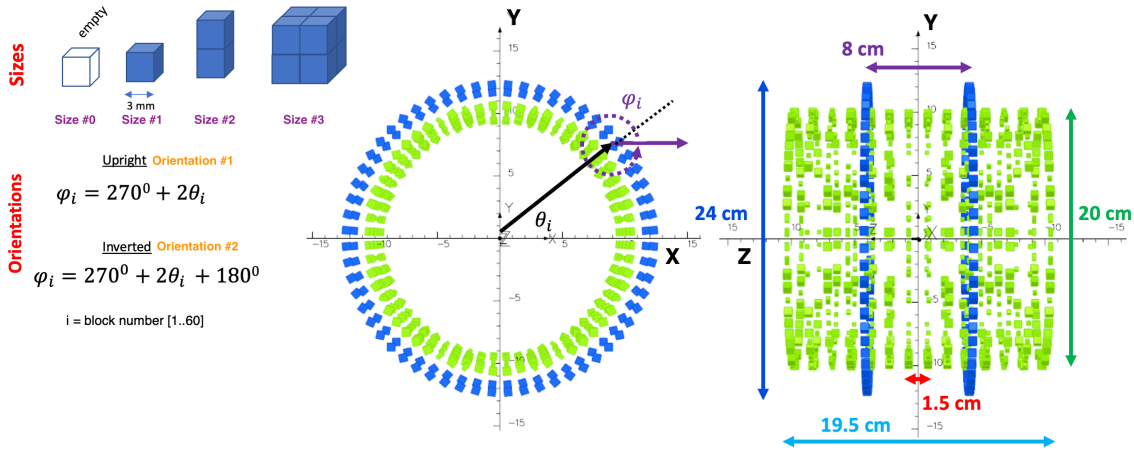

Figure 5.7: The initial shim geometry used as input to the optimization process (note: the bare Halbach magnet is not shown; the shim array presented here is inside the magnet). The shim array consists of small ferromagnetic blocks (3 mm cube) at fixed locations on a cylindrical grid (green). The blocks size and magnetization orientations are optimized to produce either a homogeneous B_0 or a linear axial B_0 gradient inside the bare Halbach magnet. Two additional dipolar Halbach rings rotated 180° to each other (blue blocks), are added to induce an axial B_0 gradient. The block sizes and axial position of the gradient rings impact the induced axial gradient strength and the B_0 distribution over the ROI. The GA chooses from four possible sizes and two possible magnetization orientations to maximize the B_0 homogeneity or axial gradient strength and linearity.

The initial shimming geometry, before optimization, is shown in Figure 5.7 and shown in other research to be an effective approach to improving the homogeneity in

Table 5.1: Summary of the B_0 shimming designs used for the Halbach magnet.

Number	**Objective**	**Description**
Design #1	B_0 homogeneity	8 rings 10.5 cm long 60 block locations per ring optimized blocks sizes and orientations
Design #2	B_0 homogeneity	14 rings 19.5 cm long 60 block locations per ring optimized blocks sizes and orientations
Design #3	Axial B_0 gradient strength	rotated end-ring of bare Halbach magnet
Design #4	Axial B_0 gradient strength	two asymmetric dipole rings 60 blocks per ring 8 cm spacing optimized block sizes
Design #5	Axial B_0 gradient strength	14 rings 19.5 cm long 60 block locations per ring optimized blocks sizes and orientations
Design #6	Axial B_0 gradient strength and linearity	two asymmetric rings (for gradient strength) 14 rings on 20 cm sleeve (for gradient linearity) 60 block locations per ring sleeve: block size and orientation asym. rings: size only

various Halbach magnets [37, 156]. A cylindrical grid fills the *unused* bore space of the constructed Halbach magnet (> 19 cm inner diameter) with small ferromagnetic blocks. There are 840 possible block locations in the shim sleeve (for B_0 homogeneity or axial gradient linearity) and 120 possible locations for two asymmetric dipolar Halbach gradient rings (for axial gradient strength). Similar to O'Reilly et al.'s (2019) shim sleeve design, we used a diameter of 20 cm for the shim sleeve (green blocks in Figure 5.7), and its length varies from 10.5 cm to 19.5 cm depending on the design approach [37]. Each ring in the shim sleeve consists of 60 blocks, axially spaced by 1.5 cm [37]. For shimming designs containing dual asymmetric gradient rings, the blocks (blue blocks in Figure 5.7) are distributed on two 24 cm diameter rings, separated by 8 cm, and comprise 60 block locations per ring. The dimensions of the gradient rings were chosen based on preliminary field simulations.

5.2.4 Optimization parameters

The blocks sizes and orientations were optimized using a discrete genetic algorithm. At each grid location (Figure 5.7), the optimization process chooses from four possible block sizes (size #0 = empty, size #1 = 3 mm × 3 mm × 3 mm, size #2 = 3 mm × 3 mm × 6 mm, or size #3 = 6 mm × 6 mm × 6 mm). If the optimal block is determined to be size #2, it is assumed to be magnetized along its long axis (i.e. the 6 mm axis). Since smaller than 3 mm × 3 mm × 3 mm neodymium ferromagnets cannot be easily fabricated and their price is low when purchased in bulk (∼ $150USD for 1000 N40UH blocks [138]), the optimization process considered an array of smallest-sized blocks. Block of larger sizes may be constructed by gluing blocks together or their custom-sizes manufactured for an additional ∼$100USD. In addition, if a block location is determined as non-empty, the optimization process selects an upright (Orientation #1) or inverted (Orientation #2) dipole contribution to the array (Figure 5.7). Recent research has found this choice of the magnetization orientation allowed more than 5-fold improvements in B_0 homogeneity in a constructed Halbach magnet [37, 135].

Considering the option of the application of gradient rings, one ring is rotated by 180^0 in relation to the other; therefore, we did not optimize the individual magnetization directions for these blocks but their sizes only.

5.2.5 Optimization procedure

The optimization method is based on the same technique that was used to design the bare Halbach magnet (Figure 4.21 in Chapter 4) with the following major differences. Generally, a database was generated using the finite element method (FEM) prior to optimization to contain field maps over the ROI of all individual blocks sizes, locations and orientations. Based on any possible request by the genetic algorithm (GA), the database is quickly called to generate the simulated field map for the full array of blocks by superposition. In addition, we expand the penalty function, used previously in the Halbach magnet design, to consider a linear axial B_0 gradient over the ROI.

1. Unlike in the magnet design, the **initial configuration** input into the optimization flow depends on whether a homogeneous or axial gradient target field in the ROI is desired. Therefore, the initial configuration consists of a shim sleeve, dual asymmetric rings or a combination of both to achieve the desired target field.

2. The **fitness/penalty function** (F_{min}) used in the GA optimization has two possible configurations depending on the optimization of the B_0 homogeneity or the axial gradient strength and linearity:

   - Type 1: B_0 homogeneity is maximized by minimizing the peak-to-peak B_0 over the ROI.

     $$F_{min} = \Delta B = B_{max}^{ROI} - B_{min}^{ROI} \tag{5.1}$$

     where B_{max}^{ROI} and B_{min}^{ROI} are the maximum and minimum simulated field strength, respectively, within the ROI.

- Type 2: An axial gradient strength with maximum linearity is achieved by using the penalty function:

$$F_{min} = \Delta B_{-0.5cm} + \Delta B_{0cm} + \Delta B_{+0.5cm} + \alpha\left||G_z^{iso}| - G_{aim}\right| + \beta\epsilon \quad (5.2)$$

where $\Delta B_{-0.5cm}$, ΔB_{0cm}, and $\Delta B_{+0.5cm}$ [G] are peak-to-peak homogeneities calculated within three axial planes of the ROI (i.e., z = -0.5 cm, 0 cm, +0.5 cm) consisting of the superposition of fields from the shim array and the bare Halbach magnet; G_z^{iso} is the calculated axial gradient using 100 simulated field points along the z-axis from -0.5 cm to +0.5 cm; G_{aim} is the desired axial gradient strength (0.7 or 2.0 used in this work) [G/cm]; ϵ is the standard fitting error of the G_z^{iso} calculation; and, α and β are weighting factors (10 and 100, respectively) so each term in Equation 5.2 begins with an equal contribution to F_{min}. The weighting factors were determined from the penalty function evaluated using the bare Halbach magnet's field with no shim array.

3. The **FEM** was used to simulate the field in each xy-plane (i.e. for z = -0.5 cm, 0 cm, +0.5 cm) for all individual block locations, sizes and orientations. The simulated fields for every block configuration was stored in a database (.mat file) and called upon during the optimization process rather than solving the full model by FEM for each fitness/penalty function evaluation which is time-consuming. FEM was also used to generate field maps produced by the bare Halbach magnet in each xy-plane. This approach significantly improves optimization time (350× faster than using FEM directly) and requires low data storage ($\sim$ 370MB per database) [113]. For each block orientation, size, and location, each xy-plane map contains 10,000 simulated magnetic field points (polar plots consisting of 100 angular divisions × 100 radial segmentations over a 12.7 cm diameter area). After the optimization process is finished, the best performing shim array and the bare Halbach magnet were simulated together

as a single model using the FEM prior to analysis of the magnetic fields.

4. The GA **parameters** were modified. Similarly to others [37, 113], we have found that generating enough individuals per generation leads to a higher genetic diversity and highest performance designs yet an increase number of individuals per generation slows down optimization. Based similarly on other shim arrays, optimized by the GA, we used 1000 individuals per generation and 350 generations for each run of the GA optimization. These numbers provide a compromise between the slow process of generating enough individuals per generation to produce high genetic diversity yet fast enough to finish optimization within one day using a Titan S522 Intel Xeon 4210 2.2 GHz (3.2 Turbo) computer. The GA was also programmed to stop if 50 successive generations occurred without any individuals with fitness improvement ('stall generations'). The GA creates 'children' by combining the genes of 'parents' by crossover (combines vector entries of a pair of parents) or mutation (random changes to a single parent). All individuals within each population are evaluated for fitness and selected for 'reproduction' based on their fitness value. The children then form the next generation and the process repeats. There are also 'elite' individuals which have the highest fitness values and survive to the next generation. For shim array optimizations demonstrated here, it was found that the best performing results occurred using the following in the GA optimization process:

   (a) A uniform creation function where the initial population is created randomly with a uniform distribution.

   (b) A scattered crossover function where the crossover occurs at scattered location(s) in the parent genes.

   (c) A stochastic uniform selection process where parent fitness values are scaled and distributed along a line with size proportional to the scaled fitness values. The parents are selected at uniform spacing along the line,

and

(d) A Gaussian mutation function where a random number is generated from a Gaussian distribution (with mean = 0) and added to each entry of the parent vector.

These functions are built into the GA package in Matlab.

5.3 Results

Since the shim array approach was shown highly effective to adjust the B_0 field in Halbach magnet's [38, 154], we applied this shim array method to improve B_0 homogeneity and, separately, to implement a linear axial gradient in the constructed Halbach magnet (see Figure 5.7).

5.3.1 Homogeneity improvement

As a first approach to B_0 shimming, we investigated the relationship between the shim sleeve length and the B_0 homogeneity within the ROI. The peak-to-peak B_0 homogeneity in the ROI was calculated as per Equation 5.1. We have considered both a short sleeve (Design #1) and a long sleeve (Design #2).

Design 1: short shim sleeve

The result of a GA optimization for a short-length shim sleeve is presented in Figure 5.8a-c. The initial shim sleeve consists of 480 block locations (8 rings $\times$ 60 blocks per ring), and each ring is separated by 1.5 cm. The best performing shim geometry, determined by GA, consists of 140 empty locations, 128 blocks of 3 mm $\times$ 3 mm $\times$ 3 mm (size #1), 108 blocks of 3 mm $\times$ 3 mm $\times$ 6 mm (size #2), and 104 blocks of size 3 mm $\times$ 3 mm $\times$ 3 mm (size #3). The final array contains 228 blocks in the upright orientations; 252 blocks in the inverted orientation.

Based on simulations, when the optimized short-length shim array was placed inside the bare Halbach magnet, the peak-to-peak B_0 homogeneity is improved by

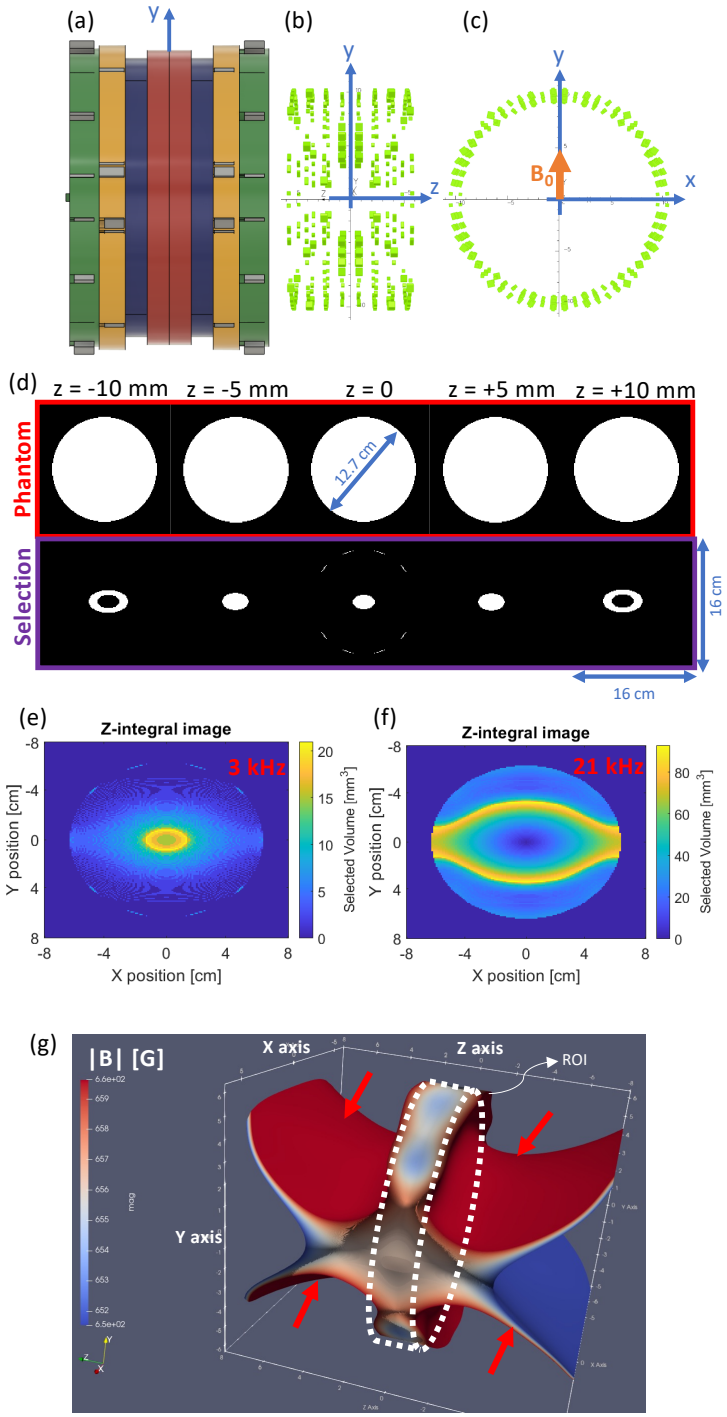

Figure 5.8: Design #1: A first approach to improve B_0 homogeneity within the ROI. The bare magnet (a) and the optimized shim array (b,c) were simulated simultaneously using the finite element method. (d) A selected 3D sub-volume, split into 2D planes at z = - 10 mm, -5 mm, 0 mm, +5 mm, and +10 mm, of a cylindrical phantom of 12.7 cm diameter and 18 cm length using a perfectly selective RF pulse with a frequency f = 2.7860 ± 0.0015 MHz. A simulated 2D image produced by a BW of (e) 3 kHz and (f) 28.2 kHz RF pulse. (g) The 3D excitation volume using a 28.2 kHz RF bandwidth pulse. Excited volume outside the ROI is still present (red arrows).

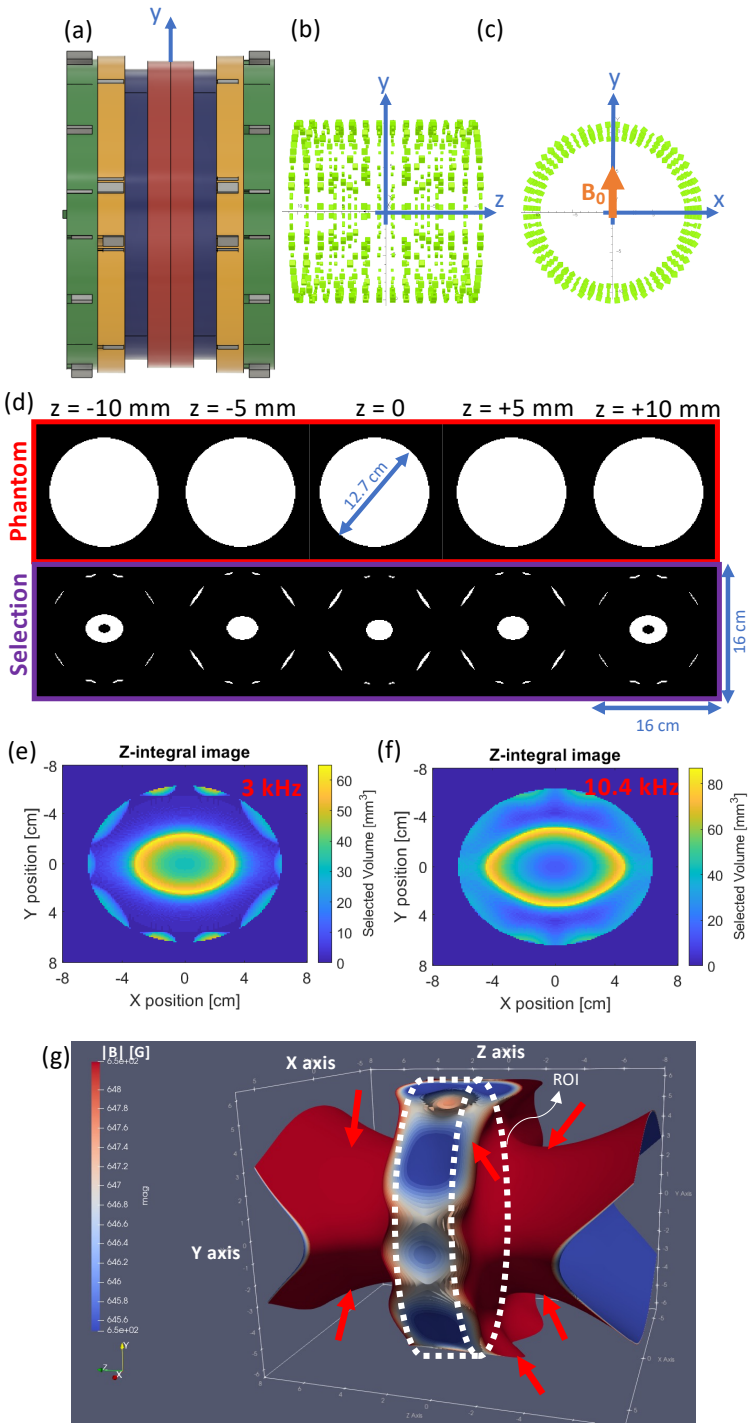

Figure 5.9: Design #2: A longer shim sleeve compared to Design #1. (a) The bare magnet model. A longer shim sleeve (b,c) was optimized in the field of the bare magnet for maximum field homogeneity. (d) A selected 3D sub-volume, split into 2D planes at z = - 10 mm, -5 mm, 0 mm, +5 mm, and +10 mm, of a cylindrical phantom of 12.7 cm diameter and 18 cm length using a perfectly selective RF pulse with a frequency f = 2.7480 ± 0.0015 MHz. A simulated 2D image produced by a BW of (e) 3 kHz and (f) 10.4 kHz RF pulse. (g) The 3D excitation volume using a 10.4 kHz RF bandwidth pulse. Excited volume outside the ROI is still present (red arrows).

$\sim$20% ($\Delta B_0 = 0.74$ mT $\rightarrow$ 0.58 mT), leading to broader excitation regions in a 3 kHz BW (Figure 5.8d). The field homogeneity improvement provides an opportunity to excite the entire ROI with a slightly smaller RF bandwidth (28.2 kHz) compared to the bare Halbach magnet (36 kHz) (Figure 5.3e-f). Although the B_0 homogeneity was improved, the excited volumes outside the ROI are still similar to the bare Halbach magnet (see red arrows in Figure 5.8g).

Design 2: long shim sleeve

The short length (aspect ratio $\sim$ 1:2) of the shim sleeve provided by Design #1 (Figure 5.8) is insufficient to significantly improve the strong inhomogeneity produced by the bare Halbach magnet. Therefore, we doubled the length (aspect ratio $\sim$ 1:1) of the shim array and re-optimized the shim using the GA. The optimized long shim sleeve is shown in Figure 5.9a-c. The initial shim geometry now consists of 14 rings, each separated by 1.5 cm (total length is 19.5 cm). The final shim array, determined by GA, consists of 160 empty locations, 208 blocks (size #1), 184 blocks (size #2) and 288 blocks (size #3). The final array contains 376 blocks in the upright orientation; 464 blocks in the inverted direction.

When the shim array is placed inside the bare Halbach magnet, the B_0 homogeneity is improved by $\sim$64% ($\Delta B_0 = 0.74$ mT $\rightarrow$ 0.27 mT) leading to larger excited volumes using a 3 kHz BW RF pulse (Figure 5.9d,e). An RF pulse BW of 10.5 kHz would be required to excite the entire ROI (Figure 5.9f,g), which is much smaller than the short shim array (21 kHz for Design # 1 in Figure 5.8) and the bare Halbach magnet (36 kHz in Figure 5.3). Nevertheless, excited volumes are still present outside the ROI for the 10.5 kHz BW (see red arrows in Figure 5.9g).

5.3.2 Introduction of an axial B_0 gradient to the bare Halbach magnet

As explained earlier, the B_0 field produced by the bare Halbach magnet is impractical for TRASE MRI mostly due to the axial distribution of the field. Furthermore,

targeting the B_0 homogeneity alone was found insufficient in simulations for slice-selective 2D TRASE, as shown by the sleeve designs in Section 5.3.1, since volume is also selected outside the ROI. Therefore, an axial field asymmetry could reduce the effect of out-of-ROI volume excitation and allow multi-slice 2D TRASE MRI. Thus, an axial B_0 gradient was added using various methods such as reconfiguring the bare Halbach magnet (Design #3), adding two asymmetric dipole rings (Design #4), using a shim sleeve to generate the axial gradient (Design #5) and a combination of a shim sleeve with two asymmetric rings (Design #6).

Design 3: rotated end ring

An axial gradient may be introduced by rotating the end ring of the bare Halbach magnet. The resulting field is shown in Figure 5.10. Implementing an axial B_0 gradient using this method makes the excited volumes inside the ROI more uniform, even for smaller RF pulse bandwidths (Figure 5.10c,d). In this configuration, the signal spreads out more uniformly over a central xy-plane ($z = 0$) than in the previous designs (Figure 5.9c,d). Unfortunately, a strong axial gradient is induced ($\sim$ 70 mT/m) at the geometric isocenter, severely reducing the slice thickness ($\Delta z \sim 1$ mm for a 3 kHz RF BW). Furthermore, the slice thickness is very thin near the ROI periphery ($\sim$0.5 mm), and therefore, total NMR signal is expected to be low for a 3 kHz BW.

Design 4: additional asymmetric dipole rings

The strong axial gradient presented in Design #3 (Figure 5.10) selects thin slices. Therefore, two weaker asymmetric dipole rings were added to the bare Halbach magnet (Figure 5.11). The two rings were optimized solely for block size with fixed separation (8 cm). The best performing GA-optimized configuration consists of 0.6 cm $\times$ 0.6 cm $\times$ 0.6 cm blocks, achieving an axial gradient of 20 mT/m ($\sim$3 mm slice thickness for 3 kHz BW) at the geometric isocenter. Axial gradient non-linearity is

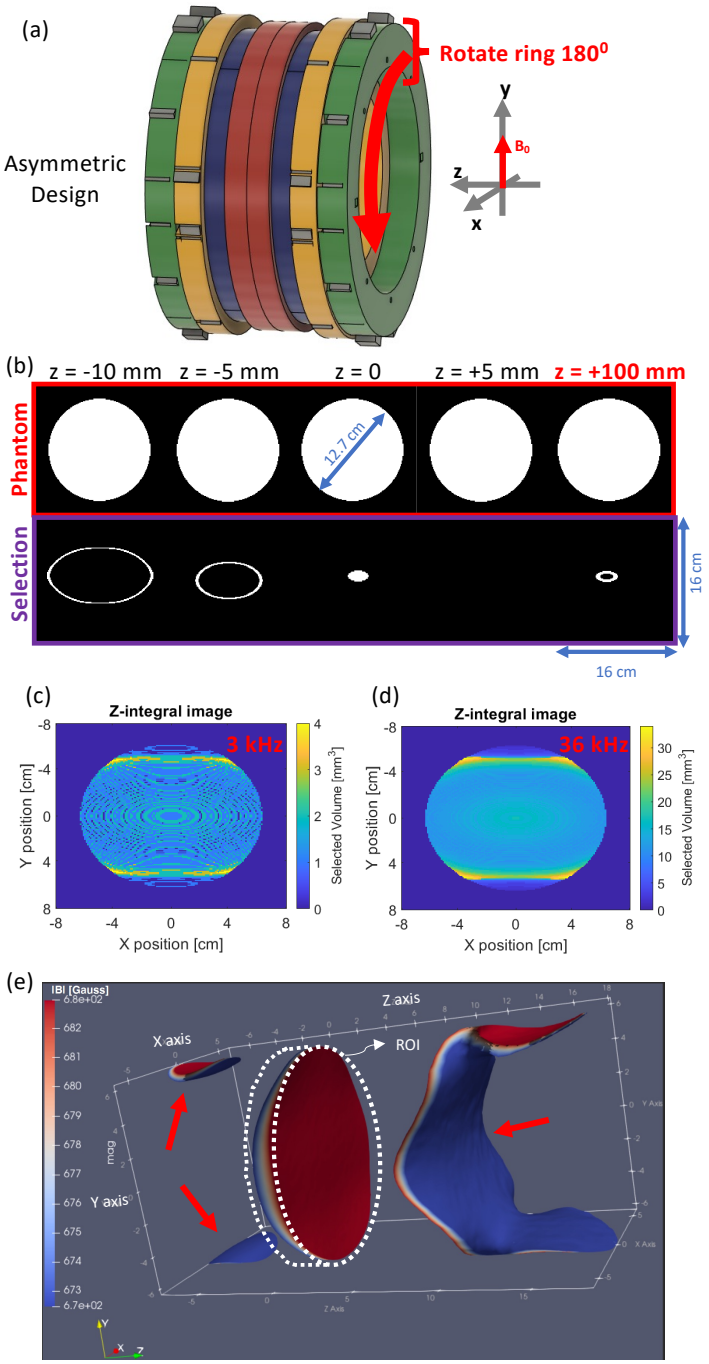

Figure 5.10: Design #3: Rotation of the end ring in the bare Halbach magnet. (a) An axial B_0 gradient is produced by rotation of the original Halbach magnet's end-ring by 180°. (b) A selected 3D sub-volume, split into 2D planes at z = - 10 mm, -5 mm, 0 mm, +5 mm, and +100 mm, of a cylindrical phantom of 12.7 cm diameter and 18 cm length using a perfectly selective RF pulse with a frequency f = 2.5800 ± 0.0015 MHz. A simulated 2D image produced by a BW of (c) 3 kHz and (d) 36 kHz RF pulse. (g) The 3D excitation volume using a 36 kHz RF bandwidth pulse. For a 3 kHz BW, slice thickness at the geometric isocenter is ∼0.98±0.01 mm and is reduced to ∼0.5 mm near the ROI periphery (in y-direction). Excited volume outside the ROI is still present (red arrows).

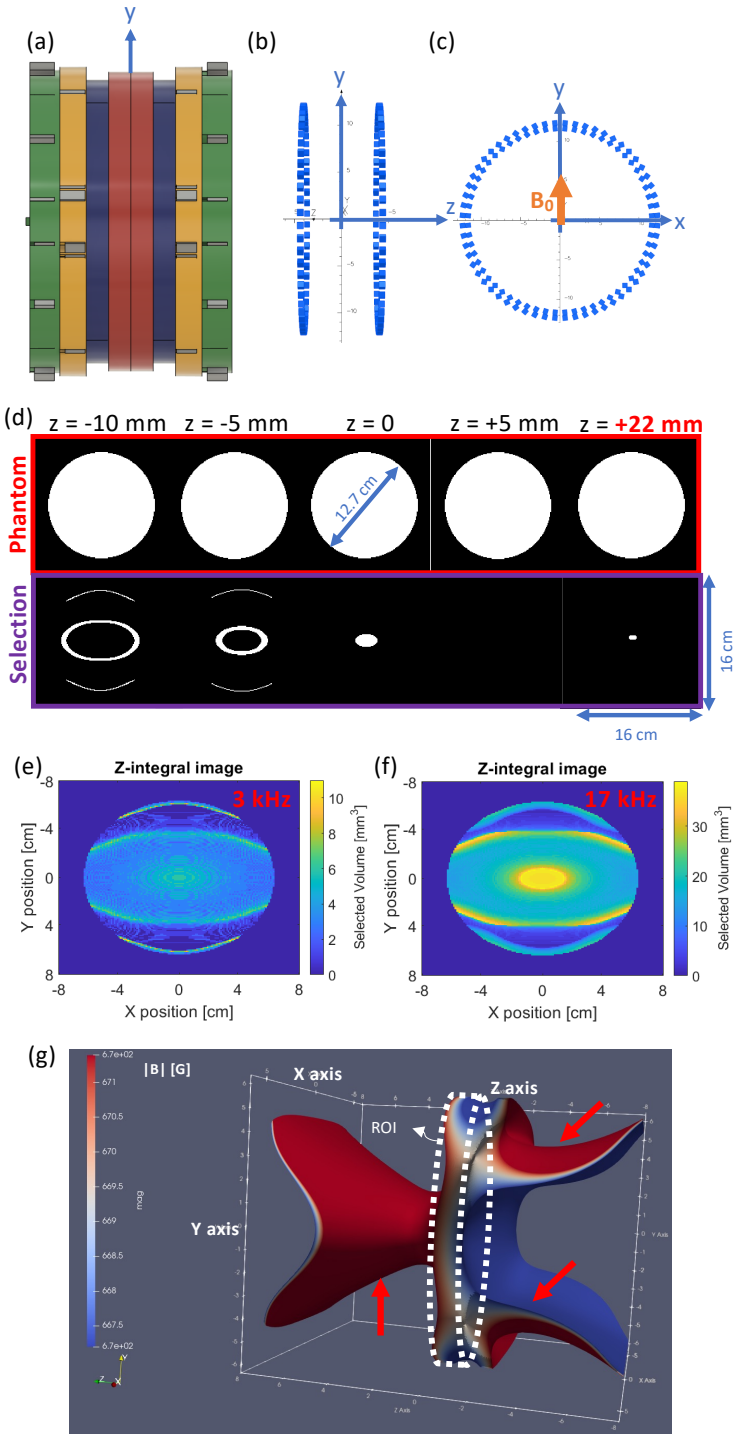

Figure 5.11: Design #4: Two thin asymmetric dipole rings generating an axial B_0 gradient in the bare Halbach magnet. (a) The bare magnet and (b,c) the asymmetric ring models are combined. (d) A selected 3D sub-volume, split into 2D planes at z = - 10 mm, -5 mm, 0 mm, +5 mm, and +22 mm, of a cylindrical phantom of 12.7 cm diameter and 18 cm length using a perfectly selective RF pulse with a frequency f = 2.8410 ± 0.0015 MHz. A simulated 2D image produced by a BW of (e) 3 kHz and (f) 17 kHz RF pulse. (g) The 3D excitation volume using a 17 kHz RF bandwidth pulse. Excited volume outside the ROI is still present (red arrows).

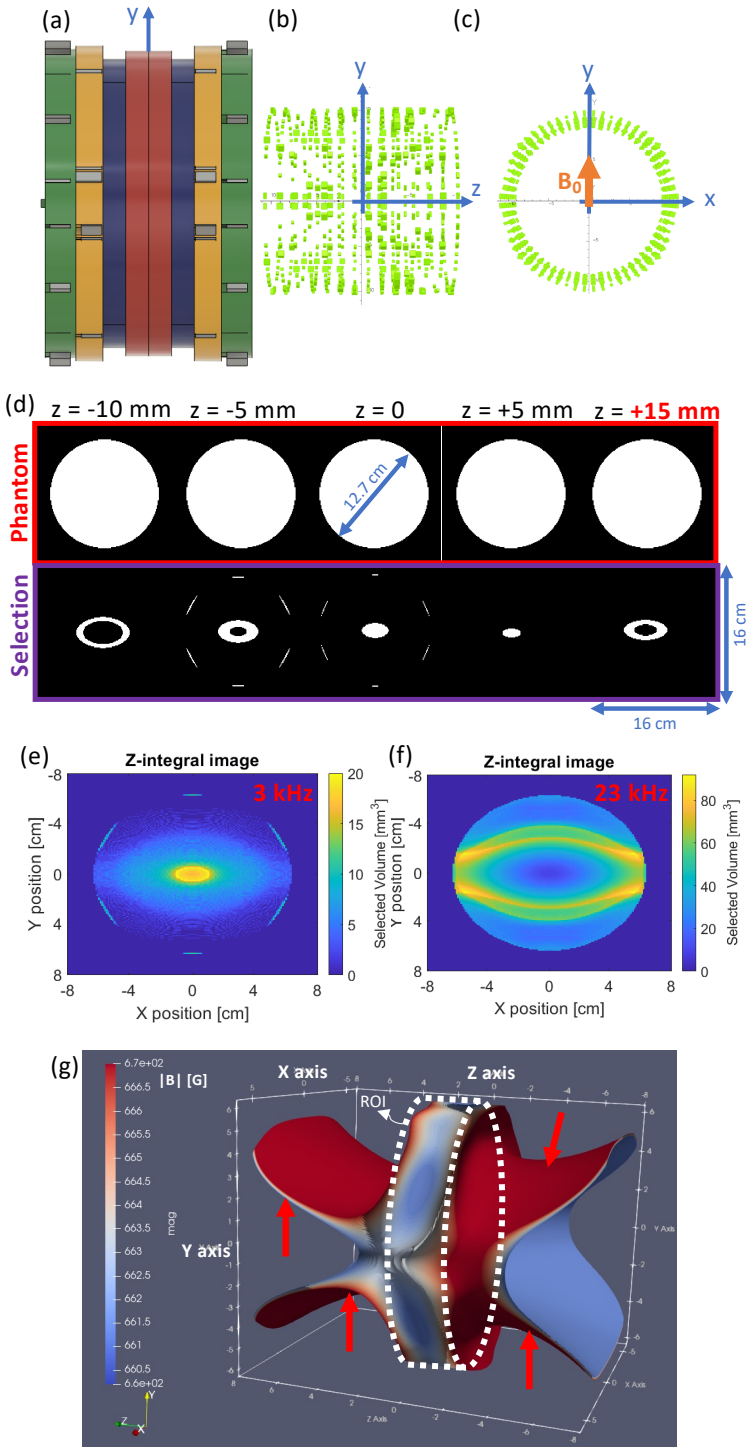

Figure 5.12: Design #5: A shim array producing an axial gradient inside the bare Halbach magnet. (a) The bare magnet model and the (b,c) optimized shim sleeve. (d) A selected 3D sub-volume, split into 2D planes at z = - 10 mm, -5 mm, 0 mm, +5 mm, and +15 mm, of a cylindrical phantom of 12.7 cm diameter and 18 cm length using a perfectly selective RF pulse with a frequency f = 2.8160 ± 0.0015 MHz. A simulated 2D image produced by a BW of (e) 3 kHz and (f) 23 kHz RF pulse. (g) The 3D excitation volume using a 23 kHz RF bandwidth pulse. Excited volume outside the ROI is still present (red arrows).

apparent due to the shape of the central excited volumes at higher RF center frequencies (Figure 5.11e-g) which, as a consequence, reduces the slice thickness to ∼1.5 mm near the edges of the ROI. Nevertheless, axial asymmetry in the B_0 field volume selection was achieved.

Design 5: weak axial gradient produced by a shim sleeve

The shim sleeve was optimized using GA to adjust the field of the bare Halbach magnet's field aiming at a linear axial B_0 gradient of 7 mT/m (Figure 5.12). The same geometry of the shim sleeve as in Design #2 (Figure 5.9) was used in this design, except the axial (z-axis) symmetry was removed during the GA optimization process. The shim sleeve consists of 840 block locations (14 rings × 60 blocks per ring), and each ring is separated by 1.5 cm. The best performing shim geometry, determined by GA, consists of 228 empty locations, 208 blocks of size #1, 252 blocks of size #2 and 152 blocks of size #3. The final array contains 404 blocks in the upright orientation; 436 blocks in the inverted direction (Figure 5.12a-c) and achieves a 7 mT/m axial gradient at the geometric isocenter of the Halbach magnet. Unfortunately, due to the nonlinearity of the axial gradient, a large RF bandwidth (∼36 kHz) is required for the ROI volume selection and, unfortunately, out-of-volume excitation remains present.

Design 6: mid-strength axial gradient

Since the long shim sleeve produced an improvement in B_0 homogeneity and the dual asymmetric rings produced an axial gradient, we decided to combine both into a single shim array to improve the axial gradient linearity and strength (Figure 5.13b,c). The optimization process used the same fixed block locations as the previous asymmetric rings (Figure 5.11) and shim sleeve (Figure 5.9). The shim sleeve blocks were optimized for block size and orientation; however, the asymmetric rings were optimized only for block size with no empty option. The shim array consists of 840 block locations (14 rings × 60 blocks per ring), and each ring is separated by 1.5

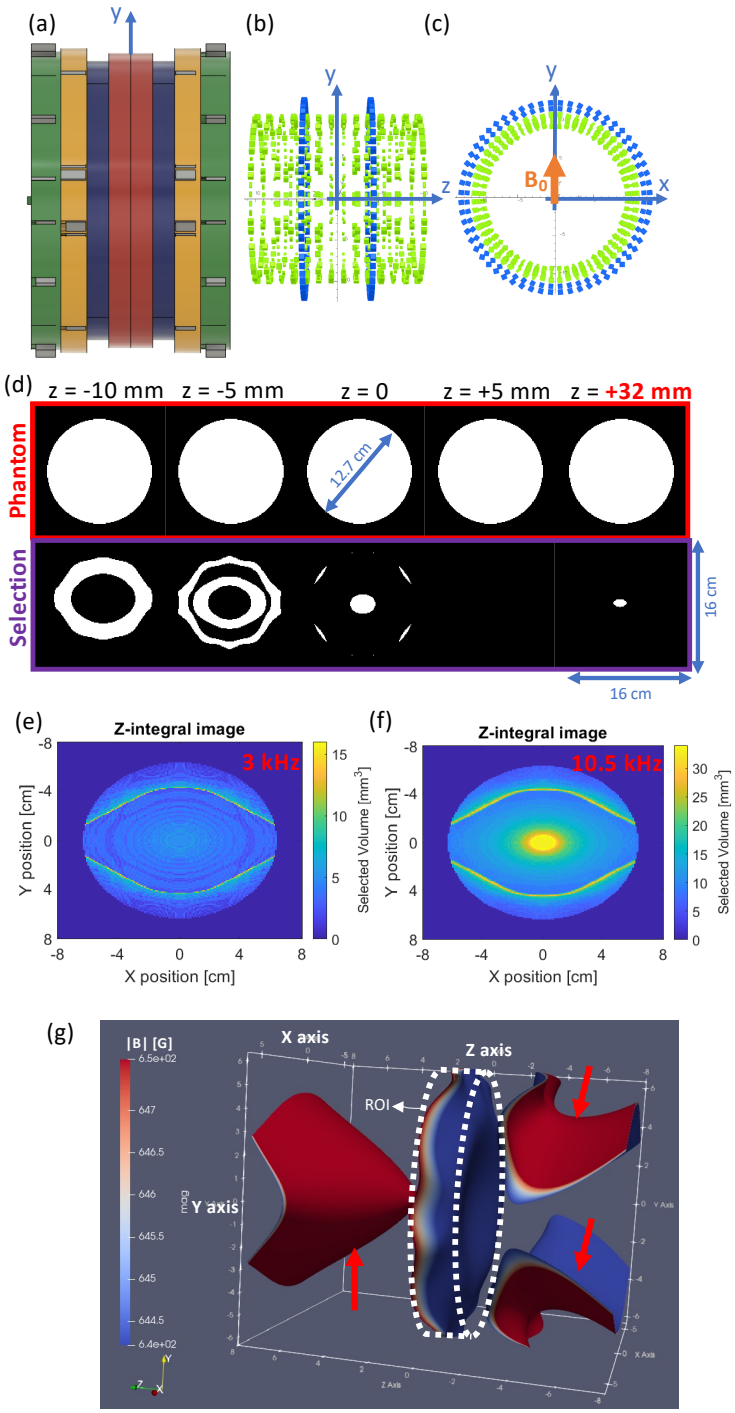

Figure 5.13: Design #6: An optimized shim sleeve and dual asymmetric rings. (a) The bare magnet model and the (b,c) optimized shim sleeve and asymmetric rings. (d) A selected 3D sub-volume, split into 2D planes at z = - 10 mm, -5 mm, 0 mm, +5 mm, and +15 mm, of a cylindrical phantom of 12.7 cm diameter and 18 cm length using a perfectly selective RF pulse with a frequency f = 2.7480 ± 0.0015 MHz. A simulated 2D image produced by a BW of (e) 3 kHz and (f) 10.5 kHz RF pulse. (g) The 3D excitation volume using a 10.5 kHz RF bandwidth pulse. Excited volume outside the ROI is still present, but separated (red arrows).

cm. The best performing shim geometry, determined by GA, consists of 216 empty locations, 256 blocks of size #1, 204 blocks of size #2 and 164 blocks of size #3 (Figure 5.13b,c). The final array contains 384 blocks in the upright orientation; 456 blocks in the inverted direction. The final gradient rings consist of 6 mm × 6 mm × 6 mm blocks.

The final shim design based on the GA optimization is shown in Figure 5.13b,c. Based on a uniform phantom as per previous designs (Designs # 1-5), selection volumes in 3 kHz and 10.5 kHz BW pulses are also shown (Figure 5.13d-f). Compared to Design # 3 (Figure 5.10), thicker slices are achieved (∼3 mm for 3 kHz RF pulse BW) since we aimed for a weaker axial gradient (20 mT/m). In addition, increased uniformity of selected sub-regions over the ROI is shown (Figure 5.12g) compared to the previous weaker axial gradient designs (Figure 5.12). Interestingly, the excited volumes outside the ROI are physically separated from the ROI for a range of RF frequencies.

5.4 Discussion

We presented six potential methods to adjust the magnetic field of the constructed Halbach magnet (Chapter 4) for improved homogeneity (Table 5.2) or axial encoding (Table 5.3). Each shim array design would be simple and cheap (<$400 CAD for magnets+PLA) to produce using custom 3D printing of formers. Nevertheless, the preliminary simulation and optimization results found that the shim array length and B_0 axial gradient strength will impact the field with various advantages and disadvantages using the TRASE MRI technique.

Initially, we investigated the impact of the shim sleeve length on B_0 inhomogeneity in the ROI of 12.7 cm diameter and 1 cm long. By extending the shim array length to 19.5 cm (14 rings instead of 8 rings), we found that the peak-to-peak B_0 inhomogeneity of the magnetic field within the ROI had improved by 64% (see Design #2 in Figure 5.9) when compared to the bare Halbach magnet instead of only 20% in

Table 5.2: Summary of the results for B_0 homogeneity improvement. All specifications calculated within the 12.7 cm diameter and 1 cm thick ROI. Volume is excited outside of the ROI in all designs.

Number	**Specification**	**Advantages**	**Disadvantages**
Bare Halbach Magnet	Homogeneity = 11,151 ppm (36 kHz)	N/A	N/A
Design #1	8740 ppm (20% improvement)	reduced excitation BW (28 kHz)	minor improvement out-of-ROI selection
Design #2	4069 ppm (64% improvement)	only 10.4 kHz RF bandwidth needed	out-of-ROI selection

Table 5.3: Summary of the results for a shim array producing an axial B_0 gradient. All specifications calculated within the 12.7 cm diameter and 1 cm thick ROI. Volume is excited outside of the ROI for all shim array designs but they are disconnected when introducing an axial gradient (>20 mT/m).

Number	**Aim**	**Advantages**	**Disadvantages**
Design #3	70 mT/m	uniform volume selection (3 kHz) out-of-ROI selection separated from ROI no construction required	1 mm thin slices (3 kHz) ~30 kHz selection for entire ROI out-of-ROI selection
Design #4	20 mT/m	3.5 mm slice selection (3 kHz)	out-of-ROI volume selection ~20 kHz selection for entire ROI
Design #5	7 mT/m	thick slice selection	highly non-uniform slice selection (3 kHz) out-of-ROI selection 36 kHz selection for entire ROI
Design #6	20 mT/m & highest linearity	3 mm slice selection (3 kHz) out-of-ROI selection separated from ROI	non-uniform slice selection (3 kHz) ~20 kHz selection for entire ROI

Design #1 (Figure 5.1). This approach would reduce the required bandwidth of the transmit RF pulse needed to excite all spins within the ROI. Unfortunately, in the current TRASE MRI technique, there is no ability to encode along the longitudinal direction of the magnet other than using the natural axial B_0 variation of the bare Halbach magnet. As shown above, the shim sleeve designs that are based on B_0 homogeneity improvements alone are ineffective for use with TRASE because they do not remove the volume of spins excited outside of the ROI or the symmetric axial distribution of the field.

Since the B_0 homogeneity improvements alone are not effective for TRASE, we have used the shim array concept to introduce an axial B_0 gradient to produce asymmetry of the axial field profile allowing a slice selection 2D TRASE MRI scheme. Figure 5.10 shows that rotating one of the end rings of the bare Halbach magnet induces an

axial B_0 gradient. The advantage of this configuration requires no extra components, eliminating construction time and costs. However, this design requires disassembling and reconfiguring of the constructed magnet, taking approximately 1 hour. Although this approach showed uniform sub-volume selection (Design #3 in Figure 5.10), the strong gradient ($\sim$70 mT/m) produced thin (1 mm) slices in a 3 kHz RF pulse bandwidth. The strong axial gradient and associated narrow slice selection window is a particularly difficult for in-vivo TRASE imaging at $\sim$66.7 mT, due to already low SNR compared to higher field strengths.

Since a shim sleeve or reconfiguration of the bare Halbach magnet was deemed ineffective to produce a linear axial B_0 gradient, we introduced two additional asymmetric rings, one rotated 180° to the other (see Design #4 in Figure 5.11). Although the axial gradient, in this case, was weaker compared to Design #3 (Figure 5.10), leading to thicker ($\sim$ 3 mm) slices for a 3 kHz BW RF pulse and hence more signal, the selection volumes within the ROI become less uniform. The non-uniformity could be overcome because a series of 2D TRASE images could be stacked, and the data could be rearranged to produce an image of spins within a cylindrically-shaped slice. Unfortunately, although the longitudinal B_0 distribution is asymmetric, the overlap of volumes outside and inside the ROI occurs at certain frequencies which brings the need of unwrapping.

As found above, the shim array itself could be used to generate a linear axial B_0 gradient; therefore, the shim sleeve was optimized again using GA (Figure 5.12). The results showed that generating an axial gradient with two asymmetric rings or a shim sleeve provides no advantage except that the two rings occupy less space and use less magnetic material than the shim sleeve. Although the shim array with a weak axial gradient ($\sim$7 mT/m) could provide the needed axial gradient at the isocenter, a shim sleeve alone could not improve the gradient linearity to acceptable levels for TRASE MRI due to the complex field distribution over the ROI. Ideally, for 2D TRASE, the out-of-ROI excitation volumes should be separated from the ROI, then phased array

receive techniques may be effective for anti-aliasing of NMR signal along the z-axis (see Figure 5.4). Nevertheless, we have assumed that consideration of the points inside the ROI would be sufficient for the B_0 adjustments. Future shim array designs may be further improved if the optimization process considers points throughout the entire bore of the bare Halbach magnet rather than only inside the ROI.

As a final approach to the shim array, we combined the shim sleeve with the asymmetric rings (Figure 5.13). The asymmetric rings provided the axial gradient while the shim sleeve was introduced for axial gradient linearization. As a result of these simulation studies, we have found that targeting an axial gradient of 20 mT/m could physically isolate the selected volumes for the range of BWs of the RF pulses (Figure 5.13) which again could be exploited using phased array receive techniques. For this shim array, the out-of-ROI volume selections are separated for a range of frequencies over the ROI. The significant advantage of this approach is also the reasonable slice thickness of each sub-ROI volume selection ($\sim$3 mm thick slices assuming a 3 kHz BW RF transmit pulse) compared to stronger axial gradients designs (such as Design #3 in Figure 5.10). The thicker slices would provide higher signal than other shim sleeve designs (shown above), and the central excited volumes could be used for a multi-slice 2D TRASE acquisition by shifting the RF center frequency.

Besides the investigated above approaches, further improvement of the B_0 field distribution is possible in the constructed Halbach magnet. First, we have not investigated optimization of the complete parameter list (ring spacing, etc.) due to increased demands for computational power and optimization time. For example, in Design #6 (Figure 5.13), excited volumes in the ROI are cone-shaped near the center of the ROI, and thinner and increasingly non-linear near the ROI periphery. We expect that filling more of the unused bore space and expanding the range of block sizes and magnetization orientations used in the optimization process, could further improve the axial gradient strength and linearity. In addition, adjusting the

axial positions of each individual block in the two asymmetric rings could be a simple first approach to improve the gradient linearity over the ROI. In any case, providing the GA with more flexibility of optimizing magnetization directions and sizes of the blocks would have impact on the distribution of the B_0 (i.e. the homogeneity and axial gradient); however, this optimization approach needs development and is expected to be slower.

The measured B_0 field of the constructed Halbach magnet should be used in designing a shim array rather than using the simulated fields. Although a high accuracy was achieved between the simulated and measured fields of the constructed Halbach magnet, the measured field was shown to deviate from the simulated field by up to 0.2 mT in certain regions within the ROI (see Chapter 4). The simulated and measured field differences in the field strength and distribution are due to remaining magnetic blocks fabrication errors, block positioning differences and measurement uncertainties. Despite that, the shim arrays presented here can adjust the peak-to-peak B_0 up to 1.8 mT over the ROI and easily customized to the measured field of the Halbach magnet.

5.5 Conclusions

B_0 shimming of the Halbach magnet is a critical next phase for producing an mobile TRASE MRI system with high-quality MR imaging capability [157]. Based on the preliminary B_0 simulations, this work shows that field improvements for TRASE are possible using an array of small permanent magnets with optimized sizes and orientations. We investigated various shim sleeves and methods to improve B_0 homogeneity or to introduce a linear axial B_0 gradient for longitudinal slice encoding in a Halbach magnet. In all designs, exciting volumes outside of the ROI require sufficient axial decoding ability before high-quality in-vivo TRASE images can be achieved. This simulation study showed that a shim sleeve with two additional asymmetric rings producing a 20 mT/m axial gradient may be strong enough to separate the out-of-ROI

volume selection from the desired ROI, yet sufficiently weak to select thick enough slices (higher signal) for adequate SNR (Design # 6 in Figure 5.13). Nevertheless, a multi-channel receive coil would likely provide a way to unwrap the aliasing volumes along the z-axis but it requires further development such as additional RF receive hardware.

Chapter 6

A Magnet Rotation System for Simplified 2D TRASE MRI

Since the TRASE method requires 3 or 4 transmit RF coils to acquire a 2D MR image, significant issues were identified due to insufficient RF coil decoupling leading to poor 2D image quality [42, 74, 76, 158]. As a result, new developments regarding active decoupling (switches) strategies [159], a parallel transmit console [149] and new image reconstruction methods (modified Fourier transform [158]) have been introduced. Yet so far, there is no demonstration of high quality 2D TRASE using 3 transmit RF coils. However, a 2D TRASE image could be obtained by rotating the Halbach magnet or the RF coils, leading to a simpler imaging technique.

6.1 Introduction

Paul Lauterbur (1973) presented the first MR imaging method by subjecting spins to a magnetic field gradient (Figure 6.1) [49]. Lautebur showed that the signal is integrated along planes perpendicular to the gradient direction forming a 1D projection of a water phantom (Figure 6.1a). By rotating the magnetic field gradient direction (or object), a series of 1D radial projections were used to generate the first 2D MR image of a dual-compartment water phantom (Figure 6.1b). Originally called "NMR zeugmatography," the technique became the conventional MR projection reconstruction imaging method.

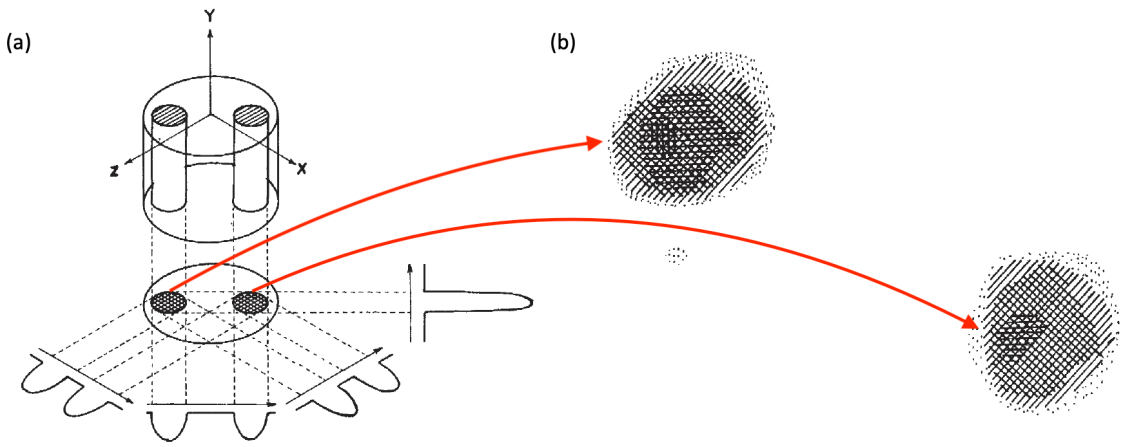

Figure 6.1: The original illustration of the NMR zeugmatography technique from Paul Lautebur's 1973 paper [49]. (a) A series of 1D NMR projections of two water phantoms obtained by changing the direction of the magnetic field gradient in the XZ-plane relative to the object. The NMR signal is integrated along planes perpendicular to the gradient direction (black arrows). (b) The 2D image was reconstructed from a set of four 1D projections. Both figures obtained from Lautebur (1973) [49] with permission from Springer Nature under license number 5324571452985.

Based on a similar idea, Cooley et al. (2015) demonstrated 2D MRI using a portable and rotating Halbach magnet with a built-in magnetic field gradient [33]. By rotating the linear B_0 gradient, the MR projection technique was used reducing the number of switched gradient axes from three to two [33]. The novel MR imaging method was called the "rotational spatial encoding method" (rSEM) and was the first to demonstrate high-quality in-vitro MR imaging using a portable Halbach magnet [33].

While rSEM is a step toward a portable MRI system, nonlinearity in the spatial encoding field distorts images [112]. The rSEM MRI system also relies on standard MRI hardware such as switching B_0 gradients (coils and amplifiers) in two orthogonal planes. Unlike rSEM, TRASE eliminates the entire gradient sub-system and eases the homogeneity requirement of the main magnet, allowing even lighter and cheaper magnets to be used, yet it requires multiple transmit RF coils bringing complications. Rotating the RF coils or the magnet reduces the number of required RF channels for 2D TRASE, decreasing costs associated with hardware and simplifying data acqui-

sition and image reconstruction. Therefore, a simple mechanical rotation system for the Halbach magnet was the next aim of this research.

6.1.1 2D TRASE by rotating coils

Sun et al (2019) showed analytically that physical rotation of the twisted-solenoid RF coil former by $+\beta°$ will result in an RF phase gradient rotation by $-2\beta°$ (Figure 6.2a) [74]. In further work by Sun et al (2020), two twisted solenoid RF coils were physically rotated by 90° from one another generating two opposing phase gradients, resulting in a doubling of the step size in k-space, ultimately increasing the TRASE spatial resolution compared to the uniform coil with a single twisted solenoid (see section 2.2.2 of Chapter 2) [42]. In principle, two opposing RF phase gradients can be rotated in the same direction in steps within ±45° to collect a series of radial 1D TRASE profiles of the object. Similar to the rSEM technique, the series of 1D TRASE profiles can be used to generate a 2D TRASE MR image by various reconstruction methods (e.g., filtered back-projection, inverse Radon transform, etc). Since sufficient decoupling of two twisted solenoids was already demonstrated for high-resolution 1D TRASE [74], [42], rotating the dual twisted-solenoid RF coils is much simpler mechanically than controlling the timing and switching of more RF coils [159]. Nevertheless, the RF coil's sensitivity to motion and coupling may require matching and tuning at each projection angle, increasing image acquisition time. In addition, the pulse sequence and image reconstruction for 1D TRASE are simpler and contains fewer artifacts than 2D TRASE (see Chapter 2).

6.1.2 2D TRASE by rotating the Halbach magnet

Although the RF phase gradient changes direction when the twisted-solenoid rotates, it will also change direction if the Halbach magnet rotates while the coil is fixed (Figure 6.2b). In Chapter 2, the B_0 direction was assumed stationary along the x-axis and Equations 2.33 and 2.34 was used to calculate the RF phase gradient for

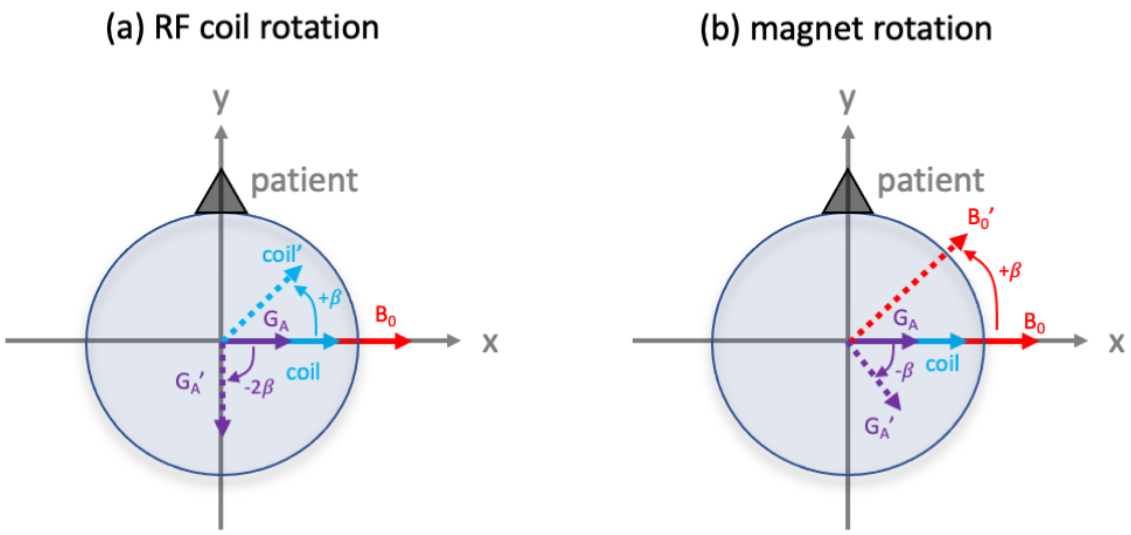

Figure 6.2: The concept of the rotating RF coil or Halbach magnet effect on the RF phase gradient. (a) Rotation of the twisted-solenoid RF coil by $+\beta$ produces a change in the RF phase gradient direction by -2β [74]. (b) Rotating the dipolar Halbach magnet by $+\beta$ produces a change in the RF phase gradient direction by $-\beta$.

any coil former rotation. However, if the B_0 rotates by $+\beta$ about the z-axis, the components of B_1 contributing to the NMR B_1 field transforms by:

$$\begin{bmatrix} B'_x \\ B'_y \end{bmatrix} = C\rho \begin{bmatrix} \cos\beta & -\sin\beta \\ \sin\beta & \cos\beta \end{bmatrix} \begin{bmatrix} \sin(\theta+\psi) \\ \cos(\theta+\psi) \end{bmatrix} \tag{6.1}$$

where C ($= -\mu_0 \frac{I}{h}\frac{A}{a^2}$) is a constant due to the static RF coil geometry factors and (ρ,θ,z) is the cylindrical coordinates. Since rotation occurs about the z-axis, the B_z component of the B_1 does not change with rotation; hence, B_z is not used in the calculation. After substitution of Equations 2.33 and 2.34 into Equation 6.1 and simplifying using trigonometric identities, the B_1 components are:

$$B'_x = C\rho\sin(\theta+\psi-\beta) \tag{6.2}$$

$$B'_y = C\rho\cos(\theta+\psi-\beta) \tag{6.3}$$

where B'_y is the relevant perpendicular component of the B_1 field. Furthermore, for any $+\beta$ rotation of the B_0 field, the coil winding shift $\psi = -2\beta$ and Equations 6.2

and 6.3 simplify:

$$B'_x = C\rho\sin(\theta - 3\beta) \tag{6.4}$$

$$B'_y = C\rho\cos(\theta - 3\beta) \tag{6.5}$$

For example, for a B_0 rotation of $\beta = \frac{\pi}{2}$, the RF phase gradient is -G_y (using Equation 2.36). An illustration of the RF phase gradient direction change in consequence of the magnet rotation is illustrated in Figure 6.2b. Clearly, the RF phase gradient rotates by an angle equal to the angle of the magnet but in the opposite direction. The main advantage of rotating the magnet rather than rotating RF coils is the simple mechanical motion with no sensitive RF coil connections. Nevertheless, rotating the magnet also requires twice the angular rotation than the RF coils (6.2). While moving the magnet is simpler than rotating the RF coils, the major problem with magnet rotation is that B_0 inhomogeneities are rotated with the magnet. A straightforward solution may be a B_0 shimming system (see Chapter 5) that, when added to the Halbach magnet, targets a cylindrically-symmetric field pattern; therefore, selecting the same volume of spins at each magnet angle.

6.2 Rotation system for the Halbach magnet

Since the constructed Halbach magnet (Chapter 4) is much lighter (25 kg) than other portable Halbach magnets (more than 100 kg) [33], an inexpensive type of electrical motor called a stepper motor and a driver system commonly used for computer numerical control (CNC) routers was used. Furthermore, the stepper motor functions and their driver electronics to modify them for magnet rotation was investigated. As noticed by Srinivas et al (2020), the NMR signal degraded in the presence of stepper motors; therefore, electromagnetic interference (EMI) mitigation techniques are required such as active external detectors [160, 161]. In their work, an external coil samples the local EMI. The data from the external coil and the MR receive coil are used to update, dynamically, a system transfer function which is then used to modu-

late the acquired k-space data before each frequency encoding step. In addition, Liu et al. (2021) used ten external coils embedded around a portable MR scanner and a deep learning neural network scheme to obtain (almost) noise-free brain images on a portable MR scanner [72]. In this work, we used a simple EMI shield made of aluminum to isolate the EMI generated by the rotation system from the RF receive coil. Furthermore, the motor was placed at distance of ∼50 cm to minimize any motor and magnet interactions that could impact B_0 homogeneity and the motor operation. Nevertheless, it is expected that the motor will operate with negligible impact on B_0 homogeneity when placed close to the magnet yet away from the open ends because Halbach magnets are self-shielded (i.e., the 5 gauss line is within 1-2 centimeters of the outer magnet's circumference).

The requirements of the magnet rotation system were:

- Adjustable settings for magnet angular steps between 0.5° and 3° increments.
- Rotation angular precision $< 0.1°$.
- Rotation rate ∼6°/s.

6.2.1 Principles of electric motors action

Electric motors convert electrical power to mechanical rotation (Figure 6.3) [77]. Many types of electric motors exist on the market, such as DC motors, servos, or stepper motors. Depending on the application, they have different specifications; for example, they may have high revolutions (rpm), high torque or both. Their applications include robotic manufacturing, 3D printing or computer numerical control (CNC) routers [77]. Typical electric motors contain a series of fixed electromagnets called phases (connected to the stator) which generate a magnetic field when a current is passing through them (Figure 6.3b,c). The shaft is connected to an internal rotor with alternating magnetic poles (Figure 6.3c). Depending on the polarity of the electromagnet's current, the magnetic field generated at the stator will attract the

teeth of the rotor causing the shaft to rotate at a fixed angle specified by the number of teeth (Figure 6.3c).

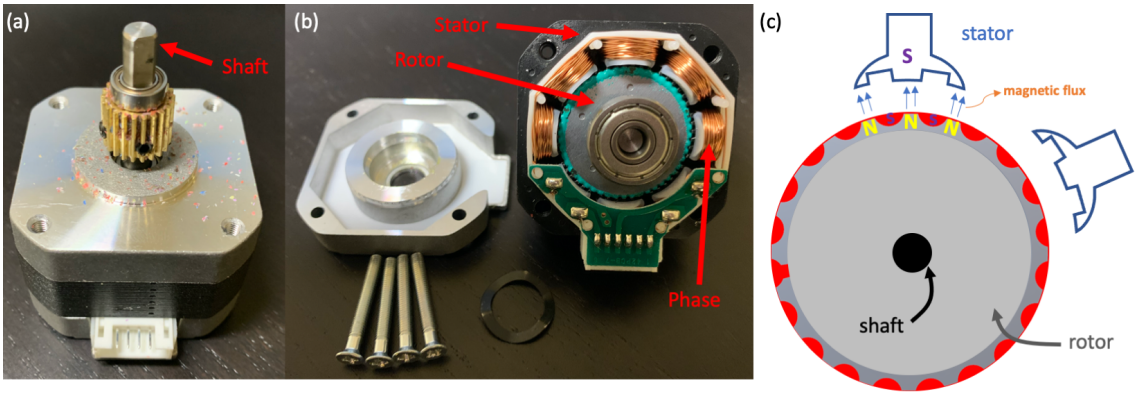

Figure 6.3: The internal hardware of the stepper motor. (a) The view of the enclosed motor; an electrical voltage at the input (white connectors at the bottom) produces a step rotation of the shaft. (b) The view of the open motor; the phases (electromagnets) in the stator and teeth on the permanent magnet rotor. (c) An expanded illustration of the teeth on each phase and rotor. When a electrical current flows through a phase, generating a magnetic field, hence a strong force is produced between the phase and the permanent magnet teeth in the rotor. The rotor and the shaft rotate at the angle defined by the number of teeth.

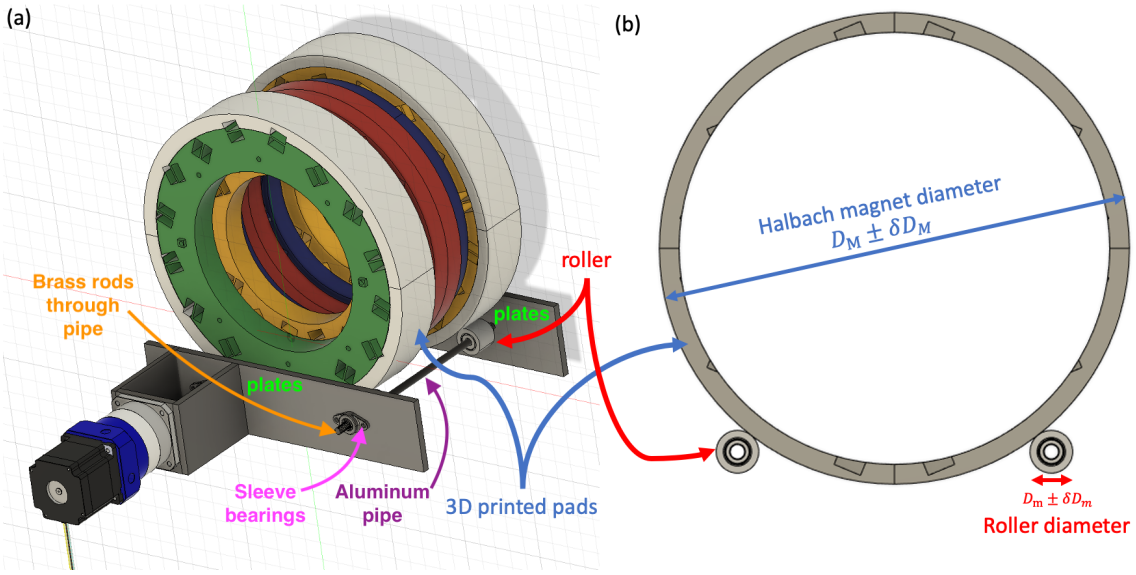

Figure 6.4: (a) An illustration of the Halbach magnet with the rotation system. (b) The relative diameters of the magnet and the roller is used to calculate the number of pulses needed for the motor to rotate the magnet by one complete revolution.

6.2.2 Torque estimate

The drive mechanism required to rotate the constructed 25 kg magnet is illustrated in Figure 6.4. The diameter of the magnet, D_M, was estimated using the average of ten diameter measurements using a ruler ($D_M = 421.06 \pm 0.84$ mm). The roller diameter was estimated similarly to be $D_m = 38.1 \pm 0.5$ mm. The angular rotation of the motor and magnet are different due to their different diameters (Figure 6.4). The gear ratio (GR) is the magnet diameter divided by the roller diameter. Including fundamental error analysis, the gear ratio in our case is $GR = 11.051 \pm 0.002$. Therefore, the roller rotates $\sim$ 11 times to complete a single magnet rotation (Figure 6.4). In addition, assuming the moment of inertia for a hollow cylinder (inner radius = 31 cm, outer radius = 43 cm) with uniform distribution of 25 kg mass throughout, the motor must provide a torque of $\sim$0.37 Nm to rotate the magnet in 1 sec by 6° from rest (since torque = moment of inertia $\times$ angular acceleration). Despite the expected error in this calculation since the mass is not uniformly distributed, a stepper motor capable of 4 Nm was used in this work (see below). A motor with a higher torque capability allows higher rotational speed and, ultimately, faster scan times.

6.2.3 Rotation system hardware and setup

While many types of motors could be used, we selected the bipolar stepper motor that activates two phases at a time producing the high torque needed to rotate MRI magnets and maintain a very high precision at low costs (<$200 CAD). The bipolar stepper requires a translator to produce the sequence of pulses needed to operate the motor (Figure 6.5). Due to lack of available circuit diagrams for the hardware used in this work, Figure 6.5 shows a simple example for operating a stepper motor. In Figure 6.5, for example, a 555 timer is used to generate the $\sim$5 V rectangular pulse waveform for the translator. The 555 timer requires a +5 V power supply and a potentiometer (R_1) to control the pulse length output. The speed of the motor is controlled with pulse width modulation (PWM). The rotation direction is

adjusted using a separate 5 V switch. In our work, we used an Arduino MEGA 2560 microcontroller to control the pulse length using simple C-language programming.

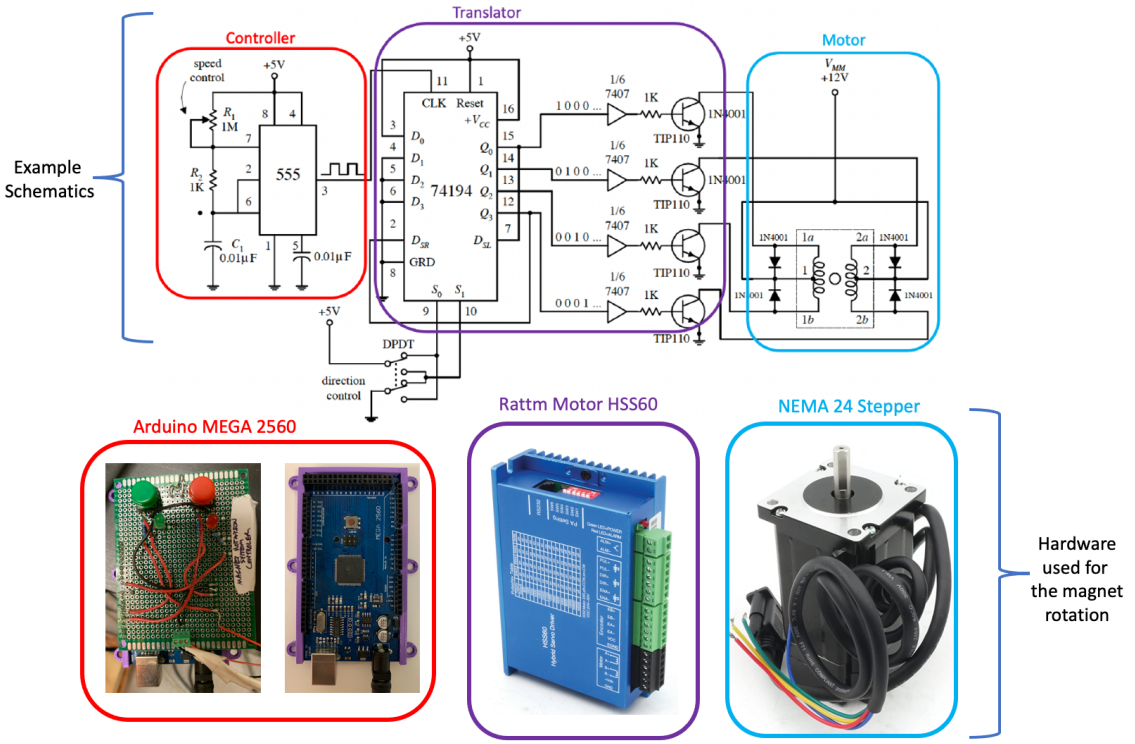

Figure 6.5: A controller and a translator are required to operate a stepper motor. (top row) Example electronic schematics of a controller, translator and motor circuitry. The schematics here do not reflect the true driver circuitry for the hardware used in this work; hence, they are illustrated here to aid understanding. (bottom row) The hardware used to control the Halbach magnet rotation. A single 5 V pulse programmed with the Arduino rotates the motor's shaft by 1 step. The step size can be adjusted using the switches on the translator (HSS60). Top circuit schematics was modified from Scherz [77] with permission from McGraw-Hill under license number 1230489-1, Arduino MEGA 2560 photo is my own, and driver and stepper motor pictures were obtained from the Rattm Motor datasheet [162].

A translator circuit produces a sequence of pulses to drive the motor (Figure 6.6). When the translator signal is applied at the input (pin 11 CLK), another input (DPDT) controls the firing sequence direction (i.e. the direction of the motor). In response to a single clock pulse, the translator sets a series of outputs high (Q_0, Q_1, Q_2, Q_3) in proper order for the motor. Another feature of the translator is counting, so the pulse sequence can continue when the controller provides the next input pulse.

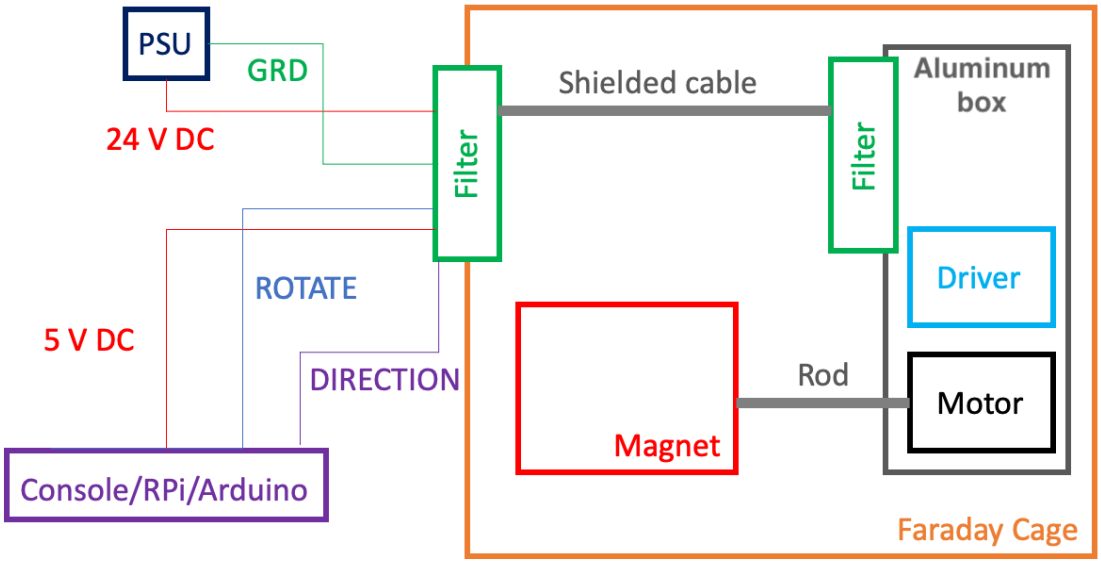

Figure 6.6: A diagram of the rotation system connections and shielding. The motor box is housed inside a Faraday cage used for RF shielding. The controller (console/Arduino) and power supply are placed outside the Faraday cage. The required control lines (ROTATE, DIRECTION) and power lines (24 V and 5 V) are shielded with a 15 pin D-Sub cable and placed inside the Faraday cage.

In modern stepper motor drivers, step resolution is not defined by the number of teeth but by a simultaneous activation of phases (i.e. micro-stepping). More details regarding microstepping to achieve angular steps per pulse $< 0.007°$ can be found in various sources [163].

In our work, we tested a single 2-phase hybrid stepper-servo driver (HSS60, Rattm Motor Co. Ltd., Changzhou, China) [162] and a single NEMA 24 hybrid stepper motor (24HS39-3008D, Stepper Online Motors and Electronics, Nicosia, 1090, Cyprus) [164] (Figure 6.5). This motor and driver are capable of high torque (4 Nm), meeting the torque requirement for Halbach magnet rotation (see Section 6.2.2) [162]. The driver can provide a wide range of stepping resolutions (400 – 51200 pulses per revolution) by setting Dual In-line Package (DIP) switches. However, the default used in this work is 400 steps (i.e. pulses) per motor revolution. An adjustable switching power supply was used to power the driver (MySweety, 480 W Adjustable DC Power Voltage Converter, China). According to the specification sheet of the motor, with

this setup, the angular motor steps of 0.900±0.045° can be achieved [162, 164].

Since the magnetic blocks protrude from the top of the constructed magnet, 3D printed pads were attached (with glue) to the outer circumference to allow for rotation (as shown in grey in Figure 6.4). In addition, we used four 1-1/2" diameter and 1-1/4" long abrasion-resistant urethane drive rollers with a non-magnetic aluminum hub (35A, McMaster-Carr, USA) as a support for the Halbach magnet. The rollers were attached to two 1/2" outer diameter aluminum pipes (Metal Supermarkets, Edmonton, Alberta, Canada). The aluminum pipes were attached to two 3D printed plates that fitted four dry-running sleeve flange bearings (McMaster-Carr, USA). Two 1/4" diameter threaded brass rods were placed through the aluminum pipes to fix the rods to the bearings. Brass bolts fixed the rods to the dry-running bearings. Four extra brass rods, nuts and washers were used to stabilize the 3D printed plates.

Since the rotation system electronics cause noise higher than the NMR signal, the motor and driver were housed inside an aluminum Faraday box (7"×7"×7") and placed inside a larger Faraday cage that houses the magnet (Figures 6.6 and 6.8a). Both the power supply and microcontroller was placed outside the Faraday cage. All pulse control lines (ROTATION, DIRECTION) and power transmission lines (+24 V) feeds the driver from outside to inside the Faraday cage using a shielded 15 pin D-Sub cable (3272-CS-DSDMDB15MM-025-ND, Amphenol Cables, Digi-Key, Canada) and connectors (FCC17A15AD280-ND, Amphenol ISS, Digi-Key, Canada) (Figure 6.6).

6.2.4 TRASE and rotation control pulse sequence

The magnet rotation was controlled using two of five connections of the D-Sub cable (Figure 6.6). The power supply was grounded to the filter panel on the front of the Faraday cage and the 24 V line was transmitted to the driver. In this work, we did not use the D-Sub filters since they are expected to change the Arduino operating pulse widths (∼250 μs) and affect motor accuracy. Nevertheless, D-Sub

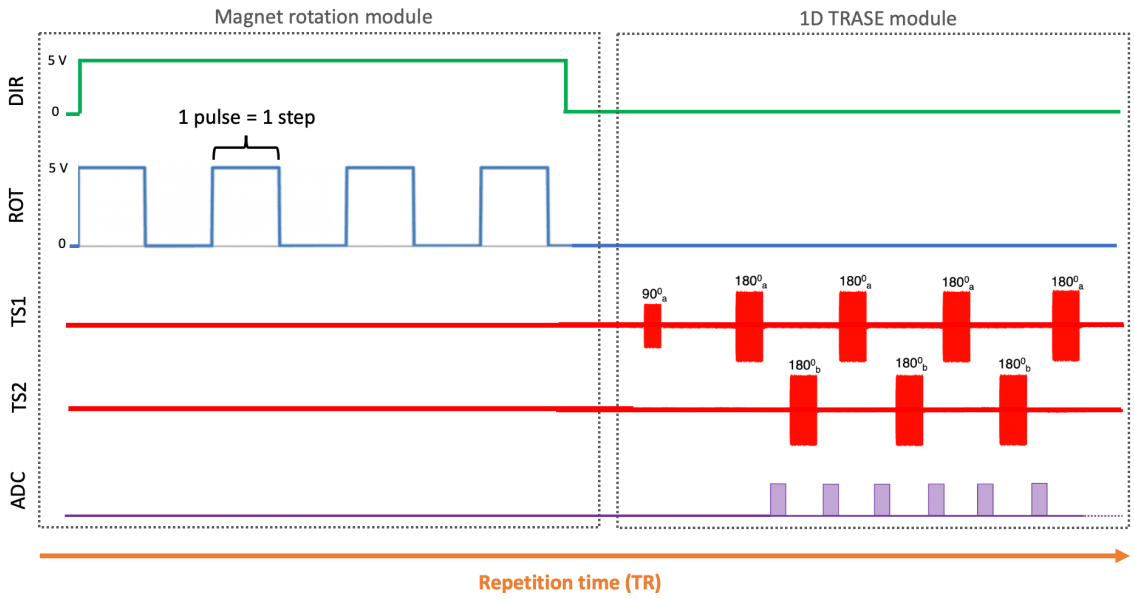

Figure 6.7: The diagram of the magnet rotation control pulses with the 1D TRASE pulse sequence. The 5 V pin (DIR) is first activated for clockwise or not activated (0 V) for counter-clockwise rotation of the magnet. A series of 5 V pulses are used during the DIR pulse to step the motor by fixed angular orientation. Many pulses (4420) on the PUL line are required for one full magnet rotation. Once a specific angular rotation is complete, the 1D TRASE projection is acquired. The experiment is then repeated (TR) at a different magnet orientation and TR $\sim$ 1 s in current experiments. Time for each module is not the same and depends on the specific experiment (for example, fast rotation and long 1D TRASE echo trains).

filters should be used for noise mitigation in future work. The pulse sequence provided by a console or microcontroller is shown in Figure 6.7. A clockwise rotation is achieved using a +5 V on the direction (DIR) line (Figure 6.7) provided by the controller; otherwise, the magnet rotates counter-clockwise (0 V). When the DIR line is active, a series of rectangular pulses follow through the cable and aluminum motor box to the driver along the rotation line (ROT in Figure 6.7). Since the driver is preset to 400 pulses per revolution, the motor rotates 0.9° for each input pulse (PUL). The total angular position is determined by the default stepper settings and the number of pulses. The frequency of the input pulse and the available torque determines the maximum rotation speed. Following the motor and magnet rotation, the one-dimensional TRASE projections were obtained, and the pulse sequence is repeated

for the next angle in a repetition time (TR).

6.3 Testing of the rotation system

6.3.1 Constructed rotation system

The on-the-bench testing setup for the magnet rotation system is shown in Figure 6.8a,b and the setup for 1D TRASE in Figure 6.8c. The angular accuracy, speed, and impact of noise on the NMR signal was measured. A series of 1D TRASE projections was obtained.

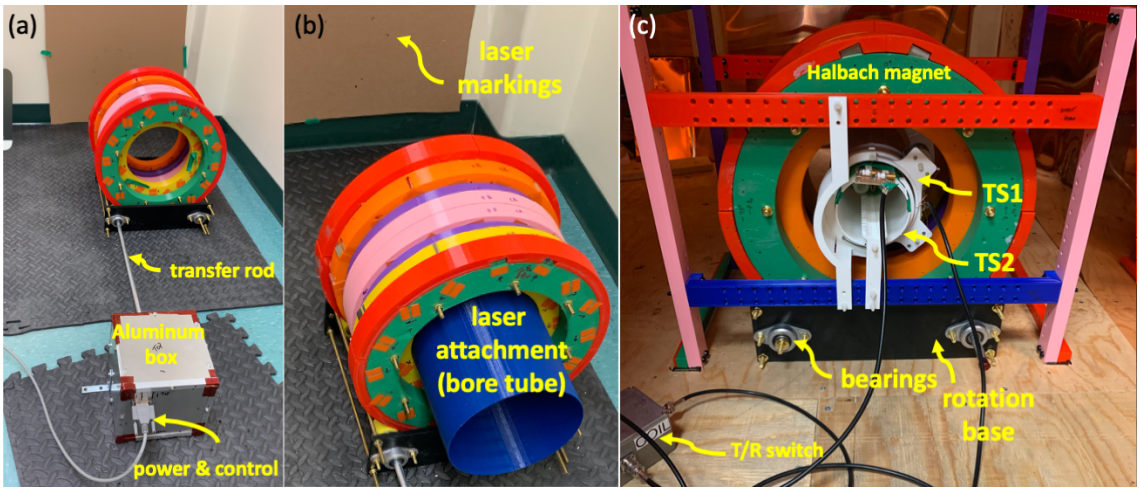

Figure 6.8: The magnet rotation system hardware and experimental setup. (a) The motor and driver are housed in an aluminum box. A transfer rod allows rotation of the Halbach magnet in response to a pulses controlling the stepper motor. (b) A laser pointer attached to the inner diameter surface of a 3D printed bore tube to test angular accuracy. (c) The experimental setup for 1D TRASE consists of the rotation system, Halbach magnet, twisted solenoid RF coils (TS1, TS2) and the T/R switch. All are placed inside the Faraday cage.

6.3.2 Angular accuracy

A laser was attached to a bore tube to test the angular accuracy (Figure 6.8b). A negligible difference was measured (< 0.5 mm arc length or $< 0.01°$ angular deviation) between the initial and final laser markings for one full magnet rotation.

6.3.3 Controlling rotation speed and direction

The magnet rotation system was tested for speed and direction control. Using a +5 V rectangular waveform (500 μs, 50% duty cycle), one full magnet rotation was complete in 70 seconds (i.e. $\sim$5.1°/s) (no TRASE acquisition used). Furthermore, the pulse length was reduced to 300 μs and it took 5 seconds to complete one full magnet rotation with no observed slippage (i.e. $\sim$72°/s). Although the driver can handle 2 μs pulses at 50% duty cycle, the rotation system could not handle pulses shorter than 260 μs because of the high torque demand. There was no difference in performance using counterclockwise and clockwise magnet rotation.

6.3.4 Noise mitigation

The noise testing showed a four times higher blanked analog-to-digital converter (ADC) level with the rotation system on (Figure 6.9). We found that the D-Sub cable inside the Faraday cage (shielded cable in Figure 6.6) was not effectively shielded for this MRI application. The noise was mitigated by running this D-Sub cable outside of the Faraday cage through a small opening closest to the aluminium box connection.

6.3.5 2D TRASE reconstruction

A series of 1D TRASE radial k-space acquisition was obtained using the above setup allowing a 2D TRASE reconstruction. A cylindrical phantom (diameter $\times$ height = 3.4 cm $\times$ 5 cm) filled with 61.6 mM NaCl + 7.8 mM $CuSO_4$ with its long axis oriented perpendicular to the RF phase gradients was used (see Figure 6.10a). 1D TRASE acquisition consisted of: number of averages = 16, ETL = 64, number of projections = 18, 2$\times$ zero-filling, 200 μs hard pulses, $\sim$10% duty cycle, TR = 1 s (per step) + 4 s (per 1D TRASE projection) and total scan time $\sim$ 20 min (19.2 min total for TRASE and 30 s total for rotation). Due to a large presence of artifacts in each projection, they were first truncated (all at the same array locations) to a 30 pixels range surrounding the known location of the phantom. After acquiring eighteen 1D

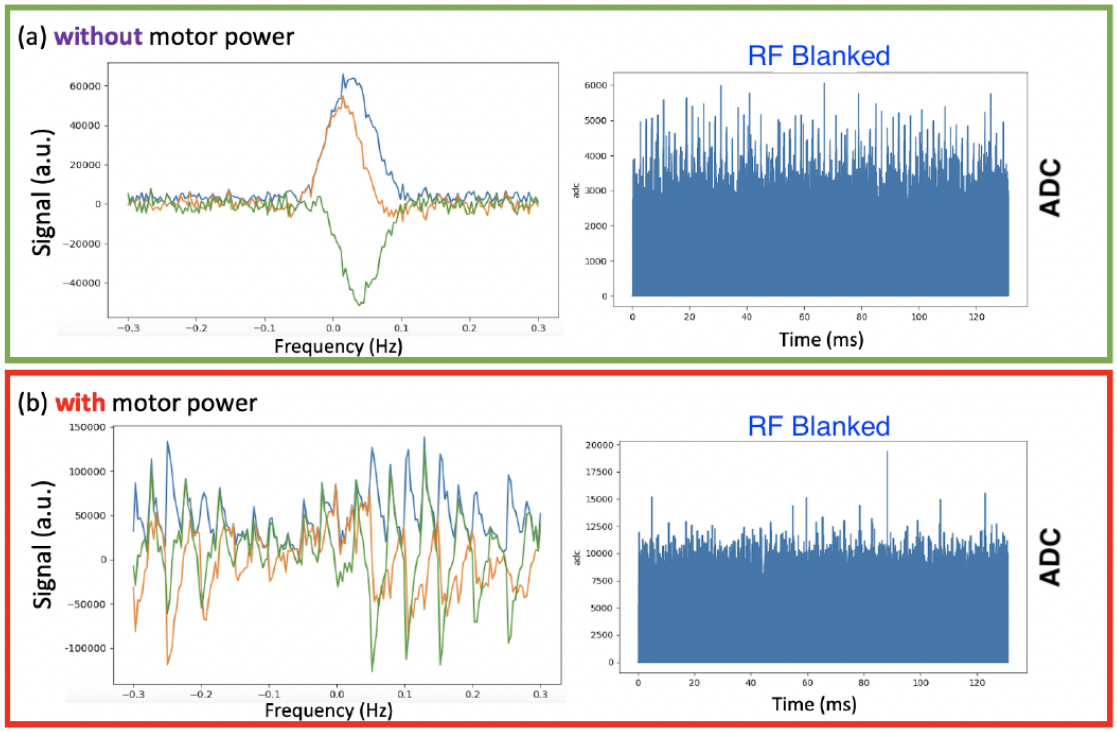

Figure 6.9: An investigation of EMI noise produced by the rotation system. (a) The NMR peak signal provides a basis for the signal and the blanked analog-to-digital (ADC) noise without the rotation system. (b) The noise produced by the rotation system was greater than the NMR signal (original cable setup). The noise level on the blanked ADC was four times higher with the rotation system compared to the baseline. After cable re-routing, motor noise was not an issue.

TRASE projections ('sinogram') through the phantom (Figure 6.10b), the sinogram data was reconstructed into 2D (Figure 6.10c) using the inverse Radon transform with a 'hamming' filter (scikit-image, Python 3.9, Python Software Foundation, Netherlands). The inverse Radon transform function first applies the Fourier transform to the spatial 1D TRASE projections and then filtered. All filtered 1D spatial frequency lines are then arranged as diameters on a circle given their known angle of projection over 180° and regridded from polar to Cartesian coordinates. The 2D slice is then reconstructed by 2D Fourier transform of the the k-space data.

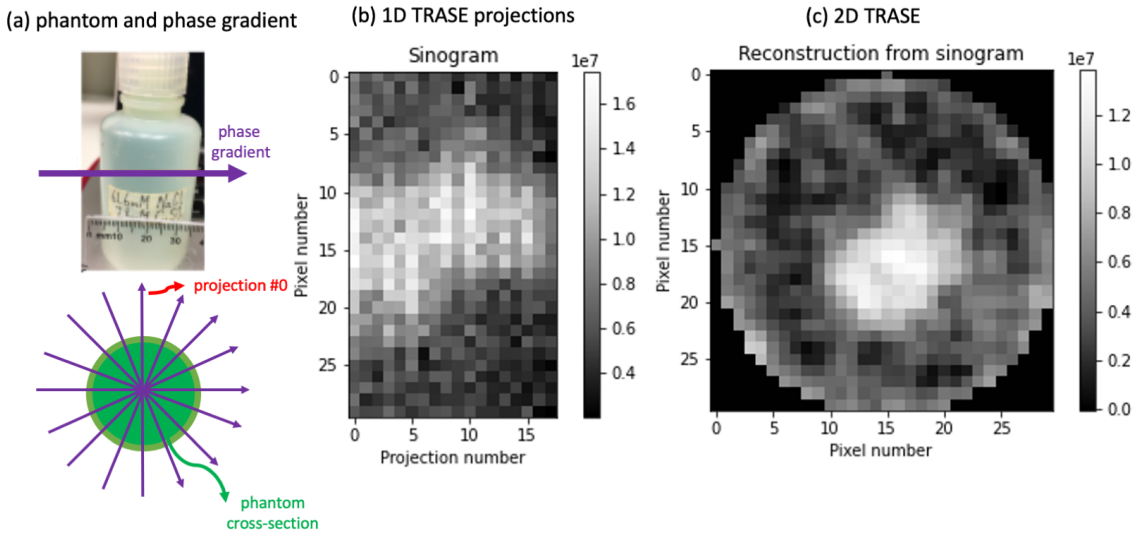

Figure 6.10: 2D TRASE testing using the magnet rotation. (a) The phase gradient projections through a small NaCl + $CuSO_4$ phantom. (b) A set of 18 1D TRASE projections ('sinogram'). (c) The 2D TRASE produced by radial reconstruction.

6.4 Discussion

This chapter presents a possible improvement and simplification of the low-cost and mobile TRASE technology by introducing a rotating magnet; hence, reducing the number of required RF coils. A high precision and inexpensive rotation system for the constructed 25 kg Halbach magnet is presented. The new application of an electronically controlled motor allows a simple 2D TRASE MRI system to be constructed, requiring only two twisted-solenoid RF coils, a two channel RF amplifier and a parallel-transmit console.

Noise mitigation was the main challenge in the implementation of the rotation system. We found that EMI produced by the "off-the-shelf" motor, driver and power cables and connectors deteriorates the NMR signal. Rather than complex EMI mitigation techniques requiring more hardware such as external detectors [160], we placed the motor and driver in a custom aluminium box (working as a Faraday cage) and ran transmission lines through shielded cables. Filtered connectors were not used; therefore, a high level of EMI within the Faraday cage was observed. To remedy this issue, we ran the transmission cable outside the main Faraday cage and through a

small opening at the back, allowing a reduction of cable length exposed inside the Faraday cage by 20×. Under this new setup, the NMR signal and noise level appeared unaffected to all operational modes of the magnet rotation system.

The high angular accuracy of the magnet was measured using large motor step sizes ($\Delta\theta = 0.9°$). The deviation between the initial and final position of a laser on a 20 cm diameter tube was measured with a ruler and found to be < 0.5 mm. In the future, even higher stepper motor angular resolution ($0.007° = 0.9°/128$) is achievable using the DIP switches provided on the driver. Therefore, the magnet can rotate by angular steps of 6.3×10^{-4} ° if needed, simply by setting the driver switches, allowing an increase in the number of radial 1D TRASE projections. Although this would increase imaging time by the factor given by the number of angular projections, the simple 2D TRASE MRI system has a potential for high-resolution imaging. Furthermore, faster 2D TRASE imaging is possible using the rotation system using shorter pulses. Rather than 70 seconds to complete one full magnet rotation (using the above preliminary test settings), the magnet can achieve one full rotation in 5 seconds. Therefore, 2D TRASE acquisition time will not be limited by the rotation system; however, it will be determined by the 1D TRASE acquisition speed. A disadvantage of increasing the magnet rotation speed is the increased vibration which is stronger using the discrete step-and-acquire pulse sequence (Figure 6.7). One method to reduce this potential issue is pulse-width modulation (PWM) to control angular acceleration which would smooth the transition of the magnet steps in faster rotation scans.

As seen above, B_0 rotation testing suggests that the MR radial reconstruction technique is a plausible method for simplified 2D TRASE MRI. Although 2D TRASE 'images' can be obtained, the artifacts and distortions in the images are expected mostly due to the B_0 inhomogeneities; therefore, further investigation is required such as novel shimming approaches (see Chapter 5). For example, a shim array that targets a cylindrically-symmetric B_0 field may allow viable 2D TRASE imaging based on the projection reconstruction method. In addition to shimming, improvements in

the spatial resolution (e.g., increasing the number of projections, higher RF duty cycle and longer pulse trains, etc) and reduction of artifacts other than B_0 will also be required (e.g., Fourier transform of the echoes, etc). These directions may support viable 2D TRASE MR images based on magnet rotation using the radial 1D TRASE acquisition method.

6.5 Conclusions

A TRASE MRI system using magnet rotation potentially has a very low cost ($<$ \$5k CAD total) and a simple operation using the two twisted-solenoid RF coils, custom RF amplifiers, and a lightweight Halbach magnet. B_0 magnet rotation provides an opportunity to reduce the number of RF transmit coils required for 2D TRASE by application of a radial acquisition and reconstruction technique.

Chapter 7

Conclusions and Future Directions of the RF Amplifier and Halbach Magnet for TRASE MRI

Since the invention of MRI, gradients of the B_0 field have been used to obtain high quality diagnostic images of human pathologies. In the last five years, research and industry have found high value and diagnostic capability of low field strengths (0.06 - 0.5 T), allowing more mobile, compact and cheaper MRI systems, although at reduced SNR per unit of time. Companies such as Hyperfine or Promaxo are already producing low-cost, low-field, and portable MRI systems for various environments such as point-of-care MRI in Canada's remote communities [26] or in-office prostate screening and biopsy [31]. Unlike these systems, TRASE uses RF gradients to spatially encode spins rather than a standard B_0 gradient system, relaxing the homogeneity requirement of the main magnet, hence, potentially increasing the compactness, lowering costs, and improving mobility of MRI systems. The hardware and techniques presented in this thesis are a step forward for TRASE, allowing improved spatial resolution and increased mobility with a novel RF amplifier and a new magnet design.

Although the hardware presented in this thesis provides some solutions for portable TRASE MRI, some limitations remain. The RF amplifier(s) delay between the gate pulse and the RF pulse limits the highest achievable duty cycle and reduces the available time for receiving the signal. Although faster switches such as transistor-

transistor logic (TTL) may reduce unwanted delays between the RF output pulses and blanking pulses, however, noise may also increase. Additionally, the gating circuit currently produces a "step-up" voltage conversion (5 V to 12 V) required by the bias network's standard operating voltage. Future designs could bypass the bias network using a voltage divider, eliminating the power supply connection and optocoupler, reducing the primary source of EMI within the gating circuit. Nevertheless, EMI mitigation and stability of the bias network voltage remains important for high power RF output stability and long term use of the amplifier. The main limitation of the constructed RF amplifier is relatively high costs (∼$4000 for main PSU and ∼$2000 per RF channel) and size. Cheaper (∼$30 CAD) and more compact PSUs are available; however, they limit the peak RF output power and duty cycle depending on the maximum current rating. Depending on peak RF power and duty cycle needs, future amplifier designs can be more compact by removing large heat sinks or using novel high power, compact, and high-efficient Gallium Nitride (GaN) transistors. However, Class D RF amplifiers may be more suitable for portable MRI with high efficiency requirements [83]. A rather large 3rd harmonic (-10 dBc) is still present in the constructed RF amplifier, which could be destructive (for the amplifier and coil) in high power applications. The development of a new RF choke assembly and a diplexer could reduce the strength of the harmonics but needs further work. In addition, the constructed RF amplifier does not have a dedicated protection circuit for overdrive or high voltage standing wave ratio (VSWR). Therefore, a protection circuit is required for the constructed RF amplifier which in the future provide clinical TRASE application to meet regulations.

The weight of the constructed Halbach magnet and aspect ratio was significantly reduced compared to other designs by reducing the imaging volume. The reduction of the imaging volume is not a limiting factor for imaging since it may be used for slice-selection. Nevertheless, 2D TRASE imaging will be constrained to transverse slices. In this work, the radial position of the magnetic blocks was the only parameter

optimized to improve the B_0 homogeneity (8.5-fold). Unfortunately, an inhomogeneity of ∼11,154 ppm remained in the target imaging volume. Future designs should consider more parameters during optimization, such as magnetization direction, block spacing and multiple ringed layers. In addition, we showed that it is possible to improve the magnetic field homogeneity or implement an axial gradient into the bare Halbach magnet using an array of small permanent magnet pieces. In this work, improvements were shown using shim arrays that did not completely fill the unused and valuable bore space inside the Halbach magnet. Future shim designs should consider all unused bore space, and external to the magnet, as potential shimming block positions leading to improved designs. Adding possible block locations to the optimization process will maximize the shim array diversity provided to the genetic algorithm, allowing higher performance shim designs to be generated. In addition, field drifts of the NdFeB magnets due to temperature instability are an expected issue. Therefore, future designs should consider inexpensive Hall-effect sensors (such as MLX9036, Melexis Technology, NV, USA) built into the Halbach magnet formers at specific locations enabling the RF frequency adjustment to compensate for the field drifts during TRASE MRI acquisition. Some alternative solutions are thermal insulation of the magnet blocks or replacing blocks with SmCo since their temperature coefficient is ∼1/10 of the NdFeB material although at a higher cost [72, 165].

2D TRASE imaging by magnet rotation is also limited due to the remaining B_0 inhomogeneities. Rotating the magnet around the patient allows 1D projections, but inhomogeneities also rotate. Therefore, a different volume of spins is selected at each magnet orientation. Further work considering magnet rotation could also target a cylindrically-symmetric magnetic field (Chapter 5) or, as discussed previously, adjust the transmit RF center frequency and bandwidth at each B_0 orientation to select the correct volume. A more elegant approach would possibly be the rotation of the RF coils to rotate the RF phase gradients, therefore, fixing the B_0 inhomogeneity orientation to the object and selecting the same spins for each 1D projection. In

addition, only one-half the coil rotation range is required compared to B_0 rotation, potentially reducing the imaging time. One possible limitation of rotating coils is matching and tuning changes at each step, which would likely increase the 2D TRASE imaging time. The current magnet rotation hardware could be reconfigured to rotate the RF coils.

Using the hardware and techniques developed in this thesis, a portable and low-cost TRASE MRI system is feasible. MRI systems based on this technique may be installed in emergency rooms and medical clinics providing soft-tissue contrast imaging without using non-ionizing radiation. Furthermore, astronauts on the International Space Station may also benefit as their muscle and bone deterioration could be monitored during space missions. The portable TRASE MRI system also provides new teaching and research opportunities and commercial opportunities in Canada.

Bibliography

[1] H. S. Huang and J. F. Hainfeld, "IJN-43770-intravenous-magnetic-nanoparticle-hyperthermia," *International Journal of Nanomedicine*, vol. 8, pp. 2521–2532, 2013. [Online]. Available: https://www.ncbi.nlm.nih.gov/pmc/articles/PMC3720579/pdf/ijn-8-2521.pdf.

[2] B. J. van der Knoop, I. A. Zonnenberg, J. I. Verbeke, L. S. de Vries, L. R. Pistorius, M. M. van Weissenbruch, R. J. Vermeulen, and J. I. de Vries, "Additional value of advanced neurosonography and magnetic resonance imaging in fetuses at risk for brain damage," *Ultrasound in Obstetrics and Gynecology*, vol. 56, no. 3, pp. 348–358, 2020, ISSN: 14690705. DOI: 10.1002/uog.21943.

[3] R. Narayan, "Encyclopedia of biomedical engineering," vol. 1-3, 2019.

[4] W. Y. Huang, G. Wu, F. Chen, M. M. Li, and J. J. Li, "Multi-systemic melioidosis: A clinical, neurological, and radiological case study from Hainan Province, China," *BMC Infectious Diseases*, vol. 18, no. 1, pp. 1–5, 2018, ISSN: 14712334. DOI: 10.1186/s12879-018-3569-8.

[5] R. Ouwerkerk and R. H. Morgan, "23na mri: From research to clinical use," *J Am Coll Radiol*, vol. 4, no. 10, pp. 739–741, 2007.

[6] M. A. Frey, M. Michaud, J. N. VanHouten, K. L. Insogna, J. A. Madri, and S. E. Barrett, "Phosphorus-31 MRI of hard and soft solids using quadratic echo line-narrowing," *Proceedings of the National Academy of Sciences of the United States of America*, vol. 109, no. 14, pp. 5190–5195, 2012, ISSN: 00278424. DOI: 10.1073/pnas.1117293109.

[7] J. P. Marques, F. F. Simonis, and A. G. Webb, "Low-field MRI: An MR physics perspective," *Journal of Magnetic Resonance Imaging*, vol. 49, no. 6, pp. 1528–1542, 2019, ISSN: 15222586. DOI: 10.1002/jmri.26637.

[8] M. Sarracanie and N. Salameh, "Low-Field MRI: How Low Can We Go? A Fresh View on an Old Debate," *Frontiers in Physics*, vol. 8, no. June, 2020, ISSN: 2296424X. DOI: 10.3389/fphy.2020.00172.

[9] R. E. Sepponen, "Low-field MR imaging - Development in Finland," *Acta Radiologica*, vol. 37, no. 3 PART 2, pp. 446–454, 1996, ISSN: 02841851. DOI: 10.3109/02841859609177679.

[10] K. P. Pruessmann, M. Weiger, M. B. Scheidegger, and P. Boesiger*, "Sense: Sensitivity encoding for fast mri," *Magnetic Resonance in Medicine*, vol. 42, pp. 952–962, 1999.

[11] B. G. Fallone, "The Rotating Biplanar Linac-Magnetic Resonance Imaging System," *Seminars in Radiation Oncology*, vol. 24, no. 3, pp. 200–202, 2014, ISSN: 15329461. DOI: 10.1016/j.semradonc.2014.02.011. [Online]. Available: http://dx.doi.org/10.1016/j.semradonc.2014.02.011.

[12] H. W. Fischer, P. A. Rinck, Y. van Haverbeke, and R. N. Muller, "Nuclear relaxation of human brain gray and white matter: Analysis of field dependence and implications for MRI," *Magnetic Resonance in Medicine*, vol. 16, no. 2, pp. 317–334, 1990, ISSN: 15222594. DOI: 10.1002/mrm.1910160212.

[13] K. Wachowicz, N. DeZanche, E. Yip, V. Volotovskyy, and B. Fallone, "Cnr considerations for rapid real-time mri tumor tracking in radiotherapy hybrid devices: Effects of b0 field strength," *Medical Physics*, vol. 43, pp. 4903–4914, 2016.

[14] S. Geethanath and J. T. Vaughan, "Accessible magnetic resonance imaging: A review," *Journal of Magnetic Resonance Imaging*, vol. 49, no. 7, e65–e77, 2019, ISSN: 15222586. DOI: 10.1002/jmri.26638.

[15] WHO, *Global atlas of medical devices*. 2017, ISBN: 9789241512312. [Online]. Available: https://www.who.int/medical_devices/publications/global_atlas_meddev2017/en/.

[16] G. I. Ogbole, A. O. Adeyomoye, A. Badu-Peprah, Y. Mensah, and D. A. Nzeh, "Survey of magnetic resonance imaging availability in West Africa," *Pan African Medical Journal*, vol. 30, pp. 1–9, 2018, ISSN: 19378688. DOI: 10.11604/pamj.2018.30.240.14000.

[17] L. L. Wald, P. C. McDaniel, T. Witzel, J. P. Stockmann, and C. Z. Cooley, "Low-cost and portable MRI," *Journal of Magnetic Resonance Imaging*, vol. 52, no. 3, pp. 686–696, 2020, ISSN: 15222586. DOI: 10.1002/jmri.26942.

[18] D. J. Emery, A. J. Forster, K. G. Shojania, S. Magnan, M. Tubman, and T. E. Feasby, "Management of mri wait lists in canada," *Healthcare Policy*, vol. 4, no. 3, pp. 76–86, 2009.

[19] J. A. Tkach, S. L. Merhar, B. M. Kline-Fath, R. G. Pratt, W. M. Loew, B. R. Daniels, R. O. Giaquinto, M. S. Rattan, B. V. Jones, M. D. Taylor, J. M. Tiefermann, L. M. Tully, E. C. Murphy, R. N. Wolf-Severs, A. A. LaRuffa, and C. L. Dumoulin, "MRI in the neonatal ICU: Initial experience using a small-footprint 1.5-T system," *American Journal of Roentgenology*, vol. 202, no. 1, 2014, ISSN: 0361803X. DOI: 10.2214/AJR.13.10613.

[20] M. Nakagomi, M. Kajiwara, J. Matsuzaki, K. Tanabe, S. Hoshiai, Y. Okamoto, and Y. Terada, "Development of a small car-mounted magnetic resonance imaging system for human elbows using a 0.2 T permanent magnet," *Journal of Magnetic Resonance*, vol. 304, pp. 1–6, 2019, ISSN: 10960856. DOI: 10.1016/j.jmr.2019.04.017. [Online]. Available: https://doi.org/10.1016/j.jmr.2019.04.017.

[21] T. C. Cosmus and M. Parizh, "Advances in whole-body MRI magnets," *IEEE Transactions on Applied Superconductivity*, vol. 21, no. 3 PART 2, pp. 2104–2109, 2011, ISSN: 10518223. DOI: 10.1109/TASC.2010.2084981.

[22] Y. Li and S. Roell, "Key designs of a short-bore and cryogen-free high temperature superconducting magnet system for 14 T whole-body MRI," *Superconductor Science and Technology*, vol. 34, no. 12, p. 125 005, 2021, ISSN: 0953-2048. DOI: 10.1088/1361-6668/ac2ec8.

[23] T. Tadic and B. G. Fallone, "Design and optimization of superconducting mri magnet systems with magnetic materials," *IEEE Transactions on Applied Superconductivity*, vol. 22, no. 2, 2012, ISSN: 10518223. DOI: 10.1109/TASC.2012.2183871.

[24] A. J. King, Q. Deng, R. Tyson, J. C. Sharp, J. Matwiy, B. Tomanek, and J. F. Dunn, "In Vivo Open-Bore MRI Reveals Region- and Sub-Arc-Specific Lengthening of the Unloaded Human Posterior Cruciate Ligament," *PLoS ONE*, vol. 7, no. 11, pp. 1–10, 2012, ISSN: 19326203. DOI: 10.1371/journal.pone.0048714.

[25] S. C. L. Deoni, M. M. K. Bruchhage, J. Beauchemin, A. Volpe, V. D'Sa, M. Huentelman, and S. C. R. Williams, "Accessible pediatric neuroimaging using a low field strength mri scanner," *NeuroImage*, vol. 238, no. May, p. 118 273, 2021, ISSN: 10959572. DOI: 10.1016/j.neuroimage.2021.118273. [Online]. Available: https://doi.org/10.1016/j.neuroimage.2021.118273.

[26] "Queen's university: Faculty of health sciences. qhs student helps make neurological mri testing accessible to remote communities," 2022. [Online]. Available: https://healthsci.queensu.ca/stories/feature/qhs-student-helps-make-neurological-mri-testing-accessible-remote-communities.

[27] Hyperfine, "Hyperfine announces plans for global expansion starting with launches in the united kingdom and pakistan," [Online]. Available: https://hyperfine.io/worlds-first-bedside-mri-system-receives-fda-510k-clearance/.

[28] C. McNulty and M. Poole, "Rotatable magnet methods and apparatus for a magnetic resonance imaging system," *US Patent: US 10324147B2*, 2019. [Online]. Available: https://rpx-patents.s3.amazonaws.com/US/1db00-US10324147B2/US10324147B2.pdf.

[29] C. Hugon, M. Poole, and T. Ralston, "Methods and apparatus for magnetic field shimming," *US Patent: US20170276747A1*, 2017. [Online]. Available: https://patentimages.storage.googleapis.com/62/a7/66/f1531df7473c0b/US20170276747A1.pdf.

[30] J. M. Rothberg, M. S. Rosen, G. L. Charvat, W. J. Mileski, T. Rearick, M. S. Poole, and K. G. Fife, "Low field magnetic resonance imaging methods and apparatus," *US Patent: US9817093B2*, 2017.

[31] Promaxo, 2020. [Online]. Available: https://vator.tv/news/2020-06-02-reinventing-the-doctor-with-in-office-technologies.

[32] S. Chiragzada, E. Hellman, D. Michael, R. Narayanan, A. Nacev, and D. Kumar, "Initial phantom studies for an office-based low-field MR system for prostate biopsy," *International Journal of Computer Assisted Radiology and Surgery*, vol. 16, no. 5, pp. 741–748, 2021, ISSN: 18616429. DOI: 10.1007/s11548-021-02364-7. [Online]. Available: https://doi.org/10.1007/s11548-021-02364-7.

[33] C. Z. Cooley, J. P. Stockmann, B. D. Armstrong, M. Sarracanie, M. H. Lev, M. S. Rosen, and L. L. Wald, "Two-dimensional imaging in a lightweight portable MRI scanner without gradient coils," *Magnetic Resonance in Medicine*, vol. 73, no. 2, pp. 872–883, 2015, ISSN: 15222594. DOI: 10.1002/mrm.25147.

[34] Z. H. Ren, L. Marechal, W. Luo, J. Su, and S. Y. Huang, "Magnet array for a portable magnetic resonance imaging system," *2015 IEEE MTT-S International Microwave Workshop Series on RF and Wireless Technologies for Biomedical and Healthcare Applications, IMWS-BIO 2015 - Proceedings*, pp. 92–95, 2015. DOI: 10.1109/IMWS-BIO.2015.7303793.

[35] J. P. Stockmann, C. Z. Cooley, B. Guerin, M. S. Rosen, and L. L. Wald, "Transmit Array Spatial Encoding (TRASE) using broadband WURST pulses for RF spatial encoding in inhomogeneous B0 fields," *Journal of Magnetic Resonance*, vol. 268, pp. 36–48, 2016, ISSN: 10960856. DOI: 10.1016/j.jmr.2016.04.005. [Online]. Available: http://dx.doi.org/10.1016/j.jmr.2016.04.005.

[36] C. Z. Cooley, P. C. McDaniel, J. P. Stockmann, S. A. Srinivas, S. F. Cauley, M. Śliwiak, C. R. Sappo, C. F. Vaughn, B. Guerin, M. S. Rosen, M. H. Lev, and L. L. Wald, "A portable scanner for magnetic resonance imaging of the brain," *Nature Biomedical Engineering*, 2020, ISSN: 2157846X. DOI: 10.1038/s41551-020-00641-5.

[37] T. O'Reilly, W. M. Teeuwisse, and A. G. Webb, "Three-dimensional MRI in a homogenous 27 cm diameter bore Halbach array magnet," *Journal of Magnetic Resonance*, vol. 307, 2019, ISSN: 10960856. DOI: 10.1016/j.jmr.2019.106578.

[38] T. O'Reilly, W. M. Teeuwisse, D. de Gans, K. Koolstra, and A. G. Webb, "In vivo 3D brain and extremity MRI at 50 mT using a permanent magnet Halbach array," *Magnetic Resonance in Medicine*, vol. 85, no. 1, pp. 495–505, 2021, ISSN: 15222594. DOI: 10.1002/mrm.28396.

[39] K. Koolstra, T. O'Reilly, P. Börnert, and A. Webb, "Image distortion correction for MRI in low field permanent magnet systems with strong B0 inhomogeneity and gradient field nonlinearities," *Magnetic Resonance Materials in Physics, Biology and Medicine*, vol. 34, no. 4, pp. 631–642, 2021, ISSN: 13528661. DOI: 10.1007/s10334-021-00907-2. [Online]. Available: https://doi.org/10.1007/s10334-021-00907-2.

[40] J. C. Sharp, S. B. King, Q. Deng, V. Volotovskyy, and B. Tomanek, "High-resolution MRI encoding using radiofrequency phase gradients," *NMR in Biomedicine*, vol. 26, no. 11, pp. 1602–1607, 2013, ISSN: 09523480. DOI: 10.1002/nbm.3023.

[41] A. R. Purchase, T. Pałasz, H. Sun, J. C. Sharp, and B. Tomanek, "A high duty-cycle, multi-channel, power amplifier for high-resolution radiofrequency encoded magnetic resonance imaging," *Magnetic Resonance Materials in Physics, Biology and Medicine*, vol. 32, no. 6, pp. 679–692, 2019, ISSN: 13528661. DOI: 10.1007/s10334-019-00763-1. [Online]. Available: https://doi.org/10.1007/s10334-019-00763-1.

[42] H. Sun, A. AlZubaidi, A. Purchase, and J. C. Sharp, "A geometrically decoupled, twisted solenoid single-axis gradient coil set for TRASE," *Magnetic Resonance in Medicine*, vol. 83, no. 4, pp. 1484–1498, 2020, ISSN: 15222594. DOI: 10.1002/mrm.28003.

[43] A. Banerjee, G. Bertolesi, C. Ling, B. Blasiak, A. Purchase, O. Calderon, B. Tomanek, and S. Trudel, "Bifunctional pyrrolidin-2-one terminated manganese oxidenanoparticles for combined magnetic resonance and fluorescenceimaging," *ACS Appl. Mater. Interfaces: 11, 13069 13078*, 2019.

[44] Q. Deng, S. B. King, V. Volotovskyy, B. Tomanek, and J. C. Sharp, "B1 transmit phase gradient coil for single-axis TRASE RF encoding," *Magnetic Resonance Imaging*, vol. 31, no. 6, pp. 891–899, 2013, ISSN: 0730725X. DOI: 10.1016/j.mri.2013.03.017. [Online]. Available: http://dx.doi.org/10.1016/j.mri.2013.03.017.

[45] A. R. Purchase, L. Vidarsson, K. Wachowicz, P. Liszkowski, H. Sun, G. E. Sarty, J. C. Sharp, and B. Tomanek, "A Short and Light, Sparse Dipolar Halbach Magnet for MRI," *IEEE Access*, vol. 9, pp. 95 294–95 303, 2021, ISSN: 21693536. DOI: 10.1109/ACCESS.2021.3093530.

[46] H. Haynes and W. M. Holmes, "The emerging use of magnetic resonance imaging (mri) for 3d analysis of sediment structures and internal flow processes.," *In Geomorphological Techniques (Online Edition) (Geomorphological Techniques (Online Edition)). British Society for Geomorphology.*, 2013. [Online]. Available: http://www.geomorphology.org.uk/assets/publications/subsections/pdfs/OnsitePublicationSubsection/31/1.5.4_imagingsediments.pdf.

[47] R. W. Brown, Y.-C. N.Cheng, E. M. Haacke, M. R. Thompson, and R. Venkatesan, *Magnetic Resonance Imaging: Physical Principles and Sequence Design*, 2nd. John Wiley and Sons Inc., 2014.

[48] E. Berry and A. J. Bulpitt, *Fundamentals of MRI: An Interactive Learning Approach*. CRC Press, 2008.

[49] P. Lauterbur, "Image formation by induced location interactions," *Nature*, vol. 242, pp. 190–191, 1973.

[50] A. Abragam, "The principles of nuclear magnetism," *Oxford University Press*, 1961.

[51] B Tomanek and J Sharp, "Magnetic resonance technology in: Biomedical imaging: Principles and applications, ed. by salzer reiner," *Wiley and Sons Inc., Public.*, 2012.

[52] C. Chen and D. Hoult, "Biomedical magnetic resonance technology," *IOP Publishing Ltd.*, 1989.

[53] F. Bloch, "Nuclear induction," *Physical Review*, vol. 70, no. 7-8, pp. 460–474, 1946, ISSN: 0031899X. DOI: 10.1103/PhysRev.70.460.

[54] E. L. Hahn, "Spin echoes," *Physical Review*, vol. 80, no. 4, pp. 580–594, 1950, ISSN: 0031899X. DOI: 10.1103/PhysRev.80.580.

[55] B. Gruber, M. Froeling, T. Leiner, and D. W. Klomp, "RF coils: A practical guide for nonphysicists," *Journal of Magnetic Resonance Imaging*, vol. 48, no. 3, pp. 590–604, 2018, ISSN: 15222586. DOI: 10.1002/jmri.26187.

[56] D. I. Hoult and B. Bhakar, "NMR signal reception: Virtual photons and coherent spontaneous emission," *Concepts in Magnetic Resonance*, vol. 9, no. 5, pp. 277–297, 1997, ISSN: 10437347. DOI: 10.1002/(sici)1099-0534(1997)9:5⟨277::aid-cmr1⟩3.0.co;2-w.

[57] A. Macovski, "Noise in mri," *Magn. Reson. Med. 36: 494-497*, 1996.

[58] H. Nyquist, "Thermal agitation of electric charge in conductors," *Phys. Rev.*, vol. 32, p. 110, 1928.

[59] J. B. Johnson, "Thermal agitation of electricity in conductors," *Phys. Rev.*, vol. 32, p. 97, 1928.

[60] C. Balanis, "Advanced engineering electromagnetics," *John Wiley and Sons, Inc. Second Edition*, 2012.

[61] D. I. Hoult and P. C. Lauterbur, "The sensitivity of the zeugmatographic experiment involving human samples," *Journal of Magnetic Resonance (1969)*, vol. 34, no. 2, pp. 425–433, 1979, ISSN: 00222364. DOI: 10.1016/0022-2364(79)90019-2.

[62] G. Giovannetti and L. Menichetti, "Litz wire rf coils for low frequency nmr applications," *Measurement*, vol. 110, pp. 116–120, 2017.

[63] I. Rabi, J. Zacharias, S. Millman, and P. Kusch, "A new method of measuring nuclear magnetic moment," *Phys. Rev.*, vol. 53, p. 318, 1938.

[64] Z. Liang and P. Lauterbur, "Principles of magnetic resonance imaging: A signal processing perspective," *Wiley-IEEE Press*, 2000.

[65] D. Moratal, A. Valles-Luch, L Marti-Bonmati, and M. Brummer, "K-space tutorial: An mri educational tool for a better understanding of k-space," *Biomedical Imaging and Intervention*, 2008.

[66] Q. Qin, "Point spread functions of the T2 decay in k-space trajectories with long echo train," *Magnetic Resonance Imaging*, vol. 30, no. 8, pp. 1134–1142, 2012, ISSN: 0730725X. DOI: 10.1016/j.mri.2012.04.017. [Online]. Available: http://dx.doi.org/10.1016/j.mri.2012.04.017.

[67] M. K. Stehling, R. Turner, and P. Mansfield, "Echo-planar imaging: Magnetic resonance imaging in a fraction of a second," *Science*, vol. 254, no. 5028, pp. 43–50, 1991.

[68] M. A. Bernstein, K. F. King, and X. J. Zhou, *Handbook of MRI Pulse Sequences*. Elsevier Academic Press, 2004.

[69] R. S. Likes, "Moving gradient zeugmatography," *US Patent: US4307343A*, 1981.

[70] R. Pohmann, O. Speck, and K. Scheffler, "Signal-to-noise ratio and MR tissue parameters in human brain imaging at 3, 7, and 9.4 tesla using current receive coil arrays," *Magnetic Resonance in Medicine*, vol. 75, no. 2, pp. 801–809, 2016, ISSN: 15222594. DOI: 10.1002/mrm.25677.

[71] A. E. Campbell-Washburn, R. Ramasawmy, M. C. Restivo, I. Bhattacharya, B. Basar, D. A. Herzka, M. S. Hansen, T. Rogers, W. P. Bandettini, D. R. McGuirt, C. Mancini, D. Grodzki, R. Schneider, W. Majeed, H. Bhat, H. Xue, J. Moss, A. A. Malayeri, E. C. Jones, A. P. Koretsky, P. Kellman, M. Y. Chen, R. J. Lederman, and R. S. Balaban, "Opportunities in interventional and diagnostic imaging byusing high-performance low-field-strength mri," *Radiology*, vol. 293, no. 3, pp. 384–393, 2019.

[72] Y. Liu, A. T. Leong, Y. Zhao, L. Xiao, H. K. Mak, A. C. O. Tsang, G. K. Lau, G. K. Leung, and E. X. Wu, "A low-cost and shielding-free ultra-low-field brain MRI scanner," *Nature Communications*, vol. 12, no. 1, pp. 1–14, 2021, ISSN: 20411723. DOI: 10.1038/s41467-021-27317-1.

[73] J. C. Sharp and S. B. King, "MRI using radiofrequency magnetic field phase gradients," *Magnetic Resonance in Medicine*, vol. 63, no. 1, pp. 151–161, 2010, ISSN: 15222594. DOI: 10.1002/mrm.22188.

[74] H. Sun, S. Yong, and J. C. Sharp, "The twisted solenoid RF phase gradient transmit coil for TRASE imaging," *Journal of Magnetic Resonance*, vol. 299, pp. 135–150, 2019, ISSN: 10960856. DOI: 10.1016/j.jmr.2018.12.015. [Online]. Available: https://doi.org/10.1016/j.jmr.2018.12.015.

[75] P. Bohidar, H. Sun, G. E. Sarty, and J. C. Sharp, "TRASE 1D sequence performance in imperfect B1 fields," *Journal of Magnetic Resonance*, vol. 305, pp. 77–88, 2019, ISSN: 10960856. DOI: 10.1016/j.jmr.2019.06.005. [Online]. Available: https://doi.org/10.1016/j.jmr.2019.06.005.

[76] P. Bohidar, H. Sun, J. C. Sharp, and G. E. Sarty, "The effects of coupled B1 fields in B1 encoded TRASE MRI - A simulation study," *Magnetic Resonance Imaging*, vol. 74, pp. 74–83, 2020, ISSN: 18735894. DOI: 10.1016/j.mri.2020.09.003. [Online]. Available: https://doi.org/10.1016/j.mri.2020.09.003.

[77] P. Scherz, *Practical Electronics for Inventors*. McGraw-Hill, 2000.

[78] S. J. Theeuwen and J. H. Qureshi, "LDMOS technology for RF power amplifiers," *IEEE Transactions on Microwave Theory and Techniques*, vol. 60, no. 6 PART 2, pp. 1755–1763, 2012, ISSN: 00189480. DOI: 10.1109/TMTT.2012.2193141.

[79] C. W. Tang and K. Y. Tong, "A compact large signal model of LDMOS," *Solid-State Electronics*, vol. 46, no. 12, pp. 2111–2115, 2002, ISSN: 00381101. DOI: 10.1016/S0038-1101(02)00238-1.

[80] H. Sigg, G. Vendelin, T. Cauge, and J. Kocsis, "D- MOS transistor for microwave applications," *IEEE Transactions on Electron Devices*, vol. ED-19, no. 1, pp. 45–53, 1972, ISSN: 00189383.

[81] J. Walker, *Handbook of RF and Microwave Power Amplifiers*. Cambridge University Press, 2012.

[82] "Electronics tutorials: Amplifier classes," 2022. [Online]. Available: https://www.electronics-tutorials.ws/amplifier/amplifier-classes.html.

[83] J. Zhen, R. Dykstra, C. Eccles, G. Gouws, and S. Obruchkov, "A compact Class D RF power amplifier for mobile nuclear magnetic resonance systems," *Review of Scientific Instruments*, vol. 88, no. 7, 2017, ISSN: 10897623. DOI: 10.1063/1.4994734. [Online]. Available: http://dx.doi.org/10.1063/1.4994734.

[84] "Analogic: The world resource for health and security technologyan8110 rf amplifer installation manual," *Analogic Corporation Medical Imaging Division, Insert no. 16-00070 REV. 02., Binder no. 28-002011, Publication no. 10-62836-01*, 2002.

[85] "Tomco technologies. 500 w pulsed rf amplifer modelbt00 beta operation manual," *Tomco Electronics Pty Ltd, Document No. T001591 Issue A, June 25*, 2002.

[86] "Communication power corporation (cpc). the worlds leading supplier of broadband power amplifiers," *Model 0.2T500M*, 2012. [Online]. Available: https://www.cpcamps.com/sheets/0.2T500M.pdf.

[87] M. Harrington, W.Heist, C. Loriatti, and J. White., "Mks instruments product specifcation document xx-s35-64. 18 kw, 1.5t linear, solid staterf pulse.," N/A. [Online]. Available: https://www.mksinst.com/f/63-87-mhz-mri-rf-amplifer.

[88] "Tomco technologies," *RF Amplifer Data Sheet BT01000-Delta.*, 2019. [Online]. Available: http://www.tomcorf.com/assets/standard_pulsed/DS006689B.pdf..

[89] "Ultra electronics herley," *RF Power Amplifier SystemModel 3900-1. 3061 Lancaster, PA, USA.*, N/A. [Online]. Available: https://www.ultraherley.com/uploads/herley/datasheets/lancaster/Medical/3900-1.pdf.

[90] "Analogic: The world resource for health and securitytechnology," *6 kW RF Power Amplifer for MRI ScannerApplications, Analogic Medical Imaging Group., ANALOGICCorporation, Bulletin No. 16-00115 REV 1 3/04, Printed in USA*, 2016.

[91] D. Myer, "Radiofrequency power amplifers for nmr and mri.," *eMagRes*, 2007. DOI: 10.1002/9780470034590.emrstm1138.

[92] E. Ivanov, A. Pogromsky, J. V. D. Brink, and J. Rooda, "Optimization of duty cycles for mri scanners," *Concepts MagnReson Part B (Magn Reson Eng)*, vol. 37B, no. 3, pp. 180–192, 2010.

[93] M. Goldman, H. Johannesson, O. Axelsson, and M. Karlsson, "Design and implementation of 13c hyper polarization from parahydrogen, for new mri contrast agents.," *C.R. Chimie*, vol. 9, no. 357-363, 2006.

[94] G. Holland and E. Heysmond, "A solid state high-power rf amplifer for pulsed nmr," *J Phys E Sci Instrum*, vol. 12, p. 480, 1979.

[95] R. Horowitz and W. Hill, *Foundations, Chap 1. In: The art ofelectronics*, 3rd. Cambridge University Press, New York, 2015.

[96] "Zhl-1-2w+ coaxial amplifer.," *50 High Power 2W 5 to 500MHz, Mini-Circuits.*, 2018. [Online]. Available: https://ww2.minicircuits.com/pdfs/ZHL1-2W.pdf.

[97] J. Klitzing, "A 1 kw sspa for 1.8–54 mhz. amateur ratiostation w6pql.," 2018. [Online]. Available: https://www.w6pql.com/.

[98] "Ampleon (2015) blf188xr; blf188xrs. power ldmostransistor product data sheet, rev. 6–1 september.," [Online]. Available: https://www.ampleon.com/products/broadcast/0-500-mhz-rf-power-transistors/BLF188XR.html.

[99] M Southam, "Tdk-lambda americas inc., user manualfor genesystm 750w/1500w programable dc power supplies.," 2013. [Online]. Available: https://www.us.tdk-lambda.com/hp/pdfs/Product_manuals/83507013.pdf.

[100] S. Sharkov, A. K. AA, and S. Polikhov, "100 kw very compact pulsed solid-state rf amplifier: Development and tests," *In: Proceedings of NAPA2016 Chicago, IL, USA. ISBN:978-3-95450-180-9*, 2016.

[101] H. Ward and et. al., "The arrl handbook for radio communications," *ARRL The national association for amateur radio: 96 Edition*, 2019.

[102] J. C. Sharp, D. Yin, R. H. Bernhardt, Q. Deng, A. E. Procca, R. L. Tyson, K. Lo, and B. Tomanek, "The integration of real and virtual magnetic resonance imaging experiments in a single instrument," *Review of Scientific Instruments*, vol. 80, no. 9, 2009, ISSN: 00346748. DOI: 10.1063/1.3202410.

[103] J. Walker, *Amplifier measurements, Chap 12. In: Handbook of RF and microwave power amplifiers*, 3rd. Cambridge University Press, New York, 2012.

[104] C. Bowick, J. Byler, and C. Ajluni, *RF Circuit Design*, 2nd. Elsevier Inc., Amsterdam, 2008.

[105] "Medical electrical equipment. iec 60601-1. international standard, 3rd edn, 2005–12. reference number: Iec60601-1:2005," 2005.

[106] G. E. Sarty and A. Obenaus, "Magnetic resonance imaging of astronauts on the International Space Station and into the solar system," *Canadian Aeronautics and Space Journal*, vol. 58, no. 1, pp. 60–68, 2012, ISSN: 00082821. DOI: 10.5589/q12-005.

[107] G. Sarty, S. Kontulainen, A. Baxter-Jones, R. Pierson, K.Turek, A. Obenaus, B.Tomanek, J. Sharp, A. Scott, and L. Piche, "Compact MRI for astronaut physiological research and medical diagnosis," *Com Dev, AIAA SPACE conference and exposition, Pasadena, California*, 2012.

[108] G. E. Sarty and L. Vidarsson, "Magnetic resonance imaging with RF encoding on curved natural slices," *Magnetic Resonance Imaging*, vol. 46, no. October 2017, pp. 47–55, 2018, ISSN: 18735894. DOI: 10.1016/j.mri.2017.10.007. [Online]. Available: https://doi.org/10.1016/j.mri.2017.10.007.

[109] J. P. Marques, F. F. Simonis, and A. G. Webb, "Low-field MRI: An MR physics perspective," *Journal of Magnetic Resonance Imaging*, vol. 49, no. 6, pp. 1528–1542, 2019, ISSN: 15222586. DOI: 10.1002/jmri.26637.

[110] K. Halbach, "Design of permanent multipole magnets with oriented rare earth cobalt material," *Nuclear Instruments and Methods*, vol. 169, no. 1, pp. 1–10, 1980, ISSN: 0029554X. DOI: 10.1016/0029-554X(80)90094-4.

[111] K. Turek and P. Liszkowski, "Magnetic field homogeneity perturbations in finite Halbach dipole magnets," *Journal of Magnetic Resonance*, vol. 238, pp. 52–62, 2014, ISSN: 10960856. DOI: 10.1016/j.jmr.2013.10.026. [Online]. Available: http://dx.doi.org/10.1016/j.jmr.2013.10.026.

[112] C. Z. Cooley, J. P. Stockmann, B. D. Armstrong, M. Sarracanie, M. H. Lev, M. S. Rosen, and L. L. Wald, "Two-dimensional imaging in a lightweight portable MRI scanner without gradient coils," *Magnetic Resonance in Medicine*, vol. 73, no. 2, pp. 872–883, 2015, ISSN: 15222594. DOI: 10.1002/mrm.25147.

[113] C. Zimmerman Cooley, M. W. Haskell, S. F. Cauley, C. Sappo, C. D. Lapierre, C. G. Ha, J. P. Stockmann, and L. L. Wald, "Design of sparse halbach magnet arrays for portable MRI using a genetic algorithm," *IEEE Transactions on Magnetics*, vol. 54, no. 1, 2017, ISSN: 00189464. DOI: 10.1109/TMAG.2017.2751001.

[114] A. Purchase, G. Sarty, L Vidarsson, K Wachowicz, P Liszkowski, H Sun, J. Sharp, and B Tomanek., "Design of a permanent magnet for mri of theankle on the international space station.," *Proc. Intl. Soc. Mag. Reson. Med.*, 2020.

[115] J. Coey, *Magnetism and Magnetic Materials*. Cambridge University Press, 2009.

[116] V. lacovacci, G. Lucarini, L. Ricotti, and A. Menciassi, "Magnetic field-based technologies for lab-on-a-chip applications," *In book: Lab-on-a-Chip Fabrication and Application*, 2016. DOI: 0.5772/61470.

[117] D. R. Lide, "Crc handbook of chemistry and physics," *CRC Press*, 2009.

[118] H. W. Sung and C. Rudowicz, "Physics behind the magnetic hysteresis loop - A survey of misconceptions in magnetism literature," *Journal of Magnetism and Magnetic Materials*, vol. 260, no. 1-2, pp. 250–260, 2003, ISSN: 03048853. DOI: 10.1016/S0304-8853(02)01339-2.

[119] C. Hugon, F. D'Amico, G. Aubert, and D. Sakellariou, "Design of arbitrarily homogeneous permanent magnet systems for NMR and MRI: Theory and experimental developments of a simple portable magnet," *Journal of Magnetic Resonance*, vol. 205, no. 1, pp. 75–85, 2010, ISSN: 10907807. DOI: 10.1016/j.jmr.2010.04.003. [Online]. Available: http://dx.doi.org/10.1016/j.jmr.2010.04.003.

[120] Z. H. Ren, J. Gong, and S. Y. Huang, "An Irregular-Shaped Inward-Outward Ring-Pair Magnet Array with a Monotonic Field Gradient for 2D Head Imaging in Low-Field Portable MRI," *IEEE Access*, vol. 7, pp. 48 715–48 724, 2019, ISSN: 21693536. DOI: 10.1109/ACCESS.2019.2909834.

[121] H. Zijlstra, "Permanent magnetic systems for nmr tomography," *Philips Journal of Research*, vol. 40, pp. 259–288, 1985.

[122] K. Halbach, "IEEE Transactions on Nuclear Science, Vol. NS-26, No. 3, June 1979," no. 3, pp. 3882–3884, 1979.

[123] T. R. Ní Mhíocháin, D. Weaire, S. M. McMurry, and J. M. Coey, "Analysis of torque in nested magnetic cylinders," *Journal of Applied Physics*, vol. 86, no. 11, pp. 6412–6424, 1999, ISSN: 00218979. DOI: 10.1063/1.371705.

[124] R. C. Jachmann, D. R. Trease, L. S. Bouchard, D. Sakellariou, R. W. Martin, R. D. Schlueter, T. F. Budinger, and A. Pines, "Multipole shimming of permanent magnets using harmonic corrector rings," *Review of Scientific Instruments*, vol. 78, no. 3, 2007, ISSN: 00346748. DOI: 10.1063/1.2713438.

[125] Z. H. Ren, W. C. Mu, and S. Y. Huang, "Design and Optimization of a Ring-Pair Permanent Magnet Array for Head Imaging in a Low-Field Portable MRI System," *IEEE Transactions on Magnetics*, vol. 55, no. 1, pp. 1–8, 2019, ISSN: 00189464. DOI: 10.1109/TMAG.2018.2876679.

[126] J. E. Hilton and S. M. McMurry, "Halbach cylinders with improved field homogeneity and tailored gradient fields," *IEEE Transactions on Magnetics*, vol. 43, no. 5, pp. 1898–1902, 2007, ISSN: 00189464. DOI: 10.1109/TMAG.2007.891727.

[127] G. Kustler, "Computation of NdFeB-halbach cylinders with circular and elliptical cross sections in three dimensions," *IEEE Transactions on Magnetics*, vol. 46, no. 9, pp. 3601–3607, 2010, ISSN: 00189464. DOI: 10.1109/TMAG.2010.2048432.

[128] Q. Chen, G. Zhang, Y. Xu, and X. Yang, "Design and simulation of a multilayer halbachmagnet for nmr," *Concepts in Magnetic Resonance Part B*, vol. 45B, no. 3, pp. 134–141, 2015.

[129] S. Tewari, T. O'Reilly, and A. Webb, "Improving the field homogeneity of fixed- and variable-diameter discrete Halbach magnet arrays for MRI via optimization of the angular magnetization distribution," *Journal of Magnetic Resonance*, vol. 324, p. 106 923, 2021, ISSN: 10960856. DOI: 10.1016/j.jmr.2021.106923. [Online]. Available: https://doi.org/10.1016/j.jmr.2021.106923.

[130] K. K. Nielsen, A. R. Insinga, C. R. Bahl, and R. Bjørk, "Optimizing a Halbach cylinder for field homogeneity by remanence variation," *Journal of Magnetism and Magnetic Materials*, vol. 514, no. June, p. 167 175, 2020, ISSN: 03048853. DOI: 10.1016/j.jmmm.2020.167175. [Online]. Available: https://doi.org/10.1016/j.jmmm.2020.167175.

[131] T. O'Reilly and A. Webb, "Deconstructing and reconstructing MRI hardware," *Journal of Magnetic Resonance*, vol. 306, no. xxxx, pp. 134–138, 2019, ISSN: 10960856. DOI: 10.1016/j.jmr.2019.07.014. [Online]. Available: https://doi.org/10.1016/j.jmr.2019.07.014.

[132] J. Perlo, F. Casanova, and B. Blümich, "3D imaging with a single-sided sensor: An open tomograph," *Journal of Magnetic Resonance*, vol. 166, no. 2, pp. 228–235, 2004, ISSN: 10907807. DOI: 10.1016/j.jmr.2003.10.018.

[133] "International Space Station Flight Crew Integration Standard (NASA-STD-3000/T)," *Nat. Aeronaut. Space Admin., Revision E, Space Station ProgramOf ce, Johnson Space Center, Houston, TX, USA, Jun.*, 2006.

[134] G. E. Sarty, K. Kontulainen, P. Bohidar, H. Ejalonibu, A. AlZubaidi, L. Vidarsson, G. Warner, P. Piche, M. Mocanita, D. McCabe, P. Cameron, K. Smith, K. Turek, P. Liszkowski, B. Tomanek, H. Sun, A. Purchase, and J. Sharp, "PT11 Magnetic resonance imaging instrument for Ankles," *Can. Space Agency, Saint-Hubert, QC, Canada, Tech. Rep. 9F063-160953/011/MTB*, 2019.

[135] T. O'Reilly, W. M. Teeuwisse, D. de Gans, K. Koolstra, and A. G. Webb, "In vivo 3D brain and extremity MRI at 50 mT using a permanent magnet Halbach array," *Magnetic Resonance in Medicine*, vol. 85, no. 1, pp. 495–505, 2021, ISSN: 15222594. DOI: 10.1002/mrm.28396.

[136] L. Vidarsson, "Magnetic resonance imaging (mri) systems and method," *U.S. Patent: 2015 0 260 809*,

[137] H. Raich and P. Blümler, "Design and construction of a dipolar Halbach array with a homogeneous field from identical bar magnets: NMR mandhalas," *Concepts in Magnetic Resonance Part B: Magnetic Resonance Engineering*, vol. 23, no. 1, pp. 16–25, 2004, ISSN: 10437347. DOI: 10.1002/cmr.b.20018.

[138] "BINIC Magnet Ltd.," 2021. [Online]. Available: http://www.binicmagnet.com/PR01.asp.

[139] A. R. Purchase, G. E. Sarty, L. Vidarrson, K. Wachowicz, P. Liszkowski, H. Sun, J. C. Sharp, and B. Tomanek, "Design of a permanent magnet for MRI of the ankle on the international space station," *Proc. Int. Soc. Mag.Reson. Med*, vol. 28, no. 1252, 2020.

[140] D. Whitley, "A genetic algorithm tutorial," *Statistics and Computing*, vol. 4, no. 2, pp. 65–85, 1994, ISSN: 09603174. DOI: 10.1007/BF00175354.

[141] L. Vidarsson, "Magnetic resonance imaging (MRI) systems and method," *U.S. Patent 2015 0 260 809 A1, Sep. 17*, 2015.

[142] ALL3DP, "3D printer test print," [Online]. Available: https://all3dp.com/2/3d-printer-test-print-10-best-3d-models-to-torture-your-3dprinter/.

[143] M. Tallon, G. Scott, M. Dorma, S. Maw, M. Bradley, and G. Sarty, "Compact MRI field mapper," *Phys. Eng. Phys. Capstone Project, Univ.Saskatchewan, Saskatoon, SK, Canada, Tech. Rep*, 2015.

[144] H. Han, R. Moritz, E. Oberacker, H. Waiczies, T. Niendorf, and L. Winter, "Open Source 3D Multipurpose Measurement System with Submillimetre Fidelity and First Application in Magnetic Resonance," *Scientific Reports*, vol. 7, no. 1, pp. 1–12, 2017, ISSN: 20452322. DOI: 10.1038/s41598-017-13824-z.

[145] C. Hugon, "Python Interface to Metrolab 3 AxisHall Probe THM1176," 2021. [Online]. Available: https://github.com/Hyperfine/pyTHM1176.

[146] J. Sungeun, "GRBL Simple Gcode Streamer," *https://github.com/grbl/grbl*, 2021.

[147] A. R. Purchase, "Three-Dimensional Magnetic FieldMapper (3DFM)," 2021. [Online]. Available: https://github.com/Aaron-Purchase/3DFM.

[148] S. C, P. A, T. B, and S. JC, "A truncated twisted solenoid rf phase gradient transmit coil for trase mri," *Proc. Intl. Soc. Mag. Reson.Med. 31:6513*, 2022.

[149] J. Sharp, A. Purchase, C. Sedlock, and B.Tomanek, "A parallel-transmit halbach magnet trase mri system," *Proc. Intl. Soc. Mag. Reson.Med. 31:5670*, 2022.

[150] H. Y. Carr and E. M. Purcell, "Effects of diffusion on free precession in nuclear magnetic resonance experiments," *Physical Review*, vol. 94, no. 3, pp. 630–638, 1954, ISSN: 0031899X. DOI: 10.1103/PhysRev.94.630.

[151] G. E. Sarty, A. Scott, L. Piche, A. McColgan, C. Earnshaw, K. Turek, P. Liszkowski, B. Tomanek, J. Sharp, R. Tyson, K. Lo, V. Volotovskyy, and D. Yin, "Wrist magnetic resonance imager: ISS-MRI," *Study Phase, Can. Space Agency, Saint-Hubert, QC, Canada, FinalRep. 9F008A130264/004/MTB, 2014.*, 2014.

[152] Y. Zhou, Z. Zhang, J. Hou, and R. Yang, "Imaging finding and arthroscopic treatment of isolated contracture of the rectus femoris muscle: A case report," *BMC Musculoskeletal Disorders*, vol. 20, no. 1, pp. 1–6, 2019, ISSN: 14712474. DOI: 10.1186/s12891-019-2696-8.

[153] A. Phair, M. Brideson, and L. K. Forbes, "A cylindrical basis set for shim coil design in magnetic resonance imaging," *Concepts in Magnetic Resonance Part B: Magnetic Resonance Engineering*, vol. 48B, no. 3, 2018, ISSN: 1552504X. DOI: 10.1002/cmr.b.21400.

[154] P. C. McDaniel, C. Z. Cooley, J. P. Stockmann, and L. L. Wald, "The MR Cap: A single-sided MRI system designed for potential point-of-care limited field-of-view brain imaging," *Magnetic Resonance in Medicine*, vol. 82, no. 5, pp. 1946–1960, 2019, ISSN: 15222594. DOI: 10.1002/mrm.27861.

[155] G. E. Sarty, "Trase mri on twin natural slices," *Magnetic Resonance Materials in Physics, Biology and Medicine. In-review.*, 2022.

[156] P. C. McDaniel, C. Z. Cooley, J. P. Stockmann, and L. L. Wald., "A target-field shimming approach forimproving the encoding performance of alightweight halbach magnet for portable brainmri," *Proc. Intrl. Soc. Mag. Reson. Med. 27:0215*, 2019.

[157] "Sarty's usask team tests technology for mri in space.," 2021. [Online]. Available: https://news.usask.ca/articles/research/2021/sartys-usask-team-tests-technology-for-mri-in-space.php.

[158] G. E. Sarty, "Merlin MRI Design Definition Document," 2020.

[159] E. Der, V. Volotovskyy, H. Sun, B. Tomanek, and J. C. Sharp, "Design of a high power PIN-diode controlled switchable RF transmit array for TRASE RF imaging," *Concepts in Magnetic Resonance Part B: Magnetic Resonance Engineering*, vol. 48B, no. 1, 2018, ISSN: 1552504X. DOI: 10.1002/cmr.b.21365.

[160] S. Srinivas, C. Cooley, J. Stockmann, P. McDaniel, and L. Wald, "Retrospective electromagnetic interference mitigation in a portable low field mri system," *Proc. Intl. Soc. Mag. Reson. Med. 28-1269*, vol. 87, no. 2, pp. 614–628, 2020.

[161] S. Srinivas, S. Cauley, J. Stockmann, C. Sappo, C. Vaughn, L. Wald, W. Grissom, and C. Cooley, "External dynamic interference estimation and removal (editer) for low field mri," *Magn. Reson. Med.*, 2022.

[162] RattmMotor, "Rattmmotor nema24 closed loop stepper servo motor 88mm 3n.m + hss60 2-phase hybrid driver for cnc router engrvaving milling machine," [Online]. Available: https://www.amazon.ca/RATTMMOTOR-Stepper-2-Phase-Engrvaving-Milling/dp/B081YK6MJN.

[163] Z. Xiaodong, H. Junjun, and S. Chunlei, "An approach of micro-stepping control for the step motors based on FPGA," *Proceedings of the IEEE International Conference on Industrial Technology*, vol. 2005, pp. 125–130, 2005. DOI: 10.1109/ICIT.2005.1600622.

[164] StepperOnline, "Dual shaft nema 24 cnc stepper motor 3.4nm (481.6 oz.in) 60x60x100mm 8 wires," [Online]. Available: https://www.omc-stepperonline.com/dual-shaft-nema-24-cnc-stepper-motor-3-4nm-481-6-oz-in-60x60x100mm-8-wires.html.

[165] E. Danieli, J. Mauler, J. Perlo, B. Blümich, and F. Casanova, "Mobile sensor for high resolution NMR spectroscopy and imaging," *Journal of Magnetic Resonance*, vol. 198, no. 1, pp. 80–87, 2009, ISSN: 10907807. DOI: 10.1016/j.jmr.2009.01.022. [Online]. Available: http://dx.doi.org/10.1016/j.jmr.2009.01.022.

[166] Y. Jun, J. Lee, and J. Cheon., "Chemical design of nanoparticle probes for high performance magnetic resonance imaging.," *Angew. Chem., Int. Ed.*, vol. 47, pp. 5122–5135, 2008.

[167] J. Ramalho, R. Semelka, M. Ramalho, R. Nunes, M. AlObaidy, and M. Castillo, "Gadolinium-based contrast agent accumulation andtoxicity: An update.," *Am. J. Neuroradiol.*, vol. 37, pp. 1192–1198, 2016.

[168] J. Crossgrove and W. Zheng, "Manganese toxicity upon overexposure.," *NMR Biomed.*, vol. 17, pp. 544–553, 2004.

[169] C. A. Massaad and R. G. Pautler, "In magnetic resonance neuroimaging; modo, m., bulte, j. w. m., eds.;" *Springer*, pp. 145–174, 2011.

[170] A. P. Koretsky and A. Silva, "Manganese-enhanced magneticresonance imaging (memri).," *NMR Biomed.*, vol. 17, pp. 527–531, 2004.

[171] H. T. Ta, Z. Li, Y Y. Wu, G. Cowin, S. Zhang, A. Yago, A. K. Whittaker, and Z. P. Xu, "Effects of magnetic field strength and particle aggregation on relaxivity of ultra-small dual contrast iron oxide nanoparticles.," *Mater. Res. Express*, vol. 4, p. 116 105, 2017.

[172] P. Caravan, C. T. Farrar, L. Frullano, and R. Uppal, "Influence of molecular parameters and increasing magnetic field strength on relaxivity of gadolinium- and manganese-based t1 contrast agents.," *Contrast Media Mol. Imaging*, vol. 4, pp. 89–100, 2009.

[173] M. F. Tweedle, E. Kanal, and R. Muller, "Considerations in the selection of a new gadolinium-based contrast agent.," *Appl. Radiol.*, vol. 43, pp. 1–11, 2014.

Appendix A: Contrast Agents

A.1 Contrast enhancement using magnetic materials

Paramagnetic (see Chapter 4) particles such as gadolinium (Gd^{3+}) or manganese (Mn^{2+}) are used as contrast agents in MRI since they reduce the T_1 relaxation time causing increased contrast in T_1-weighted images [166]. Although Gd^{3+} and Mn^{2+}-based contrast agents are predominantly used in clinical MRI, they are toxic at high does, and in some cases, they were found to be toxic at normal doses [167]. To reduce toxicity and enable multi-modality, including MRI and fluorescence imaging, paramagnetic nanoparticles (NPs) composed of paramagnetic manganese have been developed. I coauthored a paper [43] showing that pyrrolidin-2-one-capped manganese oxide NPs (MnO^{pyrr}) enable MRI and fluorescence microscopy to act as efficient bifunctional bio-nanoprobes. The method of synthesis of 10 nm MnO NPs was proposed. The r_1 relaxivity and r_2/r_1 ratio indicate that these NPs are potential T_1 MRI contrast agents at clinical (3 T) and ultrahigh (9.4 T) magnetic fields. The constructed NPs are also photoluminescent. The luminescence is ascribed to the modification of the pyrrolidin-2-one during the thermal treatment. MnO^{pyrr} NPs were successfully used to enable fluorescence microscopy of HeLa cells, demonstrating bifunctional imaging capabilities. A low cytotoxic response in two distinct cell types (HeLa, HepG2) supports the suitability of MnO^{pyrr} NPs for biological imaging applications [168].

My main contribution to the MnO contrast agents research were measurements and

calculations of the relaxation rates and relaxivities using a clinical 3 T MRI system. Relaxivities (r_1 and r_2) were determined from relaxation times measured at different concentrations using the following equation:

$$\frac{1}{T_i} = \frac{1}{T_{0,i}} + r_i C \tag{A.1}$$

where T_i is the observed relaxation time in the presence of the diluted MnO^{pyrr} solution, $T_{0,i}$ is the relaxation of de-gasified and purified water, and C is the concentration of magnetic Mn^{2+} ions. To evaluate their potential as MRI contrast agents, MnO^{pyrr} particles were dispersed in water, the solution pH was adjusted to 7.4 (the approximate pH of plasma in the blood) by the addition of a few drops of dilute sodium hydroxide solution, and the T_1 and T_2 relaxation times were measured at 3.0 T and 9.4 T (Figure A.1).

MnO^{pyrr} can be used as T_1 MRI contrast agents because of their high r_1 values and low r_2/r_1 ratio [169, 170]. This ratio is low at 3 T showing high efficacy as contrast agents at 3 T but less at 9.4 T [171, 172]. The r_1 is also slightly lower for MnO^{pyrr} contrast agents compared to commercially available Gd-based contrast agents such

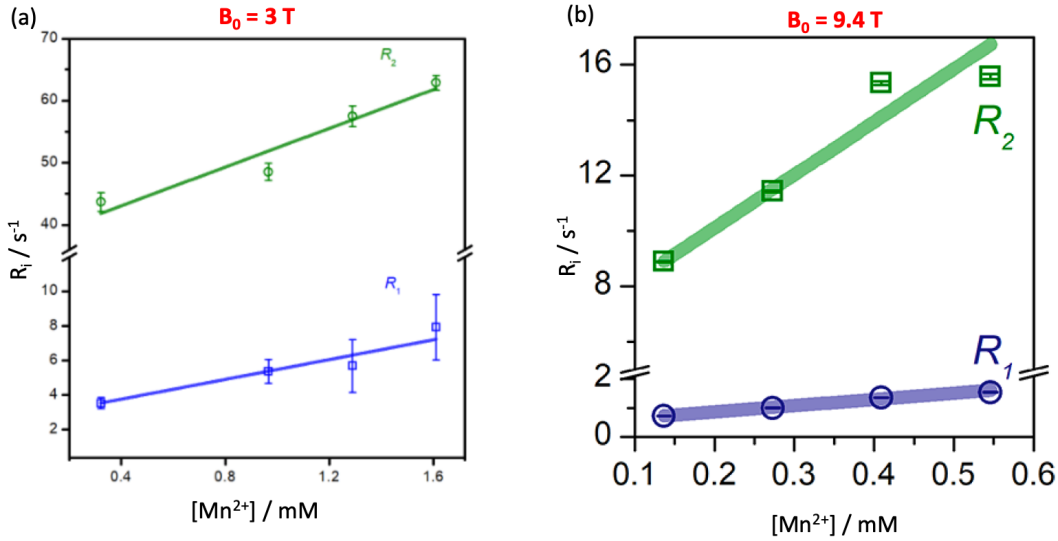

Figure A.1: Relaxivities of nanoparticles (MnO) suitable for MRI contrast agents at 3 T and 9.4 T [43]. (a) Measured relaxation rates fit: $r_1 = 2.9 \pm 0.3$ mM^{-1}, $r_2 = 15.6 \pm 2.3$ mM^{-1}, $r_2/r_1 = 5.4$. (b) Measured relaxation rates fit: $r_1 = 2.2 \pm 0.1$ mM^{-1}, $r_2 = 19 \pm 3$ mM^{-1}, $r_2/r_1 = 9$.

as Magnevist, ProHance, Dotarem, and Gadobutrol (with r_1 values in the 3.6-5.2 mM^{-1} s^{-1} range) [173]. In addition to their MRI contrast enhancement capabilities, MnO^{pyrr} was shown to exhibit photoluminescence and have lower cytotoxicity than commercial Gd^{3+}-based contrast agents, which may harness multiple complementary imaging protocols for fast and accurate diagnosis and prognosis of disease [43].